MULTI-FREQUENCY PASSIVE MICROWAVE AND

DUAL-FREQUENCY RADAR REMOTE SENSING OF SNOWFALL

by

Benjamin T. Johnson

A dissertation submitted in partial fulfillment of

the requirements for the degree of

Doctor of Philosophy

(Atmospheric and Oceanic Sciences)

at the

UNIVERSITY OF WISCONSIN – MADISON

2007

UMI Number: 3294163

INFORMATION TO USERS

The quality of this reproduction is dependent upon the quality of the copy submitted. Broken or indistinct print, colored or poor quality illustrations and photographs, print bleed-through, substandard margins, and improper alignment can adversely affect reproduction.

In the unlikely event that the author did not send a complete manuscript and there are missing pages, these will be noted. Also, if unauthorized copyright material had to be removed, a note will indicate the deletion.

UMI®

A dissertation entitled

Multi-frequency Passive Microwave and
Dual-frequency Radar Remote Sensing of Snowfall

submitted to the Graduate School of the
University of Wisconsin-Madison
in partial fulfillment of the requirements for the
degree of Doctor of Philosophy

by
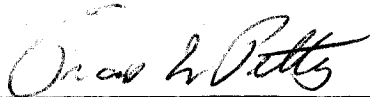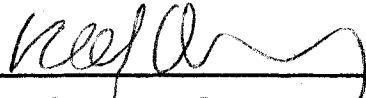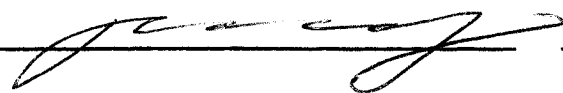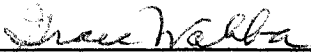
Benjamin T. Johnson

Date of Final Oral Examination: 12/10/2007

Month & Year Degree to be awarded: **December** 2007 **May** **August**

****

Approval Signatures of Dissertation Committee

Signature, Dean of Graduate School

ABSTRACT

MULTI-FREQUENCY PASSIVE MICROWAVE AND DUAL-FREQUENCY
RADAR REMOTE SENSING OF SNOWFALL

Benjamin T. Johnson

Under the supervision of Major Professor: Grant W. Petty

At the University of Wisconsin – Madison

In the middle and high latitudes, cold-cloud precipitation systems are dominant, consisting of snowfall above the freezing level and rain below. Accurate measurement of precipitation, especially in these regions, is necessary to understand and close the global water cycle and energy budget. However, cold-cloud precipitation events are poorly understood in terms of our ability to accurately retrieve and simulate their physical properties; this is partly due to a lack of field studies, suitable instrumentation, and global coverage.

The present research describes a novel precipitation retrieval algorithm using combined radar and radiometer observations of snowfall. The algorithm retrieves a 1-D vertical distribution of precipitation rate, particle size, particle density, and cloud liquid water content using aircraft- or satellite-based co-located dual-wavelength radar and passive microwave radiometer observations.

The primary basis for the retrieval has both a radar and radiometer component. A radar observing precipitation at a single wavelength is sensitive to both the number and physical size of the precipitation particles. The signal from a dual-wavelength

radar, in this case operating at 2.2 cm (13.4 GHz) and 0.84 cm (35.6 GHz), observes the same number of particles. The ratio of the two reflectivities is, therefore, sensitive primarily to particle size. Assuming an exponential particle size distribution and spherical simulated particles, the two parameters of the distribution, N_0 (intercept) and Λ (slope), can be retrieved. However, the particle composition (e.g., density) is generally unknown. To address this, a co-located passive microwave radiometer, operating at 89, 150, and 220 GHz, provides a brightness temperatures, which are sensitive to the phase, size, composition, and spatial distribution of precipitation. The radiometer brightness temperatures, compared with forward model brightness temperature simulations of the radar-retrieved 1-D profiles, provides a necessary constraint on the radar retrieval.

The 2003 Wakasa Bay field experiment over the Sea of Japan provided several high-resolution observations of snowfall using aircraft-based instruments compatible with the present technique. The dual-frequency APR-2 radar operated at 13.4 and 35.6 GHz, while the co-located the MIR radiometer made cross-track passive microwave observations of brightness temperatures at 89, 150, 220, 183.3±1, 183.3±3, 183.3±7, 220 and 340 GHz. The observations are used to test the present retrieval algorithm.

There are two primary results of this research: First is the description of an new, end-to-end, 1-D forward model for simulating the vertical profile of precipitating clouds and the subsequent radar/radiometer response. Second is the retrieval and parameterization of snow particle properties, representing a broad distribution of precipitating snow clouds over the Sea of Japan. Retrieved characteristic particle size, $D_0 = 3.67/\Lambda$, was found to follow a Gamma distributed with a mean value of 1.6 mm and a standard deviation of 0.6 mm. Retrieved N_0 values were normally distributed in $\log_{10}(N_0)$, and had a mean of 0.1 cm^{-4}, with the standard deviation ranging from 0.006 to 1.6 cm^{-4}.

Derived precipitation rates (at all levels) ranged from 0.6 to 16 mm h^{-1}, with a mean of 3.2 mm h^{-1}. For selected particle density values, agreement with published Z_{35}-R relationships were observed.

The techniques described here are being developed with an eye toward the future satellite-based Global Precipitation Measurement Mission (GPM). Parameterizations based on these retrievals are already being used to identify and communicate the key characteristics of cold-cloud precipitation to the larger remote sensing and climate modeling community.

ACKNOWLEDGMENTS

This dissertation is dedicated to "Shinie",

for her love and encouragement at times when I deserved neither.

TABLE OF CONTENTS

LIST OF TABLES

LIST OF FIGURES

1 INTRODUCTION

1.1 Synopsis

On a global scale, precipitation is a critical part of the atmospheric water and energy cycles. On a local scale, precipitation has important influences on natural water resources and atmospheric energy exchange through latent heat release. Therefore, accurate global estimation of both precipitation occurrence and intensity is essential to improving our understanding of these processes (Simpson *et al.*, 1996). However, ground based methods, such as radar and rain gauges are limited in coverage; whereas satellite-based platforms can, depending on their orbit, make global observations of precipitation.

In the middle and high latitudes, a substantial portion of precipitation reaches the surface as snow (Adler *et al.*, 2003). In contrast to rainfall, snowfall is traditionally difficult to accurately quantify using standard precipitation retrieval techniques (Skofronick-Jackson *et al.*, 2004). Broadly speaking, the present research seeks to improve our understanding of not only the physical properties of falling snow, but also the response of microwave radiation incident upon snow in the atmosphere. This is accomplished via a novel snowfall retrieval algorithm, which takes advantage of the synergy between active radar observations, passive microwave radiometer observations, and snowfall simulations. The details of the retrieval algorithm and simulation method are described in detail in the following chapters.

In recent decades, satellite-based passive microwave (PMW) observations have been employed as a method for reliably detecting and quantifying precipitation, particularly

surface precipitation rate, on a global basis (Adler *et al.*, 2003). Observations made by PMW radiometers operating in the microwave and submillimeter ranges of the electromagnetic spectrum sense radiation emitted from the surface and lower atmosphere. PMW radiometers measure the intensity of incoming radiation, which in the microwave range, is expressed in terms of a *brightness temperature* (T_B) (Petty, 2004). Unlike infrared observations, the microwave T_B is linearly related to the physical temperature of the scene being observed.

Standard microwave channel frequencies range from about 3 GHz or 10 cm wavelength, up to 300 GHz or 1 mm wavelength. The number and quality of observing channels has also increased, providing detailed observations of clouds and precipitation in the atmosphere. The addition of millimeter- and submillimeter-wavelength channels on current and future missions provides a significantly improved sensitivity to smaller-sized precipitation particles and lower number concentrations (Skofronick-Jackson, 2003). In this dissertation, the term *precipitation hydrometeor*, or just *hydrometeor*, is often used interchangeably with "precipitation particles", meaning particles of liquid water or ice present in the atmosphere large enough to fall toward the surface.

More recently, satellite-based active radar has provided observations of the vertical structure of precipitating clouds, and has served as an important validation tool for PMW observations (Bauer, 2001). In contrast to PMW radiometers, which passively observe thermally emitted radiation, radars actively emit microwave radiation at select frequencies and measure the power reflected from precipitating clouds and the surface at multiple levels in the atmosphere. Specifically, the radar frequencies used in this research are 13.4 and 35.6 GHz, which are consistent with the dual-frequency radar onboard the proposed Global Precipitation Measurement Mission (GPM) satellite (Rose

and Chandrasekar, 2004; Smith, 2007). In broad terms, the dual-frequency radar has the capability to infer information about the particle size distribution throughout the vertical profile of the snow cloud (Meneghini *et al.*, 1997). This capability serves as the primary basis for the present retrieval.

As opposed to the vertically probing radar, PMW T_B observations represent a column-integrated response to the region of a precipitating cloud within the satellite's field of view. That is, the PMW signal includes contributions from all elements in the field of view, such as the surface, air, clouds, and precipitation. In a complementary fashion, coincident radar observations provide the vertical structure information lacking in the PMW observations. This provides for a more complete characterization of the precipitating cloud within the combined fields-of-view of the passive radiometer and the radar.

In general terms, a retrieval represents the process of seeking solutions to the *inverse problem*; that is, attempting to infer information about the precipitating cloud using a limited set of observations (Tikhonov and Arsenin, 1977). In the present case, the retrieval is also *ill-posed*: for a given set of observations, there is no unique solution (Hadamard, 1902). The solutions to the retrieval are constrained by a number of techniques, which reduces the ill-posedness of the problem.

In the opposite sense of the inverse problem, the *forward problem* describes the set of possible observations arising from a precipitating cloud using physical or statistical relationships. In practice, the forward problem is simulated through a series of models, collectively called a *forward model*. The forward model, described in chapter 2, is specifically designed to simulate radar reflectivities and passive microwave T_Bs originating from a simulated physical description of a 1-D column of the atmosphere. A

suitable snowfall retrieval algorithm requires an accurate forward model to establish key relationships between the observations and the physical properties of snowfall and the surrounding environment. The present forward model provides the primary physical basis for the retrieval algorithm.

The basic structure of the present forward model begins with a physical description of the 1-D column of the atmosphere, including precipitation properties. Next, the microwave response to the precipitation physical properties is computed using a radiative transfer model (RTM). The RTM consists of a hydrometeor model, which assumes a spherical shape for our simulated hydrometeors, describes the particle size distribution (PSD), and computes the Mie-derived optical properties, such as extinction, scattering, absorption, and radar backscattering cross-sections. The RTM then simulates the passive microwave brightness temperatures at the top of the 1-D column of the atmosphere, subject to the integrated response of upwelling microwaves to the precipitation present throughout the column. At each vertical level, the radar reflectivities are also computed. In short, the forward model provides simulated "top of the atmosphere" T_Bs and a vertical profile of radar reflectivites, as may be observed by a satellite-based passive microwave radiometer and radar, for a specified 1-D column of the atmosphere.

The following sections and chapters expand upon the above general descriptions, and provide the motivation for key goals of this research. In short, the primary goal of the present research is to retrieve and characterize the physical properties of snowfall, such as particle size and composition, using a dual-frequency radar retrieval algorithm constrained by co-located passive microwave observations and forward model simulations. The essential components of the present retrieval algorithm were designed to be

applicable to the upcoming GPM satellite, and were tested against the dataset obtained from the 2003 Wakasa Bay field experiment, described in chapter 5.

1.2 The Importance of Snowfall Measurement

Most of the geophysical and atmospheric cycles of Earth influence or are influenced by precipitation. Relevant to current climate change concerns, understanding and quantifying the global energy and water cycle depends on measurements of the spatial and temporal distribution of global precipitation (Chahine, 1992; Trenberth, 1998; Stocker *et al.*, 2001; Bosilovich *et al.*, 2005). Motivated by these concerns, combined with social, political, and economic pressures, great strides are being made to improve the observation and measurement of all aspects of the world climate, with precipitation being one of the most important and difficult aspects to accurately measure (Stocker *et al.*, 2001).

A key feature of precipitation in the continental regions is its contribution to surface hydrology. From an everyday perspective, the only significant source of freshwater renewal over land comes from precipitation, whether from rain or snow (Stocker *et al.*, 2001). At higher latitudes, precipitation often reaches the surface as snow, and the subsequent accumulations of snow during the cold season bring water for the warm seasons (Singh and Singh, 2001). On the ground, snow-cover also protects fragile flora and fauna from the bitter cold (Hansson and Henttonen, 1985). In the arctic regions, land-based glaciers and ice packs rely on long-term snowfall accumulation for replenishment (Singh and Singh, 2001).

In the marine environment, precipitation reaching the surface modifies the salinity balance in the upper layers of the sea, impacting the thermodynamics and fluid density

within the mixed-layer (Huang, 1993). On short time scales, energy and moisture fluxes are influenced by these changes (Huang, 1993). Over long time scales, the ocean circulation features are influenced by regions of persistent precipitation (or persistent evaporation) (Huang, 1993).

Precipitation is also a key indicator of latent heat release in the atmosphere: the thermodynamic exchange of energy resulting from the phase change(s) from water vapor to liquid or solid phase precipitation (Houze, 1989). The result of precipitation formation is a net heating of the local environment. Although latent heating is dominant in the tropics, where surface precipitation rates are significantly higher, the middle and high latitudes are affected through teleconnection patterns such as those associated with El Nino / Southern Oscillation (Tao *et al.*, 2001), and through local latent heat release (e.g., through midlatitude cyclone formation) (Rutledge and Hobbs, 1984). The associated local latent heat release often dominates all other heating sources, thereby strongly influencing local and regional thermodynamics and dynamics (Stocker *et al.*, 2001).

From a research perspective, knowledge of the global distribution of precipitation occurrence and intensity is extremely important for validating global modeling efforts such as general circulation models (GCMs) (Hulme, 1991). Despite recent advances in computer technologies, many of the intense and localized precipitation processes are not adequately captured by GCMs because they often occur at smaller scales than the resolution of the models (Pitman *et al.*, 1990). Therefore, improved knowledge of localized precipitation characteristics can benefit GCMs and other types of large scale models.

1.3 Physical Characteristics of Middle and High Latitude Snowfall

In the mid- to high-latitudes, the formation of clouds and precipitation differ significantly from that of tropical and warm-cloud precipitation (Houze, 1993). In the tropics, precipitation is primarily formed through vigorous convective activity; whereas in the middle and high latitudes, precipitation often originates from clouds formed due to regional lifting of air-masses, typically via frontal systems, such as the mid-latitude cyclone, and areas of large scale horizontal convergence. The term *stratiform* is used to describe these types of precipitating clouds due to the layer-like structure of the clouds (Houze, 1997). In addition to regional and frontal lifting, convective storms also produce stratiform cloud layers. For example, Houze (1997); Heymsfield *et al.* (1999) observe that mid-latitude stratiform precipitation is often found trailing convective events, while having a significantly larger horizontal extent and longer lifetime than the convective portion of the storm itself.

Figure 1.1 depicts the zonally averaged *occurrence* of near-surface light precipitation (< 1 mm h^{-1}) over the ocean obtained from Comprehensive Ocean-Atmosphere Data Set (COADS) ship-based observations (Woodruff *et al.*, 1998). A few important features are evident: The first is a general increase in light precipitation occurrence from low latitudes toward the poles. Second, at latitudes greater than 60 degrees, ice-phase and mixed phase precipitation occurrence is dominant compared to liquid-only precipitation. The observation of increased occurrence with respect to increasing latitude is consistent with observation that middle and high latitude precipitation tends to be horizontally widespread and persistent in time compared to precipitation at tropical latitudes, which are generally convective in nature (Houze, 1993, 1997; Heymsfield *et al.*, 1999). A third feature is that surface precipitation rates of less than 1 mm h^{-1} is

common at the middle and high latitudes. Generally speaking, lighter precipitation is associated with smaller particle sizes (Houze, 1993; Pruppacher and Klett, 1997), rendering it more difficult to detect with traditional passive microwave or ground-based radar observations (Evans and Stephens, 1995a).

Figure 1.1 does not give a direct indication of intensity, simply occurrence and phase (ice-phase, mixed, liquid) of light precipitation. To gain insight into intensity, fig. 1.2 indicates monthly average surface precipitation rate (mm/day) for all months from 2002-2005 using AMSR-E based retrievals (blue dashed line), and from 1998-2005 using TRMM-based retrievals (green solid line). Figs. 1.3 and 1.4 show the total rainfall accumulation for January 2003 and July 2003 respectively.

These figures, in combination with Fig. 1.1, indicate that while precipitation occurrence is common in the middle and upper latitudes, the intensity tends to be significantly lower than in the tropical latitudes. Furthermore, Fig.1.3 and 1.4 show that different retrieval methods can produce widely varying results, particularly in the mid-latitudes. All three of these retrievals: "Petty", "GPROF" (Kummerow et al., 2001), and "3B43" (Huffman et al., 1997), depend on models of the physical and radiometric properties of precipitation hydrometeors. Because of this, an unknown portion of the retrieval uncertainty arises from the choice of method used to describe the particle properties and the associated radiometric relationships. It is these types of uncertainty and lack of knowledge that partially motivates this research. More specifically, we seek to improve the understanding of the microphysical nature of the precipitation through retrievals of particle size and composition obtained from real observations of snowfall, which represents the most common light precipitation type (Fig. 1.1) in the regions of largest retrieval variations (Figs. 1.3 and 1.4).
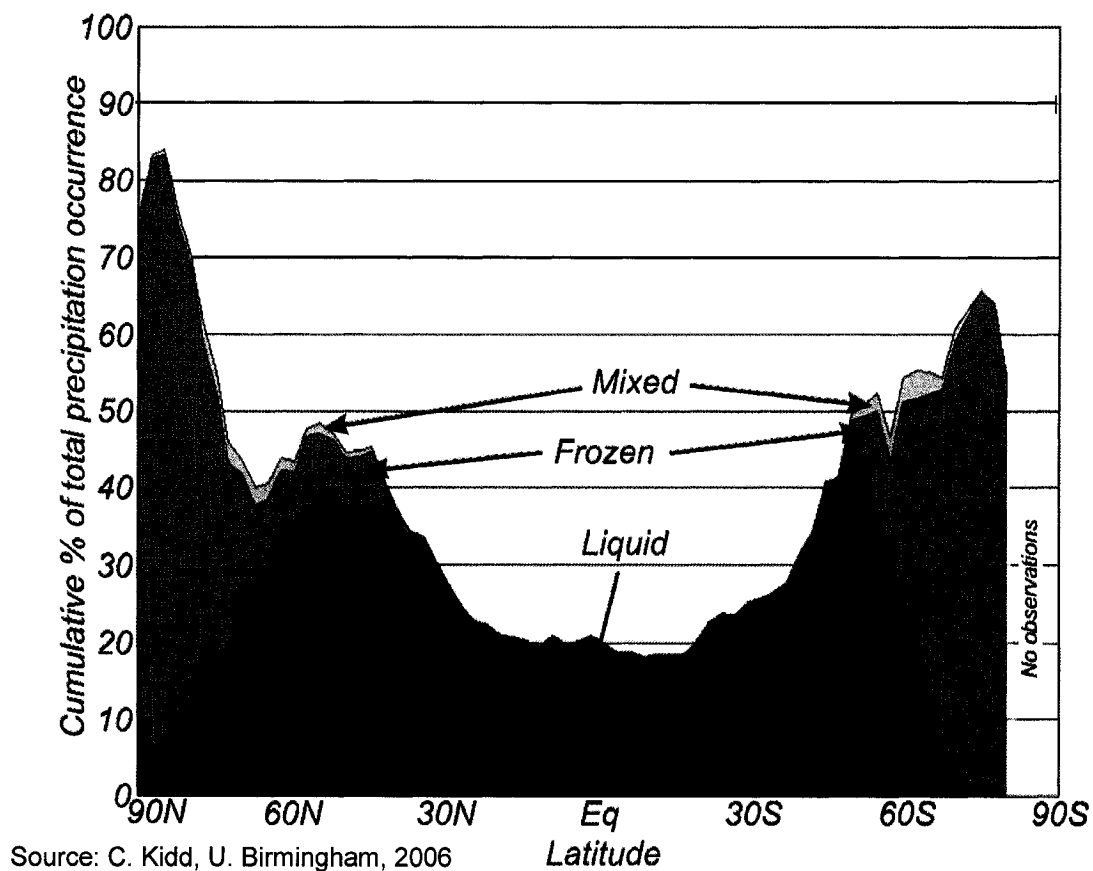
Figure 1.1. Zonally-averaged occurrence of light near-surface over-ocean precipitation (< 1 mm h^{-1}) for ice-phase (dark gray), mixed phase (light gray), and liquid (blue); obtained from COADS ship-based data. [Image courtesy of Dr. Chris Kidd, University of Birmingham; slightly modified from original.]
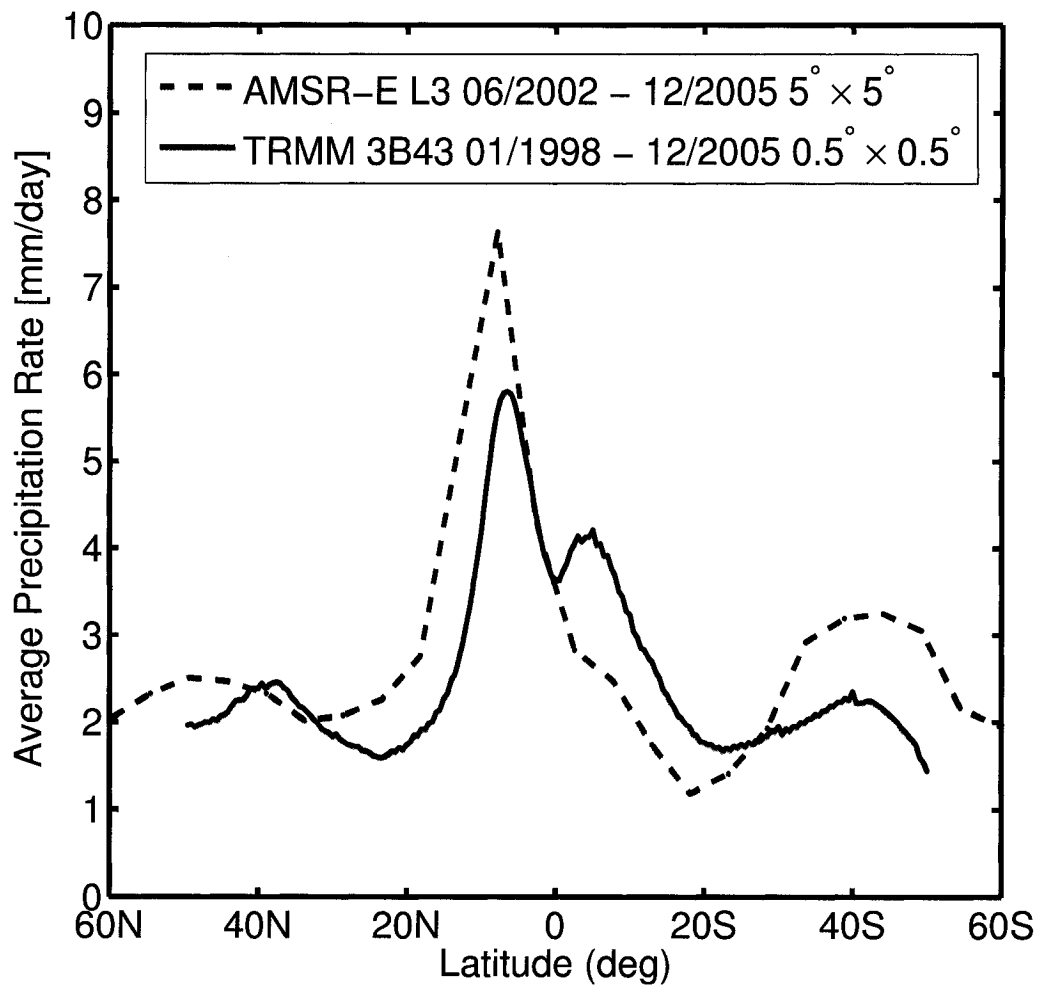
Figure 1.2. AMSR-E/AQUA monthly L3 5° × 5° rainfall accumulations, 06/2002 - 12/2005 (dashed line); and TRMM 3B43 0.5° × 0.5° rainfall accumulations 01/1998 - 12/2005 (solid line).
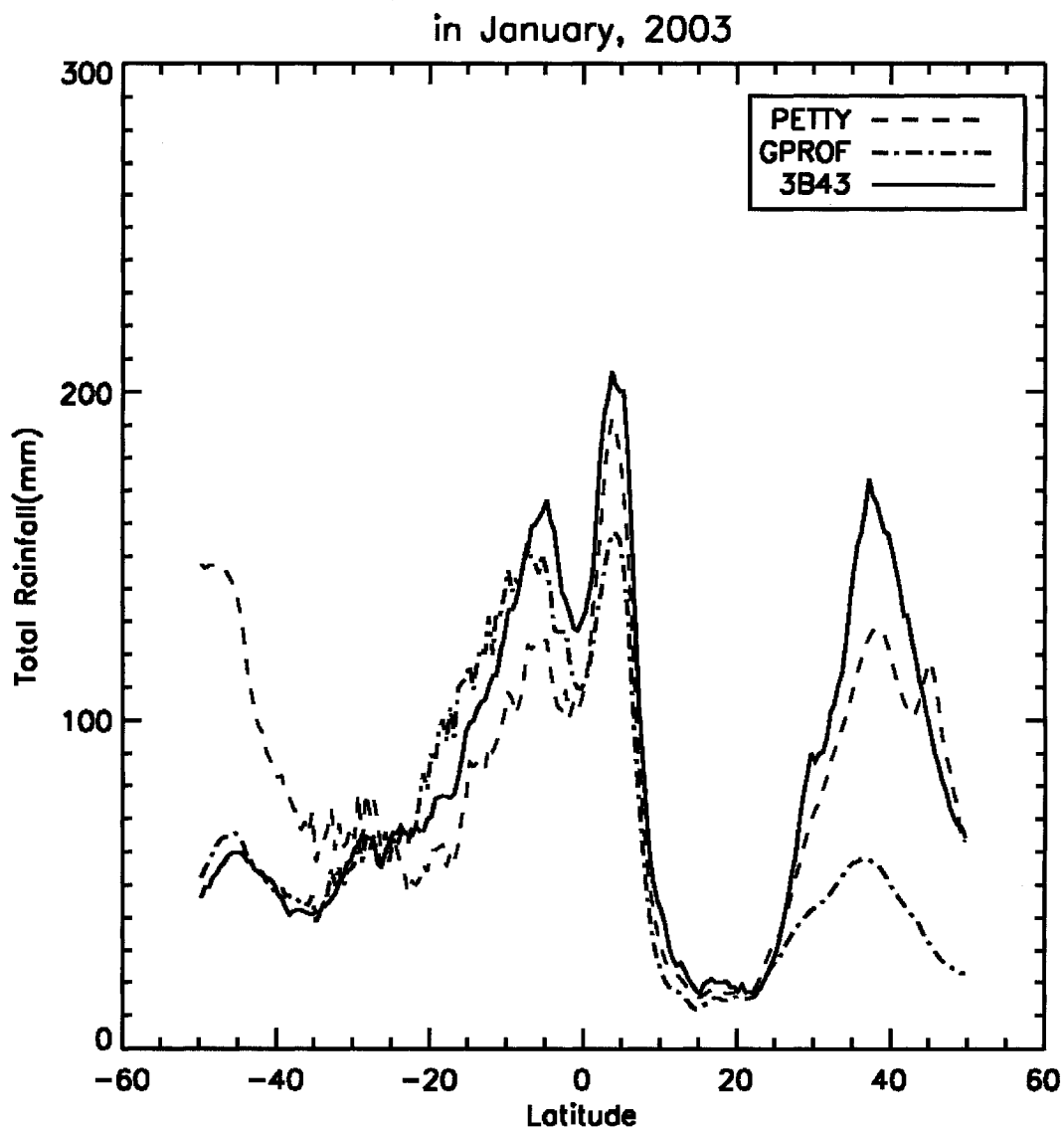
Figure 1.3. Comparison of zonally-averaged over-ocean precipitation accumulation for three major AMSR-E algorithms or products for January, 2003. The largest disagreements in this figure occur at higher latitudes where direct validation of ocean precipitation amounts has traditionally been unavailable, resulting in significant uncertainties in the retrieval methods [Petty, G.W., personal communication].
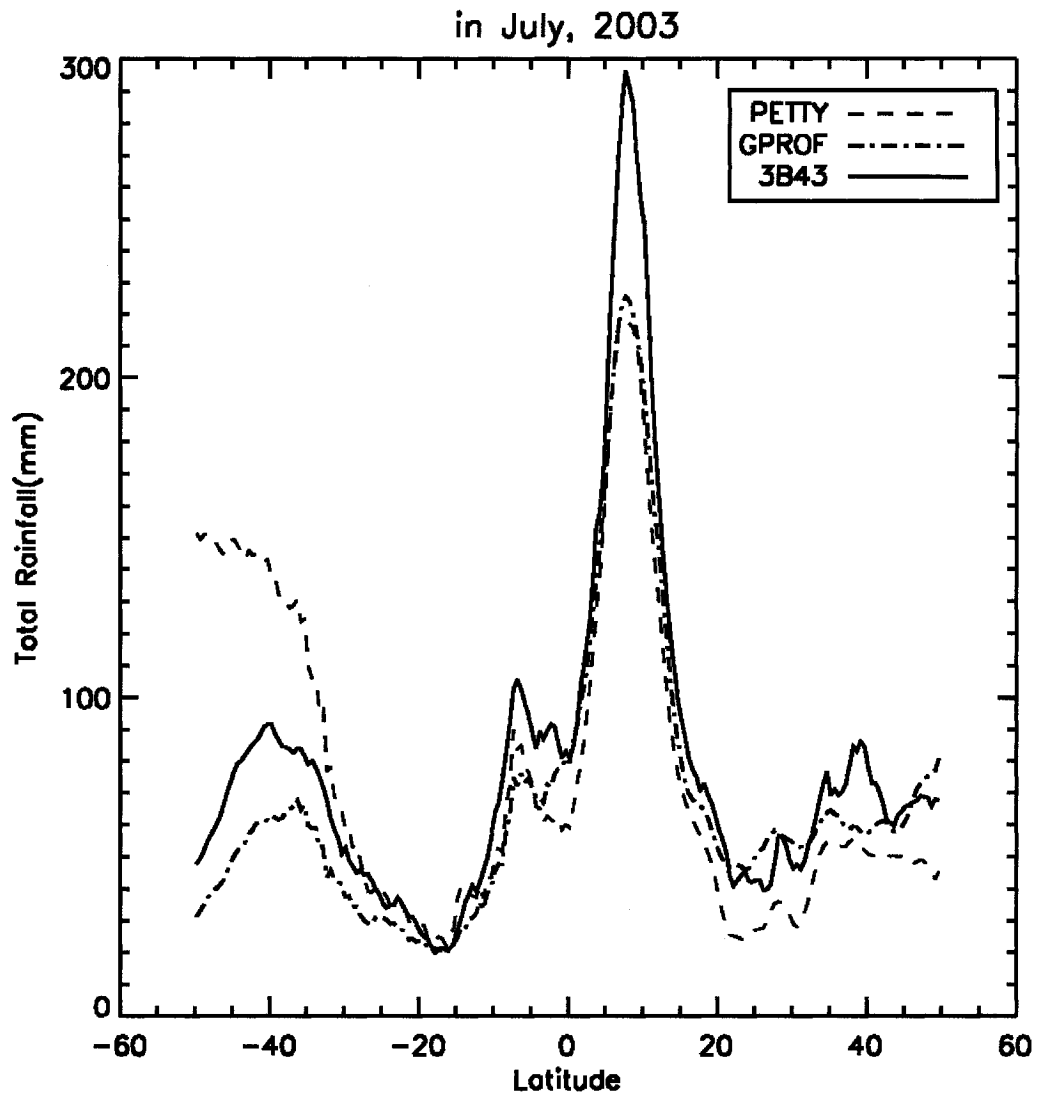
Figure 1.4. Similar to Fig. 1.3, except for July 2003. Of note is the apparent seasonal precipitation variation between January and July at middle and high latitudes for the southern hemisphere, i.e., Latitudes ¡ 0. [Petty, G.W., personal communication].

1.4 A Brief History of Snowfall Remote Sensing

In broad terms, remote sensing is the science and process of collecting observations of a remote scene and subsequently inferring information about that scene. A familiar example is human vision: we observe light scattered and emitted by objects both far and near. The brain interprets the subtle variations of the intensity and color of light arriving at the eye as information about the physical world around us.

Unlike the spectrum of colors we observe with our eyes, microwave remote sensing observes only a select few frequencies of microwave radiation. As mentioned previously, microwave remote sensing is divided into two areas: passive and active. Passive microwave remote sensing collects and analyses microwave incident upon the sensor (a radiometer) at specific frequencies. The microwave radiation in the passive case originates from external sources. On the other hand, active remote sensing, also called radar remote sensing, emits pulses of microwave radiation and measures the power returning from the various objects in the scene, such as precipitation, clouds, and the surface.

In this dissertation, the general precipitation remote sensing approach consists of a dual-frequency active radar retrieval technique with additional constraints supplied by passive microwave radiometer observations. Traditionally microwave-based precipitation retrievals have used passive microwave remote sensing. While this dissertation does not prescribe a specific passive microwave remote sensing retrieval method, it is expected that the results will directly benefit existing and future passive microwave algorithms by providing improved accuracy in the physical and radiometric relationships employed within the standard algorithms. Looking toward the future, co-located satellite-based radar and radiometer observations will be available from GPM, provid-

ing an unprecedented detailed look at the 3-D structure and temporal character of both rain and snow around the globe.

The following sections briefly describe the history of passive and active microwave remote sensing, with a focus on snowfall retrieval.

1.4.1 Passive Microwave Remote Sensing

The nature and applications of the passive microwave response to precipitation over both land and ocean have been well documented in the literature. This section provides a historical development of passive microwave (PMW) remote sensing of precipitation, with an emphasis on snowfall detection, using passive microwave observations.

Key Physical Principles

Casually speaking, upwelling microwave radiation from the surface and atmosphere is most strongly influenced by precipitation hydrometeors having sizes comparable to the wavelength of the radiation. Ice phase precipitation is a poor absorber/emitter of microwaves, but a strong scatterer. Water phase precipitation is both a strong absorber/emitter and scatterer. This difference is the primary basis for the inference of ice and liquid phase precipitation in passive microwave retrievals.

Cloud droplets, however, are much smaller than most wavelengths used in standard microwave remote sensing channels. Therefore, non-precipitating clouds are normally transparent to microwaves. With decreasing wavelength (increasing frequency), the influence of a non-precipitating cloud becomes stronger, acting to absorb/emit microwave radiation.

The ability to "see" through clouds provides microwave remote sensing with a unique advantage of having a direct relationship between the observed radiation and the precipitation itself. This is in contrast with other common remote sensing bands, such as visible and infrared, which observe radiation either respectively scattered by or emitted from the tops of clouds, with no direct relationship with underlying precipitation (if present).

Another key advantage of microwave radiation, compared to visible and infrared, is the nearly linear relationship between observed brightness temperature and the physical temperature of the scene. This results in simplified physical relationships in retrieval algorithms and improved calibration accuracy for microwave radiometers. The linear relationship, assuming the Rayleigh-Jeans approximation is valid (section 2.2), can be simply expressed as $T_B = \varepsilon T$, where ε is the emissivity, and T is the physical temperature. The *emissivity* of an object describes the ratio of the intensity of emitted radiation to the radiation that would be emitted by a theoretical perfect emitter having the same physical temperature. ϵ ranges from 0 to 1, i.e., no emission to "perfect" blackbody emission at a specific wavelength of radiation. For further details. see section 2.2 or, for example, Liou (2002); Petty (2004).

Another key feature of microwave radiation is the large range of variability of the emissivity of the land and ocean surfaces. The emissivity of the ocean surface at a nadir viewing angle, i.e., $0°$, ranges from approximately 0.3 at 3 GHz to 0.8 at 300 GHz. The emissivity of the land surface over the same frequency range and viewing angle is typically much closer to unity, but exhibits spatial variations according to soil moisture, snow cover, vegetation, surface type, and other factors. At off-nadir viewing angles, the emissivity of the ocean surface exhibits a strong linear polarization,

where the vertically polarized T_Bs are larger than the horizontally polarized T_Bs for all frequencies (Petty, 2004). Land observations, however, exhibit negligible polarization differences at any viewing angle or microwave frequency, although significant bodies of water may introduce polarization differences (Hewison and English, Jul 1999) at off-nadir angles. For the passive microwave observations used in this research, all observations are made over the ocean at a nadir viewing angle, and the emissivity of the ocean surface ranges from approximately 0.65 at 89 GHz to 0.75 at 220 GHz.

A common disadvantage of microwave compared to shorter wavelength observations, is that the intensity of observed radiation is significantly smaller than visible and infrared for the same field of view (FOV). If one imagines a cone with the point at the radiometer and the base intersecting the surface of the Earth, the FOV is, loosely speaking, the area of the intersection of the base of the cone. However, in order to collect enough microwave radiation to overcome noise, the area of the FOV is typically on the order of dozens of kilometers for long microwave wavelengths. Fortunately, as the wavelength decreases, the field of view can also decrease, resulting in improved spatial accuracy.

For precipitation remote sensing, the large FOV also means that sub-scale variability in observed precipitating clouds is not observed. The observed brightness temperature, therefore, represents an average across the FOV. The term commonly used for these types of observation is called the "beamfilling effect", i.e., the observed FOV may not be completely "filled" with a precipitating cloud. Generally this issue is more of a concern in tropical environments, where the spatial distribution of precipitating clouds tend to be much more widely varied than in the middle and high latitudes (Houze, 1993).

These topics are further described in the following sections, beginning with a historical development of passive microwave sensors used in both rain and snowfall detection.

Historical Development

A number of passive microwave radiometers have been used for precipitation estimation since the early 1970s. The Electronically Scanning Microwave Radiometer (ESMR, Wilheit (1972)) was first flown on the Nimbus-5 platform in 1972 and again on the Nimbus-6 platform in 1976. ESMR was a single channel, cross-track scanning, passive microwave radiometer that observed at a horizontally polarized frequency of 19.35 GHz, with a 25-by-25 km resolution at nadir, expanding to 160 km at the scan edge. The second ESMR, flown on the Nimbus-6 platform, was a two channel passive microwave radiometer operating at 37 GHz, with one channel measuring vertical and the other measuring horizontal polarization – obtaining some of the earliest polarized microwave observations of the atmosphere and surface from space.

One of the earliest precipitation retrieval methods, developed by Wilheit *et al.* (1977), was based on the assumption that brightness temperatures over the ocean could be quantitatively related to surface precipitation rate by means of a two-parameter physical model. The 19.35 GHz ESMR data was used in conjunction with rain gauge and radar data to validate the model. The "Wilheit model", variations of which are still in use, employed a 1-D vertical framework wherein rain concentration, with sizes described by the Marshall-Palmer distribution (Marshall and Palmer, 1948), is constant from the freezing level to the surface. Cloud water is modeled as an absorbing layer below the freezing level, with a fixed amount of cloud water. The key result is that at 19.35 GHz, a precipitating cloud over ocean emits relatively warm brightness temper-

atures (emissivity near 1) as compared to the radiometrically cold ocean background (emissivity near 0.4), allowing for the discrimination and quantification of rainfall rate.

Figure 1.5 illustrates the modeled relationship between T_B and Marshall-Palmer rain rate R for various freezing level heights.

Despite leaving out a variety of factors, such as water vapor and viewing angle, Wilheit *et al.* (1977) provides a novel model that is applicable to the inference of light to moderate surface precipitation rates 1-20 mm h^{-1} over the ocean. At high rainfall rates (> 20 mm h^{-1} , larger drop sizes), the 19.35 GHz signal becomes saturated (no surface emission through the precipitating cloud), and brightness temperatures begin to decrease again resulting from enhanced scattering.

Weinman and Guetter (1977) used the 37 GHz vertical (V) and horizontal (H) channels on the Nimbus-6 ESMR to observe rainfall over land and ocean. In particular they found that radiances emerging from precipitating clouds over water were weakly polarized (i.e., small 37V-37H) in comparison to surface water, such as lakes, which emits strongly polarized radiation. They also suggest a simple "polarization-correction" which eliminates the T_B contrast between land and water, and produces a monotonic relationship between observed T_Bs and surface precipitation rate compared to the non-monotonic relationship shown in figure 1.5. This concept was further extended by later researchers (Spencer *et al.*, 1989; Petty, 1994a; Kidd, 1998).

The first *multifrequency* radiometer was the Scanning Multi-channel Microwave Radiometer (SMMR, Gloersen and Barath (1977)) on-board the Nimbus-7 and SEASAT platforms, launched in 1978. The SMMR observed at 6.63, 10.69, 18.0, 21.0 and 37.0 GHz frequencies with vertical and horizontal polarizations for each channel. Using SMMR observations, (Spencer *et al.*, 1983) found unusually cold brightness tempera-
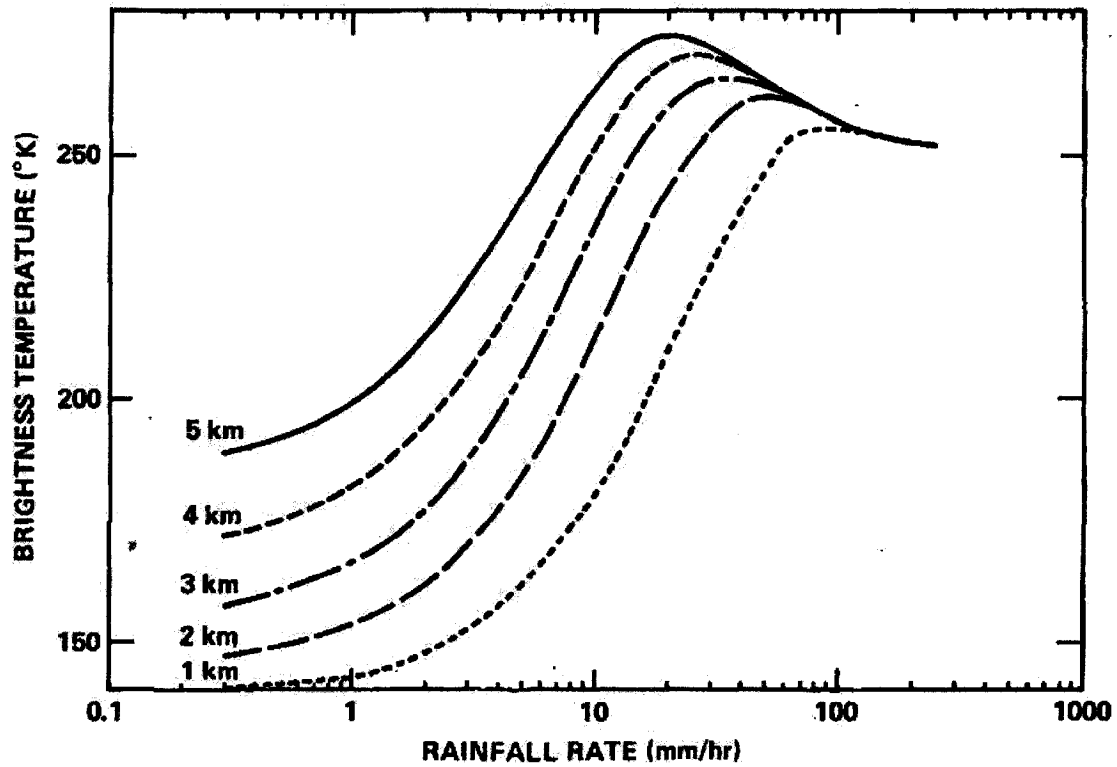
Figure 1.5. Calculated brightness temperature at 19.35 GHz horizontal polarization as a function of rain rate for freezing level heights ranging from 1 to 5 km (Wilheit *et al.*, 1977).

tures at 37 GHz over land. These cold T_Bs were correlated with surface observations of "heavy rainfall", and attributed T_B depressions to scattering by precipitation sized ice particles above the raining layer. Therefore, observed T_Bs of precipitating clouds originate not only from the emission by precipitation, but scattering plays a factor when large ice particles are present such as is the case in large convective storms.

At least three relevant concepts can be inferred from the previously described observations. First, the vertical distribution of both ice-phase and liquid hydrometeors influences upwelling microwave radiation, rather than liquid precipitation alone. Second, the observed T_B depressions due to scattering by ice-phase particles resulted in the separation of PMW precipitation retrieval algorithms into two categories: emission-based algorithms, which rely on warm emission of precipitation over radiometrically cold, polarized backgrounds; and scattering-based algorithms, which infer surface precipitation rate according to the magnitude of scattering induced T_B depression (Wilheit, 1986). Third, by comparison of 18 GHz and 37 GHz observations, Spencer *et al.* (1983) found that partially filled fields-of-view can lead to retrieval biases of surface precipitation rate. This would later be described as the "beamfilling effect", see for example: Kummerow (1998); Kummerow and Poyner (2004); Petrenko (2001). These three concepts are central to many physically-based PMW precipitation retrieval algorithms to date.

In 1987, The U.S. Department of Defense introduced the Special Sensor Microwave Imager (SSM/I) on their 5D-2 satellite platforms. The SSM/I is a seven channel, four frequency, linearly polarized, passive microwave radiometer. The instrument measures brightness temperatures at 19.3 GHz, 22.2 GHz, 37.0 GHz and 85.5 GHz (Hollinger, 1989). The instrument is conically scanning with a viewing angle is 53.1 degrees. The

addition of the 85 GHz channel improved the sensitivity to volume scattering by ice particles above that of the 37 GHz channel.

Spencer *et al.* (1989) exploited the fact that optically thick, precipitating clouds exhibit very low polarization differences ($T_{B,V} - T_{B,H}$) using SSM/I's 85 GHz channel in comparison to the ocean which exhibits a strong polarization difference. They employ the polarization corrected temperature (PCT) concept for identifying regions of strong scattering while minimizing the sensitivity to T_B variations resulting from, for example, liquid water or water vapor. These indices serve as a useful indicator of volume scattering by ice particles independent of background T_B variations and as an indicator of column optical depth respectively.

A number of studies using the SSM/I for precipitation retrievals (among many other topics) were published in the 1990s [for example, Wilheit *et al.* (1991); Liu and Curry (1992); Prabhakara *et al.* (1992); Kummerow and Giglio (1994); Petty (1994b); Ferraro *et al.* (1996); Wentz and Spencer (1998); Schols *et al.* (1999); Prigent *et al.* (2001), and others]. Despite the multichannel capabilities of the SMMR, several studies involved only one or two channel algorithms. The SSM/I channels span both the emission and scattering regimes allowing for algorithms that could take advantage of both approaches, as done by (Petty, 1994b).

In the late 1980s and into the 1990s, several algorithm intercomparison projects were undertaken to compare the capabilities of several precipitation retrieval algorithms. The Precipitation Intercomparison Projects (PIP 1-3) described in Barrett (10-14 Jul. 1995); Smith *et al.* (1997); Adler *et al.* (2001), were primarily focused on comparing rainfall estimates for selected regions over both ocean and land. Similarly, the Global Precipitation Climatology Project (GPCP) Algorithm Intercomparison Projects (AIP

1-3) sought to improve precipitation algorithms as well, with a focus on obtaining an optimal merged product. Also, different validation techniques were used, compared to PIP Ebert *et al.* (1996).

PIP-1 found, in particular, that SSM/I-based precipitation retrievals were superior to infrared retrievals for obtaining monthly/large-scale precipitation averages, signaling the decline of using IR observations exclusively for precipitation retrieval (Barrett, 10-14 Jul. 1995). PIP-2 focused instead on high-resolution instantaneous surface precipitation rate retrievals. It was noted that, relevant to the current topic, that more physically realistic forward models were becoming necessary to further refine the the accuracy of precipitation retrieval algorithms (Smith *et al.*, 1997). PIP-3 returned back to the style of PIP-1, with an emphasis on evaluating global monthly precipitation fields. A relevant finding of PIP-3 was that many algorithms exhibited an apparent low precipitation retrieval bias for middle and high-latitude ocean regions, suggesting that validation datasets for these regions should be pursued to address the low bias (Adler *et al.*, 2001).

Consistent with PIP findings, the AIP projects also found that instantaneous PMW rainfall retrievals were generally more accurate than IR techniques for rainfall estimation. However, snowfall estimation was not a significant component of any of the PIPs, although AIP-2 did include some snowfall events over both land and ocean (Ebert *et al.*, 1996). Specifically, AIP-2 found that the SSM/I algorithms underestimated light precipitation over ocean, which likely included snowfall cases, although it is not explicitly discussed in any of the AIP literature.

The study by Schols *et al.* (1999) of the microwave properties of ice-phase precipitation around a north Atlantic cyclone is particularly relevant to this dissertation. Using

SSM/I data, they compared the microwave observations of cumulonimbus clouds east of the cold-front within the cyclone with nimbostratus clouds north of the low pressure center. Generally, cumulonimbus clouds are short-lived, strongly convective clouds, associated with locally heavy rainfall. Nimbostratus clouds are longer lived, with a more horizontally distributed cloud layers with light precipitation. Using the mesoscale cloud model MM5, they simulated the cyclone to attempt to infer the microphysical structure of the storm. In their study, the results suggested that snow aggregates, with densities that decrease with increasing size, were required to simulate the observed brightness temperatures observed in the nimbostratus clouds. These inferences support the concept that the particle composition (fraction of ice vs. air) is an important factor in simulating T_Bs consistent with observations.

More recently in November 1997, the Tropical Rainfall Measurement Mission (TRMM) satellite was launched (Simpson *et al.*, 1996). The TRMM Project is a joint effort between Japan and the United States to measure rainfall over the tropics. The TRMM satellite orbits between 35° N and 35° S, confining most of the precipitation observations to the subtropics and tropics. The TRMM satellite carries a suite of sensors, including the TRMM Microwave Imager (TRMM-TMI) and first spaceborne active Precipitation Radar (TRMM-PR). TMI is a 5-channel, dual-polarized, passive microwave radiometer. The TMI measures passive microwave radiation at frequencies of 10.7, 19.4, 21.3, 37, 85.5 GHz.

The operational precipitation algorithm for TRMM TMI is the Goddard Profiling Algorithm (GPROF), described by Kummerow *et al.* (2001). GPROF relies on a large statistical database of physical profiles and associated radiances to correlate with observed radiances using Bayesian statistical techniques. However, for the mid-latitudes,

Masunaga *et al.* (2002) finds "An excess of PR over TMI (GPROF) in near-surface [precipitable water content] PWC is identified in the midlatitudes (especially in winter) ... these inconsistencies arise from TMI (GPROF) underestimating the near-surface PWC in midlatitude winter." From figure 1.2, we also saw discrepancies in TRMM surface precipitation rates vs. AMSR-E surface precipitation rates, which is especially evident at southern hemisphere middle latitudes. The key element of discrepancy tends to point toward microphysical assumptions in retrieval models, rather than satellite bias or other technical factors (e.g., Negri *et al.* (1995), as applied to the GPROF). It was these indications of deficiencies at mid-latitudes that motivated the present research.

Following the continued success of the TRMM satellite, the Advanced Microwave Scanning Radiometer (AMSR-E) was launched on May 4, 2002, aboard NASA's Aqua spacecraft. AMSR-E is a twelve-channel, six-frequency, passive microwave radiometer. It measures both horizontally and vertically polarized brightness temperatures at 6.9, 10.7, 18.7, 23.8, 36.5, and 89.0 GHz. The spatial resolution of each channel varies from approximately 5.4 km at 89 GHz to 56 km at 6.9 GHz. Similar to TRMM, GPROF is the operational precipitation retrieval algorithm. Unlike TRMM, the orbit of AMSR-E takes it into middle and high latitude regions, where GPROF retrievals tend to be deficient. Ice-phase precipitation detection remains an issue with AMSR-E. Despite nearly having global coverage, only the 89 GHz channel is sensitive to moderate and lighter snowfall rates.

The 2003 Wakasa Bay field experiment was designed specifically to examine the ability of AMSR-E to detect and quantify snowfall, and serves as a test-case for the present retrieval algorithm. Recent studies by G.W. Petty (personal communication) indicate that improved modeling of environmental parameters, combined with the use of

empirically tuned scattering indices (Petty, 1994a) at 89 GHz yields snowfall retrievals consistent with in-situ gauge measurements located at high-latitude island stations. These preliminary results indicate snowfall estimation using PMW-only algorithms is capable of good correlation and accuracy when precipitating cloud and local environmental properties are well characterized.

The present research is aimed toward developing a combined radar/radiometer global precipitation retrieval algorithm for use with the upcoming Global Precipitation Mission (GPM), scheduled to launch in 2013. The primary goal of GPM is to "develop a scientific understanding of the earth system and its response to natural and human-induced changes." The core observatory is uniquely instrumented with a conically-scanning radiometer (GMI), and a cross-track scanning Dual Frequency Precipitation Radar (DPR). The GMI instrument measures horizontally and vertically polarized passive microwave brightness temperatures at 10.65, 18.7, 23.8, 36.5, 89.0, 165.5 ± 3, and $183.31\pm3,9$. The addition of the high frequency channels is expected to provide a significantly enhanced capability to detect lighter surface precipitation rates consistent with common mid- to high-latitude precipitation types.

1.4.2 Active Radar Remote Sensing

Radar remote sensing of precipitation has a history longer than that of passive microwave observations. However, the use of radar onboard satellite platforms for precipitation detection began in earnest in 1997 with the launch of the TRMM satellite.

Key Physical Principles

In contrast to passive microwave remote sensing, which collects naturally emitted / scattered microwave radiation, radar active emits microwave radiation and measures the power of the microwave radiation reflected back toward the radar. The elapsed time of the return pulse is generally proportional to the distance from the radar, allowing for observations at multiple points along the path of the radar beam. Atlas (1990) provides a standard reference on radar remote sensing for meteorological applications.

In the descriptions that follow, a nadir/downward looking radar is assumed, such as would be found onboard an aircraft- or satellite-based platform. The primary observable of a radar is the reflectivity. Loosely speaking, the reflectivity is a measure of the ratio of received power of a pulse of microwave energy compared to the emitted power. Radar frequencies are typically chosen to minimize absorption by atmospheric gases and maximize the response to precipitation-sized particles. Standard ground-based weather radar has a frequency of 3 GHz, which is about 10 cm wavelength, where the reflectivity at 3 GHz is related to the diameter of the particles by equation 2.11. For smaller wavelengths, such as those used here, a more accurate accounting of the radar reflectivity is required – this is described in section 2.5.

Ice-phase particles, such as snow, are react differently from liquid particles, when observed by radar. In general, the reflectivity from ice-phase precipitation is smaller than liquid phase, this arises from the differences in the index of refrection of ice in water. In particular, liquid water generally has a slightly larger real component of the index of refraction than ice, implying that a water particle would reflect more radiation back toward the radar than would an ice particle of the same size. These relationships are further described in section 2.5.

The primary advantage of using radar for precipitation remote sensing is the ability to observe the vertical structure of a precipitating cloud. Combined with a suitable retrieval algorithm or "Z-R" (reflectivity-rainfall rate) relationship, estimates of the precipitation rate at multiple layers of the atmosphere, particularly the surface, are possible. This type of measurement is complementary to PMW retrievals, which indirectly infers the surface precipitation rate based on scattering or emission properties of a precipitating column of the atmosphere.

One disadvantage of radar is that it typically requires significant power levels to operate effectively, especially from a space-based platform, where power is limited. Therefore, the expenses associated with a radar can be significant compared to a passive microwave radiometer. A second disadvantage associated with precipitation retrievals is that the inferred precipitation properties depends strongly on the assumed relationship between the microwave radiation and the physical properties of precipitation. Furthermore, the two-way path-integrated attenuation by precipitation and clouds can be difficult to account for, requiring techniques to simultaneously account for the attenuation while retrieving particle properties (Meneghini *et al.*, 1997; Battaglia *et al.*, 2003).

A number of techniques have been developed to overcome these issues. The following sections presents a historical development of radar as used for precipitation detection and measurement and addresses the issues described above.

Historical Development

An important development in remote sensing technology came about during World War II at the Battle of Britain in 1940. Prior to this battle, there had been some

attempts at using microwave and radio frequencies to detect objects at a distance. Radio detection and ranging (radar), is an active remote sensing tool operating in the microwave band, initially developed for detecting and tracking aircraft. It was noticed by radar operators that precipitation within range of the radar led to noise on the radar screen, eventually leading to the development of radar being used in weather observation (Atlas, 1990).

Following the war, scientists extended their work in developing a use for the observed noise in the presence of precipitation. In the United States: David Atlas developed the first operational weather radar. Other developed countries quickly followed. Between 1950 and 1980, reflectivity radars (single frequency, single polarization) were built by weather services around the world. During the 1970s, radars were organized into formal networks. In 1964, the National Severe Storms Laboratory (NSSL) in Norman, Oklahoma experimented with dual polarization signals and on Doppler effect uses, leading to the next generation of weather radars.

Between 1980 and about 2000, weather radar networks became commonplace in many developed countries, with reflectivity radars being eventually replaced by Doppler radar to incorporate the added velocity information (among other features). In the United States, the network of next generation radars (NEXRAD or WSR-88D), began development in 1988. Canada, along with France and other European countries switched to Doppler networks by the early 2000s. Research on dual-wavelength and dual polarization radars moved into operational use, providing important additional information about the characteristics of the particles themselves.

One commonly observed feature of both ground and aircraft radar is the so-called "radar bright band" – a region of marked increase in a vertical profile of radar reflectiv-

ity. The bright band corresponds to regions in precipitating clouds where ice-phase precipitation is passing through the melting layer. The liquid water present on the otherwise ice-phase particles enhance the reflectivity of the falling snow particles (e.g., Fabry and Szyrmer (1999); Olson *et al.* (2001a); Battaglia *et al.* (2003)).

The following section continues with the development of radar, with a focus on combined radar/radiometer algorithms, such as the one described here.

1.4.3 Combined Passive and Active Remote Sensing

Prior to and following TRMM, several research radars have been incorporated into aircraft-based platforms, providing a mobile method for probing the vertical and spatial extent of precipitation (e.g., Heymsfield *et al.* (1996); Im *et al.* (2000)). TRMM provided first uses of combined radar/radiometer algorithms for space-borne precipitation retrieval (e.g., Olson *et al.* (1996); Haddad *et al.* (1997); Bauer (2001); Skofronick-Jackson *et al.* (2003), and others). Bennartz and Petty (2001) used co-located ground based radar and coincident SSM/I passive microwave observations to infer information regarding the properties of frozen particles. Their approach is conceptually similar to the present approach in that the radar data is used to retrieve particle properties, then the SSM/I brightness temperatures are computed based on those properties. Using the Scattering Index of Petty (1994a), they compare the simulated PMW T_Bs to the observed PMW T_Bs.

Historical Review and Physical Basis

The standard combined algorithm for TRMM, described in Haddad *et al.* (1997), first estimates rain profiles using the radar reflectivities, and subsequently constrains the inversion to be consistent with the radiometer-derived estimate of the total attenuation within the field of view. However, because there is only one radar frequency, two a priori assumptions, one about the particle size distribution and the other about the particle density are required to obtain adequate retrievals. Work continues on the combined radar-radiometer algorithm, with an eye toward adapting it to GPM retrievals (M. Grecu and W.S. Olson, personal communication).

Onboard the upcoming GPM satellite, the Dual Frequency Precipitation Radar (DPR) will operate at both 13.6 GHz (K_u-band) and 35.55 GHz (K_a-band). The K_a-band radar is expected to provide an improved sensitivity to snow and light rain (compared to TRMM-PR), serving as a validation point for the GMI high frequency channel observations described in the previous section. One key feature is the use of dual-wavelength radar observations, the ratio of which provides a direct relationship to particle size subject to certain assumptions (Meneghini *et al.*, 1997; Meneghini and Liao, 2000; Kuo *et al.*, 2004). This is contrast to the single frequency used on the TRMM-PR radar, which requires a priori knowledge or assumptions regarding the particle size distribution in order to perform retrievals.

The retrieval technique described in this dissertation differs from the TRMM combined algorithm(s) in the following key ways:

- A dual-frequency radar, rather than single-frequency radar is used to retrieve particle size distribution (PSD) properties of precipitation;

- The radar-based retrievals are the primary product, rather than the using the PMW retrieval first;

- PMW T_Bs are used to constrain the radar retrievals – unlike the previously mentioned studies, where radar is used to constrain PMW retrievals.

- The present technique has the advantage of a direct relationship between observation and the precipitation, whereas PMW retrievals are less direct. Although it remains unclear whether there is a distinct advantage to one approach vs. the other.

1.5 Scientific Objectives

With the above issues and concerns in mind, this dissertation addresses the following scientific objectives:

1. Construct a simple and accurate, end-to-end forward model to simulate both PMW radiances and radar reflectivities using established physical relationships;

2. Using the forward model, develop a multi-sensor method to retrieve the microphysical properties of ice-phase precipitation consistent with mid- to high-latitude cold-cloud precipitation types;

3. Quantify uncertainty in the elements of the forward model, simulated results, and retrieval methodology; and,

4. Characterize the retrieved snowfall properties in a way that is useful to the both modeling communities (e.g., GCM microphysics) and the remote sensing com-

munity for use in observations and retrievals of extra-tropical precipitating cloud systems.

The dataset obtained during the 2003 Wakasa Bay Field Experiment in the Sea of Japan (WBAY03) is used extensively in this dissertation to provide high quality in-situ, radar, and radiometric data (Lobl et al., 2007). As one of the few winter-time field experiments having co-located aircraft-based radar and radiometer data, WBAY03 provides a rare and invaluable source of information regarding extra-tropical/cold-cloud precipitation regimes. The resulting dataset is expected to provide detailed micro-physical/radiometric information to the passive microwave remote sensing community, so that existing and future models/retrieval algorithms might benefit from improved microphysical and radiative relationships.

1.6 Retrieval Approach

Given the above historical perspective and the stated scientific objectives, a qualitative description of the retrieval method is given here. The mathematical framework is provided in chapter 3.

A number of studies indicate that passive microwave remote sensing (PMW) methods developed for tropical precipitation retrieval have questionable accuracy when applied to mid- to high-latitude cold-cloud precipitation retrievals, for example, Negri et al. (1995); Vivekanandan et al. (1997); Schols et al. (1999); Adler et al. (2001); Skofronick-Jackson et al. (2004). One deficiency is in the characterization of the precipitation microphysics. A second deficiency is in the inaccurate accounting for environmental differences between tropical and extra-tropical regions. In the tropics, the

precipitation tends to be convective and often consists of intense rainfall; whereas higher latitudes tend to be more diverse, driven by large scale lifting and shallow convective mechanisms, producing lighter snow and rainfall (Houze (1993) and figures 1.2 to 1.3). These studies indicate that the tropical assumptions about particle size distribution, types of ice-phase hydrometeors, and rates of precipitation are not necessarily adequate in the mid- and high-latitude precipitation regimes.

By itself, passive microwave based precipitation retrievals attempt to relate the observed radiances or brightness temperatures (T_B), to some aspect of the precipitation, such as surface precipitation rate (R). These relationships are accomplished with varying degrees of success through a number of methods ranging from statistical correlations, for example, Spencer *et al.* (1983); Spencer (1986), to explicit physical relationships, for example, Petty (1994a,b); Wentz and Spencer (1998).

However, physically-based PMW retrievals involving ice-phase precipitation (e.g., snow, graupel, sleet) are complicated by uncertainties arising from the variety of particle types, sizes, and uncertainties regarding typical ice-phase particle size distributions; as well as a general lack of sensitivity to ice-phase precipitation at PMW frequencies in the 6 to 37 GHz range (e.g., Spencer *et al.* (1989)). Furthermore, T_Bs arising from these observations represent a column-integrated quantity, making it difficult to untangle the vertical distribution of precipitation.

One method to address this is by making higher-frequency passive microwave observations. For example, the 89 to 340 GHz range provides an improved sensitivity to smaller ice-phase particles, with a trade-off of also becoming more sensitive to atmospheric water vapor with increasing frequency due to continuum absorption (Janssen, 1993; Petty, 2004).

Another approach is to incorporate radar observations (when available) co-located with the passive microwave observations. As mentioned previously, radar has the advantage of observing the vertical structure of a precipitating cloud, and the observed reflectivities are directly sensitive to particle size (Vivekanandan *et al.*, 1997; Bauer, 2001). Dual-frequency radar observations at 13.4 GHz (2.2 cm) and 35.6 GHz (0.86 cm), combined with co-located with passive microwave observations at 89, 150, 183±(1,3,7), 220, and 340 GHz were obtained during the 2003 Wakasa Bay field experiment (WBAY03). WBAY03 is the subject of the snowfall retrieval case studies presented in chapter 5. The present retrieval technique was specifically designed to take advantage of these types of multi-frequency measurements.

To exploit the dual-frequency radar data, we follow the technique described in Meneghini *et al.* (1997), who provided a method for relating the ratio of radar reflectivities to particle size for various levels ("range gates") of the precipitating cloud. Physical relationships and standard assumptions allow for the retrieval of particle size distribution (PSD) parameters that are consistent with three radar observables: radar reflectivities at both frequencies, the ratio of the reflectivities, and the two-way path-integrated attenuation by the particles and atmosphere within the column being observed by the radar.

This results in a set of PSD parameters at each range gate – that is, a set of vertical profiles containing different retrieved microphysical properties while remaining consistent with the observed reflectivities. Additional considerations for cloud liquid water and assumptions about particle density are also required. These details are described in chapter 3.

To further constrain these profile-sets of retrieved PSD parameters, top of the atmosphere brightness temperatures are simulated for each vertical profile and compared to observed passive microwave brightness temperatures. The profiles that are consistent with the observed TBs within some tolerance are selected. The final result of the retrieval method is a set of profiles of PSD parameters that are consistent with radar reflectivities, passive microwave brightness temperatures, and model-simulated physical relationships.

1.7 Summary

The deployment and development of active and passive sensors in space, air, and on the ground is a testament to the increasing utility of these instruments and associated techniques for precipitation detection. Improvement of these precipitation retrieval techniques motivates the research presented in this dissertation. Embodied in the methods presented in the following chapters are both physical and statistical relationships linking the microphysical characteristics of ice-phase precipitation with the radiative characteristics as would be observed by remote sensing platforms.

A portion of the research presented in this dissertation describes a complete forward model for simulating a vertical profile of the atmosphere and computing the resulting passive microwave brightness temperatures and radar reflectivities. The forward model consists of a combination of both new and existing well-tested methods, all of which are described in chapter 2.

The retrieval method described in chapter 3 provides a robust characterization of the microphysical properties of extra-tropical/cold-cloud precipitation regimes, valid (at least) for the winter-time precipitation in the regions surrounding Japan. It is

expected that the relationships and datasets resulting from the retrieval technique, applied to WBAY03 data, will lead to improvements in snowfall retrievals outside the WBAY03 region as well.

The remaining chapters in this dissertation describe the detailed elements of the above goals and methods. Chapter 2 describes theoretical construction and specific elements of the forward model used in the simulations. Chapter 3 details the retrieval approach outlined above, providing a framework for which particle microphysical properties can be inferred from combined dual-frequency radar and radiometer observations. A detailed statistical analysis of retrieved quantities and associated uncertainties is presented in chapter 4. In chapter 5, the 2003 Wakasa Bay Experiment is described in detail and the dataset is used as a case-study for validating and analyzing the simulation and retrieval technique. The concluding chapter summarizes the major findings of the dissertation research, suggests how those findings can be disseminated to and effectively used by the remote sensing community, and poses the inevitable set of new questions that have come about during the course of research.

2   THE FORWARD MODEL

2.1   Introduction

In this chapter, the primary elements of the forward model are described. The forward model is composed of a series of models describing the physical and radiometric properties of a 1-D vertical atmospheric column. The goal of this forward model is to simulate the radar reflectivities and passive microwave brightness temperatures (T_Bs) for an atmospheric column containing precipitation. Portions of the forward model are used in the retrieval database described in chapter 3, and the entire forward model is used to simulate brightness temperatures T_Bs for retrieved profiles. The flowchart shown in fig. 2.1 identifies the key elements and relationships within the forward model.

In the following chapters, the term *parameters* is used to identify the quantities that are explicitly varied within the forward model and retrieval scheme. These are: the particle density parameter, n_ρ ; the cloud distribution parameter, n_β ; the cloud liquid water path, CLWP; and the near-surface wind speed, W. The term *retrieved properties* refers to the exponential particle size distribution properties obtained from the DWR-retrieval: that is, the slope, Λ; and intercept parameter, N_0. Λ is often expressed in terms of a mass-weighted mean diameter $D_0 = 3.67/\Lambda$, providing a characteristic size for the distribution. The term *derived* is applied to quantities not directly retrieved, but derived from the retrieved particle properties, such as ice water content (IWC) and precipitation rate (R). See equations 2.33 and 2.34.

However, before we get to these properties, the primary basis for the forward model and retrieval algorithm needs to be established. The following sections outline the
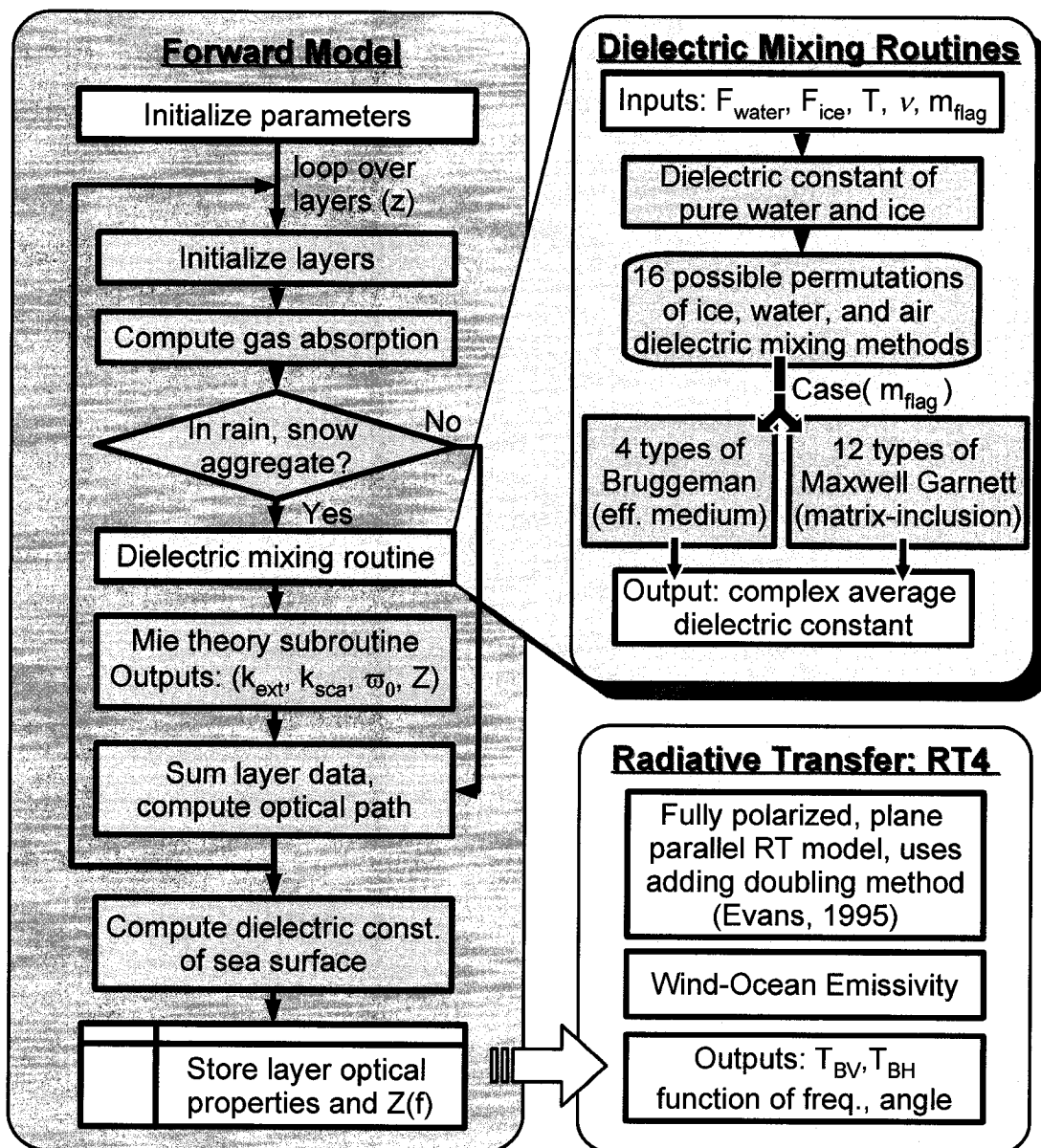
Figure 2.1. Schematic diagram depicting the elements of the forward model.

key elements of the forward model, which conceptually consists of a physical model of the atmosphere containing precipitation, a radiometric model which describes the interaction of microwave radiation with the precipitation, and a transfer model to tabulate the radiative properties throughout the entire 1-D vertical profile.

2.2 Thermal Emission

Terrestrial objects naturally emit radiation according to their physical temperature. The upper limit of thermal emission, as a function of temperature and frequency, is given by the Planck function (Janssen, 1993). Written as a function of frequency, it is

$$B_\nu = \frac{2h\nu^3}{c^2 \left(\exp\left[h\nu/(k_b T)\right] - 1\right)}, \tag{2.1}$$

where h is Planck's constant [J s], c is the speed of light in a vacuum [m s^{-1}], k_b is the Boltzmann constant [J K^{-1}], and T is the thermodynamic temperature [K]. See, for example, Petty (2004); Janssen (1993); Liou (2002) for the values of these constants. As written above, B_ν has units of [W m^{-2} sr^{-1} Hz^{-1}].

Gases, clouds, precipitation, ocean surfaces, and land surfaces, all having a temperature above absolute zero kelvin, emit microwave radiation according to the Planck function, modified by the object's *monochromatic emissivity* (ε). The monochromatic emissivity of an object is a measure, ranging from zero to unity, of how effectively a particular object emits at a specific frequency relative to blackbody emission at the same frequency (Petty, 2004). The microwave emissivity of the ocean near 89 GHz, for example, ranges from about 0.3 to 0.7, depending on a number of factors, some of which are listed below.

The microwave emissivity of an observed scene is generally a function of the following (Liou, 2002; Petty, 2004):

- thermodynamic temperature,

- material composition and dielectric properties,

- shape, roughness, and distribution of the emitters,

- concentrations of emitting materials (e.g., O_2, H_2O, clouds, precipitation)

- relative directions of observation and emission,

- frequency/wavelength of emitted radiation, and

- the polarization state of emitted radiation.

Each of these items are either explicitly accounted for in the forward model or parameterizations are used when detailed information or relationships are unavailable.

For a given observed intensity, solving the Planck formula (2.1) for temperature yields the *thermodynamic brightness temperature* also called *equivalent blackbody temperature*. This describes the temperature of a blackbody (emissivity equal to unity) having the monochromatic radiance B_ν, and is written

$$T_{\mathrm{EBB}} = \frac{h\nu}{k} \left[\log \left(2\frac{h\nu^3}{B_\nu\, c^2} + 1 \right) \right]^{-1} \tag{2.2}$$

A low-frequency approximation to Planck's formula can be made in the microwave region of the electromagnetic spectrum, simplifying the relationship between the temperature and radiance. In the low frequency limit $h\nu \ll kT$, the Rayleigh–Jeans

approximation to the Planck formula is given by (Liou, 2002; Janssen, 1993; Petty, 2004)

$$B_\nu \approx \frac{2\,\nu^2\,k\,T}{c^2}. \tag{2.3}$$

Solving for T yields the Rayleigh–Jeans brightness temperature, T_{RJ}. It is often employed in microwave remote sensing research due to the linear relationship between intensity and temperature – specifically, $T_{RJ} = \varepsilon\,T$, where ε is the emissivity of the material being observed. However, as the microwave frequency increases, the difference between T_{EBB} and T_{RJ} increases. For example, at 3 GHz the maximum absolute difference between the two is about 0.07K, 0.7K at 30 GHz, and 7K at 300 GHz. The term *brightness temperature* (T_B) is equivalent to T_{EBB} for the remainder of this dissertation. This quantity is used in all simulated passive microwave radiances. For a discussion of these definitions, see for example, Janssen (1993).

2.3   Radiative Transfer

Beyond the simple blackbody description, we are interested in how microwave radiation passes through and interacts with a region of the atmosphere containing a precipitating cloud. In the most general sense, three things can happen to microwave radiation that is passing through a portion of the cloud/precipitation: (1) it can be absorbed by gas, cloud, precipitation, or the surface; (2) it can be scattered by cloud, precipitation, or the surface; and (3) may can be transmitted, continuing along it's original path. Unimpeded, radiation may continue into outer space. Along with this simple picture, we note that all of the constituents of the surface and atmosphere are continually emitting microwave radiation, so the real process is an amalgamation of

directions, intensities, polarizations, of microwave radiation. The radiative transfer equation (RTE), described below, allows us to quantify this process. A radiative transfer model (RTM), is simply a computational implementation of the elements of the RTE.

For the present case, the layered structure of the forward model lends itself to the plane-parallel approximation for radiative transfer computations, shown in equations 2.4 and 2.5. A plane parallel atmosphere, is an approximation which assumes horizontally homogeneity in the region being computed. For the present cases, the plane parallel approximation is motivated by the computational convenience and consistence with observed cloud structures in chapter 5 which are relatively horizontally homogeneous on small scales.

The RTM implementation of the RTE used in this research is via a plane-parallel, adding doubling model, RT4, described by Evans and Stephens (1995b). The 1-D vertical geometry of RT4 provides a convenient method for computing the "top of the atmosphere" radiances for the 1-D profiles simulated by the microphysical model or arising from those profiles retrieved from the radar-retrieval method. For the ocean surface emission, RT4 has been modified to replace the standard Fresnel ocean surface emissivity/reflectivity model with the ocean surface emissivity/reflectivity model, incorporating the emissivity influence of near-surface winds described in section 2.4.1.

In equation form, the plane-parallel approximation is written following equation 11.13 in Petty (2004), it describes the incremental change in intensity of microwave radiation within an infinitely thin plane-parallel layer due to a source term J and

transmission term I. Because we're only observing at nadir, the viewing angle θ and azimuth angle ϕ are set to zero. It is written as,

$$\frac{dI}{d\tau} = I - J, \qquad (2.4)$$

where I is the intensity (or brightness temperature), τ is the optical depth of the layer. At nadir, we assume that the observed T_Bs are unpolarized, therefore 2.4 is a scalar equation. The source equation, J is

$$J = (1 - \varpi)B + \frac{\varpi}{4\pi} \int_0^{2\pi} \int_{-1}^{1} p(0, 0; \mu', \phi') I(\mu', \phi') d\mu' \, d\phi', \qquad (2.5)$$

where $\mu' = cos(\theta')$ and ϕ' are directions from which microwave radiation is scattered into the present path, and $p(0, 0; \mu', \phi')$ is the *scattering phase function*, which describes the probability distribution of microwave radiation being scattered in a given direction. B is the thermal emission arising from the Planck formula, defined by 2.1, for thermally emitted microwaves. The second term in 2.5, therefore, represents the contribution to the source term due to radiation scattered into the path of interest, typically the field of view of the radiometer. ϖ represents the *single scattering albedo*, a measure ranging from zero to unity of the ratio of scattering to the total extinction, where extinction is the sum total of scattering and absorption within a volume of the atmosphere.

$\varpi = 1$ implies perfect scattering, and the emission portion of 2.5 becomes zero, and vice versa when $\varpi = 0$, i.e., completely absorbing/emitting. For precipitation particles, ϖ depends on the size, shape, composition, phase, and frequency of radiation. $1 - \varpi$ is equivalent to the emissivity, defined in section 1.4.

Equations 2.4 and 2.5, when integrated over the entire path from surface to the top of the atmosphere, form the mathematical basis for the forward model. The remaining portions of this chapter describe the individual elements of each part of the source term,

i.e., the details of how we model each of the components, in particular the emission component and the scattering component.

The inputs to the RT4 model are the layer optical properties generated from the hydrometeor model, the thermodynamic properties from the 1-D physical model, and the surface properties derived from radiosonde and/or satellite observations. The output is the nadir brightness temperatures at the frequencies of interest.

2.4 Radiometric Response to the Atmosphere and Surface

Of interest for passive microwave remote sensing of precipitation are the bands of frequencies where the transmissivity of the atmosphere is generally high (i.e., low absorption of microwaves) called *window channels*. For example, regions from 1 GHz to about 50 GHz, and from 70 GHz to 110 GHz, are relatively transparent from space to the surface in clear sky cases (Liou, 2002; Petty, 2004). These bands are identified in fig. 2.2 for a relatively dry winter season atmosphere.

2.4.1 Surface Emission

In the absence of clouds and precipitation, the primary source of the upwelling thermal emission of microwave radiation is the surface, whether observing over land or ocean. Over land, the surface emissivity at most microwave window channels is typically near unity for dry surfaces, but can change significantly (and rapidly) with variations in vegetation, soil type, snow cover, etc. Over ocean typical ranges are from 0.3 to 0.7, depending on frequency, temperature, salinity, viewing angle, polarization, waves, and sea-foam coverage (Klein and Swift, 1977; Stogryn *et al.*, 1995; Guillou
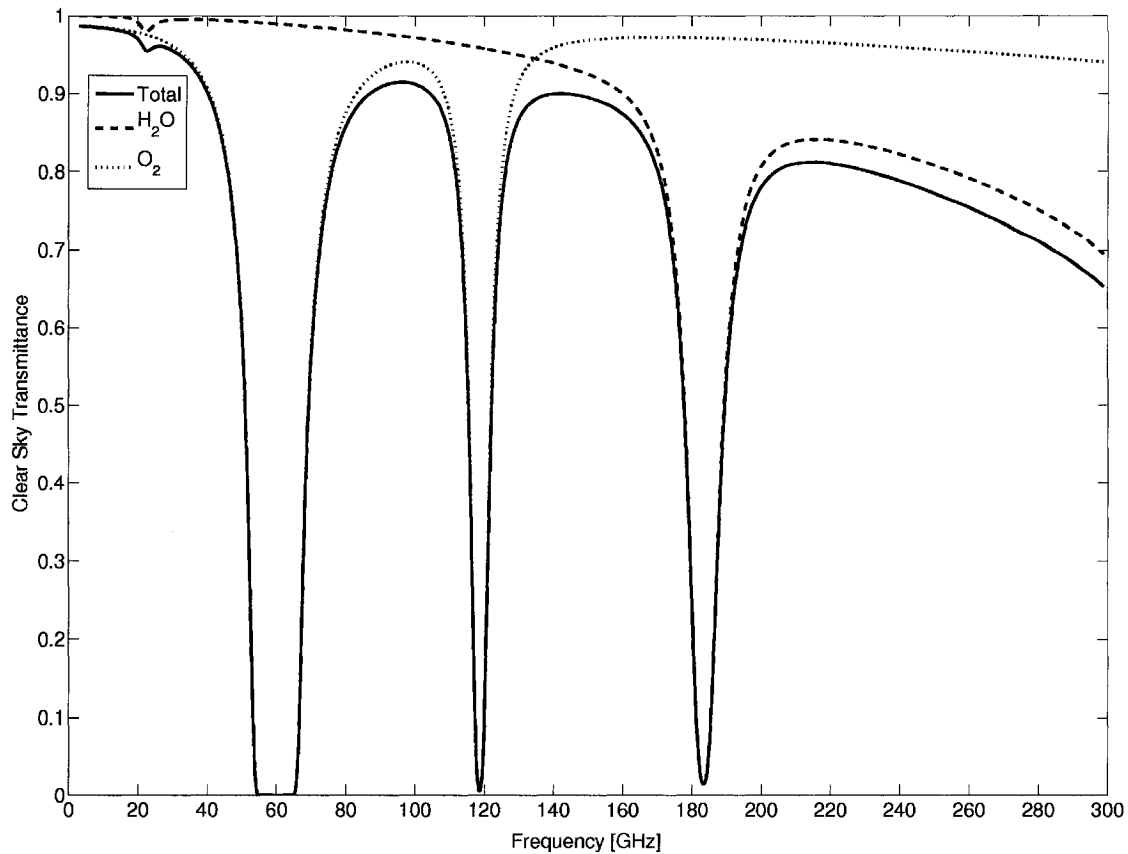
Figure 2.2. The cloud-free transmittance profile as a function of microwave frequencies between 1 and 300 GHz for a relatively dry atmosphere, typical of a winter season atmosphere. Oxygen (O_2) absorption bands are present near 60 GHz and 120 GHz, with water vapor absorption bands occurring near 22 GHz and 183 GHz. Continuum absorption by water vapor drives transmittance down with increasing frequency.

et al., 1998; English and Hewison, 1998; Meissner and Wentz, 2004). Other empirically based emissivity models have been developed in the past, for example, Klein and Swift (1977); Wentz (1999); Stogryn *et al.* (1995); Guillou *et al.* (1998); English and Hewison (1998). Surface emission is the primary contributor to the source term in equation 2.5.

A Fortran subroutine (see appendix A.2) was constructed based on the work of Meissner and Wentz (2004) to compute the complex-valued permittivity of the sea surface. The user provides the frequency (GHz) and surface temperature ($°C$); a fixed salinity of 35 permil is assumed. The Meissner and Wentz model represents an improvement in emissivity calculations for a larger temperature and frequency range compared to prior emissivity models, and is consistent with the range of temperatures and frequencies used in the present research.

Because of the difficulties in estimating land surface emissivity and correcting for terrain variations, the case studies and analysis in this dissertation were limited to over-ocean cases. However, there is no reason to believe that techniques described herein would not be equally applicable over land, assuming suitable estimates of the land surface emissivity are available (Skofronick-Jackson *et al.*, 2004). Retrievals over land will be explored in future research.

Wind-Induced Excess Ocean Surface Emissivity

Due to the significant wind speeds observed during the 2003 Wakasa Bay experiment (WBAY03) case studies, a surface emissivity correction for wind-induced excess emissivity was required. To simulate the effects of wind on surface emissivity, the wave models described in Wilheit (1979) and Kummerow *et al.* (2001) are used, and the surface foam coverage model from Monahan and Woolf (1989). Ocean surface surface

roughness is modeled following Hollinger (1971). Unfortunately very little validation data is available to verify these models at frequencies in the 89 to 340 GHz range and nadir viewing angle. Wind-direction effects on the surface emissivity at nadir-viewing angles are presumed to be negligible compared to magnitude (Tran *et al.*, 2002).

2.4.2 Gaseous Absorption

Absorption and emission by water vapor and molecular oxygen play an important role in microwave brightness temperatures observed at the top of the atmosphere. In fig. 2.2, it is evident that certain microwave frequencies are sensitive to absorption by oxygen near 60 GHz and near 120 GHz, and also by water vapor near 21 and 183 GHz (Rosenkranz, 1998). Continuum absorption/emission by water vapor becomes increasingly effective with increasing frequency, continuously decreasing the atmospheric transmittance with increasing microwave frequency. A model based on the results from Rosenkranz (1998) is used to compute gaseous attenuation by water vapor and molecular oxygen O_2.

When observations are made using window channels, the contribution to attenuation by water vapor and oxygen are generally relatively minor in comparison to precipitation (when present) (Skolnik, 1990). At higher frequencies and off-absorption-line frequencies (such as $183.3 \pm 1, 3, 7$ GHz), water vapor absorption is an important part of both absorption and emission of upwelling microwave radiation, as would be observed from a satellite or aircraft radiometer. Gaseous absorption (and emission for T_B simulations) is included in the retrieval algorithm and forward model presented here for both radar and radiometer applications.

2.4.3 Attenuation in Clouds

When liquid clouds are present, additional absorption of microwave radiation occurs compared to clear-sky observations (Matrosov, 1998). Because cloud particle sizes fall well into the Rayleigh regime (section 2.5.1), scattering by liquid cloud particles is assumed to be negligible for both passive and active observations, and is not considered for either passive or active microwave simulation or retrievals (Haddad *et al.*, 1997). However, absorption by liquid water clouds is significant and is computed according to the concentration of liquid water (Liebe *et al.*, 1991; Lipton *et al.*, 1999). The *mass absorption coefficient* [area per unit mass] of cloud liquid water, $\kappa_{\mathrm{abs,clw}}$, is written as

$$\kappa_{\mathrm{abs,clw}} = \frac{6\pi}{\lambda\,\rho_{\mathrm{liq}}} \left| \Im \left(\frac{m^2 - 1.0}{m^2 + 2.0} \right) \right|, \tag{2.6}$$

where λ is the wavelength, ρ_{liq} is the density of liquid water, and m is the index of refraction of water (Petty, 2004). All quantities are expressed in SI units.

Clouds composed of ice particles attenuate radiation much less effectively than their liquid counterparts. For microwave at frequencies less than about 50 GHz, attenuation by cloud ice can be safely neglected when precipitation is present. However, at higher frequencies scattering by cloud ice can lead to a non-negligible attenuation depending primarily on the size and concentration (number per unit volume) of ice particles and the frequency of radiation. For this research, we examine frequencies ranging from 13.4 to 340 GHz, therefore the scattering must be accounted for.

For simplicity, the forward model assumes that cloud ice is present only when ice-phase precipitation is present. The adverse effect of this assumption is that in regions where 13.4 GHz and 35.6 GHz radar observations detect no reflectivities, undetected ice clouds could still be present, and therefore influence brightness temperatures. To

compensate for the lack of an explicit cloud ice model, the retrieved snow fields also double as scattering by cloud ice. However, clear-sky cases, according to radar observations, are currently presumed to be completely cloud free. Future research will examine the sensitivity to the inclusion (or lack thereof) of an explicit cloud ice model.

2.4.4 The Passive Microwave Response to Precipitation

For a given field-of-view, thermally emitted microwave radiation as observed from space at a single channel/frequency can be characterized using one or more of the following descriptions:

- upwelling emission from the radiometrically cold, strongly polarized ocean surface;

- upwelling emission from the radiometrically warm, weakly polarized land surface;

- warm, weakly polarized, emission by liquid water, and a continuum of gaseous absorbers; and,

- cold and weakly polarized brightness temperatures from ice-phase precipitation sized particles aloft.

Figure 2.3, from Petty (2001a), illustrates an idealized relationship between over-ocean passive microwave brightness temperatures and surface rainfall rate R. An off-nadir viewing angle of approximately 53° is used, consistent with the Special Sensor Microwave Imager (SSM/I) instrument. The key features of the fig. are:

- increasing obscuration of the clear-sky polarized T_B signal as R increases;

- a T_B decrease near the point where the surface is completely obscured (i.e., no polarization signal) with further increases in R;

- and, a non-unique $T_B - R$ relationship for a fixed brightness temperature.

The second point is due to the increased role of scattering by ice particles, which are required for precipitating clouds to produce larger R. The final point can be seen by passing an imaginary horizontal line through 230 K at 37 GHz, which intercepts the curve at 2 points for each polarization, each point corresponds to different precipitation rates.

For a given window channel, the contribution to the observed brightness temperature arises not only from the surface emission but also at different vertical levels of a precipitating cloud. An additional component contributing to observed T_Bs (not shown) arises from oblique viewing of surface reflections of downwelling radiation emitted by precipitating clouds, particularly in tropical convective situations where the vertical dimension of the precipitating cloud is comparable to the horizontal dimension (Petty, 1994a). In stratiform and low-level clouds and at near-nadir viewing angles this effect is minimized – this is the standard assumption for the present studies.

In general, over the ocean, the response of brightness temperature to increases in surface rainfall rate at each frequency is non-monotonic, which is seen in fig. 2.3. This introduces additional ambiguity into the retrieval problem (e.g., Wilheit *et al.* (1977); Petty (1994a) and others). However, this behavior can be mitigated by the use of polarization information (e.g., Weinman and Guetter (1977); Petty (1994b); Kidd (1998)). With increasing frequency, the general trend is for the polarization information to saturate at increasingly smaller rainfall rates.

The inference of precipitation features from measurements made by a combination of passive and active microwave channels requires specific assumptions (models) regarding the frequency dependent physical, vertical and horizontal characteristics of the
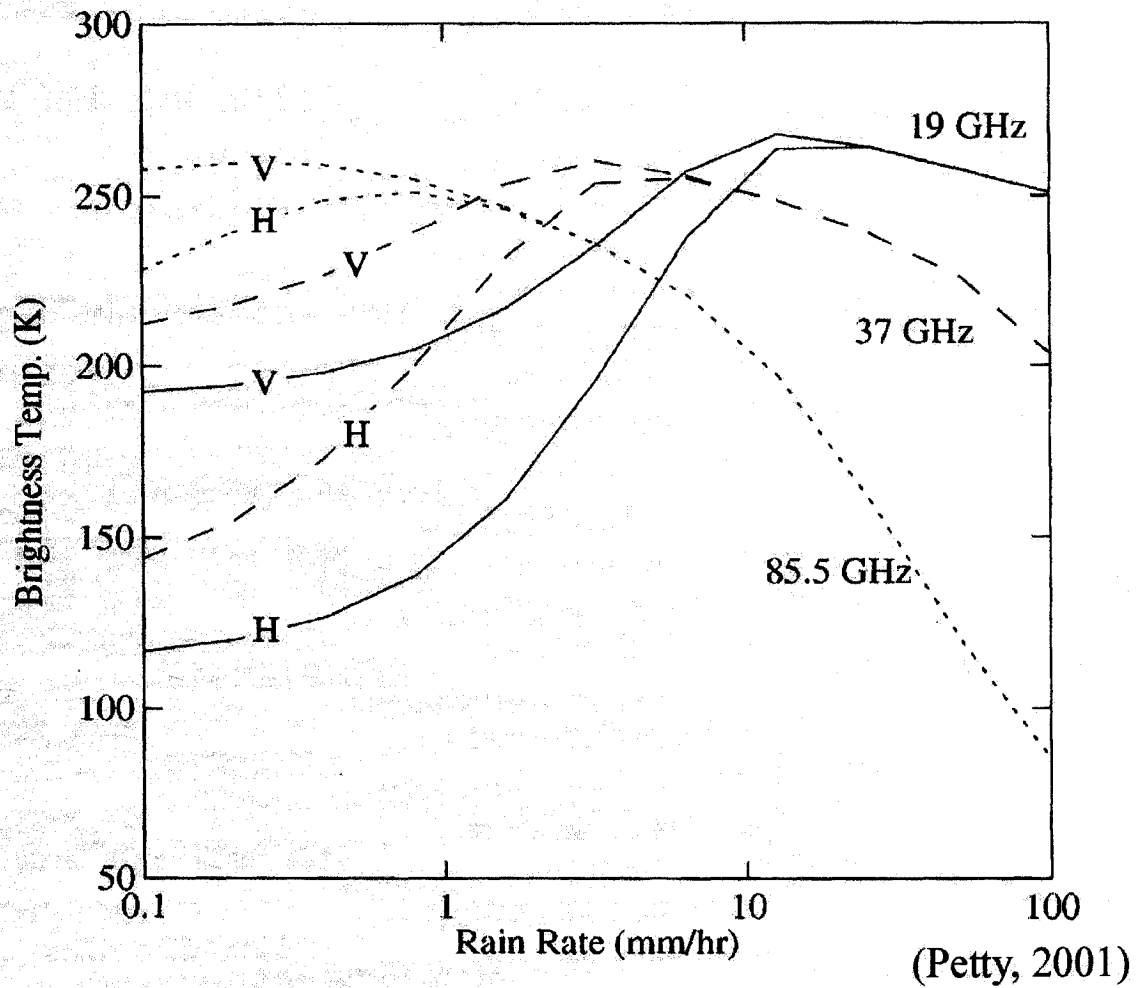
Figure 2.3. Idealized brightness temperature relationship with respect to surface rainfall rate for common passive microwave channels used in precipitation remote sensing.

precipitating cloud in order to obtain a reasonably accurate retrieval. These elements are the essence of the physical retrieval paradigm. In the present research, the roles are different in the sense that the radar observations are used as the primary source of information for the retrieval, whereas brightness temperature simulations and observations are used as a constraint on the retrieval.

2.5 The Radar Response to the Atmosphere and Precipitation

Precipitation hydrometeors are the primary contributors to the radar reflectivity profile observed at a given microwave frequency. However, both hydrometeors and atmospheric gaseous constituents attenuate the radar signal as it propagates downward from the radar and back (i.e., the two-way path-integrated attenuation). Therefore, an explicit accounting must be made for the attenuators' properties at each range bin (distance from the radar) in order to perform an an accurate integration of attenuation throughout the vertical profile.

In this section, the path from particle physical properties to a radar reflectivity (the standard observable from radar observations) is described. As was described in section 2.3, the particle will absorb and scatter a portion of the beam, with the amount of scattering and absorption determined by the dielectric permittivity (index of refraction) of the medium and the size/shape of the particle. The scattering phase function, $p(\Theta)$, describes the angular distribution of radiation scattered by the particle, Θ is the scattering angle within the scattering-plane (see Bohren and Huffman (1983)). A portion of the incident beam that is scattered backward toward the radar through a solid angle centered at $p(\Theta = 180°)$ is what the radar receives.

2.5.1 Radar Backscattering Cross Section

To quantify the amount of this backward-scattered radiation, the quantity *backscattering cross section*, σ_b, defines the surface area a theoretical perfect reflector would require in order to backscatter the same fraction of the incident radiation. For an individual particle it is expressed as

$$\sigma_b = Q_b A, \tag{2.7}$$

where Q_b is the backscattering efficiency – a dimensionless quantity which is a function of the material's index of refraction, m; and the shape and size of the particle. A is the 2-D projected-area of the 3-D particle. For a sphere of diameter D, $A = (\pi/4)D^2$, and Q_b is computed from Mie theory.

It is convenient to compare the wavelength λ of the radiation to the particle diameter D. This is expressed through the *size parameter*, $x = \pi D/\lambda$. For $x \approx 1$, the computation of Q_b requires the use of Mie theory when using spherical particles. However, when $x \ll 1$, the Mie solution for $Q_{b,\text{Mie}}$ can be approximated by using the Rayleigh scattering approximation (Bohren and Huffman, 1983). $Q_{b,\text{Ray}}$ is written as

$$Q_{b,\text{Ray}} = 4x^4 \left| \frac{m^2 - 1}{m^2 + 2} \right|^2, \tag{2.8}$$

where m is the complex-valued index of refraction of the material.

Figure 2.4 illustrates the backscattering efficiency as a function of liquid-equivalent particle diameter for the two radar frequencies, 13.4 GHz (K_u-band) and 35.6 GHz (K_a-band), used in this research. Q_b was computed for both pure ice and water spheres, as a function of the individual particle diameter. The primary feature of relevance is the shift of the beginning of the Mie regime toward smaller particle sizes at 35.6

GHz compared to 13.4 GHz for both ice and water spheres. This shift, and similarity in the shapes of the curves, is the foundation of the dual-wavelength radar retrieval method presented in chapter 3. Figure 2.5 shows the ratio of the two backscattering efficiencies, normalized by the ratio of the wavelengths to the fourth power, such that in the Rayleigh regime, the ratio is near unity for ice and liquid phase.

2.5.2   Unattenuated Reflectivity

The backscattering cross section per unit volume, η, can be expressed as sum of all of the backscattering cross sections (σ_b) of an ensemble of particles in a unit volume V:

$$\eta = \frac{1}{V} \sum_i \sigma_{b,i}. \tag{2.9}$$

Or in integral form,

$$\eta = \int_0^\infty \sigma_b(D) n(D) dD, \tag{2.10}$$

where $n(D)$ describes the distribution of particle sizes (e.g., an exponential size distribution) having dimensions of $[L^{-4}]$, and σ_b is the backscattering cross-section with dimensions of $[L^2]$.

η is sometimes called the "radar reflectivity". Additionally the term *reflectivity factor* is typically defined

$$Z = \int_0^\infty D^6 n(D) dD, \tag{2.11}$$

which is only strictly applicable when the radar is observing in the Rayleigh regime.

In precipitation remote-sensing applications, the radar receiver is receiving backscattered radiation from an ensemble of particles, which may generally consist of a number
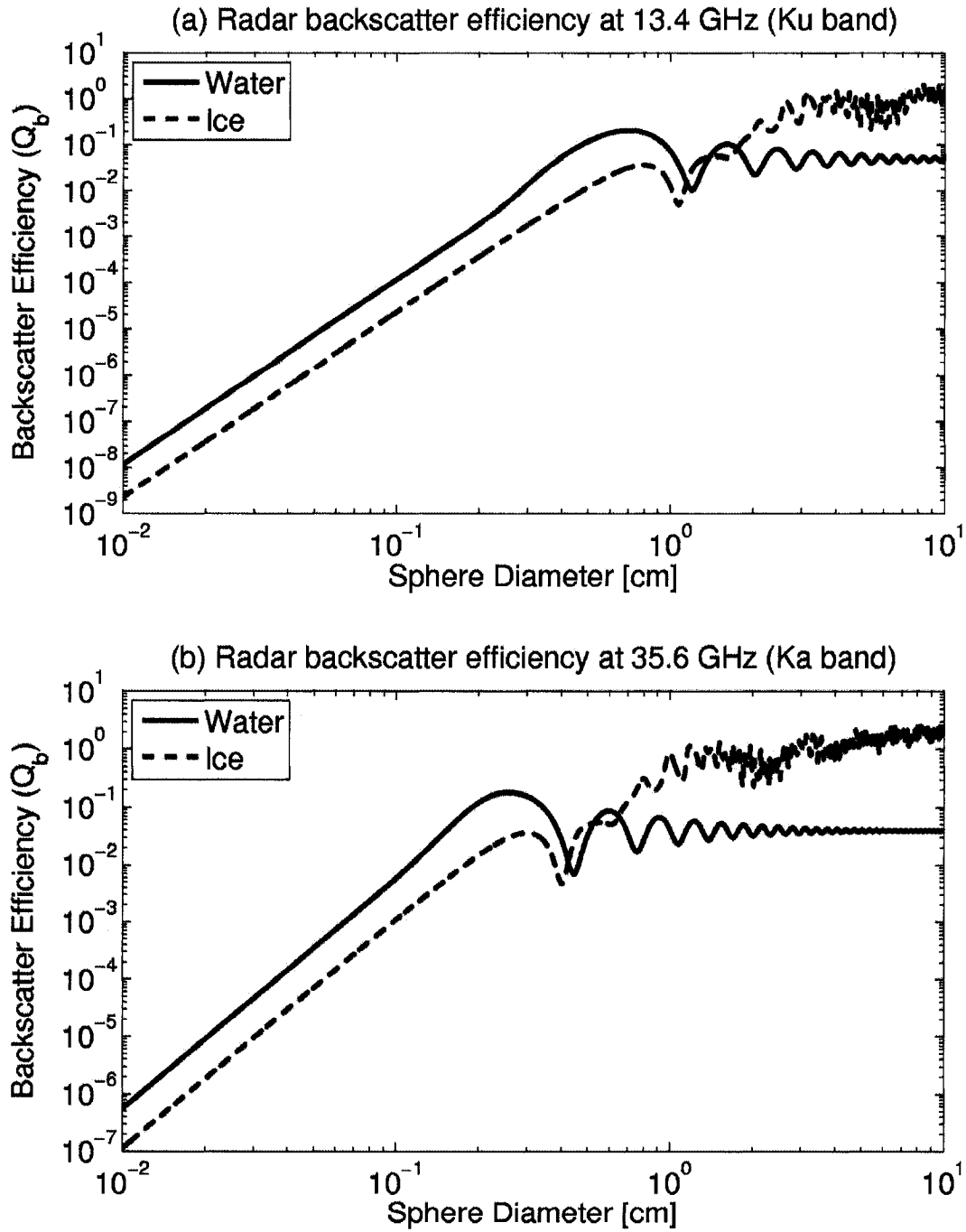
Figure 2.4. Backscattering efficiency versus liquid-equivalent particle diameter for water (solid blue line) and ice (dashed green line) at (a) 13.4 GHz (K_u-band) and (b) 35.6 GHz (K_a-band).
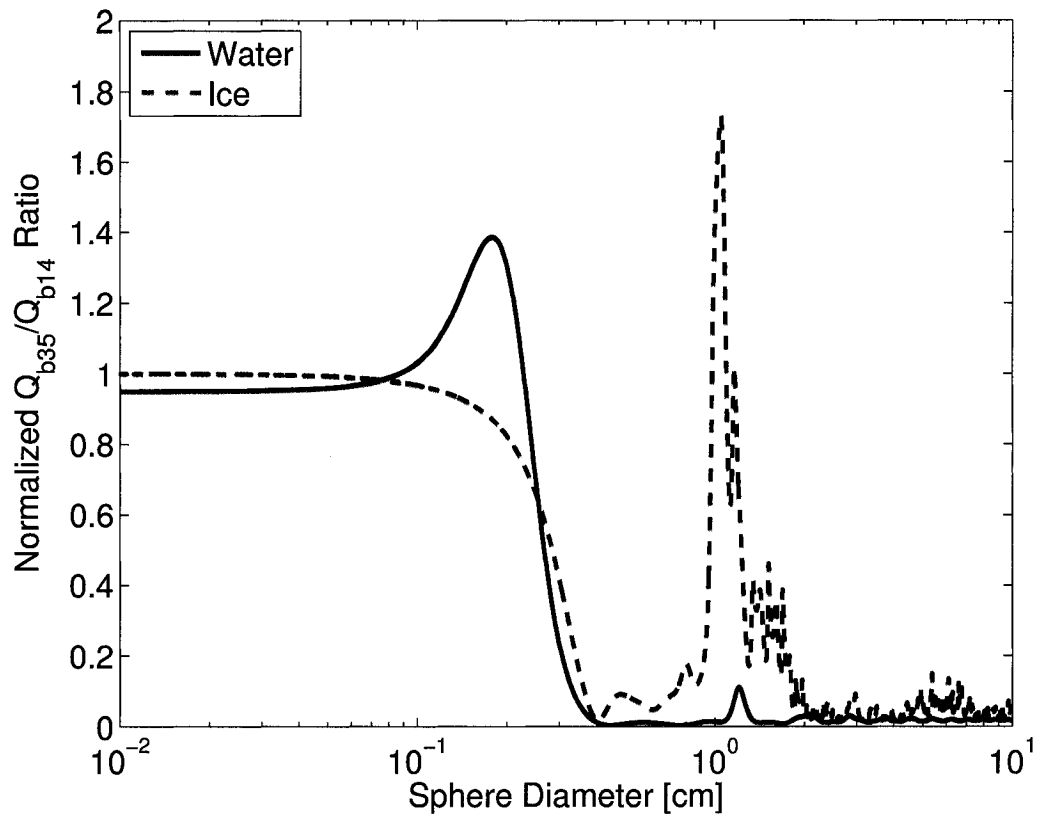
Figure 2.5. 13.4 and 35.6 GHz backscattering efficiency ratio versus liquid-equivalent particle diameter for water (solid blue line) and ice (dashed green line).

of different hydrometeor sizes, shapes, and types, such as cloud particles, snowflakes, raindrops, hailstones, and so on (Atlas, 1990). At the frequencies of interest for this research, 13.4 and 35.6 GHz, the radar typically observes in both the Mie and Rayleigh regimes when observing precipitation sized particles.

This requires an accounting for the difference between the radar reflectivity factor (2.11) and the *effective radar reflectivity (factor)* Z_{eff}. This is expressed as

$$Z_{\text{eff}}(\lambda) = \int_D D^6 f(D) n(D) dD, \qquad (2.12)$$

which is the ratio of the Mie and Rayleigh backscattering cross-sections integrated over the particle size distribution (PSD) (e.g., Liao and Meneghini (2005b)), where $f(D) = \sigma_{\text{b,Mie}}(D)/\sigma_{\text{b,Ray}}(D)$. In meteorological applications, Z_{eff} is typically expressed in either units of $[\text{mm}^6 \text{ m}^{-3}]$ or in the log-ratio units of [dBZ] by taking $10 \log_{10}(Z)$. To avoid terminology ambiguity, the term "reflectivity" will always refer to the "effective reflectivity factor" Z_{eff}.

The retrieval technique presented in chapter 3 depends on the 35.6 GHz radar observing particles primarily in the Mie regime, while the 13.4 GHz is observing particles in the Rayleigh regime. If both radar frequencies are observing in the Rayleigh regime, then the ratio $f(D)$ in 2.12 is unity, and the unattenuated reflectivity is proportional to the integral of the sixth power of the drop diameters per unit volume of air (i.e., equation 2.11).

Expanding the ratio, $f(D)$, in 2.12 and using 2.8,

$$f(D) = \frac{\sigma_{\text{b,Mie}}(D)}{\sigma_{\text{b,Ray}}(D)} = \frac{Q_{\text{b,Mie}}}{Q_{\text{b,Ray}}} \qquad (2.13)$$

$$= \frac{Q_{\text{b,Mie}}}{4x^4 |K|^2} \qquad (2.14)$$

$$= \frac{\lambda^4 Q_{b,\text{Mie}}}{4\pi^4 D^4 |K|^2}, \tag{2.15}$$

where for liquid water, the "K-factor" ($|K_w|^2$) is

$$|K_w|^2 = \left| \frac{m_{\text{liq}}^2 - 1}{m_{\text{liq}}^2 + 2} \right|^2, \tag{2.16}$$

and m_{liq} is the complex index of refraction of liquid water. In computations of the effective radar reflectivity, the K-factor is set to the conventional value used for water ($|K_w|^2 = 0.93$), employed in 3 GHz radar observations (Smith, 1984; Meneghini et al., 1997). This allows for consistent comparisons of observed reflectivities.

Substituting equation 2.15 into equation 2.12 yields

$$\begin{aligned}
Z_{\text{eff}}(\lambda) &= \int_D \frac{\lambda^4 Q_{b,\text{Mie}}}{4\pi^4 D^4 |K_w|^2} D^6 n(D) dD \\
&= \frac{\lambda^4}{4\pi^5} \int_D \frac{Q_{b,\text{Mie}}}{|K_w|^2} \pi D^2 n(D) dD.
\end{aligned} \tag{2.17}$$

Equation 2.17 represents the theoretical unattenuated effective reflectivity for arising from an ensemble of spherical hydrometeors having an arbitrary size distribution, $n(D)$.

2.5.3 Radar Attenuation

The atmospheric attenuation of a radar signal occurs through absorption by gases (air, water vapor) and extinction due to hydrometeors (cloud, ice, liquid) present in the atmosphere. As the emitted pulse from the airborne or space-based radar passes downward through these materials, the intensity of the signal decreases through both scattering and absorption. Radiation scattered backward toward the radar passes upward through the material again, resulting in a two-way path-integrated attenuation.

Loosely speaking, for a fixed amount of absorbers and scatterers in the atmosphere, the path-integrated attenuation (PIA) increases as radar frequency increases. In the present studies, the 13.4 and 35.6 GHz radar observations experienced light attenuation through snowfall. PIA ranges of 0 to 8 dBZ at 35.6 GHz, and approximately half of that at 13.4 GHz were observed.

In radar terminology, the term *range gate* refers to the the nominal volume of the atmosphere described by a pixel of radar data. This volume is defined by the horizontal and vertical resolution characteristics of the radar beam.

In order to accurately simulate a profile of reflectivities at a given frequency along a path s, knowledge of either the gaseous and hydrometeor distribution along the path or the path integrated attenuation (PIA) is required. These two descriptions are used in the "forward" and "backward" dual-wavelength ratio techniques respectively, which are described in chapter 3.

The attenuation for a given path in the atmosphere is expressed through the extinction law. At a particular range gate, r, the *attenuation factor* $\mathcal{A}(r)$ of the radar beam can be expressed as the two-way path integrated attenuation between the radar and range gate r. It is written as

$$\mathcal{A}(r) = \exp \left(-2 \int_{\text{radar}}^{r} k_{\text{ext}}(s) + k_{\text{gas}}(s) \, ds \right), \tag{2.18}$$

where k_{gas} [km^{-1}], represents the combined gaseous and cloud-liquid water extinction at the current range gate, and k_{ext} is the extinction due to hydrometeors. The factor of two accounts for the two-way path attenuation as the backscattered beam passes through the same material along the return path.

The final form of the attenuated reflectivity equation for spherical particles at a given range gate r and wavelength λ, is expressed as

$$Z_{\text{eff}}(r) = \mathcal{A}(r)\frac{\lambda^4}{4\pi^5}\int_D \frac{Q_{\text{b,Mie}}}{|K_w|^2}\pi D^2 n(D)dD \tag{2.19}$$

$$= \exp\left(-2\int_{\text{radar}}^r k_{\text{ext}}(s) + k_{\text{gas}}(s)\ ds\right)\frac{\lambda^4}{4\pi^5}\int_D \frac{Q_{\text{b,Mie}}}{|K_w|^2}\pi D^2 n(D)dD \tag{2.20}$$

Again, the units of reflectivity are typically expressed in units of [mm^6 m^{-3}], or in [dBZ] by taking $10\log_{10}(Z_{\text{eff}})$.

2.5.4 Dual-Wavelength Ratio

As described in chapter 1, the Global Precipitation Mission platform will carry an active radar capable of remote sensing at two different frequencies, specifically 13.4 GHz and 35.6 GHz (http://gpm.gsfc.nasa.gov/). Previously the only other space-based radar for precipitation remote sensing has been the Tropical Rainfall Measurement Mission Precipitation Radar (TRMM-PR), which had only one channel at 13.8 GHz (Simpson et al., 1996). Retrievals from a single radar channel can infer the intensity and vertical structure of precipitation, but requires prior assumptions about the particle size distribution and composition of the particles.

The addition of a second radar channel, sufficiently separated in frequency/wavelength, provides a much more direct relationship to the particle size distribution – potentially eliminating a large source of uncertainty in retrievals, especially in snowfall. Previous studies have exploited this feature of the dual-wavelength relationship to retrieval particle size distribution (PSD) properties from both ground-based radar and airborne radar observations (e.g., Meneghini et al. (1997), Matrosov (1998), Matrosov et al. (2005)). The key feature of the *dual-wavelength ratio* method is that one observ-

ing wavelength is sufficiently long enough such that the observed particles fall within the Rayleigh regime (i.e., $x = \pi D/\lambda \ll 1$); while the shorter wavelength observations fall outside the Rayleigh regime, $x \approx 1$ (e.g., Mie regime for spherical particles). The dual-wavelength ratio (DWR) is simply expressed as the ratio of the effective reflectivities of shorter wavelength (higher frequency) and longer wavelength (lower frequency) channels,

$$DWR = Z_{\text{eff,high}}/Z_{\text{eff,low}}, \tag{2.21}$$

where equation 2.20 defines Z_{eff}, and high refers to higher frequency channel (e.g., 35.6 GHz) and low refers to the lower frequency channel (e.g., 13.4 GHz).

DWR values less than unity are assumed to be directly related to the differences in particle size, more-or-less independent of the number-density of the particles. Given a sufficient model for radar attenuation and the microphysical properties of particles, one can determine a set of PSD properties that produce a consistent relationship between the two sets of observed radar reflectivities. This technique forms the general basis for the DWR/PSD retrieval method described in chapter 3.

Figure 2.6 shows the DWR-D_0 relationship, for 13.4 and 35.6 GHz, with the curves representing values of ice-phase (ice and air) hydrometeor density, ρ. At a constant density, the modeled relationship between DWR and the liquid equivalent mass-weighted median diameter, $D_0 = 3.67/\Lambda$, is generally monotonic for DWR less than 1 and greater than about 0.2 (for higher density particles). Given an observed DWR value, for example, 0.5, it is clear that any allowable value of particle density will return a different liquid equivalent diameter. This is because DWR is primarily sensitive to the actual

particle diameter, relatively independent of the density, as shown in fig. 2.7. The DWR relationship holds fairly well for D_0' values (actual diameter) less than 3.0 mm.

2.6 Size Distribution Properties

As a tool for parameterizing the sizes of particles present in a volume of air, functional forms for the size distribution of a given particle type are often employed. The motivations for choosing a particular form over another are typically consistency with in-situ observations and computational/analytical convenience.

2.6.1 Modified Gamma Distribution

A convenient form of a unimodal distribution is the modified gamma size distribution. It has the features of a off-median peak skewed toward smaller particle sizes, with $n(D)$ approaching zero as D approaches zero and infinity. There are four controlling parameters: N_0, μ, Λ, and γ. It is expressed as

$$n(D) = N_0 D^\mu \exp(-\Lambda D^\gamma), \tag{2.22}$$

where $\gamma = 1$ yields the "constrained-gamma" size distribution. This is the form most commonly seen in literature relevant to precipitation size distribution properties (e.g., Ulbrich (1983); Testud *et al.* (2001))
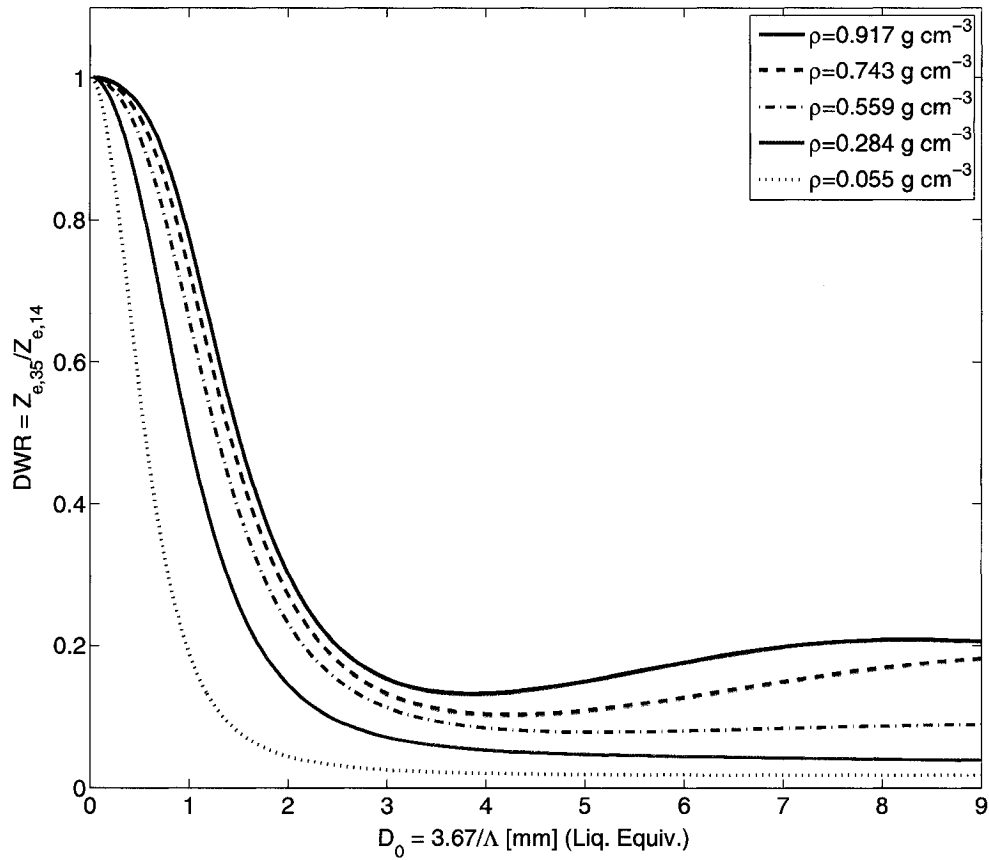
Figure 2.6. Relationship between DWR and $D_0 = 3.67/\Lambda$ [mm] (liquid equivalent mass-weighted median diameter) for various snow-particle density ρ [g cm^{-3}] values.
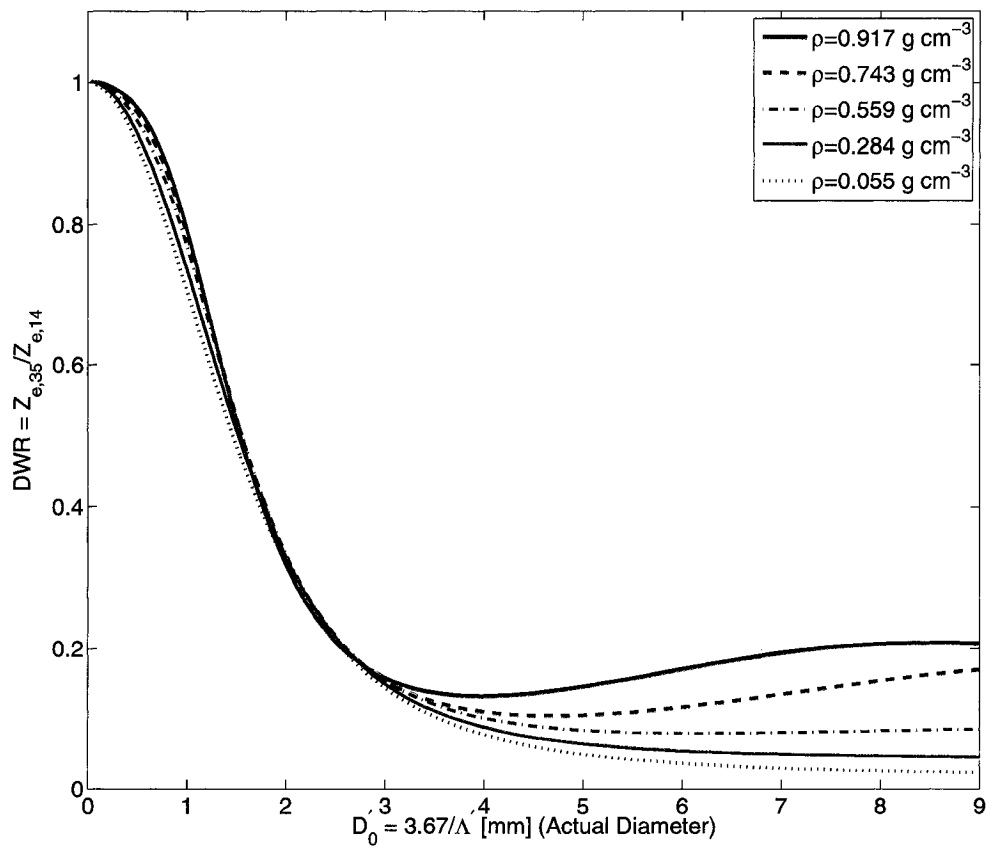
Figure 2.7. Relationship between DWR and D'_0 = $3.67/\Lambda'$ [mm] (actual mass-weighted median diameter) for various frozen-particle density ρ [g cm^{-3}] values.

2.6.2 Exponential Distribution

Setting $\mu = 0$ and $\gamma = 1$ in 2.22 results in the (negative) exponential size distribution. The exponential distribution is a two-parameter distribution where Λ describes the shape and N_0 describes the total number density. It is written

$$n(D) = N_0 \exp(-\Lambda D), \qquad (2.23)$$

where D is the diameter. The intercept parameter, N_0, has dimensions of $[L^{-4}]$; the shape parameter, Λ, has dimensions of $[L^{-1}]$.

The exponential distribution is a simple, yet non-trivial, method for modeling the size distribution of precipitation-sized particles. It also has a history tracing back to the widely-used Marshall and Palmer (1948) distribution for raindrops, which was based on field observations. In falling snow, particle sizes have also been shown to often be nearly exponential (e.g., Sekhon and Srivastava (1970); Houze *et al.* (1979)). Others have shown departures from exponential distributions, such as Mitchell (1991), who showed departures from the exponential form in regions of aggregation and initial vapor deposition growth. Mitchell (and others) have suggested using a three parameter PSD model (e.g., the modified gamma distribution in 2.22) for improved consistency with observations.

When used in conjunction with the dual-wavelength ratio technique, the retrieval consists of two independent observations (radar reflectivities) and two unknowns (N_0 and Λ), in the case of rainfall. For snow, there is an additional unknown in the particle density. Because of these relationships, general consistency with published snowfall PSDs, and for analytical convenience; the exponential distribution is used exclusively throughout the remainder of the research presented here.

Given that we now have an explicit form of the PSD, the two-way attenuation from equation 2.18 can now be expressed using the exponential size distribution as

$$\mathcal{A}(r) = \exp\left(-2\int_{\text{radar}}^{r} N_0(s)I_{\text{ext}}(\Lambda) + k_{\text{gas}}ds\right), \qquad (2.24)$$

where N_0 and Λ are the PSD parameters of interest, I_{ext} is the size-distribution-averaged hydrometeor extinction contribution to the path-integrated attenuation, and k_{gas} is the contribution of extinction by gaseous absorption. I_{ext} is written

$$I_{\text{ext}} = \int_0^{\infty} \sigma_{\text{ext}}(\lambda, D) \exp(-\Lambda D) dD, \qquad (2.25)$$

where $\sigma_{\text{ext}}(\lambda, D)$ is the extinction cross section of particles having diameter D at wavelength λ. The dimensions of I_{ext} are $[\text{L}^3]$, so that subsequent multiplication by N_0 [dimensions of L^{-4}] yields $[\text{L}^{-1}]$, usually expressed in units of $[\text{km}^{-1}]$.

The extinction cross-section for a single particle is defined by

$$\sigma_{\text{ext}} \equiv Q_{\text{ext}} A, \qquad (2.26)$$

where A is the cross-sectional area of the particle. Similar logic provides the scattering σ_{sca} and absorption σ_{abs} cross-sections. For spherical particles, standard Mie theory (Mie, 1908; Bohren and Huffman, 1983) may be used to compute the required extinction, scattering, and absorption efficiencies $Q_{\text{ext}}, Q_{\text{sca}}, Q_{\text{abs}}$.

2.7 1-D Microphysical Model

The general purpose of the 1-D model, as part of the forward model, is to describe the thermodynamic and microphysical characteristics of a 1-D column of a simulated atmosphere using meteorologically self-consistent profiles of hydrometeors based on a

relatively small number of adjustable parameters. The 1-D model used in this research was originally developed and described by Petty (2001b), and has been modified for this research. In Petty (2001b), precipitation microphysical properties were generated by model parameterizations. In the present model, hydrometeor properties and volume fractions of ice and water come from the DWR-retrieval method described in chapter 3. Thermodynamic and other physical inputs are typically provided by ancillary observations such as nearby radiosonde profiles and satellite-based observations of sea surface temperature and near surface wind speed (see chapter 5).

The standard inputs to the 1-D model are surface temperature and pressure, surface dewpoint depression, temperature and height of the tropopause, near-surface wind speed, cloud properties: base, top, water content; hydrometeor PSD properties: N_0 and Λ; and hydrometeor volume fractions of ice and water. Outputs are provided to the hydrometeor and radiative transfer model, following the forward model flowchart depicted in Fig. 2.1.

2.7.1 Background

A number of microphysical models have been previously developed for the purposes of generating simulated profiles of precipitation, and are subsequently used in forward models and retrieval models. For example, the recent model of Thériault *et al.* (2006) describes a 1-D model employing a 2-moment bulk microphysical scheme to generate a larger variety of precipitation particle types, including graupel, slush, dry snow, wet snow, freezing rain, ice pellets, and rain. The Goddard Profiling algorithm [GPROF, Kummerow *et al.* (2001)] employs a database composed of a large number of individual 1-D profiles (originating from a 3-D cloud resolving model) of precipitation

and associated 1-D radiometric signatures. Similar to the forward model presented here, GPROF uses an exponential particle size distribution (PSD), and provides an additional constraint by specifying a fixed relationship between the two parameters of the PSD. The present technique retrieves these quantities separately.

The primary motivation for using a 1-D model is both computational convenience and situational relevance. When applied to stratiform mid-latitude cold-cloud precipitation cases, the 1-D model seems to be equally acceptable compared to a 2-D or 3-D model, particularly when simulating nadir looking observations of reflectivity and brightness temperature. However, if applied to deep convective cases, such as in the tropics, cloud geometry becomes a potentially important issue (Petty, 1994a; Roberti and Kummerow, 1999). The 1-D model is also quasi-steady state, where vertical derivatives of hydrometeor properties are directly related to local hydrometeor growth rates. In strongly convective situations, however, this relationship is no longer strictly valid. Therefore, the validity of the present studies are limited to stratiform, and to a lesser extent, shallow convective cases.

2.7.2 General Considerations

Assuming an exponential distribution of particles (Eq. 2.23), the k-th moment of the distribution is given by

$$\int_0^\infty N_0 \exp(-\Lambda D) D^k dD = \frac{N_0}{\Lambda^{k+1}} \Gamma(k+1), \tag{2.27}$$

where $\Gamma(k+1)$ is the mathematical Gamma function evaluated at $k+1$, and D is the liquid equivalent diameter of a spherical particle.

Prior to this section, the term "diameter" has been used loosely. In reality, precipitation particles, especially ice-phase precipitation, are commonly non-spherical, composed of ice, water, and/or air. Throughout the remainder of this dissertation, the terms "diameter" and "liquid equivalent diameter", D, are synonymous, referring to the diameter of an equivalent-mass sphere of liquid water having a constant density of 1000kg m^{-3} . The term "physical diameter" D' will be used to refer to the diameter of the simulated particle when composed of a mixture of ice, water, and/or air. These quantities are related by $D = \beta D'$, where $\beta = (\rho_h/\rho_{\text{liq}})^{1/3}$ with ρ_h and ρ_{liq} as the densities of the simulated particle and liquid water respectively.

It is assumed that hydrometeor fall speed v_s and liquid equivalent volume V can be expressed using power-law relationships as

$$v_s(D) = aD^b, \tag{2.28}$$

and,

$$V(D) = cD^d. \tag{2.29}$$

The coefficients a and b are functions of particle density, shape and air viscosity and density (Petty, 2001b). a has dimensions of $[\text{L}^{1-b}\text{T}^{-1}]$, whereas b, c, and d are dimensionless. In the case of spherical particles $c = \pi/6$ and $d = 3$, forming the equation for the volume of a sphere having liquid equivalent diameter D. The physical volume of the simulated spherical particle is $V'(D') = c(\beta^{-1}D)^d$.

Three quantities are commonly employed to describe the characteristic size of a PSD. They are the *mass-weighted median diameter* D_0, *volume-weighted mode diameter*, D_v,

and the *mass-weighted mean diameter*, D_m. Assuming an exponential PSD with slope parameter Λ, these are written

$$D_0 = 3.67/\Lambda \tag{2.30}$$

$$D_v = 3.0/\Lambda \tag{2.31}$$

$$D_m = \frac{\int_0^\infty D^4 N(D)\,dD}{\int_0^\infty D^3 N(D)\,dD} = 4.0/\Lambda \tag{2.32}$$

respectively (Ulbrich, 1983). D_0 marks the diameter where 50% of particle masses in the distribution are above and below this point, D_v indicates the peak of the distribution of volumes, and D_m is the mass-weighted average diameter of the distribution. In this dissertation D_0 is employed as the "characteristic" particle size of the exponential PSD, whereas D_v is provided for clarity and comparison with other published research.

Using equation 2.27, non-integral expressions for the mass density or *liquid water content* (LWC), w, can be written as

$$w = \int_0^\infty N_0 \exp(-\Lambda D) c D^d \rho_{\text{liq}} dD = \frac{N_0 \rho_{\text{liq}} c}{\Lambda^{d+1}} \Gamma(d+1), \tag{2.33}$$

where the dimensions are $[\text{ML}^{-3}]$, typically expressed in units of $[\text{g m}^{-3}]$. In the present study spherical particles are used, therefore $d = 3$ and $c = \pi/6$.

Similarly, the *liquid equivalent precipitation rate*, R, is written

$$R = \int_0^\infty N_0 \exp(-\Lambda D) c D^d a D^b dD = \frac{N_0 a c}{\Lambda^{d+b+1}} \Gamma(d+b+1), \tag{2.34}$$

where the dimensions are $[\text{L T}^{-1}]$, typically expressed in $[\text{mm hr}^{-1}]$.

In general, the fall-speed coefficients a, and to a lesser extent b, depend on the particle shape, density of air, and the hydrometeor composition. A novel method for modeling these dependencies is employed in the forward model as

$$a = a_0 \sqrt{\frac{\rho_{a0}}{\rho_a}}. \tag{2.35}$$

where ρ_{a0} is the density of air at a temperature of 0 °C and a pressure of 1013 millibars, and ρ_a is the density of air at current temperature and pressure. In snow the value of $a_0 = 7.2059$ (SI units) and $b = 0.311$ is used following Petty (2001b), who derived this value based on snowfall relationships provided in Sekhon and Srivastava (1970). In rain, $a_0 = 628.17$ (SI units) and $b = 0.7619$ are derived from the Marshall-Palmer distribution (Marshall and Palmer, 1948; Petty, 2001b).

The mass-weighted fall speed of the precipitation, v_m, can also be related to the precipitation rate and LWC by

$$v_m = \frac{R\rho_{\text{liq}}}{w} = a\Lambda^{-b}\frac{\Gamma(b+d+1)}{\Gamma(d+1)}.$$ (2.36)

2.7.3 Environmental Profile

Petty (2001b) describes a method for generating the environmental profile within the 1-D model framework, and a similar method is employed here, with a few exceptions. To summarize, the temperature profile is linear between the user-defined near-surface and tropopause temperatures. A separate surface "skin" temperature has been added to specify surface temperatures that are different than the air-temperature of the lowest layer – a requirement for accurate brightness temperature computations. In the present research, the skin temperature is obtained from the sea surface temperature product of F. Wentz (http://www.ssmi.com).

Relative humidity is generally controlled by two parameters, the clear sky relative humidity and the surface dewpoint depression. In layers containing cloud liquid water, the relative humidity is set to 100%, otherwise either the clear sky relative humidity or the relative humidity with respect to ice is used.

As in Petty (2001b), the vertical profile of pressure obeys the hydrostatic law in a dry atmosphere. Surface pressure, P_0 is user-defined. Like temperature and relative humidity, the surface pressure is obtained from radiosonde observations.

Cloud liquid water (CLW) distribution is handled by a separate variational model, allowing for the rapid production of a variety of CLW profiles, more-or-less independent of the particle properties. There is no explicit cloud ice model in the current forward model implementation. The CLW model is described in section 3.3.2.

2.8   Hydrometeor Model

The purpose of the hydrometeor model is to compute the Mie properties for a distribution of spherical hydrometeors composed of ice, water, and air – depending on the volume fractions of each constituent. The inputs to the hydrometeor model are temperature, wavelength of radiation, dielectric permittivities of the ice and water, volume fractions of ice and water, N_0 and Λ (assuming an exponential distribution). The computed Mie properties are extinction cross-section σ_{ext} (eq. 2.26), absorption cross-section σ_{sca}, single scattering albedo $\varpi_0 = \sigma_{sca}/\sigma_{ext}$), and radar backscattering cross-section σ_b (eq. 2.7). From the backscattering cross-section, the radar reflectivity factor can be derived given N_0 and Λ.

For computational convenience, we have adopted the simplest possible shape model for an individual hydrometeor; namely, an effectively homogeneous dielectric sphere of mass M composed of a blend of ice, air, and liquid water, with F_{ice}, F_{air}, and F_{liq} giving the corresponding volume fractions, so that

$$F_{liq} + F_{ice} + F_{air} = 1. \tag{2.37}$$

The hydrometeor density, ρ_h, is specified by the volume-weighted average of the densities of the individual components

$$\rho_h \approx F_{\text{liq}}\rho_{\text{liq}} + F_{\text{ice}}\rho_{\text{ice}}, \qquad (2.38)$$

where ρ_{liq} is the density of liquid water and ρ_{ice} is the density of solid ice. Here the mass of air is neglected, but not the volume. The melted-equivalent particle diameter is expressed as

$$D = \left(\frac{3M}{4\rho_{\text{liq}}}\right)^{1/3}, \qquad (2.39)$$

and the physical or actual diameter is

$$D' = D\left(\frac{\rho_{\text{liq}}}{F_{\text{liq}}\rho_{\text{liq}} + F_{\text{ice}}\rho_{\text{ice}}}\right)^{1/3}. \qquad (2.40)$$

For spherical particles, standard Mie theory (Mie, 1908; Bohren and Huffman, 1983) may then be used to compute the required extinction and scattering efficiencies Q_{ext} and Q_{sca}, backscattering efficiency Q_{b}, and asymmetry parameter g. These quantities depend on both the particle size parameter $x = \pi D'\lambda^{-1}$ (where λ is the wavelength in the same units as D') and on the particle's complex dielectric permittivity ϵ or, equivalently, the complex index of refraction N, where $\epsilon = N^2$ for most nonmetallic substances (Bohren and Huffman, 1983).

By increasing F_{air} in a particle of fixed mass, the physical cross-section is increased while decreasing its density and thus, presumably, its extinction and/or scattering efficiencies. Radar reflectivities are strongly sensitive to the particle size. For example, Z is proportional D^6 in Rayleigh scattering (section 2.5.1), so there may be competing effects between decreasing optical properties and increasing particle size. This notion is indirectly examined in chapter 4.

2.8.1 Dielectric Averaging of Ice, Water, and Air

To this point little has been said about the dielectric properties of ice, water, and air – the materials that form a generalized hydrometeor. In reality, a hydrometeor is often a complex amalgamation of ice with pockets of air, possibly having dendrites, and other complex structures. When melting occurs the actual physical description becomes even more complicated due to the distribution of liquid water on ice-phase hydrometeors (Oraltay and Hallett, 2005). While the present case studies do not include a melting or rainfall case, these sections (along with the melting layer model) are presented for completeness in the description of the forward model and to highlight the novel features of the retrieval algorithm.

Given our assumption of spherical hydrometeors composed of a single homogeneous dielectric material, we are faced with the task of taking highly complex structures – represented as distributions of ice, water, and air and simulating a homogeneous dielectric material with approximately the same bulk-average dielectric properties as the actual particle.

The bulk dielectric properties of water, ice, and air depend primarily on the wavelength of incident radiation and the temperature of the material. It is assumed that the dielectric permittivity of air is essentially indistinguishable from that of a vacuum for the purpose of computing scattering properties of particles. Therefore the absolute permittivity and the relative permittivity of the particle is the same for computational purposes.

The dielectric permittivity of a material, represented as a complex number, consists of a real and an imaginary component. Loosely speaking, the magnitude of the real component plays a dominant role in determining the degree of scattering or reflection

from a particle or surface, while the imaginary component determines the bulk absorptivity by the material. If the imaginary component is zero, then the material will scatter but not absorb microwave radiation. Both the real and imaginary components change with wavelength and temperature, with wavelength having a significantly larger impact than temperature within the ranges commonly encountered in the Earth's atmosphere.

2.8.2 Permittivity of Pure Water and Ice

For liquid water, the dielectric model of Liebe *et al.* (1991) is used. The Liebe model corrects previous models (e.g., Ray (1972)) for frequencies above 100 GHz by considering additional relaxation and resonance terms, also known as the double-Debye model terms. The salient characteristic of liquid water is that both the absorption and scattering properties have the same order of magnitude over the frequency range between 3 GHz and 300 GHz; thus larger particles of liquid water tend to strongly attenuate microwave radiation both by scattering and absorption.

For the complex permittivity of ice, we use a routine that interpolates the tabulated values of Warren (1984), who based these on a critical survey of published laboratory values. Unfortunately, laboratory measurements in the microwave band are limited, and there remain considerable uncertainties, especially with respect to the imaginary part and its dependence on temperature. It is noted that Matzler (2006) has recently collected and performed measurements for the dielectric properties of ice at microwave wavelengths, although it remains to be determined whether or not the results are significantly different or provide an improvement over that of Warren.

Ice is often regarded as a scattering-only material, having very little absorption within the frequency/wavelength ranges of interest. This is due to the relatively low

imaginary component of the dielectric permittivity. On the other hand, the dielectric permittivity of liquid water has a relatively large imaginary component, leading to significant absorption/emission properties. In fact, the presence of small amounts of liquid water on an otherwise dry, ice-phase particle raises the effective value of the imaginary component sufficiently to drastically reduce the single-scatter albedo (Olson *et al.*, 2001a; Liao and Meneghini, 2005a).

The presence of liquid water also serves to increase the backscattering cross-section of an otherwise ice-phase particle, leading to an enhanced radar signal when ice-phase particles begin to melt. This effect partially contributes to the observed radar feature called the "radar bright-band", a region of enhanced radar reflectivity consistent with particles melting as they fall below the freezing level in the atmosphere (Zawadzki *et al.*, 2005). The radar bright-band is regularly observed in precipitating stratiform-clouds containing a melting layer (Houze, 1993).

2.8.3 Dielectric Mixing

When computing microwave properties of a particle containing several distinct dielectric components, such as ice, water, and air; Mie theory is only applicable under the assumption that the mixed-phase spherical particle is effectively homogeneous from an electrodynamic perspective. Practically speaking, this requires that any discrete inclusions of dissimilar materials are much smaller than the incident wavelength and are randomly distributed throughout the surrounding matrix (e.g., ice inclusions in an air matrix or a homogeneous mixture of ice and air molecules). See Bohren and Huffman (1983) for additional discussion of the validity of the homogeneity assumption.

Two Component Mixtures

Two general methods for two-component dielectric mixing are considered: the Bruggeman (Bruggeman, 1935) or effective medium approximation, and Maxwell Garnett (Maxwell Garnett, 1904) or matrix-inclusion method (Bohren and Huffman, 1983). Both methods are commonly used in the literature (Meneghini and Liao, 2000; Olson et al., 2001b; Petty, 2001b; Liao and Meneghini, 2005a; Kim, 2006) The Maxwell Garnett (MG) method requires one constituent to be identified as the matrix and the other as the inclusion. Reversing the roles leads to a different computed value of the effective permittivity. The Bruggeman method, by contrast, treats both constituents symmetrically — that is, there is no distinction between "matrix" and "inclusion".

For two components, the Bruggeman method has the following form

$$f_1 \frac{\epsilon_1 - \epsilon_{\langle 1\,2\rangle}}{\epsilon_1 + 2\epsilon_{\langle 1\,2\rangle}} + (1 - f_1)\frac{\epsilon_2 - \epsilon_{\langle 1\,2\rangle}}{\epsilon_2 + 2\epsilon_{\langle 1\,2\rangle}} = 0, \qquad (2.41)$$

where ϵ_1 is the dielectric permittivity of component 1, ϵ_2 is the dielectric permittivity of component 2, $\epsilon_{\langle 1\,2\rangle}$ is the desired average effective dielectric permittivity of the two materials, and f_1 is the volume fraction of material 1.

The Maxwell Garnett method for two components is written as

$$\epsilon_{\langle 1\,2\rangle} = \epsilon_2 \left[1 + \frac{3f_1\,(\epsilon_1 - \epsilon_2)\,/\,(\epsilon_1 + 2\epsilon_2)}{1 - f_1\,(\epsilon_1 - \epsilon_2)\,/\,(\epsilon_1 + 2\epsilon_2)} \right]. \qquad (2.42)$$

The details of the above formulas are described in the appendix, section A.1.

Note that in actual ice-phase and mixed-phase hydrometeors, the choice as to which component should serve as matrix and which as inclusion is far from unambiguous, especially when all three components are present. It seems reasonable to suppose

that when one component has the largest volume fraction, that component is more likely than than the others to exist as an electrically connected matrix; especially if the constituent in question is rather conductive (i.e., the imaginary part of the permittivity is significantly greater than zero), as is the case for liquid water.

This connectedness can give the constituent a disproportionate influence on the computed effective permittivity. This observation is reflected in the findings of of Szyrmer and Zawadzki (1999) and Bauer *et al.* (2000) who, among others, employed the MG method, with ice inclusions in a water matrix, and found that the addition of very small volume fractions of liquid water to a ice-phase particle produced significantly warmer microwave brightness temperatures than the Bruggeman method or MG with water inclusions in an ice matrix.

The reason for the unusually warm simulated T_B arises from the fact that the MG formulation (2.42) is only strictly valid in cases where the volume fraction of the inclusion material is significantly less than the volume fraction of the matrix material (Lakhtakia and Shanker, 1993; Mackay, 2005). Furthermore, the discrete inclusions should be such that their size parameters, $x = \pi D' \lambda^{-1}$, of the inclusions are much less than unity (Bohren and Huffman, 1983). Figures A.1 and A.2 show the potential disparities that arise through the inappropriate application of the MG formulas compared to the Bruggeman formula.

The above limitations observations in actual composite particles (Mackay, 2005). As the volume fractions of inclusions increase, the following issues arise: (i) the inclusions are no longer able to maintain a random distribution within the matrix material; (ii) it becomes increasingly difficult for the discrete inclusions maintain sufficient separation such that they are not "electrically" connected; and (iii) the discrete inclusions are

required to be electrically small such that their size parameters are much less than unity. A. Lakhtakia, personal communication, indicates that a $\gtrsim 0.3$ volume fraction of MG inclusion components serves as an upper bound. There exist alternative methods that are contrived to circumvent these problems by way of incremental or differential application of the Maxwell Garnett formulation, such as Lakhtakia (1998); Michel *et al.* (2001). However, these formulations are beyond the scope and purpose of this research.

Three Component Mixtures

When dealing with mixtures of ice, water, and air, a three component mixing method is desired. One possibility is to apply the two-component methods twice (e.g., Schols *et al.* (1999)). However, this results in twelve different permutations of three component mixtures for the Maxwell Garnett approach and three permutations for Bruggeman approach, which is no longer symmetric when three components are used (see table A.1 in the appendix). Given the volume fraction limitations of the Maxwell Garnett approach, we derived a Bruggeman approach that is symmetric with respect to changes in the order and volume fractions of mixing ice, water, and air. The detailed formula is described in the appendix in section A.1.2, the generating formula is given by

$$f_1 \left(\frac{\epsilon_1 - \epsilon_{av}}{\epsilon_1 + 2\epsilon_{av}} \right) + f_2 \left(\frac{\epsilon_2 - \epsilon_{av}}{\epsilon_2 + 2\epsilon_{av}} \right) + (1 - f_1 - f_2) \left(\frac{\epsilon_3 - \epsilon_{av}}{\epsilon_3 + 2\epsilon_{av}} \right) = 0 \qquad (2.43)$$

where ϵ_{av} is the effective dielectric permittivity. It is easy to verify that interchanging constituents has no effect on ϵ_{av}. We conjecture that this is the general symmetric form for the three-component Bruggeman formula. The three-component form reduces

to the two-component form when one of the constituent volume fractions is zero. By following the same logic, this suggests that the form can be extended to N dielectric components. However, a solution for ϵ_{av} may not be analytically possible to compute for $N > 4$ constituents, however, a numerical solution could be used.

In fig. 2.8, the permittivities for a melting "fluffy" particle, i.e., one that contains ice, water, and air, are shown at each stage in the melting process for a frequency of 89 GHz and temperature of 0 °C . At each square marker, labels indicate the values $F_{ice} \equiv F_{air}$, where $F_{liq} = 1 - F_{ice} - F_{air}$. All sixteen permutations of the three-component MG and Bruggeman formulas are presented without explicit labeling. The purpose of doing so is to highlight the potential for variation within the complex-valued permittivities arising from these permutations. In particular, it is clear that the Bruggeman results fall within the bounds defined by the MG results. This suggests that the Bruggeman results are well behaved with respect to changes in constituent volume fractions throughout the entire range.

Because of the symmetric nature (consistent with the two-component Bruggeman formula) and the smooth behavior over all volume fractions, the symmetric three-component Bruggeman method (Eq. 2.43 and the explicit solution in A.18) is used exclusively throughout the remainder of this dissertation for two and three-component dielectric mixing.

2.8.4 Particle Shape DDA versus Mie Theory

Precipitation hydrometeors are most commonly modeled as homogeneous dielectric spheres, so that standard Mie codes may be utilized to compute local radiative transfer properties such as mass extinction coefficient κ, single scattering albedo ϖ_0, and the
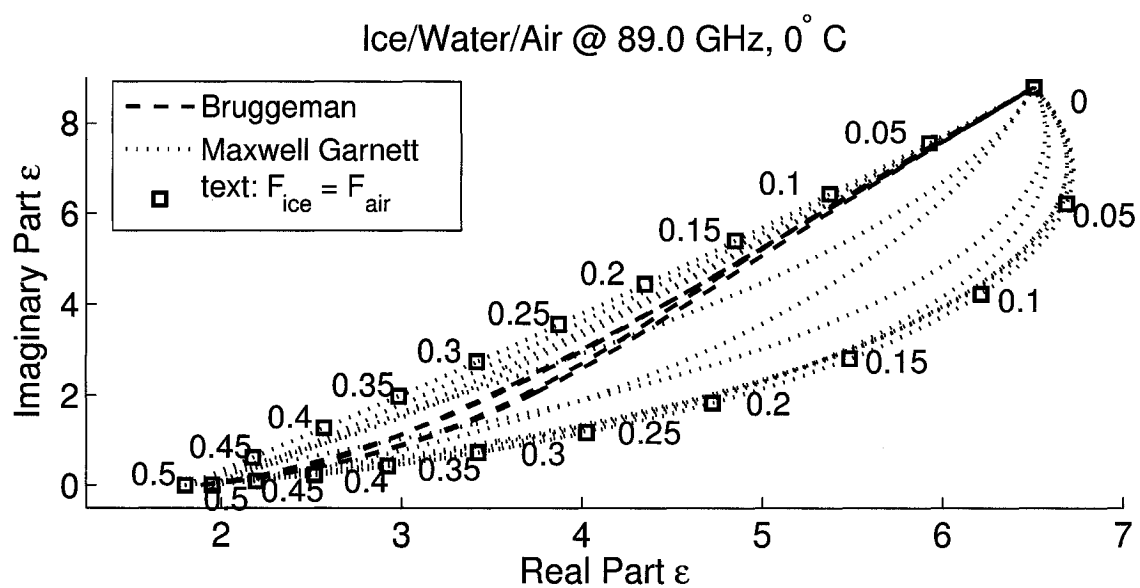
Figure 2.8. Real and imaginary components of the dielectric permittivity of a melting "fluffy" particle for varying volume fractions of ice, water, and air at 89.0 GHz at 0 °C . Text labels indicate $F_{ice} \equiv F_{air}$, where $F_{liq} = 1 - F_{ice} - F_{air}$. All sixteen permittivity mixing methods are shown.

scattering phase function $P(\Theta)$. In the case of raindrops, the spherical model is clearly acceptable, at least for smaller drop sizes (Beard and Chuang, 1987; Pruppacher and Klett, 1997). For most ice-phase hydrometeors (snow crystals and aggregates, rimed graupel particles, etc.), the spherical assumption is motivated more by convenience, and by the lack of practical alternatives, than by realism. For example, both observations and calculations indicate that there are significant polarization effects that arise in connection with non-spherical ice particles (Evans and Stephens, 1995a; Prigent *et al.*, 2001; Czekala and Simmer, 2002).

Nevertheless, it seems reasonable to postulate that a snow aggregate or graupel particle might be at least approximately modeled as a mass-equivalent sphere with an effective dielectric permittivity appropriate to a mixture of ice, air and, possibly, liquid water, since most of the internal structure of such a particle typically occurs on scales much smaller than common passive microwave wavelengths. At submillimeter wavelengths, however, scattering of microwaves by fine scale structures in ice-phase hydrometeors (e.g., snowflakes) becomes important (Liu, 2004). Other computational methods are probably necessary at these frequencies, such as the Discrete Dipole Approximation (Kim, 2004).

The Mie-based methods described here are likely limited to the range of microwave frequencies between 3 GHz (10 cm) and 200 GHz (1.5 mm) when using spheres to simulate non-spherical hydrometeors. This frequency range is consistent with channels on present day passive microwave radiometers such as the Advanced Microwave Scanning Radiometer for EOS (AMSR-E) and the upcoming Global Precipitation Mission (GPM) Microwave Imager (GMI). During the 2003 Wakasa Bay experiment (WBAY03), radiometer observations ranging up to 340 GHz were made. In the present research,

brightness temperatures were simulated for frequencies up to 220 GHz. Studies are currently in progress to determine the error induced by using spherical versus non-spherical particles.

2.9   Melting Layer Model

In this section, the melting layer model portion of the forward model is described. In present case studies, however, no rainfall cases were examined since the model is still being tested. The section is presented for completeness in describing the forward model and retrieval algorithm. Future research will focus on the specific issue of melting particles.

Melting particles in the atmosphere remain poorly understood both from a microphysical perspective and a radiometric perspective. A number of studies have attempted to untangle the issues associated with melting particles from the perspective of both passive microwave remote sensing and radar remote sensing. Schols *et al.* (1999), for example, identifies issues associated with observations of mid-latitude precipitation, particularly low rainfall rates, melting particles, and the associated microwave signatures. Melting layer (radar "bright band") modeling has been a recent topic of interest due to the uncertainty surrounding the microphysical and radiative properties of melting particles (Szyrmer and Zawadzki, 1999; Fabry and Szyrmer, 1999; Bauer *et al.*, 2000; Olson *et al.*, 2001b; Battaglia *et al.*, 2003; Sassen *et al.*, 2005).

Physical studies involving the melting of particles in wind tunnels has also yielded some important observations. For example, Mitra *et al.* (1990) notes that the distance for melting dendrites increases by 100 meters when the environmental relative humidity changes from 100% to 90%. They also note that meltwater tends to initially form

on the tips of dendrites, then migrate inward as they grow larger. Oraltay and Hallett (2005) corroborates the latter observation in their own wind-tunnel observations for dendrites. They also suggest that shedding of meltwater could contribute to supercooled liquid water clouds and/or provide a secondary ice-production mechanism through the riming/splintering process. It is evident from these studies that detailed in-situ observations of melting particles would still contribute greatly to the knowledge of microphysical properties of melting particles. At the present time, however, adequate instrumentation and observing platforms remain lacking to make accurate and robust measurements of these systems.

2.9.1 Physical Considerations

Qualitatively the approach for developing the present melting layer model is to model the mass of melted water as a function of distance below the freezing level (0 °C isotherm). The thermodynamic process followed is similar to Mitra *et al.* (1990) and Pruppacher and Klett (1997). However, the present model does not allow for a "continuous" modification of the particle size distribution (PSD) from snow to rain, as is expected in real situations (Pruppacher and Klett, 1997). Instead, the mass median diameter of the exponential PSD, $D_m = 4.0/\Lambda$, was chosen as the defining particle size for modeling melting. Once particles of this size have melted, then half of the mass of the distribution is melted, and then the model automatically switches to a rain-only regime.

Clearly this approach is lacking in a number of ways. However, it is superior to autoconversion techniques or simple linear melting models which do not explicitly account for the particle mass and relative humidity effects on the melting distance below the

melting layer. One final assumption made is that the vertical air motions in the melting layer are negligible, a seemingly reasonable assumption for stratiform precipitation. Given this restriction, the melting model is not suitable for convective precipitating clouds.

2.9.2 Theoretical Formulation

The theoretical construction of the melting model loosely follows that of Pruppacher and Klett (1997) and Mitra *et al.* (1990); starting with an empirically derived relationship for diffusional growth of ice crystals (Eq. 13-3 in Pruppacher and Klett (1997)),

$$D_V = 0.211(T/T_0)^{1.94}(p_0/p), \tag{2.44}$$

where D_V is the diffusion coefficient [cm^2 sec^{-1}], T is the air temperature [K], p is the pressure [mb], with constants $T_0 = 273.15$ K, and $p_0 = 1013.25$ mb.

The surface temperature of the ice crystal is influenced by ventilation, relative humidity, evaporative cooling, and other factors. A critical temperature T_{crit} is defined for the environmental temperature required for melting to begin. It is written as

$$T_{crit} = T_0 + \frac{D_V \, L_E \, M_W}{k_a \, R_{gas}} \left(\frac{e_i(T)}{T_0} - RH \frac{e_w(T)}{T} \right), \tag{2.45}$$

where $L_E = 797.3$ cal gm^{-1} is the enthalpy of evaporation, $M_W = 18$ gm mol^{-1} is the molecular mass of water, $k_a = 5.69 \cdot 10^{-5}$ cal (cm s °C)$^{-1}$ is the thermal conductivity of air, $R_{gas} = 8.314 \cdot 10^7$ erg (mol K)$^{-1}$ is the universal gas constant, e_w and e_i are the saturation vapor pressures of water and ice respectively [Pa], and RH is the relative humidity expressed as a fraction (rather than percent). The constant values are taken from Mitra *et al.* (1990).

The ventilation coefficient for vapor and heat transfer are set equal, and assigned a singular value, f_v, given by

$$f_v = \begin{cases} 1 + 0.14\chi^2 & \text{for} \quad \chi < 1 \\ 0.86 + 0.28\chi & \text{for} \quad \chi >= 1 \end{cases} \tag{2.46}$$

Given the above quantities, the melting rate (mass of ice converted to liquid per unit time) is expressed as

$$\frac{dm_w}{dt} = \frac{4\pi \, f_v \, C_i}{L_M} \left(k_a \, (T - T_0) + \frac{D_V L_E M_W}{R_{gas}} \left[RH \, \frac{e_w(T)}{T} - \frac{e_w(T_0)}{T_0} \right] \right), \tag{2.47}$$

where dm_w/dt is the increase of melt-water mass per unit time, $C_i = 1.0$ is the capacitance of the snowflake, and $L_M = 79.7$ cal gm^{-1} is the enthalpy of melting.

The mass of melt water (grams per layer) produced as snow falls through the layer is

$$M_{melt} = \frac{1}{v_s} \frac{dm_w}{dt} dz, \tag{2.48}$$

where v_s is the fall speed [m s^{-1}], dz is the thickness of the layer (nominally 30 meters).

Melting particle fall speeds are continuously modified following Zawadzki *et al.* (2005). These are expressed as modifications of 2.35,

$$a = a_{0,\text{rain}} \frac{\sqrt{\rho_{a0}/\rho_a(T, P)}}{(a_{0,\text{rain}}/a_{0,\text{snow}} - c_g F_{\text{liq}} - c_g F_{\text{liq}}^2)}, \tag{2.49}$$

where,

$$c_g = 0.5 \left(\frac{a_{0,\text{rain}}}{a_{0,\text{snow}}} - 1 \right) \tag{2.50}$$

and for b,

$$b = \frac{b_{0,\text{rain}}}{(b_{0,\text{rain}}/b_{0,\text{snow}} - d_g F_{\text{liq}} - d_g F_{\text{liq}}^2)} \tag{2.51}$$

where,

$$d_g = 0.5 \left(\frac{b_{0,\text{rain}}}{b_{0,\text{snow}}} - 1 \right).$$ (2.52)

In the above equations, $a_{0,\text{rain}} = 628.17$, $a_{0,\text{snow}} = 7.2059$, $b_{0,\text{rain}} = 0.7619$, and $b_{0,\text{snow}} = 0.311$ in SI units where appropriate. These equations simply express a transition from snowfall to rainfall fall speeds as a function of liquid water volume fraction, F_{liq}. At $F_{\text{liq}} = 0$ and $F_{\text{liq}} = 1$, the fall speeds are equivalent to the speeds for dry snow and rain respectively.

At each layer below the freezing level, the mass of melt water is summed, and divided by the mass of snow to obtain the updated water volume fraction,

$$F_{\text{liq}} = \frac{\sum_{z=z_{\text{fl}}}^{z_i} M_{\text{melt}}(z)}{\pi/6(4/\Lambda(z))^3 \rho_h(z)},$$ (2.53)

where z_{fl} is the height of the freezing level, z_i is the current level, $z_i = z_m$ is the level at which "complete melting" occurs, and ρ_h is the average density of the melting particle.

2.10 Summary

In this chapter, the various key elements of the forward model were described and referenced. The goal in developing this model was to simulate a precipitating atmosphere and the associated radar and radiometric response. The combination of elements in the forward model provides a method for computing the vertical profile of radar reflectivities and top of the atmosphere brightness temperatures for a 1-D column of a precipitating atmosphere.

However, no model is a perfect representation of reality, and certainly this is the case here. Several physical and simulation assumptions were made in development of this model. Specifically it is assumed that

- the use of spherical particles composed of up to three dielectric components: ice, water, and air is a sufficient description of the bulk dielectric properties of actual snow/melting/rain particles;

- 1-D vertical geometry is sufficient to characterize rain and snow events consistent with mid-to-high latitude precipitation;

- photon single-scattering is dominant, no multiple-scattering is explicitly accounted for in radar reflectivity simulations;

- the exponential particle size distribution provides an acceptable basis for both mid-latitude/cold-cloud snow and rain;

- scattering by ice clouds can be lumped into scattering by smaller-sized snow particles, while scattering by liquid clouds is negligible;

- directional effects in surface winds have a negligible effect on surface emissivity; whereas wind magnitude, surface roughness, and foam effects are accounted for.

The next chapter describes the retrieval method and how the forward model is used in that framework. Chapter 4 is devoted to error and sensitivity analysis, where the uncertainties/errors related to the above assumptions and the retrieval method are discussed. Following that, the 2003 Wakasa Bay experiment is described in chapter 5, with case studies to illustrate the application of the retrieval method and forward model simulations.

3 RETRIEVAL METHODOLOGY

The previous chapter described the forward model, which is used to generate radar reflectivities and brightness temperatures for a simulated 1-D column of a precipitating atmosphere. Several of the physical and radiative relationships employed in the forward model are also used in the retrieval methods described in this chapter. Symmetry between the forward model and retrieval method ensures that the necessary simulated relationships present in the retrieval are also employed in the forward model, avoiding potential inconsistencies in the overall retrieval scheme.

The retrieval methods described in this chapter expect observations (input) in the form of co-located, dual-wavelength, vertical, 1-D, radar reflectivity profiles and co-located passive microwave observations of the same scene. All observations should be made at near-nadir viewing angles, as would occur from aircraft or satellite based observations looking straight down toward the Earth's surface. The 2003 Wakasa Bay field experiment (WBAY03) made observations fitting these criteria, and are used as a case studies for the retrieval methods presented here.

The chapter proceeds as follows: First, the dual-wavelength radar retrieval method is described. Next, the method for constraining the radar-based retrievals using forward model brightness temperature simulations and observed brightness temperatures is described. Finally, several simulated contrived cases are examined to ensure consistency between the forward model and retrieval method.

3.1 Dual-Wavelength Ratio Method Description

The goal of the dual-wavelength ratio retrieval method is to estimate the two unknown exponential particle size distribution (PSD) parameters, N_0 and Λ, using dual-wavelength radar observations. Having two observations and two unknowns allows one to construct a linear system of equations. However, the relationship between the observed reflectivities and the true PSD properties at a given range gate is influenced by a number of factors, including path-integrated radar attenuation and the physical composition/characteristics of the volume of the atmosphere being observed.

The dual-wavelength ratio (DWR) is defined as the ratio of the unattenuated radar reflectivities for a radar system operating at two different wavelengths. The relationship is expressed as

$$\text{DWR} = \frac{Z_1}{Z_2}, \tag{3.1}$$

where Z represents either the attenuation corrected observed reflectivities, Z_m, or the simulated reflectivities, I_b, defined in the next sections. Subscripts 1 and 2 represent the higher frequency channel and lower frequency channel respectively (e.g., Z_{35} and Z_{14}).

A database of simulated radar reflectivities and extinction properties is created for use in the retrieval. These simulated quantities are expressed as a function of the exponential distribution slope parameter Λ, temperature T, volume fraction of water F_{liq}, and volume fraction of ice F_{ice}. The density of individual particles, ρ_h, is determined by the volume fractions of ice, water, and air (Eq. 2.38). It is assumed that both radar frequencies are observing the same number of particles (i.e., the same physical volume of the atmosphere), therefore the simulated DWR is defined to be

independent of N_0. Once Λ, F_{ice}, and F_{liq} are known, retrieval of N_0 at each range gate requires a single observed and simulated reflectivity and a measure of attenuation at the current range gate, r.

3.1.1 Theoretical Considerations

In the previous chapter, the effective radar reflectivity factor (Eq. 2.20) was derived in terms of an unspecified PSD, and an attenuation factor $\mathcal{A}$. Expressing (2.20) in terms of the exponential size distribution (Eq. 2.23) yields

$$Z_{\text{eff}}(r) = \mathcal{A}(r)\frac{N_0\lambda^4}{4\pi^5|K_w|^2}\int_D Q_{b,\text{Mie}}(D)\pi D^2 \exp(-\Lambda D)dD, \tag{3.2}$$

where λ is the wavelength of the radar radiation, $|K|$ is the K-factor (eq. 2.16), $\mathcal{A}$ is the attenuation factor (eq. 2.18), $Q_{b,\text{Mie}}$ is the backscattering efficiency from Mie theory, and D is the liquid-equivalent diameter.

In the retrieval database (section 3.1.2), the simulated reflectivities are stored independent of N_0,

$$I_b = \frac{\lambda^4}{4\pi^5|K|^2}\int_D Q_{b,\text{Mie}}(D)\pi D^2 \exp(-\Lambda D)dD, \tag{3.3}$$

where the dimensions of I_b are L^7 and, therefore $Z = N_0 I_b$. Similarly, the DWR for the retrieval database is computed by,

$$\text{DWR} = \frac{I_{b,1}}{I_{b,2}}. \tag{3.4}$$

For the cases examined in this dissertation, *observed* DWR values range from near zero to 1.2 (after compensating for attenuation). For spherical particles, the simulated maximum DWR value is unity, which implies that both radar wavelengths/frequen-

cies are observing particles within the Rayleigh regime. Therefore, the particle size information becomes more ambiguous.

An observed DWR of greater than unity implies that observed reflectivities at, for example, 35.6 GHz (K_a-band), are larger than the 13.4 GHz (K_u-band) reflectivities. In the WBAY03 observations, DWR values greater than unity typically occur near the tops of the precipitating structures, where pristine ice crystals are more likely to be present. It is hypothesized that the DWR values greater than unity arise from particle shape influences on the observed reflectivities. Other possibilities include biases in the radar calibration at low reflectivities and a sensitivity to smaller particles at 35.6 GHz (S. Tanelli, personal communication, 2006). Future work on incorporating non-spherical particles will be used to test this hypothesis, and it is hoped that additional calibrations will also be performed on the datasets from WBAY03.

3.1.2 Database Generation

The forward and backward DWR retrieval methods use a Mie-derived lookup table containing optical properties and radar reflectivities as a function of the exponential distribution slope parameter Λ, temperature T, volume fraction of water F_{liq}, volume fraction of ice F_{ice}, and radar frequency ν (at 13.4 and 35.6 GHz). The primary elements are derived from the hydrometeor model described in section 2.8. Equations 3.3 and 3.4 describe the computation of the N_0-normalized reflectivities and dual-wavelength ratio. The Fortran code for generating the database and associated subroutines are contained in appendix A.2. Figure 3.1 describes the basic features of the database used for lookups in the DWR retrieval method.

Database Model
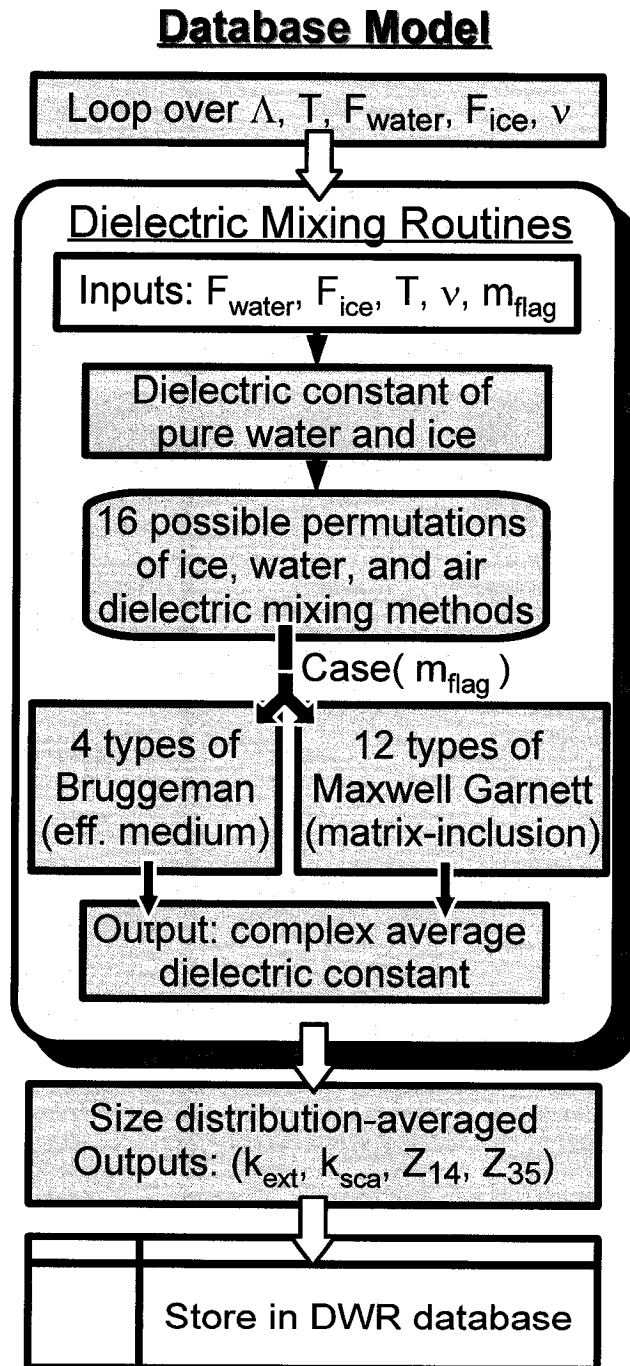
Figure 3.1. Schematic diagram depicting the elements of the database of Mie-derived parameters used in the dual-wavelength ratio retrieval method.

In the current implementation, the snowfall database is a three dimensional database; it is 4-D if melting is included, and is stored as a flat file. Table 3.1 denotes the variables for the snow-only (no melting) hydrometeor database as implemented. If melting occurs in the retrieval, an extension to the database is employed which covers all combinations of ice, water, and air, in addition to the other parameters present in the snow-only database. The respective ranges, resolution, and units for each variable are noted in the table.

In table 3.1, $\mathcal{K}_{\text{ext}}$ represents the extinction coefficient such that $k_{\text{ext}} = N_0 \, \mathcal{K}_{\text{ext}}$, and similarly $Z_{\text{eff}} = N_0 \, I_{\text{b}}$.

The database is used by the retrieval scheme as follows:

1. Given the attenuation corrected observed DWR value at a given range gate, the nearest bracketing database DWR values are found.

2. Linear interpolation between the bracketed DWR values is used to estimate Λ bracketing values.

3. Given the choice of particle density, the bracketing F_{air} values are found.

4. Given these quantities, the pre-computed backscatter I_{b} and extinction $\mathcal{K}_{\text{ext}}$ properties are selected from the database (sans N_0).

Figure 3.2 shows the primary database quantities, DWR and mass-weighted median diameter ($D_0 = 3.67/\Lambda$), plotted against each other in the case of ice-phase precipitation ($F_{\text{liq}} = 0$). Particle density variations are defined by the colorbar. The dependence on temperature in the database is neglected, since the sensitivity to temperature changes in the retrieval is much smaller than the sensitivity to natural variations in other parameters, such as the particle density.

Table 3.1

Mie derived lookup database used in DWR retrieval. Lists variables, ranges, increments and units used in the ice-phase hydrometeor database, where square brackets [...] denote an integer range. Melting requires an addition of F_{liq} to the database to encompass all combinations of ice, water, and air.

Variable	min	max	progression	units
Λ	4.0	1000	$\sum_{i=2}^{500} 1.0111\,\Lambda(i-1)$	cm^{-1}
F_{air}	0.0	0.98	$[0:100]/100.0$	–
F_{liq}	0.0	0.0	–	–
$I_{\text{b},13.4}$	$\sim 10^{-11}$	$\sim 10^{8}$	–	$\text{mm}^6\ \text{m}^{-3}\ \text{cm}^4$
$I_{\text{b},35.6}$	$\sim 10^{-11}$	$\sim 10^{8}$	–	$\text{mm}^6\ \text{m}^{-3}\ \text{cm}^4$
$\mathcal{K}_{\text{ext},14}$	$\sim 10^{-17}$	0.026	–	cm^3
$\mathcal{K}_{\text{ext},35}$	$\sim 10^{-16}$	0.070	–	cm^3
$\text{DWR}_{35.6,13.4}$	0.022	1.000	–	–

Panel (a) indicates that the database quantities are smoothly varying across the entire domain, which supports the idea of using interpolation as a means to reduce memory storage requirements while maintaining the precision of the retrieval.

Panel (b) of figure 3.2 is similar to figure 2.6 in section 2.5.4. For a fixed DWR value, a large range of applicable D_0 (liquid equivalent) values are possible when the density is unknown. It is also evident that for DWR values below 0.2, D_0 values greater than about 3.5 mm no-longer have a 1-to-1 relationship with DWR, and retrievals are somewhat ambiguous. To address this, the current retrieval scheme examines D_0 values in nearby layers to determine which side of the minima (for a given particle density) the database-lookup should occur on. This allows for a more intelligent selection of D_0 for a given DWR value within the non-monotonic regions, and allows for retrievals at significantly larger particle sizes.

Given the above database, we now have a lookup table from which the retrieval method can infer relevant microphysical and attenuation parameters from radar reflectivity and DWR observations.

3.2   Forward DWR Method: Theory

The forward method for the DWR retrieval method starts at the storm top, the first radar range gate, and proceeds downward, layer-by-layer. Each step accumulates attenuation information from gas, water vapor, and hydrometeors. Attenuation from prior levels is used to provide an attenuation corrected dual-wavelength ratio at each range gate via the two-way path integrated attenuation.
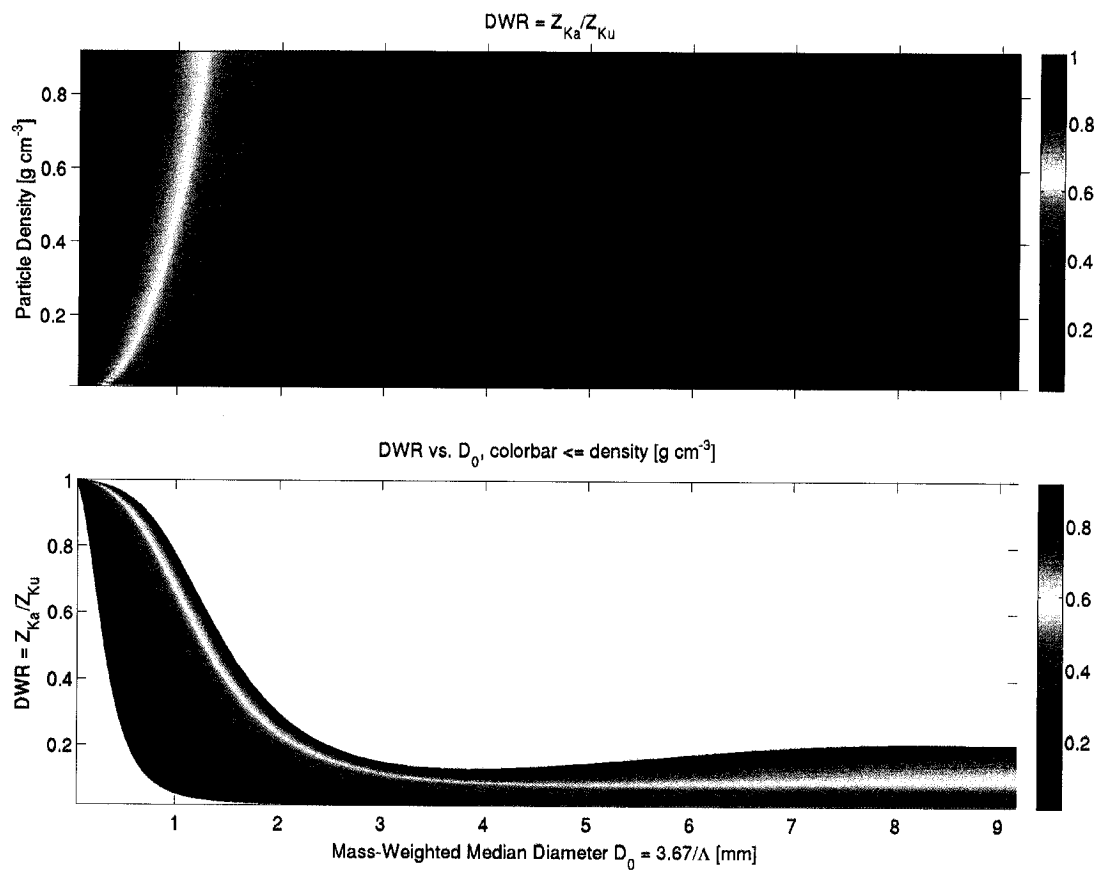
Figure 3.2. Relationship between particle density $\rho_{\rm snow}$, dual-wavelength ratio, and median particle diameter D_0. Λ and $\rho_{\rm snow}$ are independent variables; DWR is a function of these three variables for the snow case.

Similar to Meneghini *et al.* (1997), the (forward) DWR method equations at the j-th range gate and i-th frequency, are written

$$\mathcal{A}_i(r_j) \approx \exp\left[-2\delta_z \sum_{n=1}^{j-1}\left(k_{\mathrm{ext}}(r_n) + k_{\mathrm{gas}}(r_n)\right)\right], \tag{3.5}$$

$$\mathrm{DWR}_{\mathrm{m},1,2} = \frac{Z_{\mathrm{m},1}(r_j)\mathcal{A}_2(r_j)}{Z_{\mathrm{m},2}(r_j)\mathcal{A}_1(r_j)} \tag{3.6}$$

$$\mathrm{DWR}_{1,2} = \frac{I_{\mathrm{b},1}(\Lambda(r_j), \rho_{\mathrm{snow}}(r_j))}{I_{\mathrm{b},2}(\Lambda(r_j), \rho_{\mathrm{snow}}(r_j))} \tag{3.7}$$

$$\Lambda = \mathrm{DWR}_{1,2}{}^{-1}\left[\mathrm{DWR}_{\mathrm{m},1,2}(r_j)\right] \tag{3.8}$$

$$
\begin{aligned}
N_0 &= \frac{Z_{\mathrm{m},1}}{I_{\mathrm{b},1}\left(\Lambda(r_j), \rho_{\mathrm{snow}}(r_j)\right)\mathcal{A}_1(r_j)} \\
&= \frac{Z_{\mathrm{m},2}}{I_{\mathrm{b},2}\left(\Lambda(r_j), \rho_{\mathrm{snow}}(r_j)\right)\mathcal{A}_2(r_j)}.
\end{aligned} \tag{3.9}
$$

Equation 3.5 represents the accumulated attenuation contribution from gas and hydrometeors from the radar to the current range gate (similar to equation 2.18). δ_z represents the thickness of the current layer, and the units of the sum cancel. It is important to note that the attenuation correction assumes that the only sources of attenuation are from hydrometeor extinction, cloud liquid water absorption, and gaseous absorption. Furthermore, any errors or uncertainties in the estimates of these quantities propagate as the retrieval progresses from the top of the cloud toward the bottom. If the total path-integrated attenuation is large, then this method of solution is subject to increasingly large uncertainties as the retrieval works toward the surface.

Equation 3.8 represents the "retrieval" of Λ by matching the observed $\mathrm{DWR}_{\mathrm{m}}$ and simulated DWR, then finding the Λ in the database that is consistent with the two

reflectivity values and DWR. Retrievals are only currently performed if $DWR_m < 1.0$, which is generally the case in snow and light rainfall for the 13.4 GHz and 35.6 GHz combination.

Once Λ is known, N_0 can be retrieved using either of the reflectivities, as indicated in equation 3.9, although the results aren't always equivalent due to sensitivity differences between the two radar frequencies. For consistency, the high-frequency channel is always used to retrieve N_0 in the current retrieval scheme, since it is likely to be sensitive to smaller particles. At each range gate, a large range of "candidate" Λ and N_0 values are retrieved if the particle density is unspecified or unknown. Section 3.3.3 describes the method for specifying particle density profiles in order to provide an artificial constraint on the retrieval.

The present DWR method proceeds by successive repetition of equations 3.5 through 3.9 starting at the cloud-top, i.e., the first observed reflectivity value, and progressing toward the surface. The two-way path integrated attenuation (3.5) accumulates from top-to-bottom.

An alternative method (not shown here), described by Meneghini *et al.* (1997), starts at the surface and proceeds toward the radar. This is the so-called "backward" method, which is primarily used in regions of strong attenuation. The present method is referred to as the "forward" DWR method (not to be confused with the forward model).

3.3 DWR Implementation

The flowchart for the DWR retrieval method is presented in figure 3.3. This depicts the actual implementation of the equations presented in the preceding section.
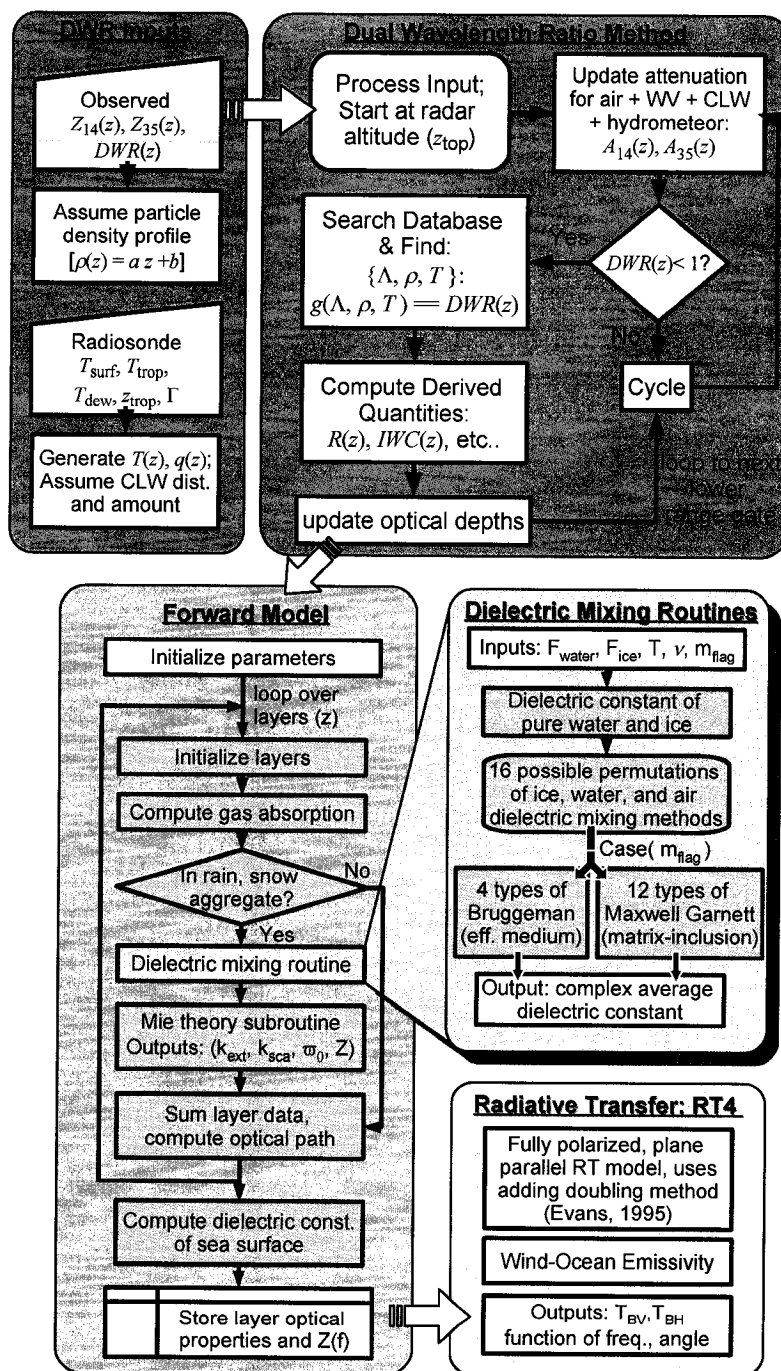
Figure 3.3. Schematic diagram depicting the elements of the DWR retrieval algorithm.

3.3.1 Interpolation

As described previously, the relatively low resolution of the database requires interpolation between simulated DWR values to match observed DWR values. Accordingly, the retrieved values are also interpolated, assuming linearity between bracketing DWR, F_{liq}, F_{air}, Λ, $I_{\text{b,i}}$, and $\mathcal{K}_{\text{ext,i}}$ quantities. Visual inspection of figure 3.2 indicates smooth variations over all ranges of interest within the database, so that interpolation is expected to only introduce very small uncertainties. An additional benefit of using interpolation is a factor of 10 or more reduction in computation time compared to when a higher resolution database is used (not shown). On a modern computer, the DWR-retrieval requires approximately 30 minutes to preform all permutations for the entire snowfall case, consisting of 450 individual observed 1-D radar profiles, presented in section 5.3. However, T_{B} computations for each permutation on the entire dataset requires a few weeks of continuous operation. A method for reducing the T_{B} computation time is discussed in section 3.4.

3.3.2 Cloud Liquid Water Variational Model

Radar observations in the presence of precipitation are also affected by cloud liquid water and, to a lesser extent, water vapor and atmospheric gaseous absorption. No explicit modeling of cloud ice is performed, since it is assumed that precipitation sized particles (when present) would swamp any reflectivities originating from cloud ice. Also, the sensitivity range for the DWR-method, using 13.4 and 35.6 GHz observations, precludes measurement of cloud ice particle sizes.

Cloud liquid water (CLW) behaves differently from ice-phase precipitation in both the radar and radiometric observation regimes, due to the differences in the dielectric properties of ice and water (Evans and Stephens, 1995a). At 13.4 and 35.6 GHz, it is assumed that cloud liquid water only absorbs the radar beam without contributing to the observed reflectivities. Specifically, the retrieval method assumes that observed reflectivities arise only from precipitation sized particles, whereas the two-way path attenuation has contributions from precipitation, cloud, water vapor, and gaseous absorption.

It should be noted that at higher radar frequencies, such as 95 GHz, cloud particles are no longer a negligible source of reflectivity and should be considered explicitly. Although WBAY03 had 95 GHz radar observations co-located with the 13.4 and 35.6 GHz observations, the present research does not use the 95 GHz observations due to uncertainties in the calibration and the strong path-integrated attenuation present in heavy precipitation. Future research will examine the inclusion of the 95 GHz channel within the retrieval framework, as it could be employed for determining both cloud water contents and particle density.

A novel model for the inclusion of CLW information in the retrieval framework was developed to compensate for the lack of external/ancillary CLW observations. The CLW model consists of 10 possible variations in cloud liquid water height and distribution, given a user-provided maximum cloud top height (z_{top}) and cloud liquid water path (CLWP). The n_β parameter is used in the forward model and retrieval to identify these 10 variations; the respective values are listed in table 3.2.

To model the vertical distribution of CLW, a parabolic CLW distribution model, following Petty (2001b) is employed. For the case study presented in chapter 5, 16

values of CLWP ranging from 0.0 to 3.0 kg m^{-2} are used. Cloud liquid water content (CLWC) values at a given level are determined by the following: the CLWP, the n_β parameter, and the value of the parabolic shape at the given level in the 1-D profile. Table3.2 lists the various choices for cloud height and thickness options. The purpose of this model is not to precisely retrieve cloud liquid water amount and distribution, but rather attempt to provide a suitable amount and position of CLW such that the forward model simulated T_Bs are consistent with observations.

Each DWR retrieval is performed for all ten values of n_β, to provide a set of possible CLW position and extent. $n_\beta = 0$ represents the "no attenuation" case, where $\mathcal{A} = 1.0$ throughout the entire profile. In the case studies presented in chapter 5, each of the 9 variations ($n_\beta = [1:9]$) of cloud position and extent, and up to 16 values of CLWP are computed. This results in as many as 144 possible cloud liquid water variations for each retrieved profile of PSD properties. Section 5.3.3 provides further descriptions on how the CLW profiles are used in the retrieval method.

Figure 3.4 illustrates the distribution of cloud liquid water for various values of n_β. As an example case, the cloud liquid water path is constant at 0.3 kg m^{-2} for each curve, while the vertical distribution differs.

3.3.3   Particle Density Variational Model

Radar-based retrievals of ice-phase precipitation particle properties are sensitive to both the particle size and the dielectric properties of the material, namely ice and air. In a ice-phase particle, the actual size and average dielectric constant are controlled by the particle density or, equivalently, the volume fractions of ice and air (Eq. 2.38).

Table 3.2

Variable parameters provided by cloud liquid water model. z_{top} is the user-provided maximum possible cloud top height.

n_β	description	position and extent
0	no cloud	$z_{\text{top}} = z_{\text{surface}}$
1	low, narrow	$0.15 z_{\text{top}} \pm 0.125 z_{\text{top}}$
2	low, medium	$0.15 z_{\text{top}} \pm 0.250 z_{\text{top}}$
3	low, broad	$0.15 z_{\text{top}} \pm 0.500 z_{\text{top}}$
4	mid, narrow	$0.50 z_{\text{top}} \pm 0.125 z_{\text{top}}$
5	mid, medium	$0.50 z_{\text{top}} \pm 0.250 z_{\text{top}}$
6	mid, broad	$0.50 z_{\text{top}} \pm 0.500 z_{\text{top}}$
7	high, narrow	$0.85 z_{\text{top}} \pm 0.125 z_{\text{top}}$
8	high, medium	$0.85 z_{\text{top}} \pm 0.250 z_{\text{top}}$
9	high, broad	$0.85 z_{\text{top}} \pm 0.500 z_{\text{top}}$
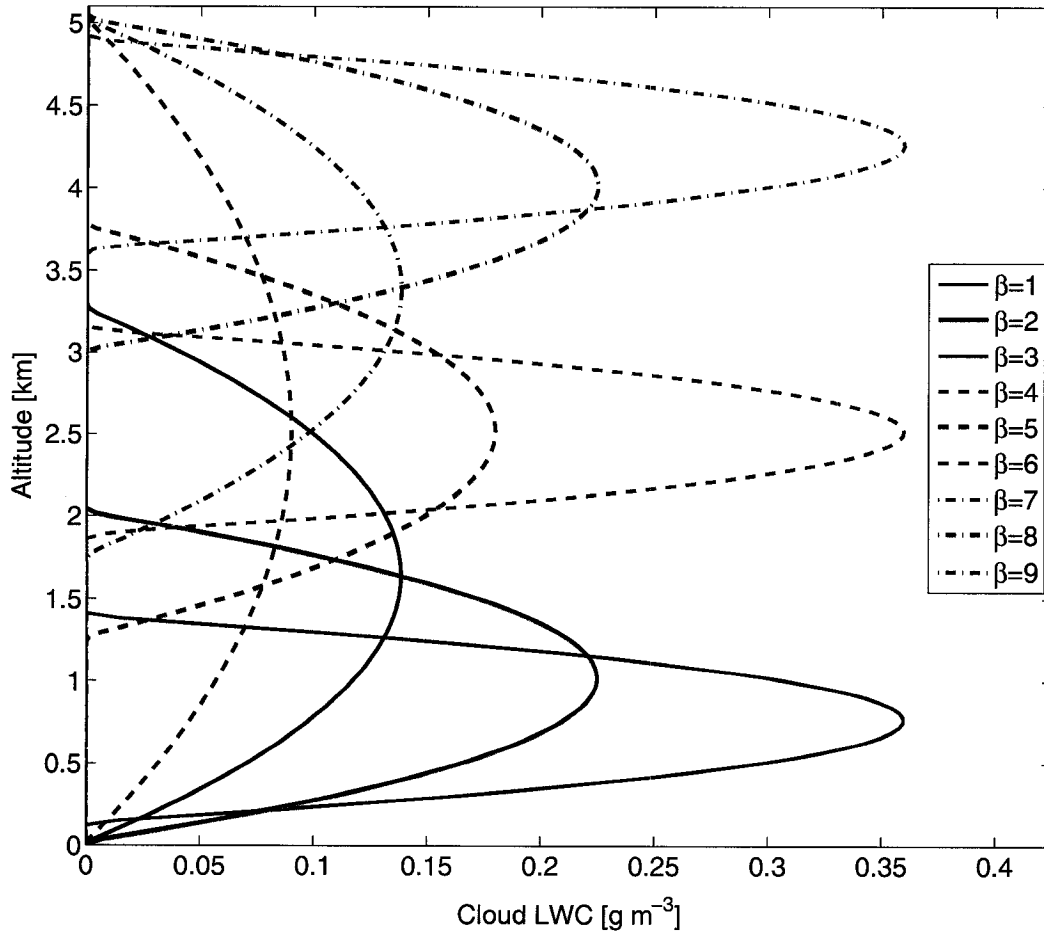
Figure 3.4. Example vertical profiles of cloud liquid water (CLW) for the n_β parameters from table 3.2. The cloud liquid water path for each curve is 0.3 kg m^{-2} .

As mentioned in previous sections, the particle density is an important, yet unknown parameter in the present DWR-retrievals. Figure 3.5 provides an example where the DWR retrieval method is allowed to choose the "best fit" with an unconstrained possibility of densities at each range gate. The scattered results show that the retrieved particle properties can yield valid mathematical solutions to the retrieval problem for a wide range of variations of particle densities at each layer. Such variations are unlikely, therefore subjective assumptions regarding the vertical distribution of particle densities are required.

In the present case studies, a novel approach is taken to prescribe a vertical profile of particle density. This approach is contrasted with that of Meneghini *et al.* (1997) who have employed a constant density value. The present assumption is that the volume fraction of air in the ice-phase particles varies linearly with altitude in the model, independent of the structure of the precipitating cloud. This allows for a consistent application of the particle density model for a variety of cloud heights having tops below 5 km (for the present case). The slope of the density profiles mimics observations that pristine crystals (highest density) occur at high altitudes and aggregates/dendrites (low density) occur at lower altitudes (Pruppacher and Klett, 1997). Some profiles are simply constant throughout the vertical column. The wide variety in the density profiles are intended to reasonably cover the entire range of particle density variations expected in winter-time mid-latitude precipitation.

Variations of the linear density profiles for snow are computed as a function of altitude. The sensitivity of changes in density to the retrieved hydrometeor properties are explored in section 3.5 and in chapter 4. In all, 14 total density profile variations (n_ρ) were explored. The individual density profiles are described in table 3.3, and are

Figure 3.5. Example radar reflectivity profile (a) and dual-wavelength ratio (b) taken from Wakasa Bay observations on 29 January 2003 (snow case). Panels (c) and (d) show retrieved Λ and N_0 values in the case where the vertical profile of ice-phase particle density is unconstrained.

expressed in terms of the density of the snow particle as a function of altitude (in some cases). Figure 3.6 graphically depicts the prescribed density height relationships for various values of n_ρ .

Given the above density constraints, the resulting retrieval at $n_\rho = 2$ ($\rho_{snow} = 0.4$ g cm^{-3}) is shown in figure 3.7. Compared to unconstrained-density retrieval shown in figure 3.5, the application of the linear density constraint results in a more smoothly varying retrieval of Λ and N_0. In actual stratiform precipitation, it has been observed that the ice-phase precipitation density generally varies relatively smoothly through standard growth or depletion processes (Houze, 1993; Rogers and Yau, 1989). By using the linear density model, we have assumed that the particle density is either constant or decreases with decreasing altitude, consistent with the model of having pristine ice crystals near the cloud tops and growth by vapor deposition, aggregation, and riming as the particles fall through the atmosphere (Pruppacher and Klett, 1997). These growth modes results in a lower bulk density (ρ_{snow}) when using the spherical approximation of real particles.

3.4 Brightness Temperature Retrieval Constraints

Because of the ill-posedness of the DWR-retrieval method, particularly in the choice of density and cloud liquid water distribution, additional constraints on the retrieval are desirable. During the 2003 Wakasa Bay (WBAY03) field experiment, the aircraft made not only dual-wavelength radar observations, but also co-located passive microwave observations using the MIR instrument (section 5.1.2). To constrain the DWR-based retrievals using passive microwave brightness temperatures (T_Bs), the DWR-retrieved

Table 3.3

Parameters for the 14 linear particle density models used in the retrieval algorithm. The units of the altitude, **alt**, is kilometers. The maximum density values assume an aircraft altitude of ~ 5 km.

n_ρ	equation [g cm^{-3}]	min(ρ_{snow}) [g cm^{-3}]	max(ρ_{snow}) [g cm^{-3}]
0	$\rho_{\text{snow}} = 0.10$	0.10	0.10
1	$\rho_{\text{snow}} = 0.20$	0.20	0.20
2	$\rho_{\text{snow}} = 0.40$	0.40	0.40
3	$\rho_{\text{snow}} = 0.60$	0.60	0.60
4	$\rho_{\text{snow}} = 0.80$	0.80	0.80
5	$\rho_{\text{snow}} = \text{alt}/17.0 + 0.10$	0.10	0.40
6	$\rho_{\text{snow}} = \text{alt}/17.0 + 0.30$	0.30	0.60
7	$\rho_{\text{snow}} = \text{alt}/17.0 + 0.50$	0.50	0.80
8	$\rho_{\text{snow}} = \text{alt}/17.0 + 0.70$	0.70	0.917
9	$\rho_{\text{snow}} = \text{alt}/33.0 + 0.25$	0.25	0.40
10	$\rho_{\text{snow}} = \text{alt}/33.0 + 0.45$	0.45	0.60
11	$\rho_{\text{snow}} = \text{alt}/33.0 + 0.65$	0.65	0.80
12	$\rho_{\text{snow}} = \text{alt}/33.0 + 0.05$	0.05	0.20
13	$\rho_{\text{snow}} = \text{alt}/33.0 + 0.20$	0.20	0.50
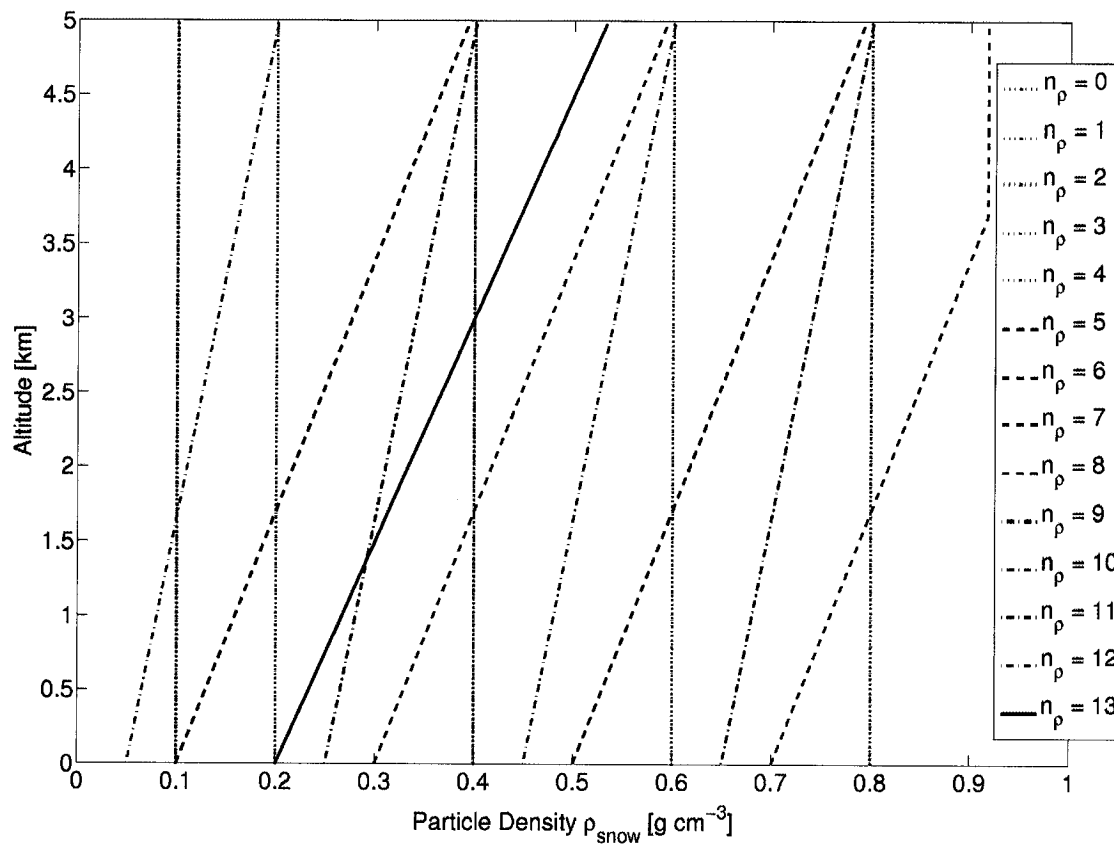
Figure 3.6. Linear vertical hydrometeor density profiles used in retrieval at $n_\rho = 0$ to $n_\rho = 13$. See table 3.3 for respective relationships.

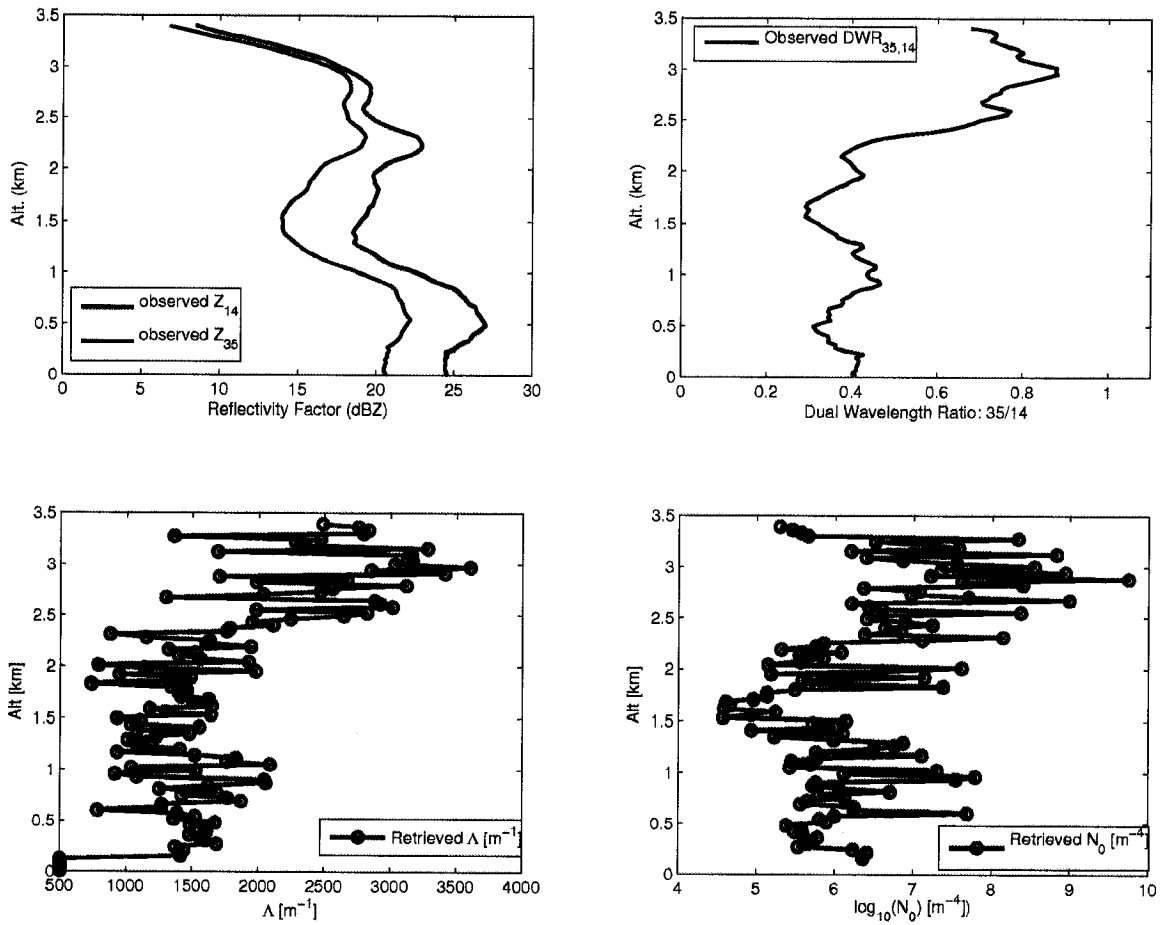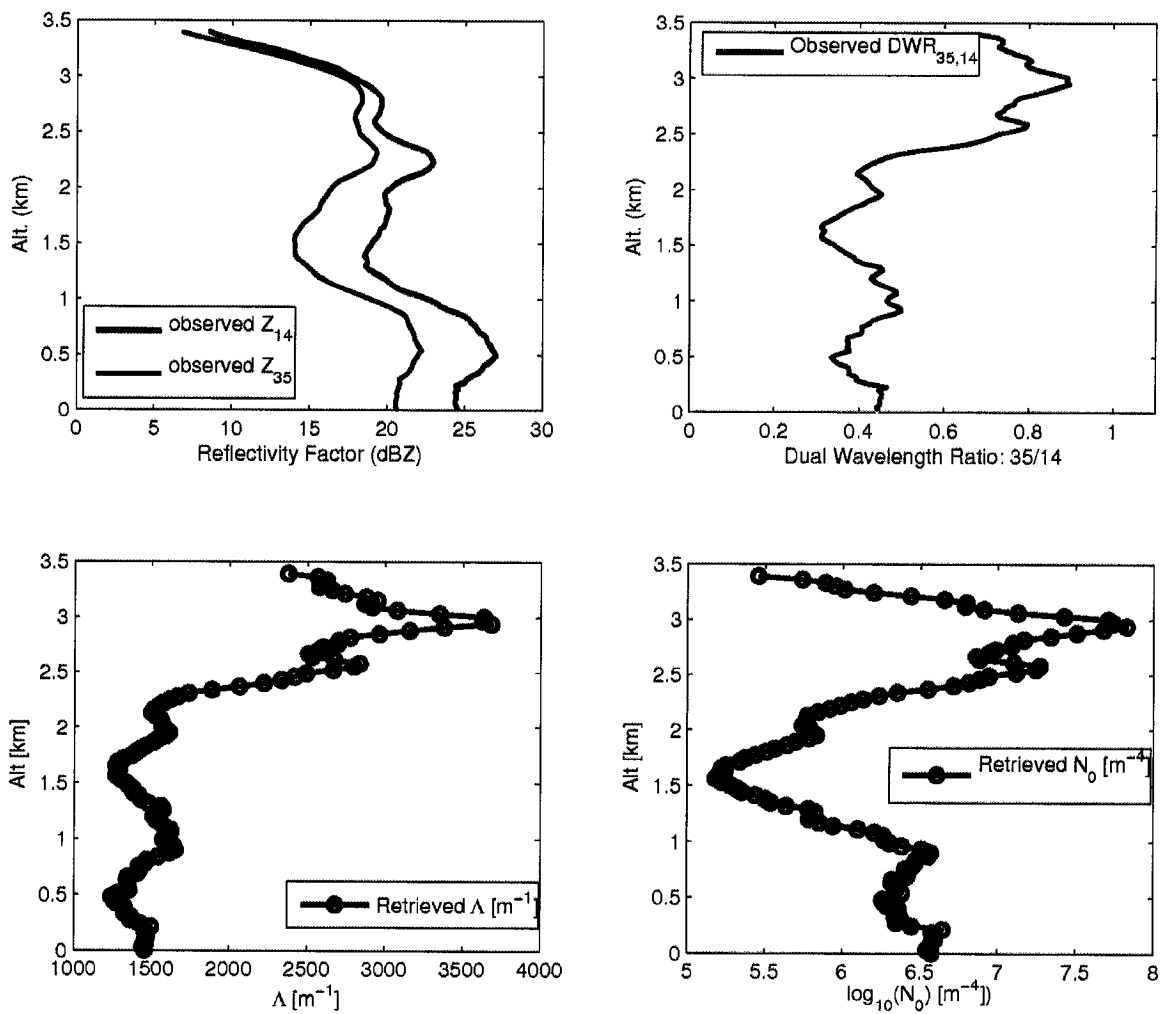Figure 3.7. Example radar reflectivity profile (a) and dual-wavelength ratio (b) taken from Wakasa Bay observations on 29 January 2003 (snow case). Panels (c) and (d) show retrieved Λ and N_0 values in the case where the vertical profile of ice-phase particle density is constrained at $n_\rho = 2$ ($\rho_{\text{snow}} = 0.4 \text{ g cm}^{-3}$).

set of candidate profiles are fed into the forward model described in chapter 2 to generate a set of simulated T_Bs at the same frequency as the observed T_Bs.

The simulation of passive brightness temperatures requires information about the sea surface temperature and surface emissivity, which are additional parameters not required in the DWR-only retrieval. Over open ocean, the primary source of variations of surface emissivity is the near-surface wind speed. For each retrieved DWR profile, a large number of T_B simulations must be made at each frequency to cover the possible range of variability in the surface wind speed. However, rather than computing numerous T_B simulations for each possible wind speed value, detailed sensitivity studies were performed (not shown here) to determine the best-fit wind-speed over clear-sky regions in the case studies presented in chapter 5. The optimal wind speed value of 17 m s^{-1} for the WBAY03 snowfall case was then presumed to be constant for the entire observation set, consistent with AMSR-E and radiosonde observations.

A standard error measure, the root-mean-square error (RMSE), is computed by first obtaining the mean of the summed squared error between observed and simulated T_Bs(summed over the number of channels), then the square root is applied (Taylor, 1997). The RMSE is written as

$$\text{RMSE} = \left(\frac{1}{n} \sum_{\nu=1}^{n} \left[(T_{B,\text{obs},\nu} - T_{B,\text{sim},\nu})^2 \right] \right)^{1/2}, \tag{3.10}$$

where n represents the number of radiometer channels (frequencies) present; $n = 3$ in the present studies ($\nu = $ 89, 150, and 220 GHz). Minimizing the RMSE for all simulated T_Bs, a "best fit" to the observed T_B data is determined. The parameters n_ρ, n_β, cloud liquid water path, and wind speed resulting in the best-fit (i.e., the lowest RMSE between simulated and observed T_Bs) are said to be the parameters of the T_B-

constrained retrieval. Combined with the N_0 and Λ profile, these quantities provide the complete results of the present retrieval algorithm.

3.5 Contrived Retrieval Case

The most basic test of the retrieval method is apply it to a contrived set of observations where the microphysical profile and thermodynamic structure is known ahead of time. Using the forward model, a single 1-D profile was created such that it smoothly and continuously increased in reflectivity from the top near 5 km down to the surface. Figure 3.8 shows the contrived profile. In the following figures, the "true" values are represented by blue x's, and the simulated/retrieved values are black circles. To simplify the initial analysis, the forward model is set to have no attenuation throughout the vertical profile, similarly the retrieval assumes no attenuation (i.e., $n_\beta = 0$ and, thus, $\mathcal{A}_i = 1.0$).

3.5.1 Basic Retrieval

To test the retrieval method, the first step is to apply the DWR-algorithm to the "observed" radar-reflectivities for while modifying the particle density parameter, n_ρ . The results for a single, first guess density ($\rho_{snow} \simeq 0.7$g cm^{-3} using $n_\rho =11$) is shown in figure 3.8. Clearly, the retrieved N_0 and D_0 profiles are not close to the true quantities, despite a perfect match for both the radar reflectivities and dual-wavelength ratio. As with real data, it is impossible to discern which n_ρ value provides an optimal fit using the DWR-method alone. Additional constraints are imposed here via simulated brightness temperatures for each of the available n_ρ values, listed in table 3.3. Each

simulated T_B set is compared to the "true" forward-model T_B set to determine the best fit.

The true particle density profile was chosen ($\rho_{snow} = 0.4$ g cm^{-3}) such that none of the standard 14 n_ρ values provided a sufficient T_B fit to the "true" T_Bs. Therefore, an additional "floating" n_ρ value was added to the retrieval and was adjusted until the simulated T_Bs fit the observed T_Bs. The constant value of $\rho_{snow} = 0.4$ g cm^{-3} was found to provide the best $T_B$fit, and the results are shown in figure 3.9. The only change between figure 3.8 and 3.9 is in the particle density, from $\rho_{snow} \simeq 0.7$ g cm^{-3} to $\rho_{snow} = 0.4$ g cm^{-3} .

These figures illustrate the application of the retrieval method for contrived cases where the truth is known *a priori*. Even in these contrived cases, some imperfection is expected due to numerical differences between the forward model and retrieval algorithm. Slight variations in the forward model density relating to changes in density with temperature also result in some deviations from a perfect retrieval.

It should be noted that there's an implied assumption here that the particle density is largely responsible for the goodness of fit between observed and simulated T_Bs. Other parameters, such as wind speed, temperature, water vapor profile etc. also influence observed T_Bs. Without external validation of the selected density, it is impossible to select the "most correct" density profile for a given retrieval. We cannot state with any certainty that it is the best representative particle density for the actual particle. Rather, the compelling argument here is that the selected density profile provides a general consistency between the radar observations, radiometer observations, and simulations.s
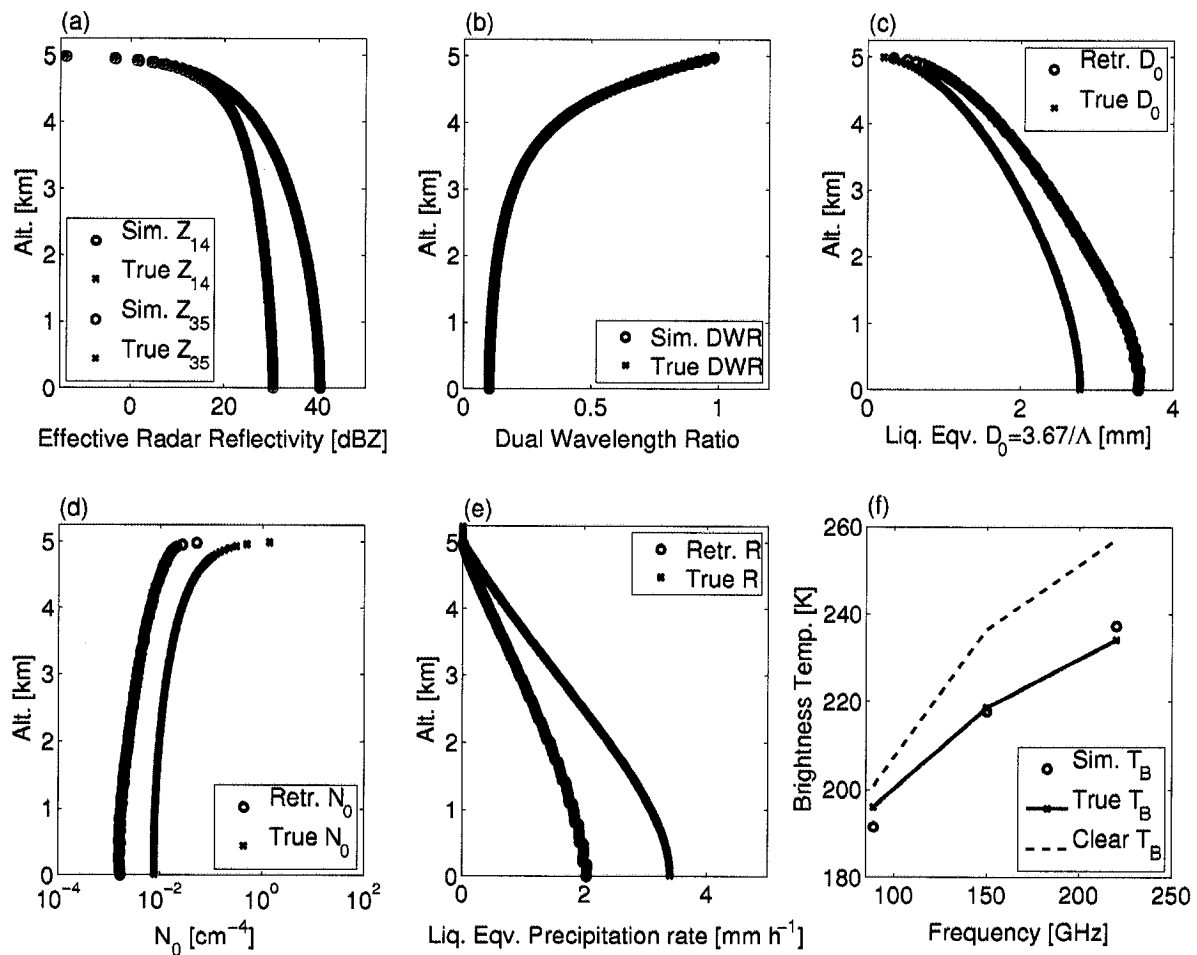
Figure 3.8. Forward model "truth" (blue x's) and simulated / retrieved quantities (black circles) are shown for a contrived case. The density is assumed to be $\sim\rho_{\text{snow}}=0.7$ g cm^{-3} , resulting in retrieved quantities different than the true values.
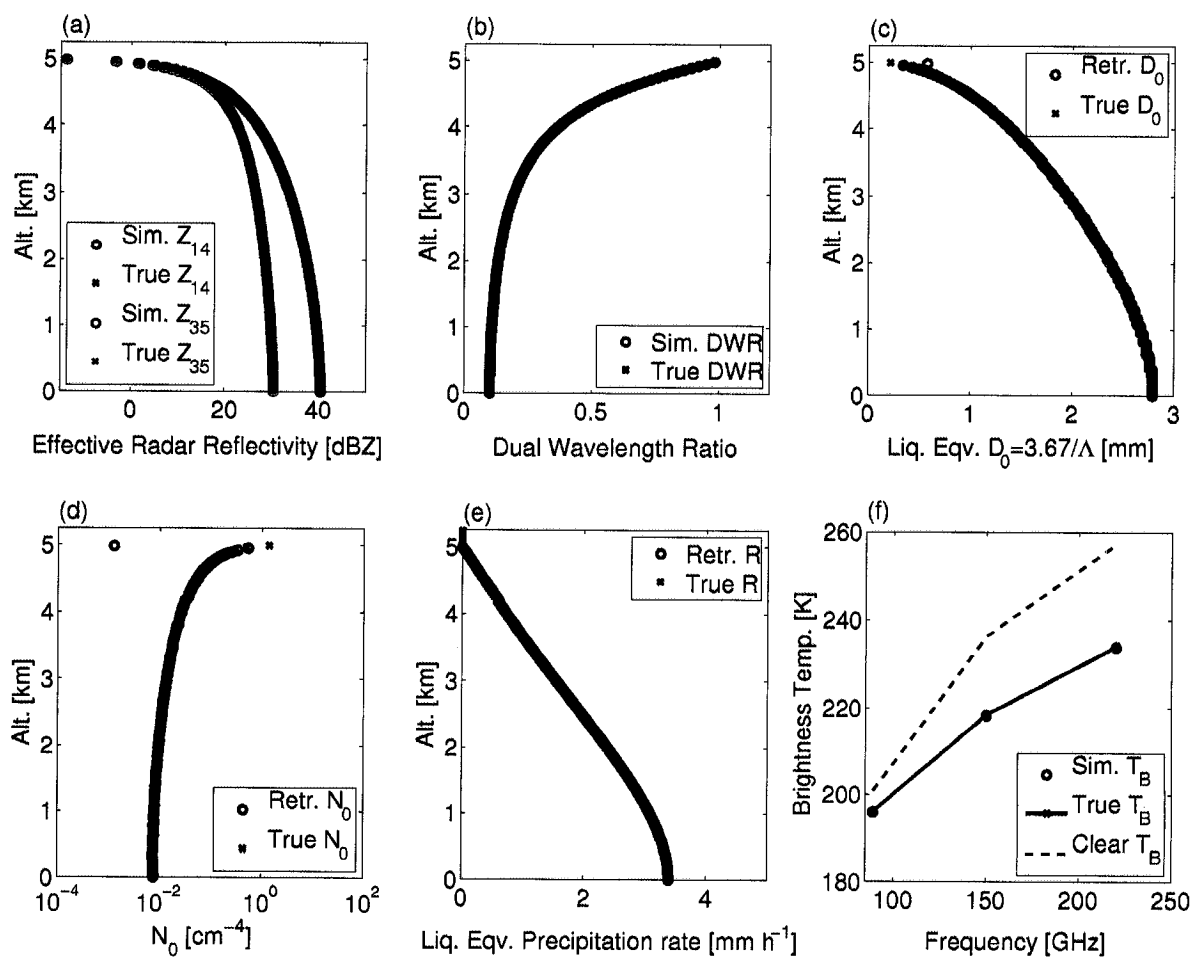
Figure 3.9. Similar to figure 3.8, except that the T_B-constraint method has been applied to find the particle density value providing the smallest RMSE between the true and simulated T_Bs. The best-fit density is found to be $\rho_{snow} = 0.4$ g cm^{-3}, equivalent with the true particle density.

3.5.2 Basic Retrievals With Reflectivity Noise

In the previous section, the basic retrieval was performed on a smoothly varying dataset. In real data, the source and magnitude of radar "noise" is generally unknown – it could be due to real variations in the precipitation microphysics, instrument noise, viewing geometry, etc.

To simulate the retrieval under noisy conditions, random noise in the range of ± 0.5 mm h^{-1} was added to the liquid equivalent precipitation rate: a basic quantity that the forward model simulates, which in turn influences the other simulated values, such as the true/"observed" radar reflectivity – the primary input to the retrieval algorithm.

Figure 3.10 shows the result of adding noise to the precipitation rate in the forward model. The true/observed reflectivities and DWR are clearly influenced by the noise; however, the DWR-retrieval is still able to retrieve N_0 and D_0 accurately. As in the base example, the true particle density is $\rho_{snow} = 0.4$ g cm^{-3}, and the T_B-constraint method correctly identifies this in the retrieval. These results indicate that the retrieval is robust in the presence of variations in the observed radar reflectivities, while the true particle density remains smooth or constant.

3.5.3 Basic Retrievals With Particle Density Noise

In real observations, the particle density is unlikely to be constant throughout the entire profile. However, the DWR-retrieval always assumes a linear density profile. By adding noise to the density profile, the robustness of the retrieval method is tested.
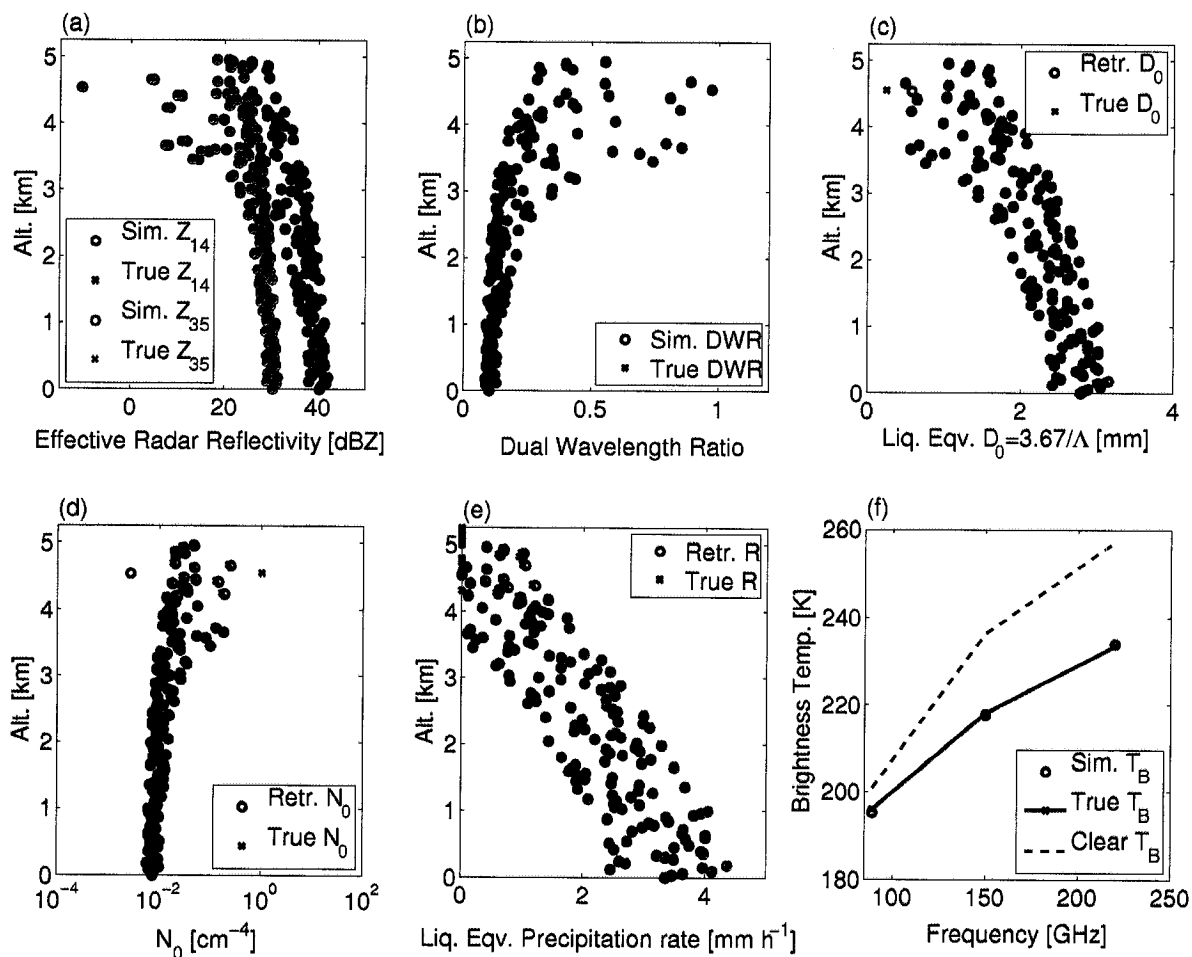
Figure 3.10. Random noise in the range of ± 1 mm h^{-1} is been added to the base precipitation rate (fig. 3.9) in the forward model, and the retrieval algorithm is subsequently applied. The true particle density of $\rho_{snow} = 0.4$ g cm^{-3} is unchanged. The T_B-constraint method was applied and the particle density value of $\rho_{snow} = 0.4$ g cm^{-3} provides the best T_B fit.

Figure 3.11 shows the effect of adding random noise to F_{air} in the range of ± 0.15 relative to a base value of F_{air}=0.56, which results in a particle density range of approximately $\rho_{snow} = 0.4 \pm 0.14$g cm^{-3} . Despite the large variation in retrieved properties, the T_B-constraint portion of the retrieval finds that the particle density value of $\rho_{snow} = 0.4$ g cm^{-3} provides the best average fit.

To reduce the spread in the retrieved quantities, a 9-layer smoothing window is applied to the vertical profile of reflectivities, this is shown in figure 3.12. This has the effect of smoothing out rapid variations in the vertical profile, however there's no longer a direct match between the observations and simulations. The best $T_B$fit density is, as before found to be $\rho_{snow} = 0.4$ g cm^{-3} . Relative to figure 3.11, the simulated T_B values are slightly higher than the true values after the application of smoothing. The retrieved D_0 and N_0 values are more closely constrained to the true observations, despite some telescoping effects near the storm bottom. A similar smoothing technique is applied to WBAY03 observations to reduce spurious retrievals, and is described in section 5.2.3.

3.5.4 Basic Retrievals With Both Density and Reflectivity Noise

If noise is added to both the precipitation rate *and* to the true particle density profile, as seen in figure 3.13, the accuracy of the DWR-retrieval further decreases. The precipitation rate and density noise are randomly added as previously described. The addition of both sets of noise results in an large spread in both true and retrieved parameters. While the retrieval is able to find simulated DWR and reflectivities that match the observations, the retrieved properties have a large spread, even under the best-fit T_B-constraint simply due to the fact that our simple linear density profiles
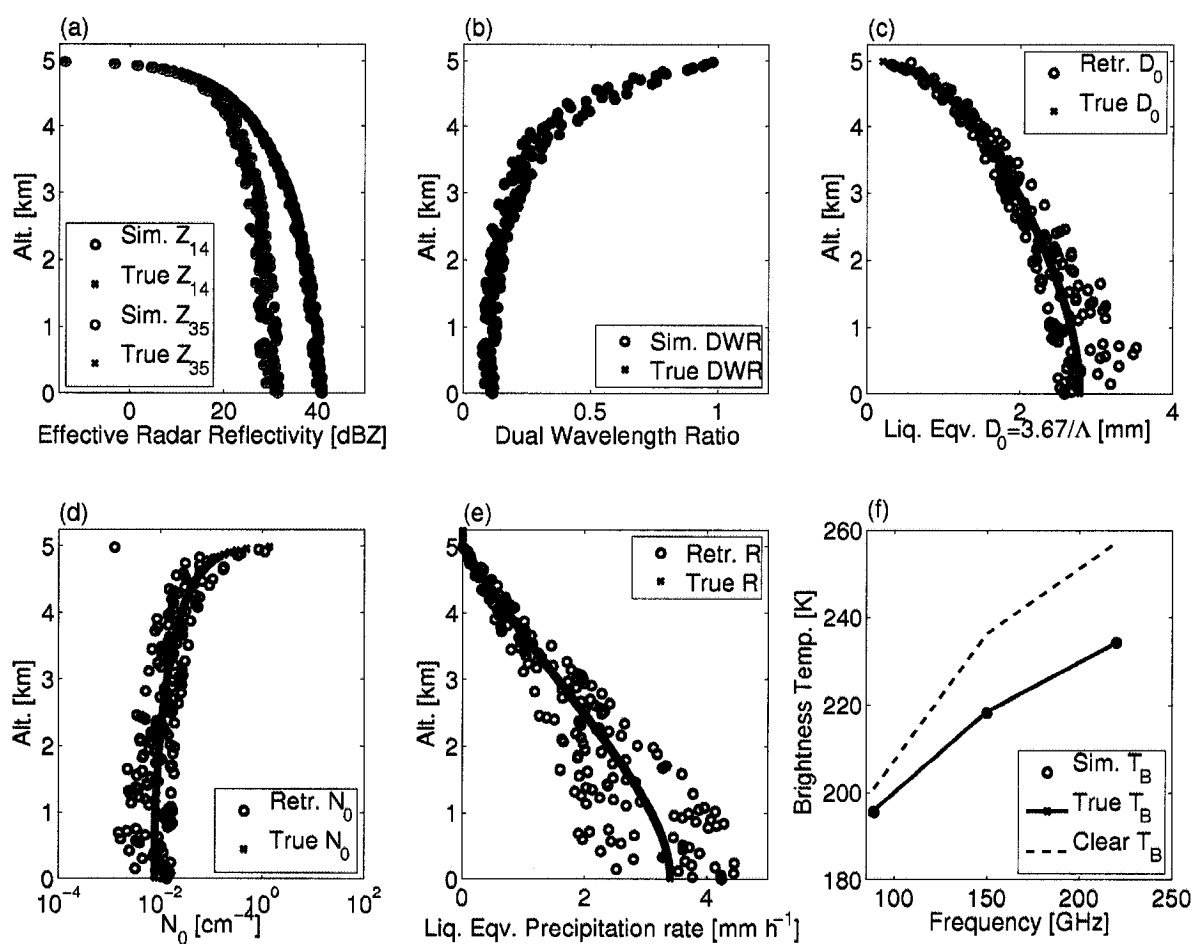
Figure 3.11. Following figure 3.10, random noise added to the true particle density profile, rather than to the precipitation rate. The retrieval, however, assumes a constant density, which results in a large spread in retrieved properties relative to the true values. Nevertheless, the T_B-constraint method correctly finds the particle density value of ρ_{snow} 0.4 g cm^{-3} to provide the lowest RMSE value.
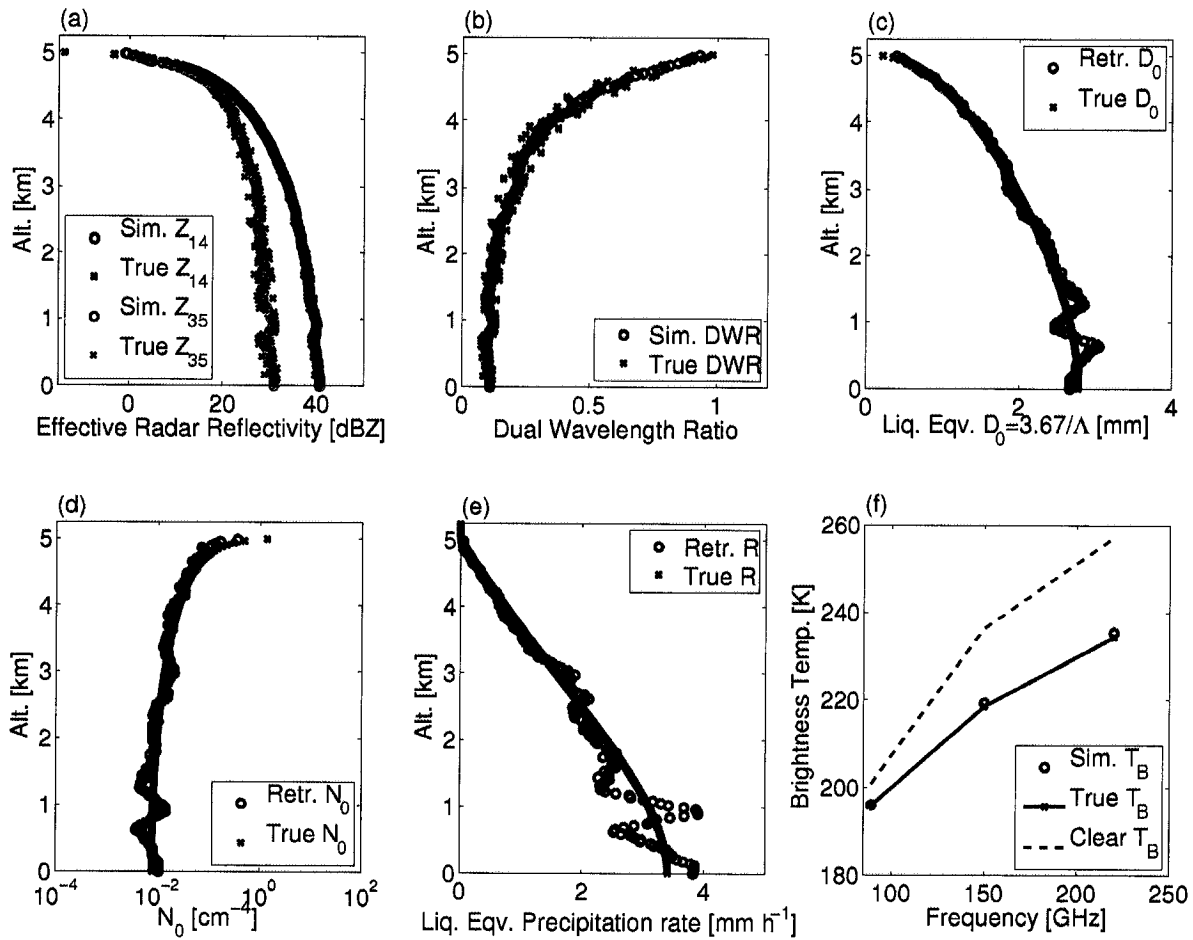
Figure 3.12. Similar to figure 3.11, although a 9-layer smoothing window is applied to the reflectivity data prior to the retrieval. Compared to fig. 3.11, smoothing results in a much cleaner retrieved profile of particle size properties. T_B values are still consistent, with a slightly high bias in the simulated vs. the true values.

cannot capture the random variations in the true densities. Nevertheless, the best fit particle density is still found to be near the true value of $\rho_{\text{snow}} = 0.4$ g cm^{-3} , this is presumably because the *average* true particle density still falls near this value.

This finding is of interest since it implies that while an actual retrieval may not accurately characterize the true particle density at each level, a characteristic linear density profile may be found such that the retrieval requirements are satisfied within a certain tolerance. In this case, the simulated and true T_{B} values are nearly identical, indicating the utility of the T_{B}-constraint method.

In figure 3.14, smoothing is again applied, as was done in the density-noise-only case (fig. 3.12). In this case, the retrieved profiles are much more confined in their variations. However, the smoothing results in simulated T_{B}s having higher values compared the true T_{B}s when the retrieval assumes the true particle density value of $\rho_{\text{snow}} = 0.4$ g cm^{-3} . This indicates that the smoothing method may introduce unintended biases into the retrieval. This issue will be explored in future research.

In this case, if the T_{B}-constraint method is applied, we find that $n_\rho = 6$ ($\rho_{\text{snow}} = 0.3$ to 0.6 g cm^{-3}) results in a closer agreement between observed and simulated T_{B}s, as illustrated in figure 3.15 It should be noted that this range of values is not far from the true particle density value of $\rho_{\text{snow}} = 0.4$ g cm^{-3} .

3.6 Summary

The retrieval method described in this chapter has two primary components. The first component uses the dual-wavelength ratio method to obtain particle size distribution properties. This method exploits the fact that two wavelengths of radar radiation will be influenced by the same physical volume (number density) of particles. Because
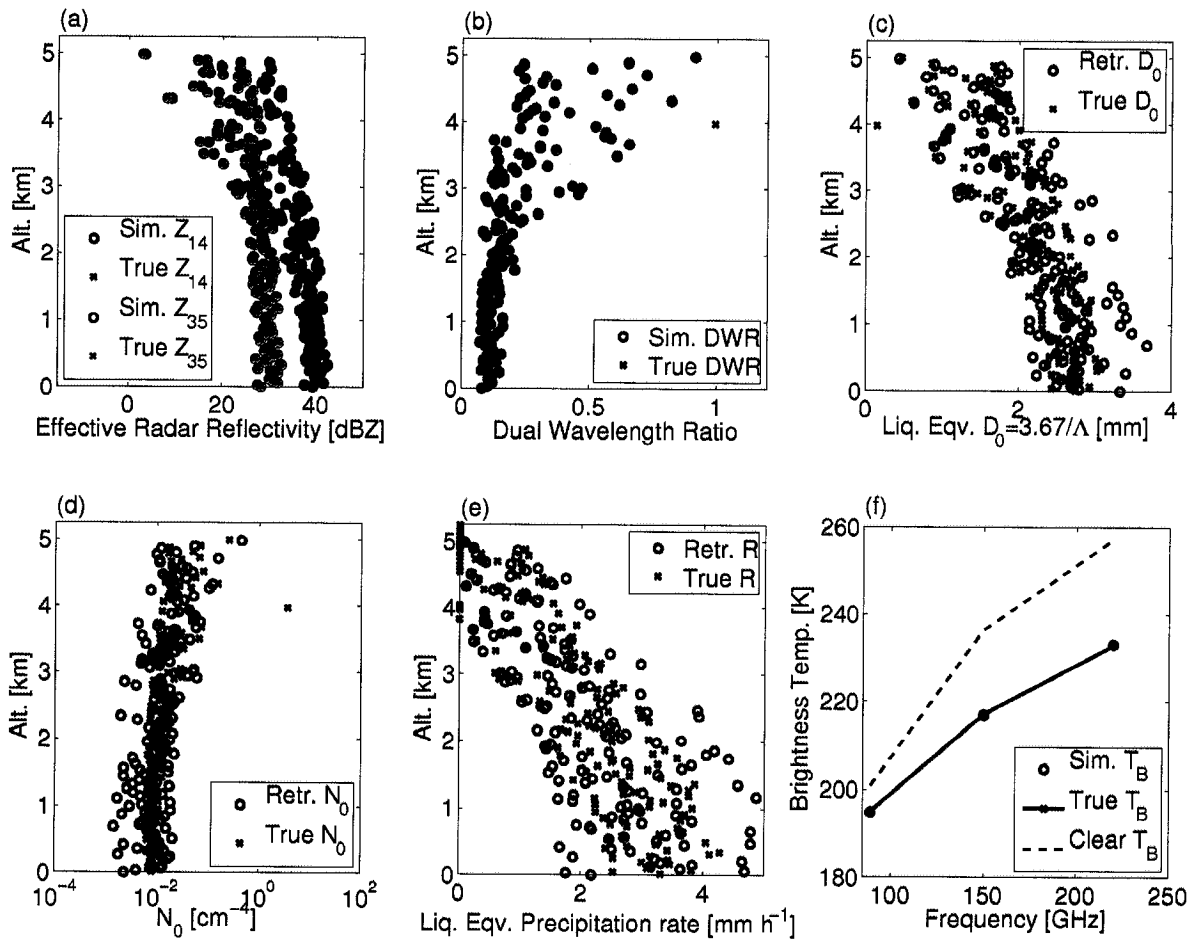
Figure 3.13. Random noise is added to both the precipitation rate and the density in the "truth" forward model to test the robustness of the retrieval. The result is a large spread in both true and retrieved parameters. The simulated and retrieved T_B values are quite similar when the retrieval density matches the true particle density, $\rho_{snow} = 0.4$ g cm^{-3}.
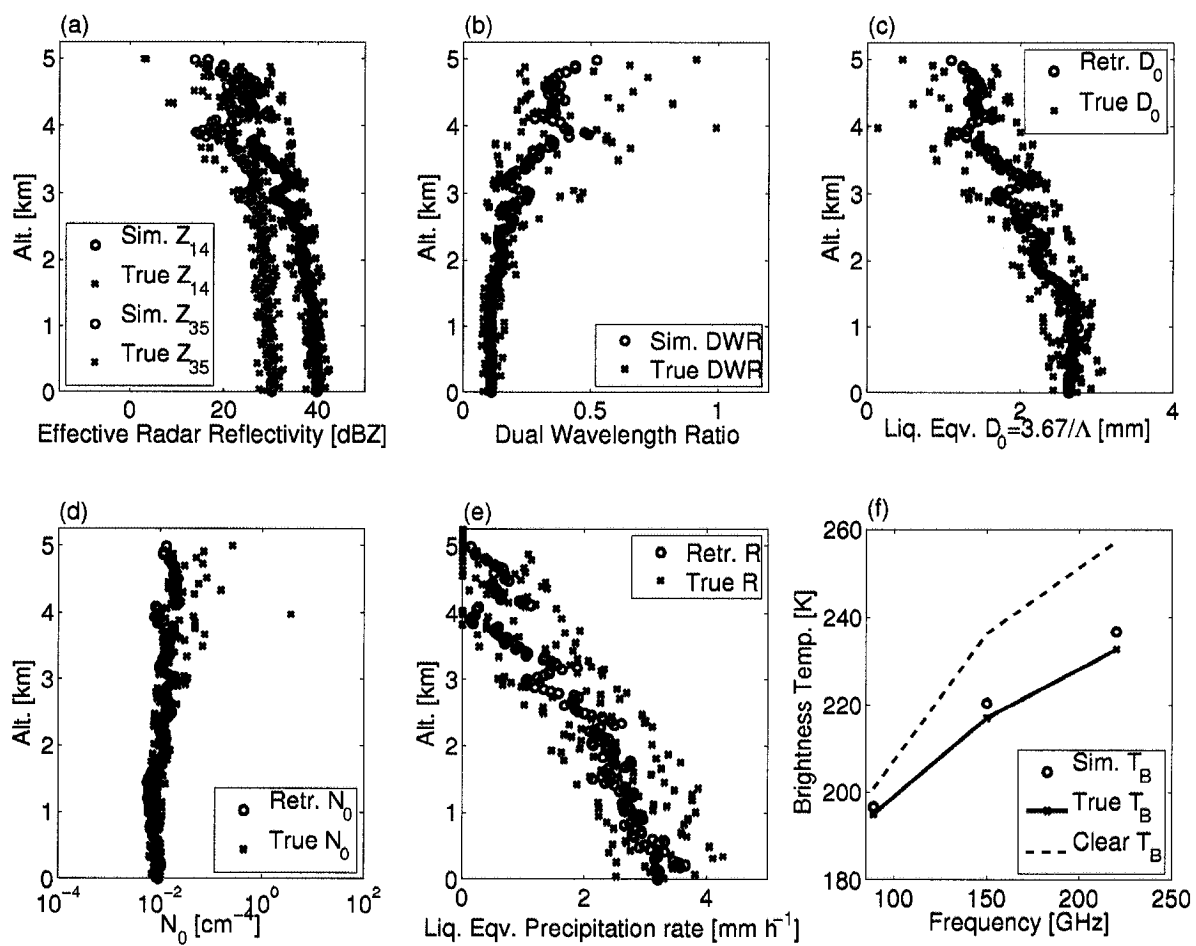
Figure 3.14. Similar to figure 3.13, except a 9-layer smoothing window has been applied to the reflectivity profiles. Here we've simply assumed that $\rho = 0.4$ g cm^{-3} in the retrieval.
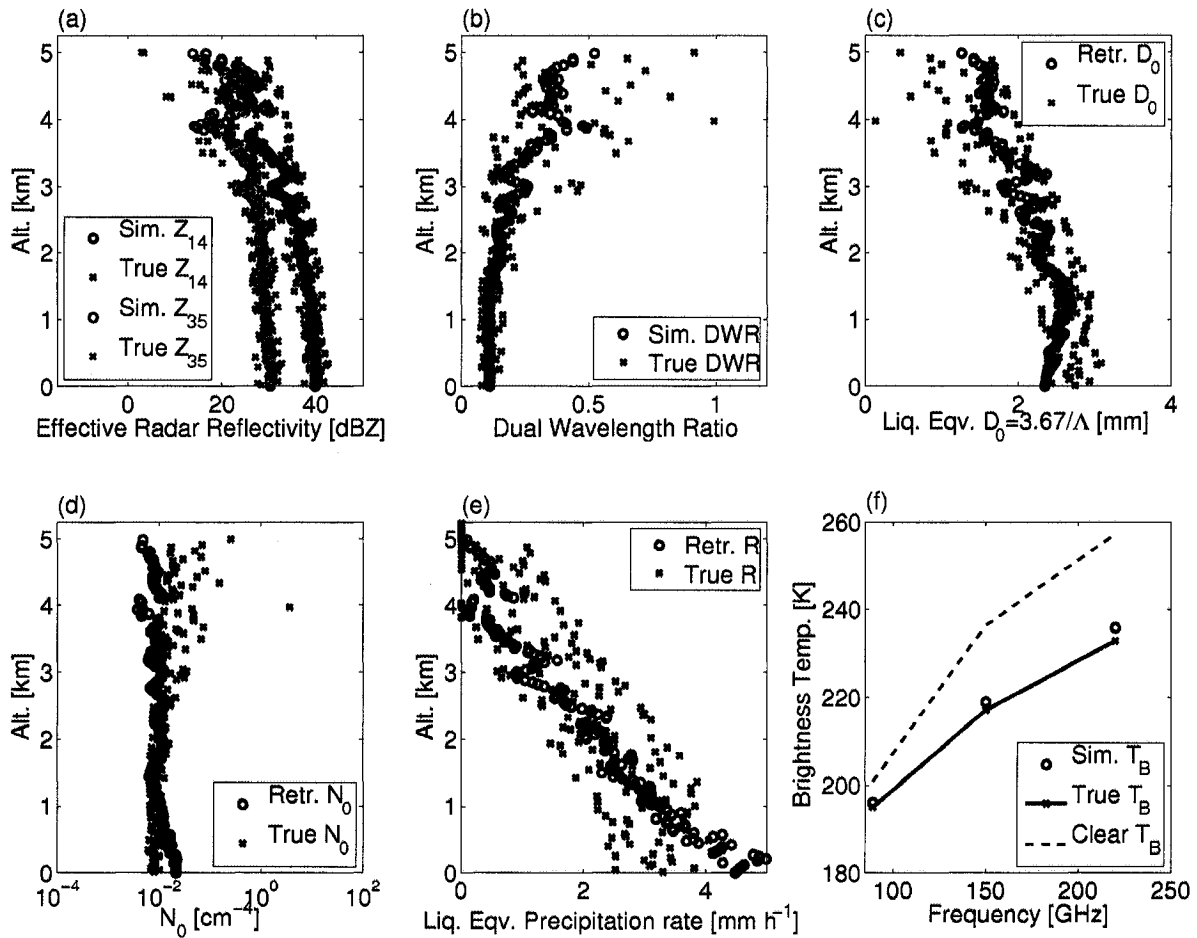
Figure 3.15. Similar to figure 3.14, although the T_B-constraint identifies $n_\rho = 6$ ($\rho_{snow} = 0.3$ to 0.6 g cm^{-3}) as the optimal density profile, rather than the true value of $\rho_{snow} = 0.4$ g cm^{-3}. This is presumably due to the result of the data smoothing technique.

of this, the ratio of the two radar reflectivities is presumed to be independent of N_0 parameter, and therefore is only sensitive to variations in particle size, shape, composition, and the path-integrated integration. Under the spherical particle shape assumption, particle size and composition (density) act as proxy parameters for the lack of shape knowledge.

Particle size can only be accurately retrieved when the particle composition (i.e., density) is correctly specified. However, the particle composition/shape/density of a true particle is generally unknown or largely uncertain. To compensate for this, 14 different linear profiles of density were tested. An additional unknown for both radar and radiometer simulations is the amount and vertical distribution of cloud liquid water. A set of 10 distribution profiles for cloud liquid water is employed, with 16 values of total cloud liquid water path ranging from 0 to 3.0 kg m^{-2} . This results in a set of approximately 2000 DWR-retrieved particle profiles for a single set of radar reflectivity observations – all of which are mathematically valid solutions to the DWR-retrieval method, but not all of which are necessarily physically realistic.

To address this, the second component of the retrieval method seeks to constrain the ill-posed DWR-retrieval by comparisons between simulated and real passive microwave brightness temperatures. This constraint method allows for the selection of the density and cloud liquid water parameters that provide best-fit retrieved profiles, which are consistent both the observed radar data and the co-located radiometer brightness temperatures.

Retrievals were performed on contrived cases, where the true values were known a priori. These cases showed that the T_B-constraint method is essential to obtaining an accurate retrieval of N_0 and D_0 when the particle density is unknown. When applied

to a larger set of observational data, the retrieval method provides a three-way (simulation, radar, radiometer) consistent set of particle-size parameters which can be further distilled into general relationships for use in a variety of meteorological applications.

The next chapter seeks to apply standard statistical methods to estimate the uncertainties in the observations, simulations, and retrieval processes described in this dissertation.

4 UNCERTAINTY ANALYSIS

In the previous chapters, the framework for the forward model and retrieval algorithm was described. The uncertainty and sensitivity to various aspects of the model were discussed qualitatively. In this chapter, the uncertainties arising from observations, simulations, and retrieval methods are quantified.

4.1 Considerations

Broadly speaking, all observation and simulation of physical phenomena are naturally subject to uncertainty due to the inherent limitations of either the measuring/observing device or the lack of knowledge of the properties of the phenomena. That is, no measurement is perfect, especially for remote sensing where the "true value" of the quantity being observed or simulated is generally unknown within a potentially large range of uncertainty.

The difference between the measured value of a given quantity and true value is the *error*. Often the true value is unknown, making the error difficult to quantify. The term *uncertainty*, as used here, is defined as the typical range of error that occurs when simulating a quantity or making an observation/measurement. That is, repeated measurements or simulations of the quantities under similar conditions has a range of probable values. This range of probable outcomes from these processes is the uncertainty, and is expressed as some base value $\pm\delta$.

The terms error and uncertainty are often used interchangeably and informally to indicate a sense of confidence in measurement or simulation Taylor (1997). Given the

vagaries of the usage of these terms, the primary concern of this chapter falls under the category of "uncertainty analysis"; that is, attempting to identify and quantify both the magnitudes and propagation of key sources of uncertainty associated with the various observations, methods, and models described in this research.

Uncertainty can be further divided into two distinct types: uncertainty arising from variations in the physical and simulated systems, sometimes termed random or stochastic uncertainty. This will be termed "Type A" uncertainty. Type A uncertainty arises from sources that are defined, such as the mathematical and physical models that comprise the forward model, or a set of events that occur within a discrete system. "Type B" uncertainty, sometimes termed epistemic, reducible, or subjective uncertainty; is that which results from a lack of knowledge of the physical systems under consideration. Type B uncertainty is more prevalent in the present study, but also less quantifiable than Type A (see for example, http://physics.nist.gov/cuu/Uncertainty/index.html).

There are cases where both Type A and Type B uncertainties of a particular method are either unknown or unable to be estimated without significant time, specialized equipment, and years of effort. In fact, a primary stated goal of the present research is to reduce total uncertainty in the simulation and retrieval of particle size distributions of snowfall. However, due to the considerable task of performing a complete and rigorous uncertainty analysis, two relatively straight-forward approaches for quantifying the uncertainty are employed to reduce the effort involved.

In this chapter, we estimate localized uncertainty through sensitivity studies using published uncertainties when available. Given the results of these individual analyses, a combined uncertainty is estimated for the observations, simulations, and retrieved

properties. Unless otherwise specified, the uncertainty estimates are presumed to be independent from one another. The propagation and computation of uncertainties follows Taylor (1997).

In the following sections, the sources of uncertainty contributing significantly to the overall simulation and retrieval uncertainties are quantified. Secondary sources of uncertainty are identified when knowledge is available.

4.2 Observation and Instrument Uncertainties

A number of different instruments provided data that was used in the present research, their uncertainties are described in this section. Satellite based observations and retrievals from AMSR-E were used to initialize and guide constraints within the retrieval and forward model portions of this research. Radiosonde profiles from stations in close proximity to the flight path, for the 2003 Wakasa Bay field experiment (WBAY03), described in chapter 5, were used to initialize the vertical profile of temperature and humidity for the radiative transfer portion of the retrieval scheme. APR-2 radar reflectivities (section 5.1.1) provided radar data, which were used in the DWR-retrieval method. Passive microwave observations of brightness temperature were obtained from the MIR instrument (section 5.1.2) and were subsequently used to constrain the DWR-retrievals.

4.2.1 Satellite-Based Observations: AMSR-E

Products based on AMSR-E observations were used to initialize the ocean surface properties and the atmospheric thermodynamic profile for T_B computations from the

WBAY03 case studies presented in chapter 5. Specifically, the sea surface temperature (SST), Cloud Liquid Water (CLW), and near-surface wind speed values were inferred from images obtained at http://remss.com/ (see acknowledgment). Preliminary estimates of the retrieval error of these quantities are shown in table 4.1 (Wentz, 2000).

4.2.2 Radiosonde Profiles

Radiosonde profiles from the Wajima and Fukui radiosonde sites in Japan were used in this research (see table 5.3). However, the types of radiosondes used were unknown to the author. Instead, we use the uncertainty results summarized in Fetzer *et al.* (2003) and reproduced in table 4.2, which state the generalized measurement uncertainties resulting from numerous radiosonde observations of the troposphere.

4.2.3 APR-2 Radar Reflectivities

According to Tanelli *et al.* (2006), the 13.4 GHz channel (K_u-band) calibration uncertainty is estimated to be ± 1 dB, and the 35.6 GHz (K_a-band) calibration uncertainty is estimated to be ± 1 dB relative to 13.4 GHz, resulting in ± 2 dB uncertainty for K_a. Beamwidth uncertainty from a quasi-specular surface is on the order of 0.2 dB or less at nadir. 35.6 GHz reflectivities were under-illuminated to provide a comparable beamwidth with 13.4 GHz (see table 5.1 for beamwidths). It should be noted that the APR-2 data used in the present studies was recalibrated after the official release of the data, these uncertainty estimates apply to the original released data – the current dataset may have reduced uncertainty values.

Table 4.1

Estimated retrieval error for AMSR-E observations of sea surface temperature, wind speed, columnar water vapor, columnar cloud water and precipitation rate (Source: Wentz (2000)).

Observable	Error
Sea-Surface Temperature	0.58 °C
Wind Speed	0.86 m s^{-1}
Columnar Water Vapor	0.57 mm
Columnar Cloud Water	0.017 mm
Precipitation Rate	2 mm h^{-1}

Table 4.2

Estimated uncertainties from radiosonde retrievals for parameters relevant to simulations and retrievals in the current model. R.H. is the relative humidity. (Source: Fetzer *et al.* (2003))

Observable	Uncertainty
Temperature	0.2 to 1.5 K, increasing with altitude
Lower Troposphere R.H.	5%, absolute
Upper Troposphere R.H.	15%, absolute

4.2.4 MIR Brightness Temperatures

According to Racette *et al.* (2006), the brightness temperature (T_B) uncertainty of the MIR instrument is less than 1 K within the range of 240 to 300 K.

Given this set of observational uncertainties, the next section explores how these uncertainties impact the overall retrieval uncertainties.

4.3 Retrieval Sensitivity to Input/Observation Uncertainties

In this section, the uncertainties identified in section 4.2 are applied as biases to a single 1-D vertical profile taken from the 29 January 2003 snowfall case from the WBAY03 experiment (section 5.3). The bias approach explores the "worst case" scenarios by assuming that the observations are biased by the maximum value of the uncertainty. The resulting uncertainty in the T_B simulations or retrieval is identified.

4.3.1 Retrieval Sensitivity to Uncertainty in 13.4 and 35.6 GHz Reflectivities

Scan number 395 (Fig. 3.7), from WBAY03 29 January 2003 at ~0315 UTC WBAY03 is shown in Fig. 5.11, was used for the baseline reflectivity profile. We assume, based on nearby radiosonde temperature profiles, that this single profile contained only snowfall (i.e., no melting or rain) and very little cloud liquid water. For consistency, the same profile is used for all of the sensitivity studies in the following section.

The worst-case scenarios for radar reflectivity uncertainties are simulated by adding or subtracting the maximum uncertainty from observed 13.4 and 35.6 GHz reflectivities, i.e., a constant bias. There are 9 permutations with respect to how the bias can be added or subtracted, including the unbiased option. For each of the 9 permutations, there

are 14 choices of particle density profiles used in the DWR-retrieval (see section 3.3.3).
Because we're dealing with real observations, the true particle density is unknown.
Therefore, the T_B-constraint method is applied to determine the best-fit T_B values
(relative to the co-located MIR observation) and associated density parameter n_ρ .

Table 4.3 shows the result of this analysis. The notation, $[+-\times, +-\times]$, represents
whether a reflectivity bias was added $(+)$, subtracted $(-)$, or not applied $(\times)$ to the
base $[Z_{14}, Z_{35}]$ reflectivities respectively (i.e., $[+, -] = [Z_{14} + 1.0$ dBZ, $Z_{35} - 2.0$ dBZ]),
where the uncertainties were described in section 4.2.3.

For this specific profile, the lowest T_B RMSE is 1.95 K, which is the base case
(no bias added). These results indicate that if the worst-case biases were present in
the observed reflectivities, this would result in inconsistencies when simulated T_Bs are
compared to observed T_Bs. That is, there would no longer be a 3-way consistency
between simulation, radar observations, and radiometer observations. It is possible,
however, that certain biased cases could be contrived to have equally low RMSE value
and still be biased. Without additional information, the current retrieval method would
not be able to determine which is is the more appropriate solution.

Figures 4.1 and 4.2 shows the radar-retrieved vertical profiles of the particle size
distribution properties, N_0 and $D_0 = 3.67/\Lambda$, subject to the uncertainties in the APR-
2 reflectivities described above. In both figures, the error is computed relative to the
"base" value. When the uncertainties are combined (Fig. 4.2), the resulting errors are
are typically larger than the errors due to the uncertainties applied to each channel
individually.

Table 4.3

An example of T_B sensitivity to 1-D profiles retrieved from biased radar reflectivities. $[+ - \times, + - \times]$ represents whether a reflectivity bias was added (+), subtracted (−), or not applied (×) to the $[Z_{14}, Z_{35}]$ reflectivities respectively (i.e., $[+, -] = [Z_{14} + 1.0$ dBZ, $Z_{35} - 2.0$ dBZ]). For each bias option, $T_{B,MIR} - T_B$ are shown for the T_B-constrained retrievals (i.e., the "best-fit" profiles). The density parameter, n_ρ (table 3.3), resulting in the best-fit is also provided.

type units	$T_{B,89}$ [K]	$T_{B,150}$ [K]	$T_{B,220}$ [K]	RMSE [K]	optimal n_ρ
MIR	193.9	196.4	206.2	0.00	— —
$[\times, \times]$	-1.9	2.3	-1.6	1.95	13
$[+, \times]$	-0.3	9.2	11.6	8.55	9
$[-, \times]$	2.1	3.6	-14.0	8.44	1
$[\times, +]$	2.5	-5.0	-21.1	12.61	1
$[\times, -]$	3.0	19.5	27.7	19.63	9
$[+, +]$	10.5	10.4	-4.3	8.88	0
$[+, -]$	4.0	22.2	30.3	21.81	7
$[-, +]$	15.3	3.4	-16.2	13.00	1
$[-, -]$	2.4	16.9	22.7	16.40	9
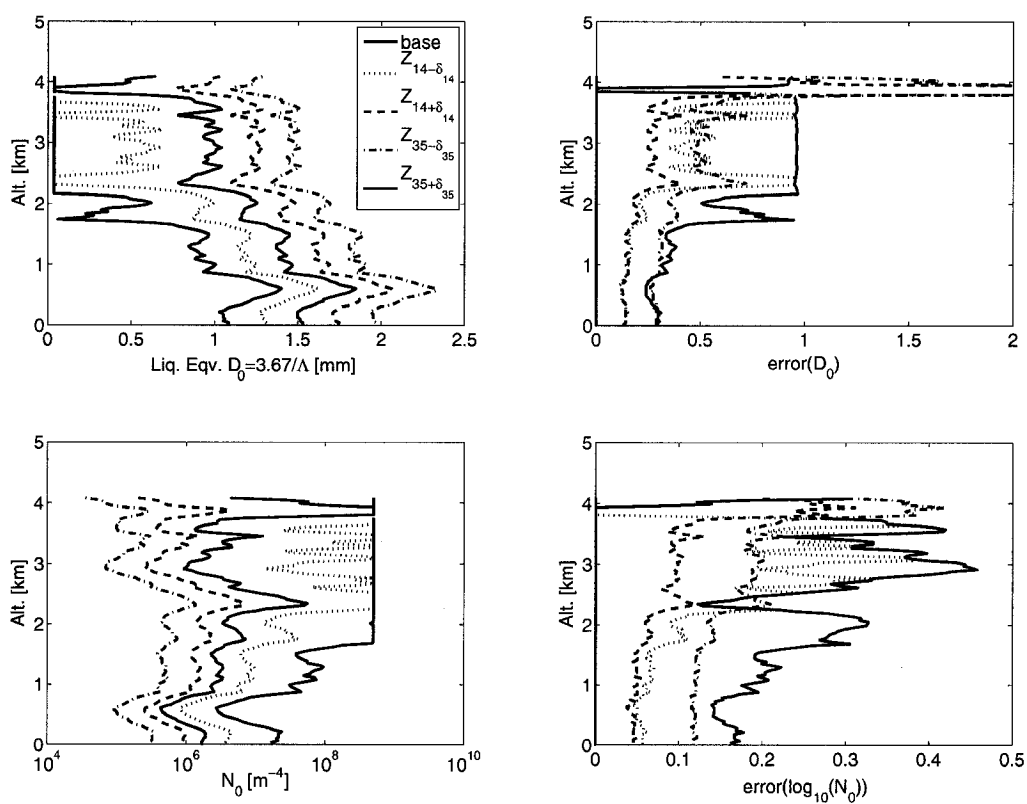
Figure 4.1. N_0 and D_0 retrieval uncertainties associated with APR-2 reflectivity uncertainties for *single* channel variations.
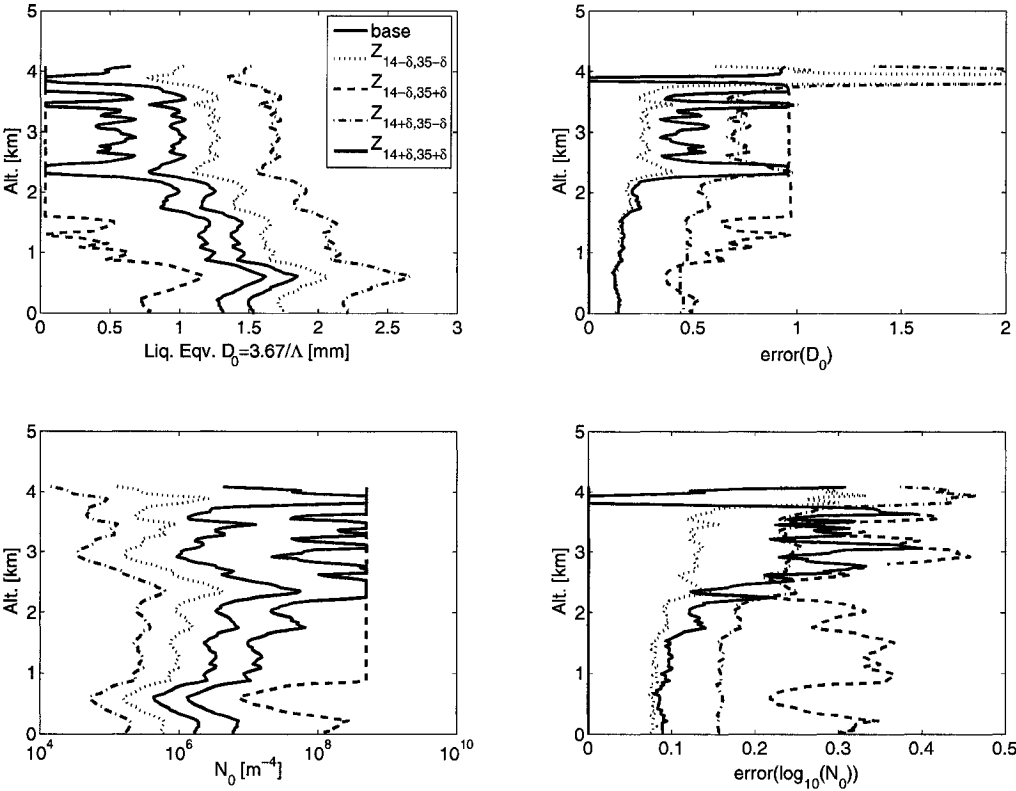
Figure 4.2. N_0 and D_0 retrieval uncertainties associated with APR-2 reflectivity uncertainties for *dual* channel variations (see table 4.3).

Figure 4.2 shows the worst possible case scenario of error if the maximum APR-2 uncertainties are treated as biases. The result is an approximate uncertainty of ± 0.75 mm for retrieved D_0, and $-15\%, +30\%$ in retrieved N_0 values.

These cases highlight the worst possible case given the stated uncertainties of the APR-2 radar. In reality, instrument noise contributing to the uncertainty in observed reflectivities is likely to be more randomly distributed about a mean value – resulting in smaller RMSE values than stated here (Tanelli *et al.*, 2004). The contrived examples presented in section 3.5 further indicate that the T_B-constraint is relatively insensitive to random errors.

Similarly, biases are unlikely to be constant, but not randomly distributed. Dr. Simone Tanelli at NASA-JPL has indicated, via personal communication, that the APR-2 biases are largest at low reflectivities, i.e., typically near the cloud tops and cloud edges, and smallest at the highest reflectivities. However, there is no indication that the biases on the APR-2 observations are nearly as large as simulated here.

4.3.2 Retrieval Sensitivity to Uncertainty in Observed MIR Brightness Temperatures

As described in section 4.2.4, the observed MIR brightness temperature uncertainties are on the order of ± 1 K. Using the same data and analysis method as section (4.3.1), the single-profile retrieval is performed for the worst-case possibilities – namely, when the MIR T_Bs are individually biased by the minimum and maximum values of the observation uncertainty. Table 4.4 shows the results of the analysis.

In this case, biases added to the MIR observed brightness temperatures result in several RMSE values that are smaller than the base value, $[\times, \times, \times]$. This indicates that uncertainties in the observed brightness temperatures have an influence on the

Table 4.4

An example of T_B sensitivity to 1-D profiles retrieved from biased MIR T_Bs. $[+-\times, +-\times, +-\times]$ represents whether a T_B bias was added $(+)$, subtracted $(-)$, or not applied $(\times)$ to $[T_{B,89}, T_{B,150}, T_{B,220}]$ respectively (i.e., $[+, -, \times] = [T_{B,89} + 1$ K, $T_{B,150} - 1$ K, $T_{B,220} + 0$ K$]$). For each bias option, the T_B-difference relative to the base MIR value are shown for the retrieval (i.e., the "best-fit" profiles). The density parameter, n_ρ , resulting from the best-fit is also provided.

type units	$T_{B,89}$ [K]	$T_{B,150}$ [K]	$T_{B,220}$ [K]	RMSE [K]	optimal n_ρ
MIR-base	193.9	196.4	206.2	0.00	$--$
$[-,+,-]$	0.85	-1.32	0.62	0.98	13
$[-,+,\times]$	0.85	-1.32	1.62	1.31	13
$[\times,+,-]$	1.75	-1.32	0.82	1.35	9
$[-,\times,-]$	0.85	-2.32	0.62	1.47	13
$[\times,+,\times]$	1.85	-1.32	1.62	1.61	13
$[-,\times,\times]$	0.85	-2.32	1.62	1.71	13
$[\times,\times,-]$	1.75	-2.32	0.82	1.75	9
$[-,+,+]$	0.85	-1.32	2.62	1.77	13
$[+,+,-]$	2.75	-1.32	0.82	1.83	9
$[\times,\times,\times]$	1.85	-2.32	1.62	1.95	13
$[\times,+,+]$	1.85	-1.32	2.62	2.00	13
$[-,-,-]$	0.85	-3.32	0.62	2.01	13
$[+,+,\times]$	2.85	-1.32	1.62	2.04	13
$[-,\times,+]$	0.85	-2.32	2.62	2.08	13
$[+,\times,-]$	2.75	-2.32	0.82	2.13	9
$[-,-,\times]$	0.85	-3.32	1.62	2.19	13
$[\times,-,-]$	1.75	-3.32	0.82	2.22	9
$[\times,\times,+]$	1.85	-2.32	2.62	2.29	13
$[+,\times,\times]$	2.85	-2.32	1.62	2.32	13
$[+,+,+]$	2.85	-1.32	2.62	2.36	13
$[\times,-,\times]$	1.85	-3.32	1.62	2.39	13
$[-,-,+]$	0.85	-3.32	2.62	2.49	13
$[+,-,-]$	2.75	-3.32	0.82	2.54	9
$[+,\times,+]$	2.85	-2.32	2.62	2.61	13
$[\times,-,+]$	1.85	-3.32	2.62	2.67	13
$[+,-,\times]$	2.85	-3.32	1.62	2.70	13
$[+,-,+]$	2.85	-3.32	2.62	2.95	13

retrieval because RMSE is the common selector for "best-fit" T_B values. Additionally, some of the lower values find $n_\rho = 9$ ($\rho = 0.25$ to 0.40 g cm^{-3}) to be the optimal density parameter, rather than the base value of $n_\rho = 13$ ($\rho = 0.2$ to 0.5 g cm^{-3}). However, the density profiles are quite similar, both represent "moderate density" snow particles. There appears to be no significant impact on the overall retrieval scheme, since the primary purpose of the T_B-constraint portion of the retrieval is to identify the best-fit n_ρ values.

4.3.3 Sensitivity to Environmental Parameters

Other than the observed radar reflectivities, the retrieval method and forward model are also sensitive to the environmental parameters, such as ocean-skin temperature (T_{skin}), temperature profile (T_{surf}, T_{trop}), clear-sky relative humidity (RH_{clear}), near surface wind speed (W), and cloud liquid water path (CLWP). Given the uncertainties in section 4.2, a sensitivity analysis was performed for a single precipitation profile – the same one used in section 4.3.1. The goal here is to determine the influence of the uncertainty of environmental inputs on the radar-retrieved microphysical properties and simulated T_Bs.

Table 4.6 shows the T_B variations due to changes in the above listed environmental parameters. "Base" defines the standard baseline value selected from the T_B constrained retrieval applied to the nominal WBAY03 observations/. "MIR" represents the observed T_Bs at the current scan position. Each variable is modified from a base value by adding (+) or subtracting (−) the uncertainty (listed in table 4.5), while other variables are held at their base values. Conservative estimates of the uncertainty are made by adding and subtracting the stated errors from table 4.1. "Total(+)" is

the T_B value when all of the positively contributing uncertainties are applied, rather than each one individually. Similarly for "Total$(-)$", with the combined negatively contributing uncertainties applied.

In table 4.6, the quantities having the largest T_B sensitivity are cloud liquid water path (CLWP), wind speed (W), Total$(+)$, and Total$(-)$. Figure 4.3 shows the radar-retrieved profiles and associated error (relative to the base value) that arise from the Total$(+)$ and Total$(-)$ contributions. "CLW" cases refer to when cloud liquid water $(0.3$ kg m^{-2} $)$ was artificially placed in the retrieval, "no CLW" is the standard case without cloud liquid water present.

From Fig. 4.3, the error in retrieved D_0 and N_0 resulting from Total$(+)$ and Total$(-)$ in the environmental parameters is relatively small compared to the error due to uncertainties in the radar observables (Fig. 4.2).

4.4 Retrieval Sensitivity to Hydrometeor Model Relationships

In the spherical-particle approximation, Mie theory is used to compute the optical properties of individual spherical particles. Mie theory requires that the sphere be composed of a homogeneous isotropic dielectric material (Bohren and Huffman, 1983). In order to obtain a homogeneous mixture (i.e., a single dielectric constant value for the entire sphere), two dielectric mixing formulas were employed: the Maxwell Garnett and Bruggeman formulas, which are also known as "matrix-inclusion" and "effective medium approximation" respectively. The details of these formulas are discussed in section 2.8.3.

Figure 4.4 shows the dielectric constant at 89 GHz for varying volume fraction of ice and air, where $F_{ice} + F_{air} = 1$. Square brackets in the legend indicate the inclusion com-

Table 4.5

Uncertainties in the user-defined model environmental parameters. Base values and associated uncertainties are taken from section 4.2.

Variable	Uncertainty	Description
T_{skin}	10 ± 0.58 °C	Sea surface temperature
T_{surf}	0 ± 0.20 °C	Surface air temperature
RH	0.2 ± 0.01	Clear Sky relative humidity
W	17 ± 0.86 m s^{-1}	near-surface wind speed
CLWP	0.3 ± 0.017 kg m^{-2}	Cloud liquid water path
Total(+)	–	combined positive uncertainties
Total(−)	–	combined negative uncertainties

Table 4.6

Simulated passive microwave response (Kelvin) to DWR-retrieved profiles subject to uncertainties in the model environmental parameters (table 4.5). The T_{B} differences due to the various uncertainties are expressed are relative to the base values, as appropriate.

ν	base	$T_{\text{skin}}(+/-)$	$T_{\text{surf}}(+/-)$	$T_{\text{trop}}(+/-)$
89 GHz	191.1 K	-0.2/0.7 K	0.0/ 0.0 K	0.0/ -0.1 K
150 GHz	200.4 K	-0.1/0.1 K	0.0/ -0.1 K	0.1/ -0.1 K
220 GHz	207.9 K	0.1/0.0 K	0.1/ 0.0 K	0.2/ -0.1 K

ν	base	RH (+/−)	W(+/−) (no CLW)	
89 GHz	191.1 K	0.1/ -0.1 K	1.2/ -1.2 K	
150 GHz	200.4 K	0.2/ -0.2 K	1.4/ -1.4 K	
220 GHz	207.9 K	0.2/ -0.2 K	1.5/ -1.4 K	

ν	base(w/CLW)	CLWP(+/−)	Total(+) (no CLW/CLW)	Total(−) (no CLW/CLW)
89 GHz	220.0 K	0.9/ -0.9 K	1.1/ 1.9 K	-1.2/ -1.8 K
150 GHz	225.5 K	0.5/ 0.3 K	1.6/ 1.3 K	-1.7/ -1.4 K
220 GHz	228.5 K	0.6/ -0.5 K	2.0/ 1.3 K	-1.9/ -1.3 K
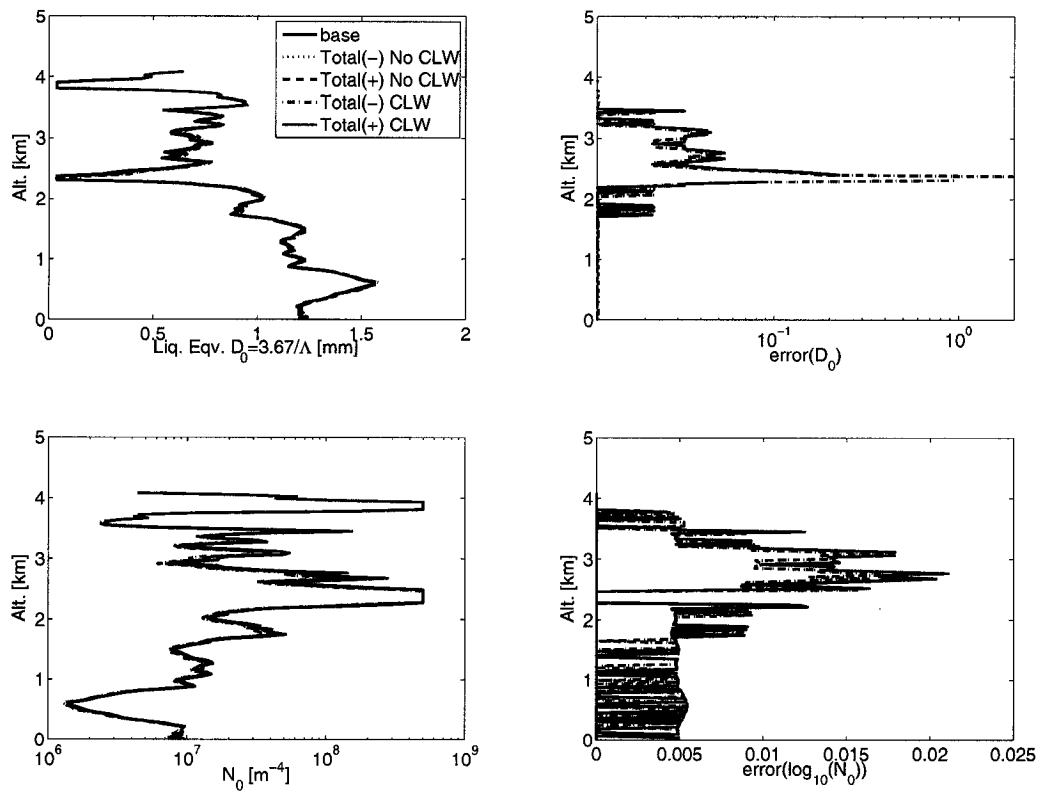
Figure 4.3. N_0 and D_0 retrieval uncertainties associated with sum-total positive and negative uncertainties in environmental parameters.

ponent for the Maxwell Garnett dielectric mixing formulas. Angle brackets represent the averaging of the constituents. Other frequencies exhibit similar characteristics, but they are not shown here. Loosely speaking, the imaginary component of the dielectric constant is proportional to absorption and tends to increase with increasing frequency (not shown). The real component is proportional to scattering. For ice, the real component approximately 200 times larger than the imaginary component, and remains nearly constant with increasing frequency (not shown).

For all of the frequencies of interest in this research, i.e., 13.4, 35.6, 89, 150, and 220 GHz, ice is predominantly a scattering medium. Specifically, this means that a large fraction of microwave radiation at these frequencies incident upon an ice particle will be scattered rather than absorbed. In comparison, liquid water has a nearly equal real and imaginary component of the dielectric constant. This makes water much more effective at extinguishing, through both scattering *and* absorption, incident radiation than an equivalent mass of dry ice.

Figure 4.5 and table 4.7 show the influence of the choice of dielectric mixing formula on the DWR-retrieved particle size distribution properties, and on the forward model simulated T_Bs. In Fig. 4.5, no variations are observed in the retrieved D_0 values (panel b), while the variations in N_0 (panel c) are primarily responsible for the variations in the liquid equivalent precipitation rate (panel d). For all of the retrievals in this research, the default choice of dielectric mixing is the Bruggeman technique. As described previously, the Bruggeman technique is valid for all ranges of ice volume fraction F_{ice}, whereas the Maxwell Garnett methods are only strictly valid for inclusion volume fractions of less than 0.3. This was also described in section 2.8.3.
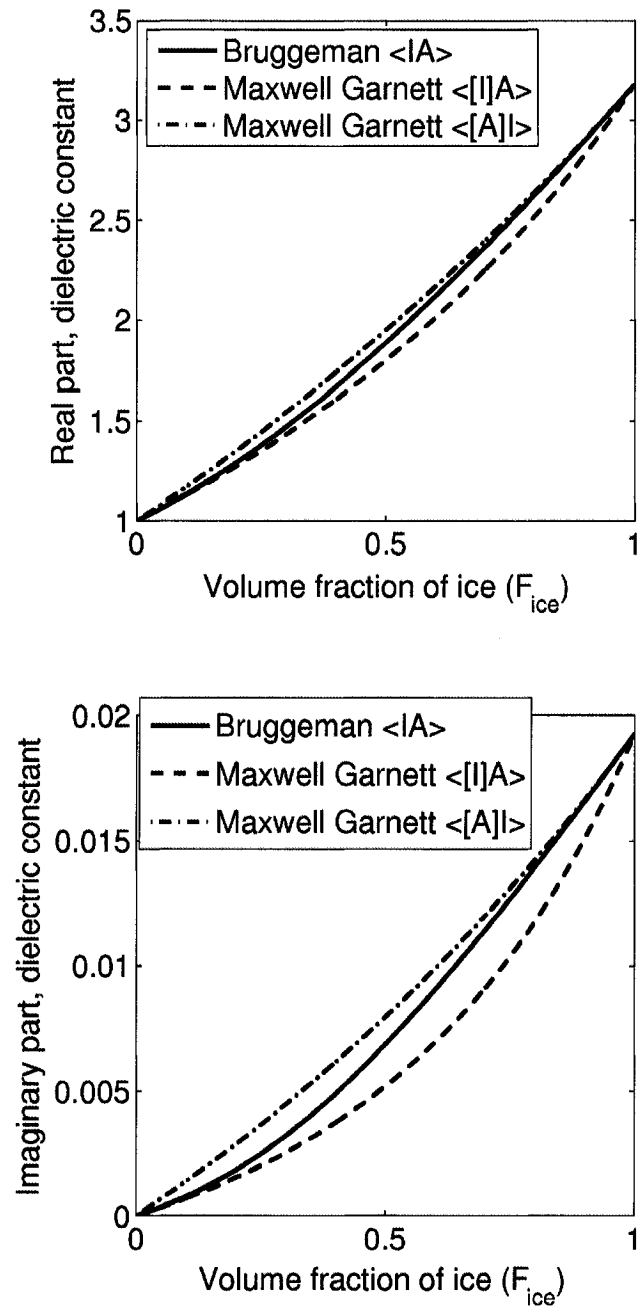
Figure 4.4. Real and Imaginary components of the dielectric constant for three choices of dielectric averaging methods versus ice volume fractions at 89 GHz, where $F_{ice}+F_{air}= 1$. Square brackets indicate the inclusion component within the external matrix in the Maxwell Garnett cases.
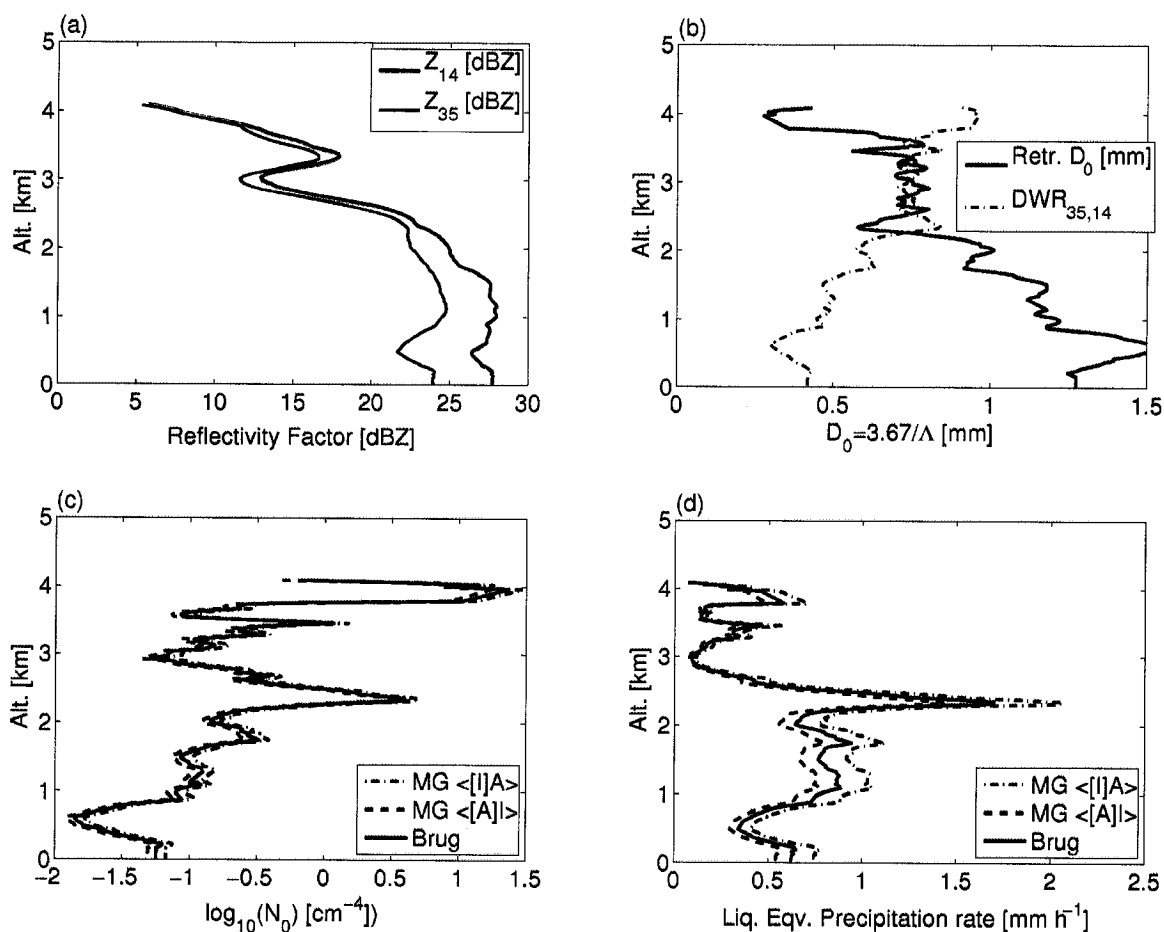
Figure 4.5. Retrieved D_0, N_0, and precipitation rate for three choices of dielectric mixing formula (ρ_{snow}=0.4 g cm^{-3}). Panel (a) shows the observed, smoothed, radar reflectivity factor; (b) shows the dual-wavelength ratio (green line) and the retrieved mass-weighted median diameter, D_0; (c) shows N_0 for the three choices of dielectric mixing, and (d) shows the derived liquid equivalent precipitation rate and the influence of the dielectric mixing formula choice.

Table 4.7 shows that the various choices of dielectric averaging method can result in slightly different brightness temperature RMSE values. The three lowest RMSE values for each mixing method are shown, along with the associated optimal n_ρ value, i.e., the density parameter. For the Maxwell Garnett approach with ice as the inclusion, MG $\langle[\text{I}]\text{A}\rangle$, the RMSE values are relatively larger. Also, compared to the Bruggeman method, the optimal n_ρ value switched from 13 ($\rho_{\text{snow}}= 0.20$ to 0.50 g cm^{-3}) to 9 ($\rho_{\text{snow}}= 0.25$ to 0.40 g cm^{-3}). This does not represent a significant change in terms of an average density, but it is representative of the sensitivity of the retrieved parameters to slight changes in the dielectric properties.

4.5 Summary

This chapter examined the sensitivity of the forward model and retrieval algorithm to uncertainties in observational data, and to uncertainties in the simulated relationships. In particular, the overall uncertainty is dominated by the stated uncertainties in the observed radar reflectivities of $Z_{14}\pm1$ dBZ and $Z_{35}\pm2$ dBZ. Other sources of uncertainty/error are approximately a factor of 5 to 10 smaller. Therefore, a conservative estimate of the total uncertainty is covered by the APR-2 observational uncertainty alone. Simulated T_Bs are certain to within $\pm10\%$, or approximately ±20 K at 220 GHz. The resultant uncertainties in the characteristic particle size, D_0, are on the order of ±0.75 mm, and $-15\%, +30\%$ in N_0. However, as previously noted, if such large biases were actually present, the 3-way consistency between radar, radiometer, and forward-model simulation would break down. Therefore, a judicious, although subjective, choice of allowable T_B RMSE values is required to obtain a reasonable retrieval.

148

Table 4.7

Using the same observed profile as Fig. 4.5, three best fit T_Bs (lowest RMSE) for three choices of dielectric mixing method are shown here. The the largest T_B variations relative to the base observed MIR values occur at 220 GHZ. In the first column, "BR" stands for the Bruggeman dielectric mixing method, and "MG" stands for Maxwell Garnett method. Square brackets represent the inclusion component for the MG cases.

type	$T_{B,89}$	$T_{B,150}$	$T_{B,220}$	RMSE	optimal
units	K	K	K	K	n_ρ
MIR	193.9	196.4	206.2	0.00	——
BR ⟨IA⟩	-1.6	2.4	-1.7	1.96	13
BR ⟨IA⟩	-1.7	2.4	-1.6	1.96	9
BR ⟨IA⟩	-1.3	3.2	-2.5	2.48	2
MG ⟨[I]A⟩	-1.7	2.3	-2.4	2.18	9
MG ⟨[I]A⟩	-1.6	2.3	-2.6	2.23	13
MG ⟨[I]A⟩	-1.4	3.1	-3.6	2.88	2
MG ⟨[A]I⟩	-1.6	2.4	-1.7	1.96	13
MG ⟨[A]I⟩	-1.7	2.4	-1.6	1.96	9
MG ⟨[A]I⟩	-1.3	3.3	-2.3	2.46	2

In the next chapter, a snowfall retrieval case study from the 2003 Wakasa Bay field experiment is examined. A maximum T_B RMSE value of 10 K is subjectively chosen for the T_B constraint in the retrieval, rather than $\sim$20 K RMSE that would be imposed by the worst-case combined uncertainties. The 10 K constraint on the maximum RMSE enforces a more stringent consistency between simulations and radar/radiometer observations, but also presumes that any biases or noise present in the radar/radiometer observations and simulations are not on the order of these worst case scenarios presented here. For most of the observations in the case study, the best-fit RMSE values falls well below the 10 K threshold value.

5 2003 WAKASA BAY PRECIPITATION EXPERIMENT

The Wakasa Bay Precipitation Field Experiment conducted in 2003 (WBAY03) over Japan and the Sea of Japan was designed as a validation experiment for the Advanced Microwave Scanning Radiometer, AMSR and AMSR-E, radiometers. The primary stated goal is to validate AMSR and AMSR-E light rainfall and snowfall retrieval capabilities using an ensemble of ground and aircraft based active and passive observations. The experiment is part of the AMSR Rainfall Validation Implementation Strategy 2001-2005 (Wilheit *et al.*, 2002).

The data collected during the experiment included downward-looking aircraft-based radar measurements at 13.4, 35.6, and 95 GHz, and passive microwave radiometer measurements ranging from 10.65 to 340 GHz. Several nearby radiosonde stations operated at regular intervals, and a variety of Japanese ground-based and aircraft instruments were employed. Currently the Japanese data is not publicly available. The dual-wavelength ratio (DWR) retrieval algorithm described in chapter 3 was used to retrieve the particle size distribution (PSD) properties of snow-clouds over the Sea of Japan. However, the DWR method is ill-posed due primarily to two key unknowns: particle density / composition and cloud liquid water content / distribution. Brightness temperature (T_B) observations from the MIR instrument were compared to simulated T_Bs to further constrain the DWR retrievals.

5.1 Instrument Description

Figure 5.1 summarizes the dates, types of observations, and general location of the P-3 aircraft-based observations made during WBAY03. Figure 5.2 illustrates the positions of the instruments onboard the P-3 aircraft. Image Source:
http://www.nasa.gov/centers/goddard/news/topstory/2003/0122japansnow.html.

Several instruments were deployed for WBAY03, the following list introduces the capabilities of the various instruments onboard the P-3 aircraft:

- **Airborne Multi-channel microwave Radiometer (AMMR)**, passive T_B observations at 21 and 37 GHz; upward-looking observations of clouds and precipitation

- **Millimeter-wave Imaging Radiometer (MIR)**; passive T_B observations at 89, 150, 183±1,3,7, 220, and 340 GHz; conical or cross-track scanning radiometer

- **Advanced Precipitation Radar 2 (APR-2)**; active radar at 13.4 and 35.6 GHz; HH / HV polarization, 30 m vertical resolution

- **Polarimetric Scanning Radiometer (PSR)**; passive T_B observations at 10.7, 18.7, 21.5, 37, and 89 GHz; conically scanning; V and H polarization

- **Airborne Cloud Radar (ACR)**; active radar at 94 GHz; 120 m vertical resolution.

Wakasa Bay Flight Summary

Colorado State University — *Knowledge to Go Places*

Flight	Date	ACR	PR-2	PSR	AMMR	MIR	Gulfstream	Low flight	Location	Satellite Overpass	Comments
1	14-Jan-03	✓	✓		✓	✓		✓	Sea of Japan	A	Rain then snow, BB visible
2	15-Jan-03	✓	✓	not 89	✓	✓			W Japan, GTS	—	Snow & some rain over land; brief water crossing
3	19-Jan-03	✓	✓	✓	✓	✓		✓	W Pacific	A	Warm rain cells, frontal cross, BB visible, occ. ACR total atten., light icing high
4	21-Jan-03	✓	✓	✓	✓	✓		✓	W Pacific	A*	Snow/rain, occasional BB
5	23-Jan-03	✓	✓	✓	✓	✓			W Pacific	T(x3)	Strong & widespread rain, supercooled water, BB visible, squall line
6	26-Jan-03	✓	✓	✓	✓	✓		✓	W Japan, GTS	A	Weak cloud, mostly clear
7	27-Jan-03	✓	✓	✓	✓	✓	✓	✓	Sea of Japan	—	Stratiform rain or cloud only; strong rain during return over land
8	28-Jan-03	✓	✓	✓	✓	✓	✓	✓	Sea of J, GTS	A,T	Oceanic snow cells, also rain, mixed precip?, 10° bank turn, snow over land
9	29-Jan-03	✓	✓	✓	✓	✓	✓	✓	Sea of J, GTS	—	Heavy snow over ocean (up to 5 km), also snow over land
10	30-Jan-03	✓	✓	✓	✓	✓	✓	✓	Sea of J, GTS	A,T	Strong snow cells, clear & cloud-only areas, 15°/20° turns, snow over land
11	01-Feb-03	✓	✓	✓	✓	✓		✓	W Japan, GTS	A,T	Thin Sc, fresh snow on surface
12	03-Feb-03	✓	✓	✓	✓	✓		✓	W Pacific	A,T	Scatt rain cells, fly through melting layer, icing above, 10° bank turn

Figure 5.1. A summary chart describing the P-3 flight dates and data summary for the Wakasa Bay Experiment.
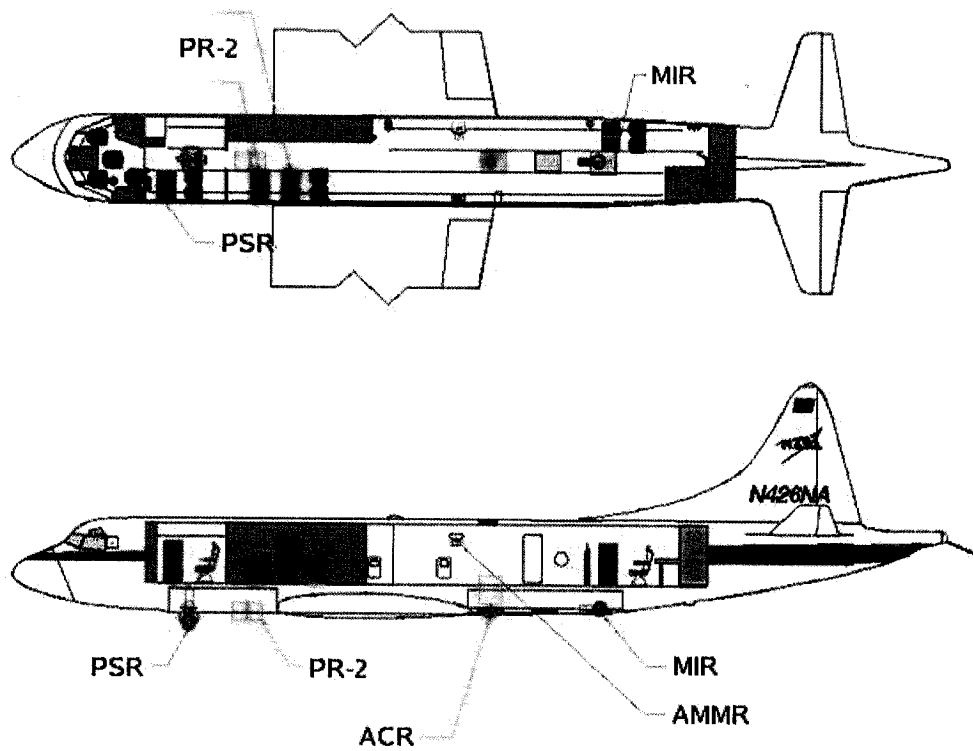
Figure 5.2. Schematic showing the relative locations of the primary observation instruments onboard the P-3 aircraft.

5.1.1 Airborne Second-Generation Precipitation Radar (APR-2)

The Airborne Second Generation Precipitation Radar (APR-2) made observations during precipitating events over the sea of Japan on board the NASA P-3 aircraft. Observations were made at 13.405 (K_u-band) and 35.605 GHz (K_a-band) in a downward-looking, cross-track scanning geometry. In the present research, only the downward-looking nadir beams are used. Table 5.1 summarizes some of the relevant instrument characteristics of the APR-2 (Im *et al.*, 2000; Sadowy *et al.*, 2003).

The Level 1 data product consists of the calibrated reflectivity at both 13.405 and 35.605 GHz, as well as the Doppler-velocity and linear depolarization ratio (LDR) at 13.405 GHz (Im, 2003). Due to a later (unreleased) data re-calibration, the doppler-velocity data was deemed to be unreliable due to low sensitivity and velocity magnitude issues. The APR-2 reflectivity data is currently calibrated on a case-by-case basis through Simone Tanelli at NASA Jet Propulsion laboratory. There appear to be no plans (at the time of writing) to release a complete recalibrated dataset.

Figure 5.3 conceptually illustrates the role of the APR-2 in estimating precipitation rate. The essential elements of the APR-2 are the dual frequency radar beams, separated in frequency such that light rainfall/snow and heavy rainfall/snow are covered by at least one radar frequency. In the region where the two overlap, particle size distribution information can be directly inferred using the DWR method described in chapter 3.

Table 5.1

APR-2 instrument characteristics during the 2003 Wakasa Bay Experiment (WBAY03) prior to data recalibration

Frequency	13.4 GHz	35.6 GHz
Polarization	HH, HV	HH, HV
Antenna diameter	0.4 m	0.14 m
Beamwidth	3.8°	4.8°
Antenna scan angle	±25°	±25°
Antenna gain	34 dBi	33 dBi
Polarization isolation	-25 dB	-25 dB
Peak power	200 W	100 W
Bandwidth	4 MHz	4 MHz
Pulse width	10-40 ms	10-40 ms
Pulse Rep. Freq. (PRF)	5 kHz	5 kHz
6 dB Pulse Width	60 m	60 m
Vert. Range Bin spacing	30 m	30 m
Hor. Resolution (@ 6 km)	400 m	500 m
Ground Swath (@ 6 km)	4.5 km	4.5 km
(10 km range)	5 dBZ	5 dBZ
Doppler precision	0.4 m s^{-1}	$> 1 \text{ m s}^{-1}$
Scan Cycle	1.82 s	1.82 s

Measurement of light rain in middle and high latitudes requires 35-GHz band radar.

1. Sensitivity enhancement with high frequency
2. Distinguishing between rain and snow by differences in attenuation
3. Accurate estimation of rainfall rate based on differences in attenuation

35-GHz radar beam

14-GHz radar beam

intense scattering

low attenuation in snow

heavy attenuation in rain

attenuated scattered wave

weak scattering

low attenuation in snow

low attenuation in rain

scarcely attenuated scattered waves

Source: http://www2.nict.go.jp/kk/e414/shuppan/kihou-journal/journal-vol49no2/2-03.pdf

observable range by 35-GHz band radar

observable range by 14-GHz band radar

Rain in tropical zone

rain in middle and high latitudes

Frequency

rainfall rate → (heavy rain)

(light rain)

Rainfall that becomes observable following the addition of 35-GHz band radar

Figure 5.3. A summary illustration describing the benefits and objectives of the APR-2 precipitation radar.

5.1.2 Millimeter-wave Imaging Radiometer (MIR)

The Millimeter-wave Imaging Radiometer (MIR) is a six-channel aircraft-based passive microwave radiometer designed to observe millimeter and submillimeter radiation originating from the surface, water vapor, clouds, and precipitation. Table 5.2 shows the MIR's primary instrument characteristics (Racette *et al.*, 2006).

Data obtained by the MIR instrument during the 2003 Wakasa Bay field experiment (WBAY03) is used extensively in this research to provide nadir-viewing observations of passive microwave brightness temperatures co-located with APR-2 radar data (Wang, 2003). See Fig. 5.11 for the MIR T_B values used in the present studies.

5.1.3 Radiosonde Observations

Table 5.3 shows the locations of nearby radiosonde stations in use during WBAY03 in 2003. Radiosonde observations are used to initialize the near surface air temperature, relative humidity, and tropopause height and temperature profile in the retrieval and radiative transfer portions of the model. Figure 5.4 indicates the location of sounding stations on land (yellow points) and on ship (brown points).

5.2 Data Description

Datasets for each instrument employed in the present studies (APR-2, MIR, radiosonde) were obtained from the 2003 Wakasa Bay field experiment ftp-site at

ftp://sidads.colorado.edu/pub/DATASETS/AVDM/data/rainfall/wakasa_bay/.

The data storage format for each product is different: APR-2 data is stored using Hierarchical Data Format version 4 (HDF4), MIR uses a customized binary format, and

Table 5.2
MIR instrument characteristics during WBAY03

Frequency (GHz)	Bandwidth (GHz)	Sensitivity (K)
89.0	1.0	0.13
150.0	1.0	0.16
183.3 ± 1.0	1.0	0.34
183.3 ± 3.0	2.0	0.28
183.3 ± 7.0	2.0	0.28
220.0	3.0	0.26
340.0	3.0	< 0.35
Scan Angle	±50 °	
Scan Cycle	3.0 sec	
Beamwidth	3.5 °	

Table 5.3
Latitude, longitude, name, and station ID of the P-3 aircraft, radiosonde sites, and the observing ship used during the WBAY03 29 January 2003 observations.

Latitude	Longitude	Name	Station ID
37.4N	136.9E	Wajima	47604
35.4N	133.4E	Yonago	47744
36.1N	136.2E	Fukui	47616
36.2N	133.4E	Chofu-Maru	Ship (0300 UTC 29 Jan. 2003)
36.6N	135.5E	P-3 Aircraft	Segment Start at 0318 UTC
38.6N	135.5E	P-3 Aircraft	Segment End at 0337 UTC
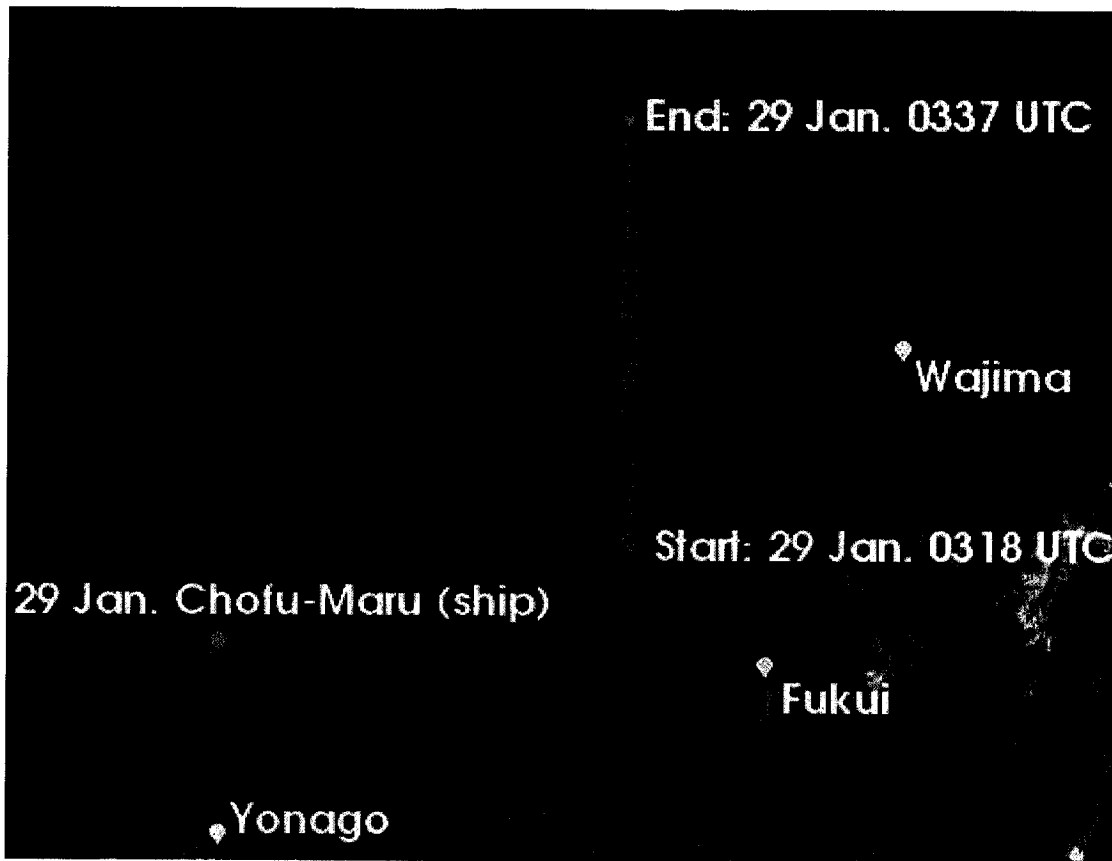
Figure 5.4. Map of Wakasa Bay region indicating location of sounding stations, ships, and start and end points for the flight line used in the 29 January 2003 case study presented in section 5.3. Table 5.3 provides the latitude and longitude of the land and ship-based sounding sites.

radiosonde data from several Japanese land and ocean sites comes in form of ASCII files and postscript plots, originally obtained from the website. However, radiosonde data taken during the experiment appears to be no longer publicly available via the website.

The specific details of the data formats and structures are provided in the appendices. For APR-2, see section A.3.1, and for MIR see section A.3.2.

Although the MIR and APR-2 were onboard the same aircraft, careful consideration of the spatial and temporal co-location of the observational data was required. Both of these instruments were operating in the cross-track scanning mode during the 29 January 2003 case. In the interest of generating vertical profiles of retrieved quantities and simplifying co-location, only the nadir beam was selected.

5.2.1 Nadir Beam Position Location

The APR-2 dataset contains information regarding the 3-D orientation of the radar relative to a locally fixed earth coordinate system. This is called the "look vector" (see table A.2 in the appendix); it is a 3 component unit-vector describing the x, y, and z orientation of the radar emitter/receiver relative to a fixed reference frame.

Because the aircraft itself is not a fixed platform, the look vector changes in response to changes in aircraft pitch, roll, and yaw. The goal for obtaining the nadir beam is to pick the beam number that has the minimum (closest to -1) z-component look vector using the following pseudo-code relationship

$$\text{nadir\_beam\_number}(i) = \text{find}(\texttt{look\_vector}(i,:,3) == \min(\texttt{look\_vector}(i,:,3))), \quad (5.1)$$

where i is the scan number, ":" is the range of beam numbers, 3 is the z-component of the look vector. By locating the nadir-most beam (i.e. the one that is closest to looking straight down), we provide the retrieved 1-D vertical profiles with a stronger physical basis.

No look vector data is provided in the MIR dataset, therefore the roll and pitch (see table A.5) are used to attempt to locate the most nadir-viewing position when MIR is operating in the cross-track scanning mode.

The first of two steps of the relationship is, in pseudo-code form,

$$\text{nadir\_beam\_MIR}(i) = \text{round}(29 - \text{sign}(\texttt{roll}(i))\,(270(1 - \cos(\texttt{roll}(i))))), \qquad (5.2)$$

where i is the scan number, 29 represents the nominal nadir beam position for level aircraft flight. This method assumes that roll is the only factor affecting the left-right adjustment of the beam position. Yaw and pitch combinations contribute to the beam position, however, large pitch and yaw maneuvers are already filtered from the observations by the time it reaches this point in the processing. The second step occurs through the data rejection bounds described in section 5.2.3. After application of the roll and pitch bounds from MIR data and the previously described APR-2 nadir location, the set of observations that are accepted represent reasonably stable/level flight in terms of both the APR-2 instruments and MIR instrument observations.

5.2.2 Temporal Co-location

The temporal sampling at the nadir position is different between the APR-2 and MIR instruments. The MIR and APR-2 instruments make observations at the nadir position every 3.0 seconds and 1.82 seconds respectively. At each APR-2 scan position,

the nearest MIR observation (in time) was selected. The time difference between the MIR and APR-2 position was never larger than $3.0/2 = 1.5$ seconds, with a mean absolute difference of 0.7 seconds. For a nominal P-3 aircraft ground speed of approximately 180 m s^{-1} , this difference translates into a maximum surface offset of up to approximately 270 meters and mean offset of approximately 130 meters, relative to the APR-2 beam position.

5.2.3 Data Rejection and Noise Removal

Aircraft-based observations are influenced by the motion of the aircraft itself, requiring a method for either adjusting for the motion or rejecting the data. In the previous sections the methods for selecting the nadir beam were discussed. However, the observational data still needs to be further quality controlled. In this section, the methods for data rejection are described.

The MIR and APR-2 data for all cases described in this dissertation are limited to over-ocean observations. Although some over-land cases were observed during WBAY03, the purpose of using over-ocean cases was to ensure a relatively easy to simulate ocean surface emissivity, and to remove any topographical influence on the radar and radiometer observations. The APR-2 `surface_index` variable (section A.3.1) provides the basis for acceptance or rejection of observations by surface type. If the `surface_index`$== 1$, the data is over ocean and was accepted for further analysis.

Figure 5.5 shows an example of "Pulse compression sidelobes" (PCS), a noise feature in the observed APR-2 reflectivities occurring near the surface reflection (Tanelli *et al.*, 2004). This significant noise source presented a serious drawback for particle size distribution (PSD) retrievals within approximately 750 meters from the surface.

Observation of the noise feature in near-surface higher reflectivity regions revealed that a signal was still present, although increasingly positively biased as the radar range gates approached the surface.

The following approach was devised for PCS noise removal. First, a running mean was applied to the region affected by noise, which is typically located within 1 km of the surface. Next, a polynomial fit was applied to the smoothed region. The polynomial was subtracted from the original data to reveal the signal. The signal itself was also proportionally biased by the magnitude of the contamination. An additional reduction, using the same polynomial, was applied to the signal to obtain a signal having a dynamic range and behavior consistent with radar observations outside of the noise contaminated portion of the profile. While this approach is preliminary, it is preferred over the alternative approach of simply removing the range gates affected by the PCS noise or replicating the lowest unaffected range gate to the surface. Future research will focus on a more accurate noise characterization, removal methods, and physical models to simulate the noise will also be explored.

Figure 5.5 panel (a) shows a typical Z_{14} and Z_{35} vertical reflectivity profile prior to noise removal near the surface (solid line); the signal with the PCS noise removal applied is plotted for comparison (dashed line). Panel (b) shows the change in dual-wavelength ratio before and after PCS noise removal.

5.2.4 Data Smoothing

For APR-2 observations, the original reflectivity data appeared to be noisy by visual inspection, containing rapid variations in reflectivity. This also resulted in unrealistic variations in the computed DWR, i.e. the solid black line in Fig. 5.6. To address this,
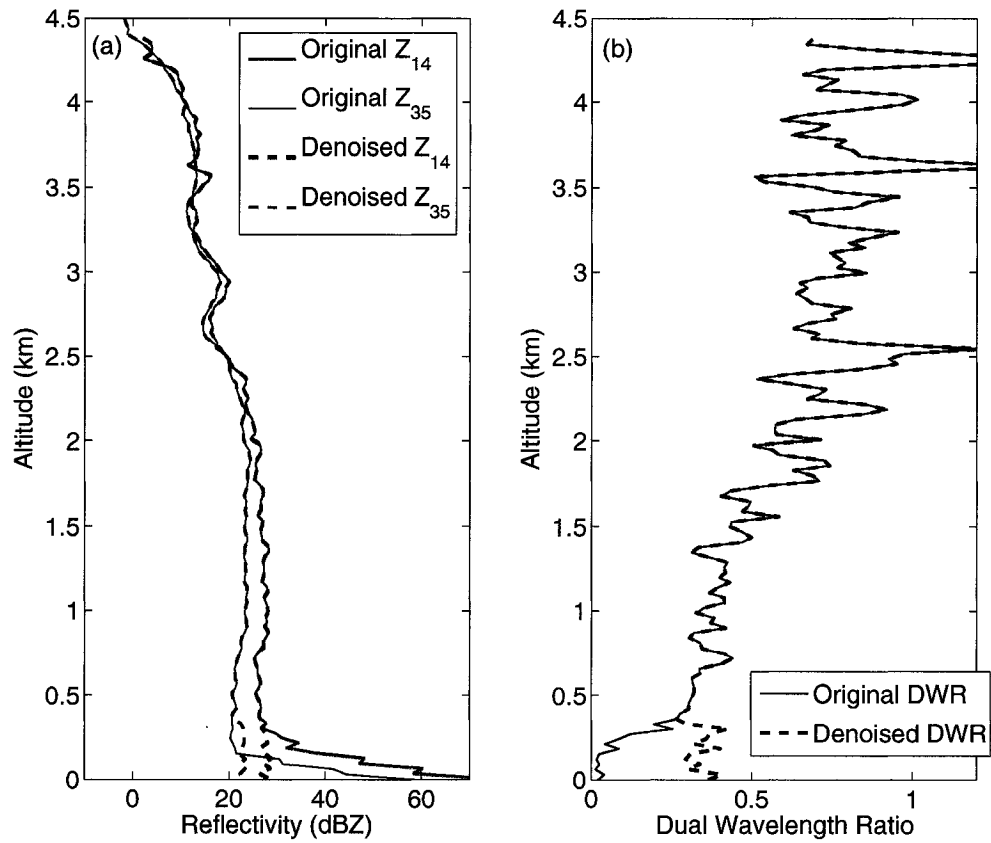
Figure 5.5. (a) Example vertical profile comparing observed 13.4 and 35.6 GHz reflectivities before and after pulse-compression sidelobe noise removal, and (b) dual-wavelength ratio comparison.

the reflectivity profiles (Z_{14} and Z_{35}) were averaged using a 9-bin (30 meters per bin) window average, starting at the cloud top, and proceeding to the surface. No smoothing was applied to LDR or doppler data.

Figure 5.6 shows an example profile of 13.4 and 35.6 GHz reflectivities before and after smoothing (panel a). This also resulted in the smoothed DWR profile, shown in panel (b). It is apparent that the original DWR is sensitive to noise in the reflectivities, and that smoothing helps to alleviate spurious DWR values, improving overall PSD retrieval quality.

Finally, reflectivities (Z_{14}, Z_{35}) and linear depolarization ratio (LDR) values less than -30 dBZ are presumed to be either clear or completely attenuated, depending on the vertical location within the scan. Scans having layer where no reflectivities are present above the surface (after noise removal) are considered clear-sky scans. Layers with reflectivities above the current layer are presumably either attenuated or overlaying cloud. The former can usually be discerned by high reflectivities within scan. Low reflectivity regions with empty spaces beneath them are likely to be sub-detectable clouds or clear air. In the present studies, clear-sky scans are skipped in the retrieval, since the primary interest is in retrieving precipitation particle properties.

5.3   Snow Case: 29 January 2003

On 29 January 2003, widespread snowfall were forecast and observed moving into the sea of Japan. From the flight report:

> Weather: The low that had been just west of Hokkaido had
> moved northwards to the middle of Sakhalin Island and deepened
> to 979 mb. Strong northwesterly flow over all of the Sea of
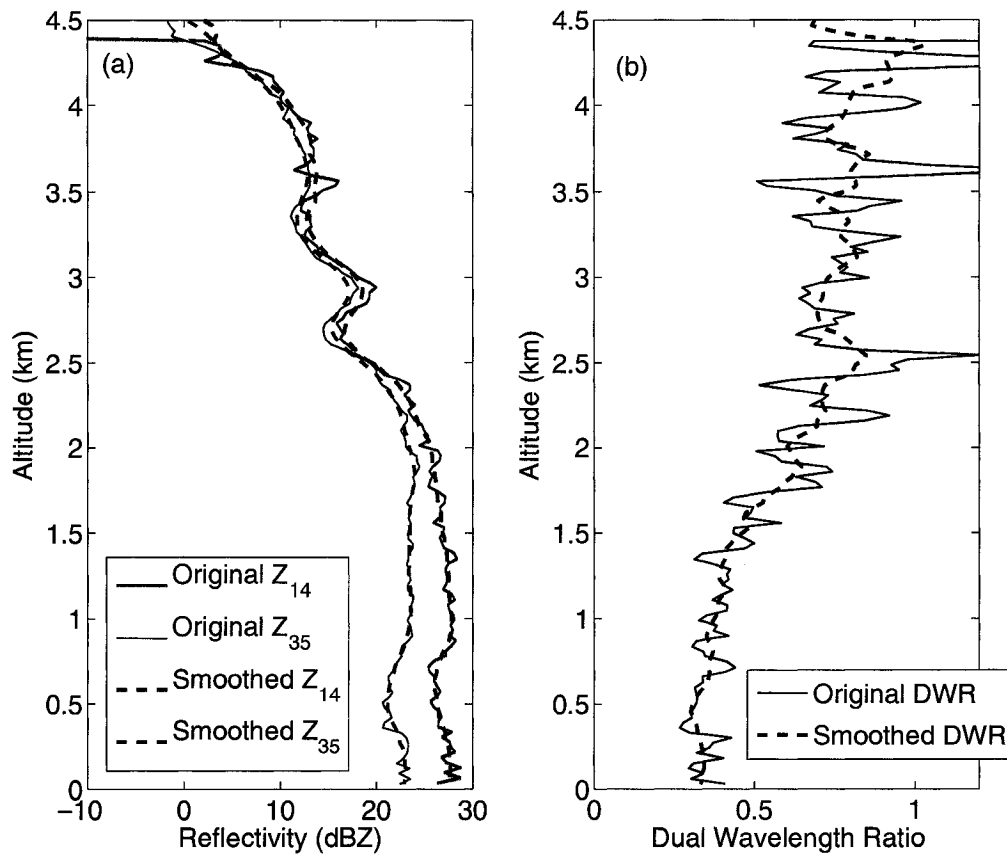
Figure 5.6. (a) Example vertical profile comparing observed reflectivities with and without smoothing applied. (b) dual-wavelength ratio resulting from reflectivity smoothing. A 9-bin (30 meters per bin) window average was used for smoothing.

Japan and extensive areas of snow off the coast of Honshu and
the western side of the Japanese Alps.
Flight Lines: We departed Yokota over chino to kocho where we
began a northward run over the ground truth site at Fukui and
headed westward over the Sea of Japan to our entry point (36
25N; 135 38E) into the protected airspace. We defined a line
from 36 30N; 135 30E to 38 30N; 135 30E and flew it three
times each way beginning at the south end. On the second and
third trip to the north end we flew the PSR calibration
maneuver. As we approached the south end for the third time,
the Gulfstream II was about 10 minutes behind us on their
final leg. We doubled back and flew north to the approximate
position of the Gulfstream II before departing to the east.
We flew to Komatsu and then to Fukui to overfly the ground
truth site again. These data lines were at FL 220. There
wasn't a useful Aqua pass. There was a TRMM pass at about the
time of our landing that may be marginally useful for the
overland portion of the return trip. Takeoff was at 0212Z for
a duration of 4h 43m. The Gulfstream II flew the line at
altitudes ranging from 15500 ft down to 1500 ft.
Instruments: The AMMR was inoperative for the whole
flight--it was also irrelevant to the flight lines flown. The
ACR lost about 5 minutes of data because of an apparently
false over-temperature indication. The MIR, PR2 and PSR
worked flawlessly.
Observations: Widespread snow was observed on the western
slopes of the Japanese Alps and into the Sea of Japan. The
radars observed snow more often than not as we flew the flight
lines and over water transits. Through the few holes in the
clouds we could see that the wind at the sea surface was quite
strong and there was a great deal of whitecapping.
Results: This case with wide-spread snow coverage complements
the previous day's scattered snow showers. We have a rather
good snow data set now.

The flight segment used for this case study begins at approximately 0318 UTC and
continues until 0337 UTC, starting from 36.6 degrees north latitude and 135.5 degrees
east longitude and continuing to 38.3 degrees north latitude and 135.5 degrees east

longitude (a straight line from south to north). Figure 5.4 indicates the line for the 29 January 2003 case relative to Japan and nearby sounding stations.

5.3.1 Observations

Figure 5.7 shows the 0000 UTC 29 January 2003 6-hour forecast of weather patterns, encompassing the flight time range. The black box denotes the region of interest following Fig. 5.4. Wind vectors are labeled using wind barbs. Wind direction is given by the orientation of the post, with speed given by the barbs and/or flags at the end of the post. The head of the post is the location at which the wind was determined; speeds are indicated using three symbols : a flag (triangle) indicating units of 50 knots, a full-barb (long line) indicating units of 10 knots, and a half-barb (shorter line) indicating units of 5 knots. For reference, 1 knot equals approximately 0.514 meters per second.

Figure 5.8 indicates the AMSR-E derived sea surface temperature (SST), wind speed, column water vapor, and column cloud liquid water obtained from www.ssmi.com, (courtesy of F. Wentz). Wind speed comparisons appeared to be consistent with the 6-hour forecasted wind speeds and with the AMSR-E derived winds for the region of interest. The forecast for 0600 UTC was 30 knots (approximately 15 m s^{-1}). AMSR-E derived winds, shown in panel (b), indicated wind speeds ranging from 12-20 m s^{-1} along the flight line. Regional wind speeds were no less than 10 m s^{-1} , and often larger.

Radiosonde observations taken from Wajima (Fig. 5.9) and Fukui stations (Fig. 5.10) were the nearest in time and space to the flight path. The Wajima sounding, taken at
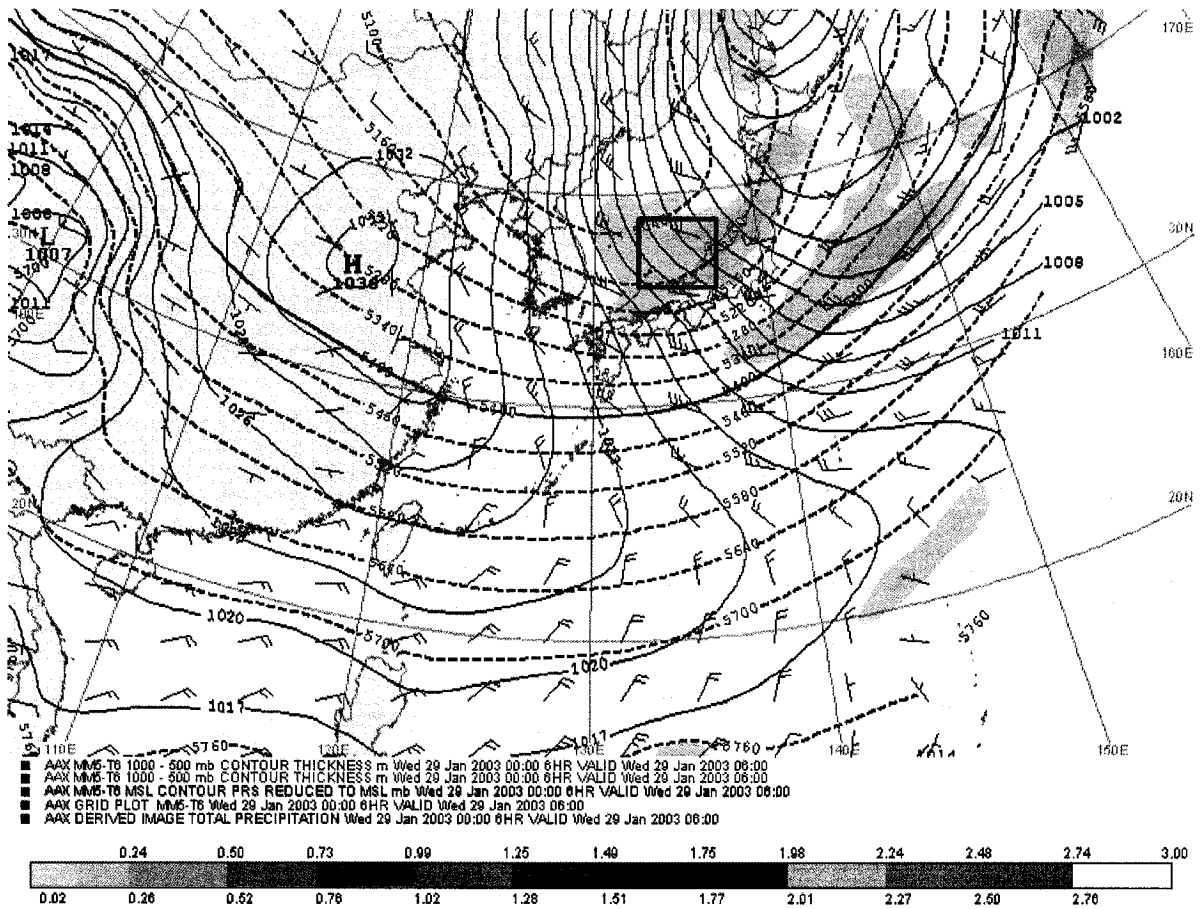
Figure 5.7. 0000 UTC 29 January 2003: 6-hour forecast for Japan and surrounding regions. The black rectangle depicts the region of interest.
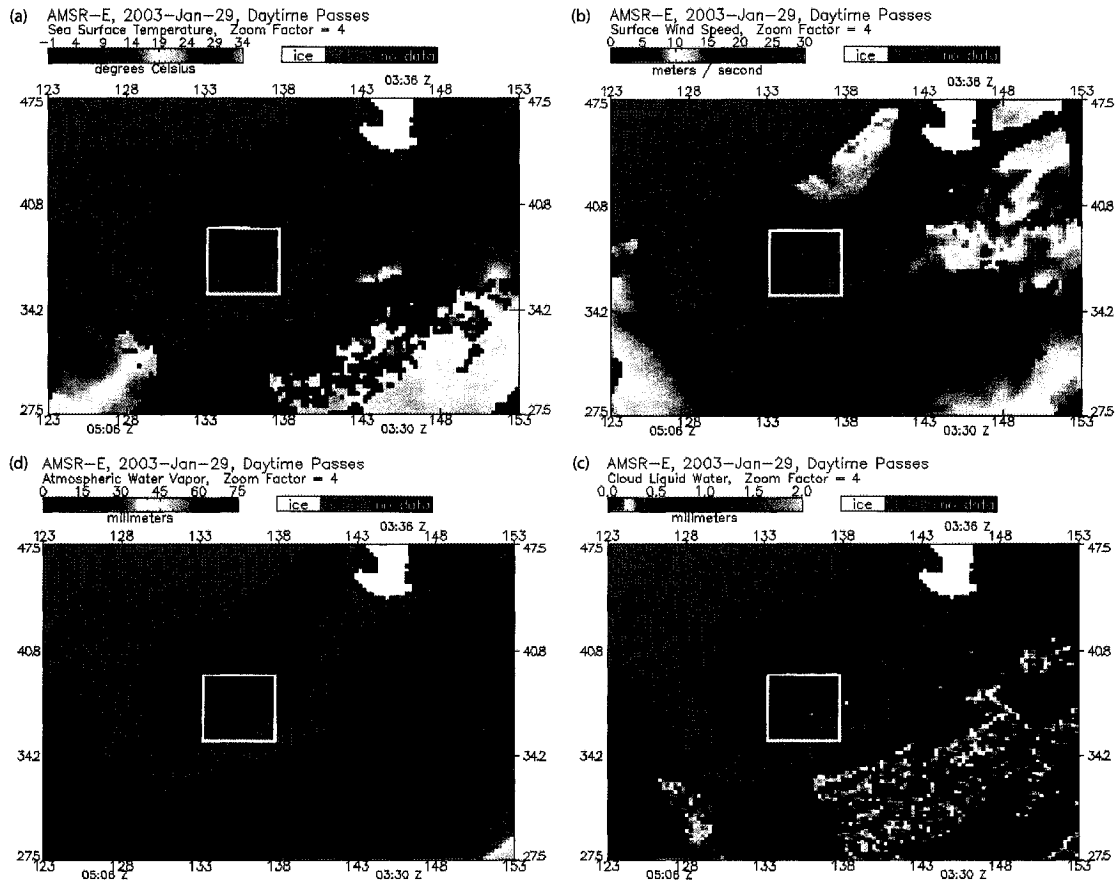
Figure 5.8. 29 January 2003: (a) AMSR-E derived sea surface temperature (C), (b) wind speed (m s^{-1}), (c) column water vapor (mm), and (d) column cloud liquid water (mm). The white rectangle depicts the region of interest.

0230 UTC, was closest to the flight time ranging from 0318 UTC to 0337 UTC. The Fukui sounding at 0000 UTC is included for comparison.

Observed radar reflectivities for the 29 January 2003 case are shown in Fig. 5.11 panels (a) Z_{14}, and (b) Z_{35}. Panels (c) and (d) show the co-located nadir-looking passive microwave brightness temperature (T_B) observations made by the MIR instrument (Table 5.2). Based on the temperature profiles from the soundings, and the lack of brightband information in the radar observations, it is assumed that the reflectivities arise primarily from frozen precipitation particles from cloud-top (i.e., the highest altitude reflectivity) to the surface ($z = 0$ km). The two-way path attenuation of the radar signal occurs from precipitation, cloud liquid water, and gaseous absorption.

Figure 5.11 showed a number of interesting features when T_B observations are paired with the radar observations. Colder T_B depressions were correlated with higher altitude storm tops, with a few lower frequency T_B peaks associated with regions of strong attenuation in radar (for example, panel (d), near 6.5 minutes). Doppler data (not shown) also indicated strong vertical updrafts in this region. Clear sky regions tended to show a separation of about 20 K between each of 89, 150, and 220 GHz respectively. This was observed from about 4.5 minutes to 6.25 minutes, and is to a lesser extent between 2.1 and 2.9 minutes.

The water vapor channels near 183.3 GHz are primarily sensitive to cloud top height in the snow regions. The 183.3 ± 1 GHz channel senses nearest to a strong water vapor emission line, therefore the channel generally shows the coldest T_Bs as it is strongly sensitive to emission from cloud liquid water and water vapor near the cold cloud tops. The 183.3 ± 3 and 183.3 ± 7 GHz channels sense deeper into the cloud, revealing relatively warmer T_Bs in most cases.
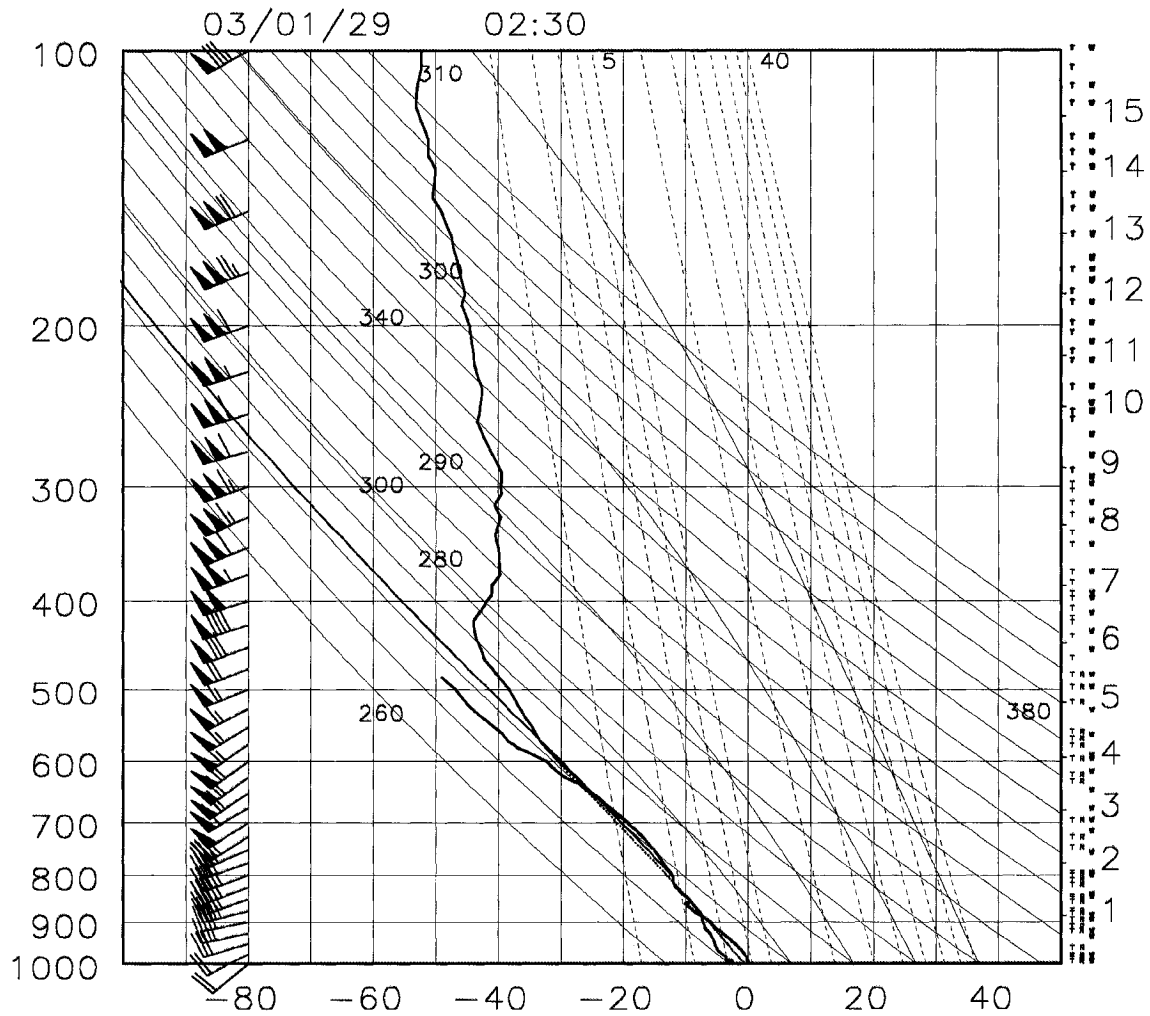
Figure 5.9. 0230 UTC 29 January 2003: Radiosonde observation from Wajima (37.4N, 136.9E). Surface air temperature is approximately 0 °C . Surface wind speed is approximately 20 knots (10 m s^{-1}).
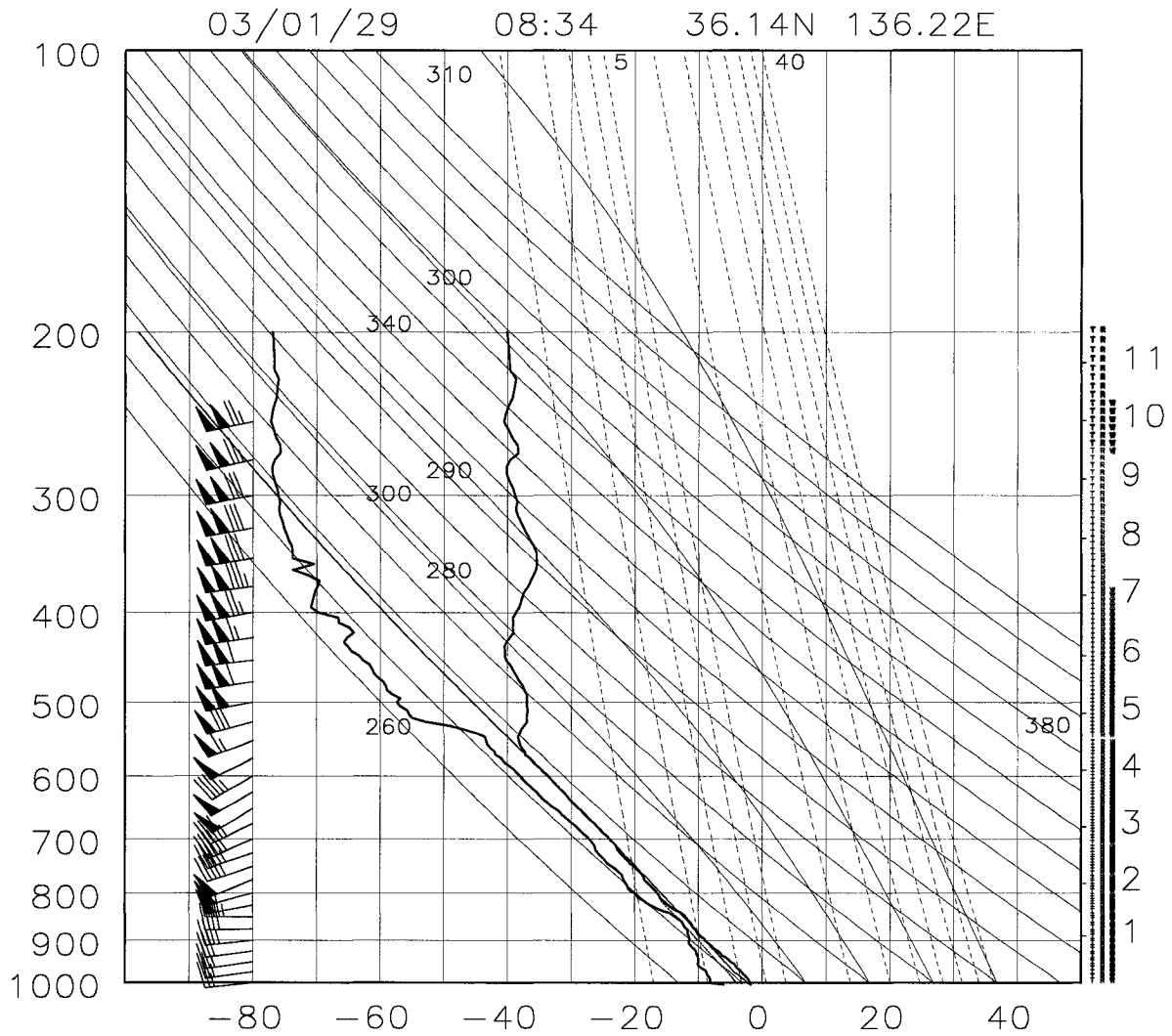
Figure 5.10. 0000 UTC 29 January 2003: Radiosonde observation from Fukui station (36.1N, 136.2E). Surface air temperature is approximately -3 °C . Surface wind speed is approximately 25 knots (13 m s^{-1}).
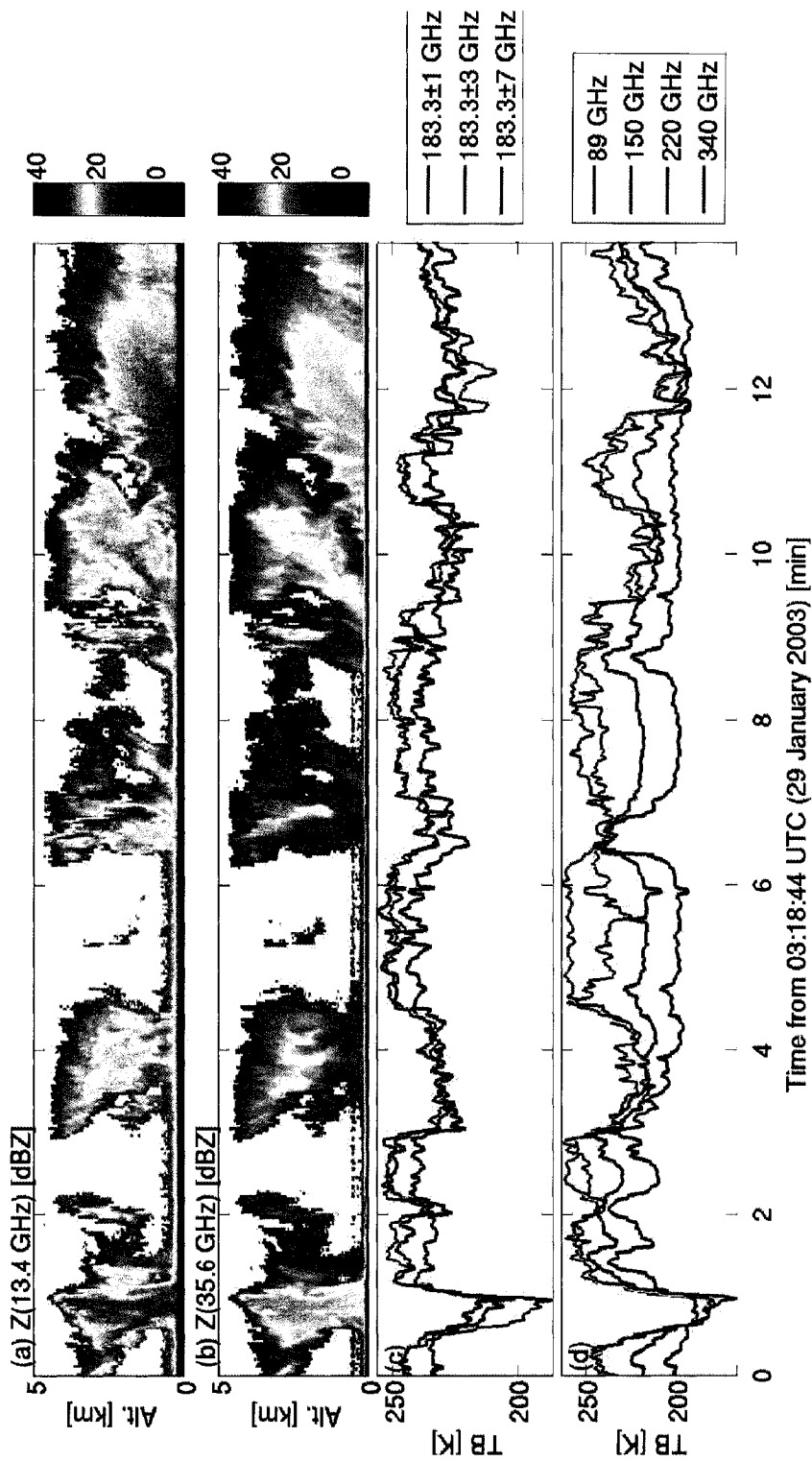
Figure 5.11. 29 January 2003: (a) Original APR-2 Z_{14} and (b) Z_{35} observed reflectivities; (c) Observed MIR brightness temperatures at 183.3±1, 183.3±3, 183.3±7; (d) observed MIR brightness temperatures at 89, 150, 220, and 340 GHz, co-located with APR-2 reflectivities.

In the present retrieval scheme, the passive microwave and radar observations are quite complementary to each other. Radar observations sense the vertical structure and distribution of precipitation within the cloud. Cloud liquid water exhibits a minor influence on radar path-integrated attenuation. Dual-frequency radar observations are directly sensitive to particle size and composition (i.e., density for simulated dry snow spheres).

On the other hand, passive microwave (PMW) measurements represent a column integrated measurement; only limited vertical information can be inferred based on T_B values. PMW observations are also quite sensitive to thermal emission from liquid water and scattering by frozen precipitation particles. The combination of both radar and radiometer observations provides the primary observational data for the retrieval algorithm. In the present case study, only the 89, 150, and 220 GHz MIR channels are used for T_B-constraints (section 3.4) on the DWR-retrieved vertical profiles.

In the brightness temperature (T_B) constraint portion of the retrieval (section 3.4), both parameters and size distribution properties are said to be "retrieved" in that we find the set of parameters and properties that minimize the root-mean-square error (RMSE) between observed and simulated T_Bs. The final products of the present retrieval scheme are, therefore, the parameterized values of: particle density ρ_{snow}, particle size distribution D_0 and N_0, the vertical structure of precipitation, cloud liquid water (CLWP) and vertical distribution (CLWC), and the near surface wind speed W. From the retrieved PSD properties N_0 and D_0, additional derived quantities such as the precipitation rate and ice water content can be computed.

5.3.2 Retrieval Results

As was described in chapter 3, the DWR-retrieval technique was applied to the APR-2 radar observations, and subsequently constrained by the T_B-constraint technique. To initialize the retrieval, radiosonde information was obtained from the nearby Fukui and Wajima sites. From the radiosonde data a simple linear profile of temperature was inferred from the surface to the tropopause. Humidity information was taken from the dew point depression at the surface and was converted to relative humidity. This value is assumed to be the clear sky relative humidity throughout the column. When liquid clouds are present, the model assumes 100% relative humidity in those regions.

The sea-surface temperature (SST), critical for accurate T_B simulations, was visually estimated from the Wentz/AMSR-E SST product. There was no assumption of equality between the lowest layer air temperature and the SST. For the 29 January 2003 case study, the SST was approximately 10 °C , whereas the near-surface air temperature was near 0 °C , according to nearby radiosonde observations.

The Wentz/AMSR-E wind speed product indicated a surface wind speed in the 12-22 m s^{-1} range (Fig. 5.8, panel (b)). This range was also consistent with the visual observations described in the flight report. The effect of wind on the ocean surface is an increase in the surface emissivity through wave and foam action. The models used to simulate these effects were described in section 2.4.1.

The 0000 UTC January 29 2003 sounding from the Fukui radiosonde site indicates near-surface winds at 25 knots (approximately 13 m s^{-1}). The 0230 UTC January 29 2003 sounding from Wajima indicates a 20 knot near-surface wind speed (approximately 10 m s^{-1}). According to a sensitivity study in clear sky regions, a nominal surface wind speed of 17 m s^{-1} was found; this was also consistent with the AMSR-E estimated wind

speeds and visual observations of whitecapping from the P-3 aircraft (Stogryn *et al.*, 1995).

Table 5.4 lists the thermodynamic and physical parameters that define the atmospheric state. These values are obtained from either ancillary observations, such as radiosondes and AMSR-E products, or from testing and intercomparisons. The dielectric mixing method (selected by "mixflag") used was the Bruggeman method, which was previously described in section 2.8.3.

Figure 5.12 shows an example of the retrieved slope Λ and intercept N_0 parameters for the 29 January 2003 snowfall case for a fixed density profile with $n_\rho = 10$ (0.45 to 0.6 g cm^{-3}), see table 3.3 in section 3.3.3). In this case, the single density profile was applied consistently for each of the 450 scans, i.e., 450 1-D profiles of dual-wavelength radar reflectivity.

Taking an individual profile from Fig. 5.12 at approximately minute 12, Fig. 5.13 shows vertical profiles of reflectivity, dual-wavelength ratio, retrieved mass median diameter (eq. 2.30), and retrieved N_0 displayed on a $\log_{10}$ scale. According to the retrieval, the median particle size increases as altitude decreases, consistent with expectations for natural snow growth processes (Pruppacher and Klett, 1997; Rogers and Yau, 1989).

For comparison with retrieved snowfall rates, a Z_{35}-R relationship for snowfall described in Noh *et al.* (2006) was used. Expressing their relationship in terms of precipitation rate R yields

$$R_{35,\text{snow}}(j) = \frac{1}{88.97} Z_{35}(j)^{1/1.04}, \tag{5.3}$$

where Z_{35} is the observed reflectivity values at 35.6 GHz, computed at the j-th range gate. The units of the liquid equivalent snowfall rate, R is [mm h^{-1}], and Z_{35} has

Table 5.4

Standard atmospheric parameters used in retrievals and simulations
for the 29 January 2003 0318-0337 UTC segment.

parameter	value	units	description
T_{skin}	10.0	°C	ocean skin temperature
T_{surf}	0.0	°C	surface air temperature
T_{trop}	-43.0	°C	tropopause temperature
T_d	2.0	°C	dew point depression
z_{trop}	6.25	km	tropopause height
z_{snow}	0.0	km	snow region base
$z_{snowtop}$	4.5	km	snow region top
RH_{clear}	0.2	–	clear air Rel. Humidity
RH_{ice}	1.0	–	R.H. for ice/snow
W	17.0	m s^{-1}	near surface wind spd.
mixflag	'BRUG'	–	dielectric mixing method
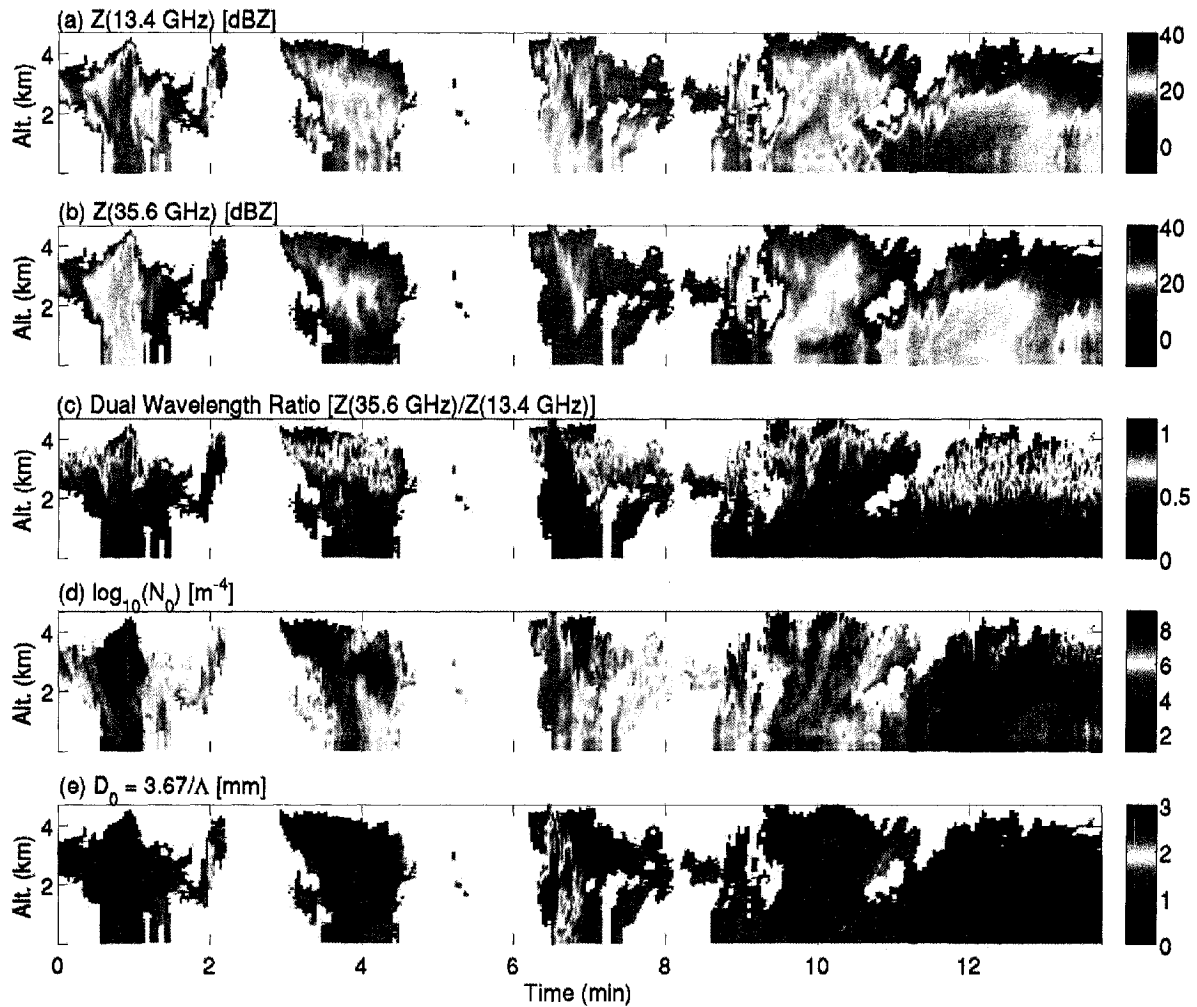
Figure 5.12. 29 January 2003: (a) Denoised/smoothed Z_{14} reflectivities [dBZ], (b) denoised/smoothed Z_{35} reflectivities [dBZ], (c) dual-wavelength ratio, (d) Retrieved exponential distribution intercept parameter: $\log_{10}(N_0)$ [m^{-4}], (e) Retrieved mass-weighted median diameter: $D_0 = 3.67/\Lambda$ [mm]. DWR-only retrieval was performed using $n_\rho = 10$ (0.45 to 0.6 g cm^{-3}).

Figure 5.13. 29 January 2003: (a) Denoised Z_{14} reflectivities [dBZ] and denoised Z_{35} reflectivities [dBZ], (b) dual-wavelength ratio, (c) Retrieved mass-weighted median diameter: $D_0 = 3.67/\Lambda$ [mm], (d) Retrieved exponential distribution intercept parameter: $\log_{10}(N_0)$ [m^{-4}], for $n_\rho = 10$ (0.45 to 0.6 g cm^{-3}).

units of $\text{mm}^6\,\text{m}^{-3}$. Figure 5.14, panel shows the Z_{35}-R relationship applied to the 29 January 2003 case.

The ice water content can written with respect to the rainfall rate using the form: $w = R\rho_{\text{liq}}/v_m$, where R and v_m are defined by equations 2.34 and 2.36,

$$w_{35,\text{snow}} = R_{35,\text{snow}}\Lambda^b \frac{\Gamma(d+1)}{a_0\Gamma(d+b+1)}, \tag{5.4}$$

where $b = 0.311$, $a_0 = 7.2059$, $d = 3$, and Λ is the liquid equivalent slope parameter. All of the values are expressed in SI units. These quantities and relationships were previously described in section 2.7.2.

Following equations 2.33 and 2.34, the ice water content and liquid equivalent precipitation rate are computed using the retrieved N_0 and D_0 values. The results are displayed in Fig. 5.14. For comparison, Z_{35}-R and Z_{35}-IWC relationships (Eqs. 5.3 and 5.4) from Noh *et al.* (2006) are shown in panels (d) and (b) respectively. Agreement is good in most regions. Comparing panels (c) and (d), The Z_{35}-R relationship seems to be over estimating precipitation rate in 1-4 km altitude region of the left-most cloud system, whereas the retrieval produces a more consistent precipitation rate throughout the column, presumably due to the inherent attenuation correction in the present retrieval algorithm. Simple Z-R relationships cannot explicitly account for attenuation, and therefore tend to underestimate precipitation rates as attenuation increases.

A single profile taken from the segment shown in Fig. 5.14 at approximately 12 minutes into the flight is shown in Fig. 5.15. Z_{35}-R relationship slightly underestimated precipitation rate relative to the retrieval when using the density parameter $n_\rho = 10$ (0.45 to 0.6 g cm^{-3}). Retrievals in the lowest 0.5 km were generally treated as suspicious, due to the significant pulse compression side lobe contamination – which has been partially accounted for here, but in an ad hoc fashion.
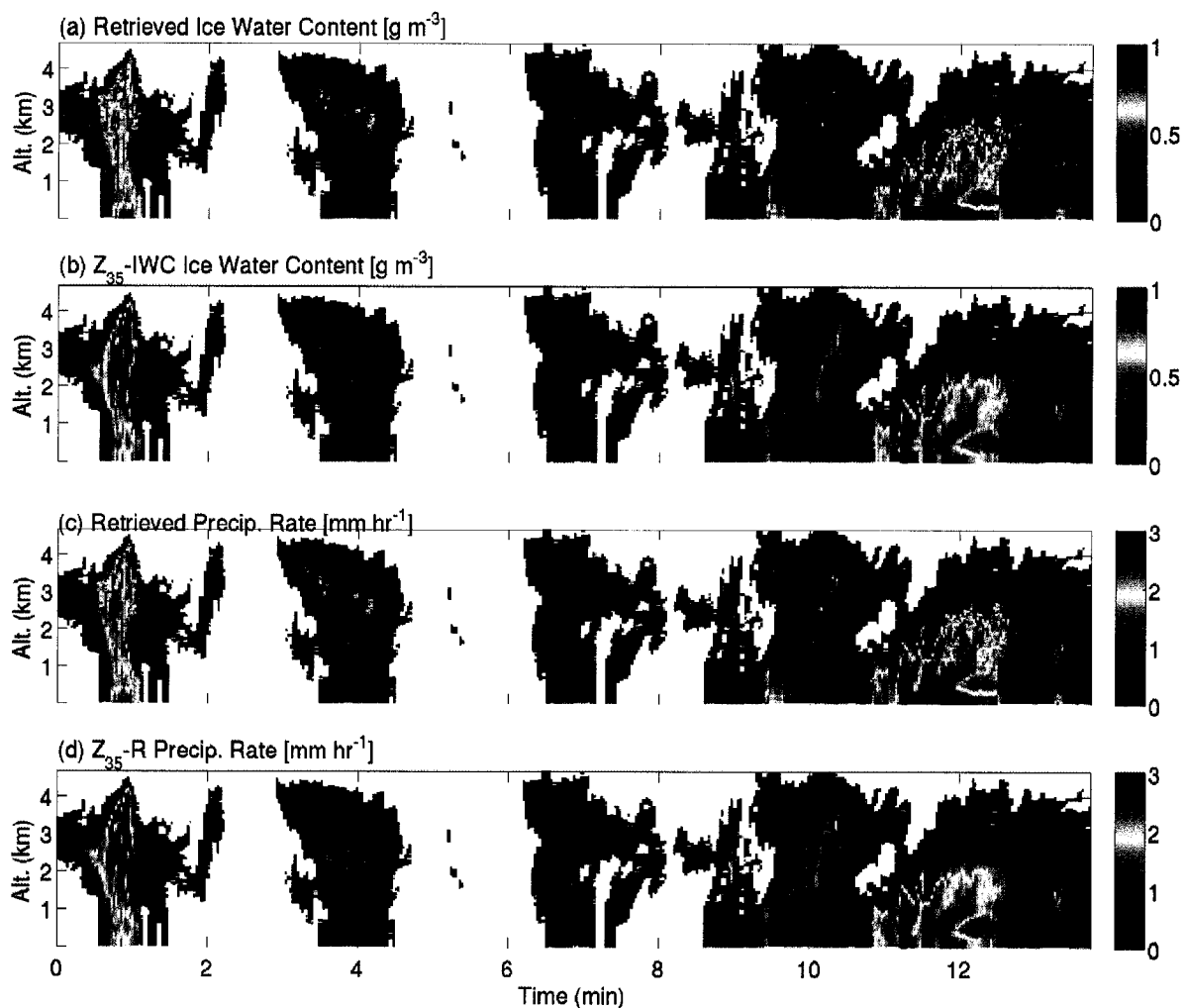
Figure 5.14. 29 January 2003: (a) Derived ice water content [g m^{-3}], (b) Z_{35}-IWC relationship computed using 5.4, (c) Derived liquid equivalent precipitation rate [mm h^{-1}], (d) liquid equivalent Z_{35}-R relationship computed using equation 5.3 from Noh *et al.* (2006). DWR-only retrieval performed using a constant value of n_ρ =10 (0.45 to 0.6 g cm^{-3}, see table 3.3).

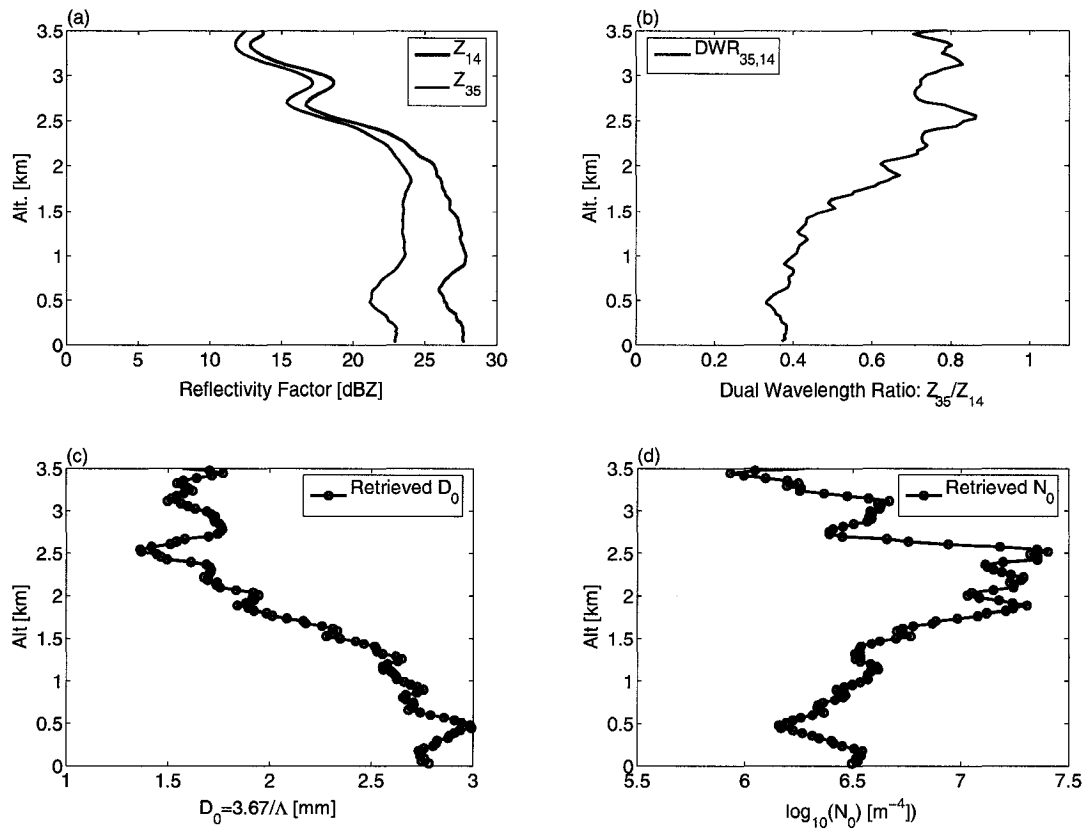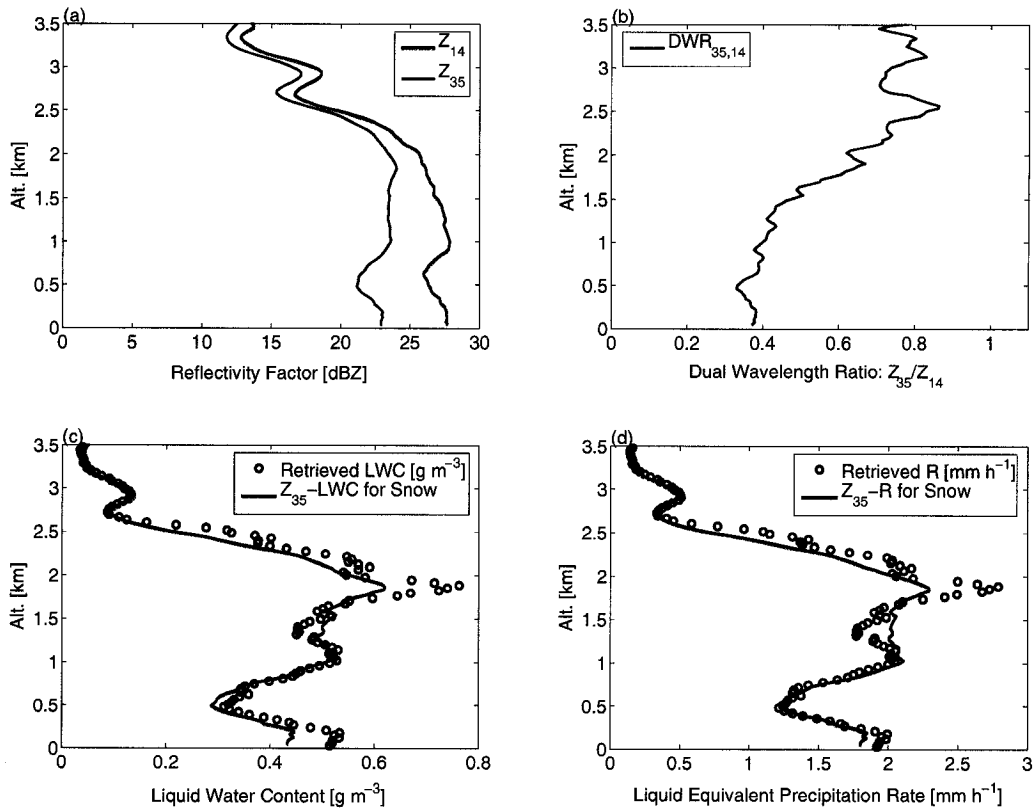Figure 5.15. 29 January 2003: A single profile taken from Fig. 5.12 showing (a) the denoised Z_{14} reflectivities [dBZ] and denoised Z_{35} reflectivities [dBZ], (b) dual-wavelength ratio, (c) derived ice water content [g m^{-3}] and Z_{35}-IWC relationship, and (d) Derived liquid equivalent precipitation rate [mm h^{-1}] and liquid equivalent Z_{35}-R relationship from Noh et al. (2006) (eq. 5.3).

Example T_B simulation

The profiles from the above Z_{35}-R comparisons (depicted in Figs. 5.12 to 5.15) were passed into the forward model to simulate the passive brightness temperatures for each vertical profile. These results were then compared to co-located MIR observations at the same frequencies, with the results shown in Fig. 5.16.

Casual inspection reveals deficiencies in the T_B simulations in Fig. 5.16. Because the DWR retrieval method cannot retrieve cloud liquid water (CLW), no information about CLW was available. To compensate for this, the cloud liquid water path (CLWP) was allowed to vary between 0 and 3.0 kg m^{-2} , and the n_β parameter (representing cloud height and thickness) was varied between 0 and 9. Wind speed was fixed at 17 m s^{-1} . The particle density parameter was fixed at n_ρ =10. The mean T_B RMSE value, averaged over the entire flight segment, was 4.5 K with a standard deviation of 2.8 K.

Despite the derived properties in Fig. 5.14 having a strong similarity with the Z_{35}-R relationships, this approach for handling a DWR retrieval did not appear to accurately represent the atmospheric state in the retrieval due to the mismatch in simulated vs. observed brightness temperatures. Therefore, we sought solutions to the retrieval problem such that the DWR-retrieved profiles provided simulated T_Bs that were more consistent with observations. The following sections describe these efforts.

A Plethora of Solutions

Prior to this point, the choice of n_β (CLW model parameter) and n_ρ (particle density model parameter) has been subjectively chosen by comparison with with the
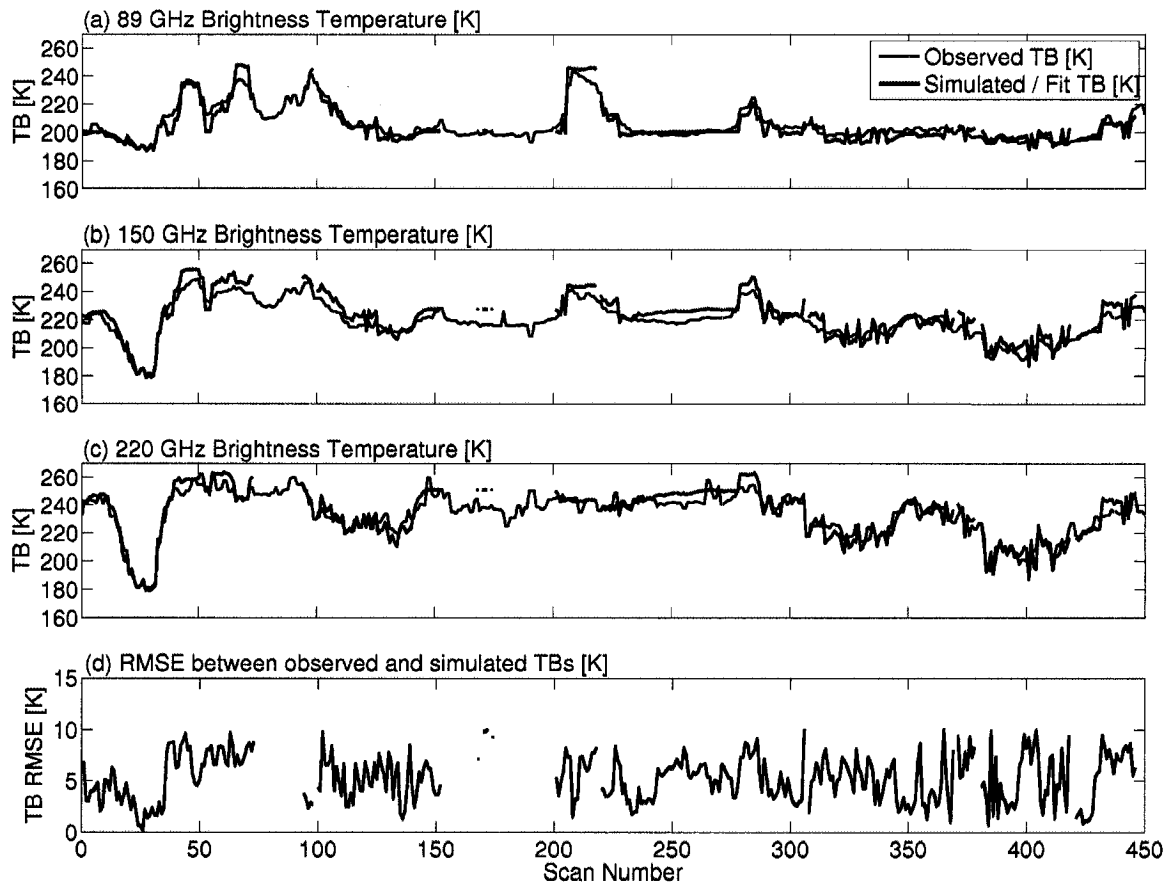
Figure 5.16. 29 January 2003: Red lines represent the observed MIR T_Bs, and black lines are the simulated T_Bs assuming a fixed value of $n_\rho = 10$. The best fit was obtained by minimizing summed RMSE between observed and simulated T_Bs for all three channels. Panels: (a) T_B at 89 GHz, (b) T_B at 150 GHz, (c) T_B at 220 GHz, and (d) RMSE for simulated T_Bs compared to MIR T_Bs.

Z_{35}-R relationship. Figure 5.17 shows the entire range of possible retrievals using only the DWR method for a single observed reflectivity profile. These included 14 variations in density profiles, 10 variations in cloud liquid water profiles, and 11 values of liquid water path resulting in approximately 1400 candidate profiles. Black profiles indicate the 4 lowest RMSE-valued profiles constrained by the T_B method described in section 5.3.3 and table 5.5. N_0 and DWR were artificially limited in their maximum extent to avoid computations falling outside the physical limits defined by the retrieval method.

The primary point of Fig. 5.17 is to show the entire range of variation in DWR-only retrievals. All of these profiles are "mathematically acceptable" solutions to the DWR retrieval under the current set of constraints. To further constrain the candidate solutions, additional observations or assumptions were necessary.

5.3.3 Constraining Retrievals Using MIR Brightness Temperature Observations

From the theory presented in chapter 3, the DWR-based retrievals of Λ and N_0 were shown to be ill-posed. More specifically, there are a nearly infinite number of combinations of Λ, N_0, particle density, and other factors within the multiple vertical layers of a 1-D profile of the atmosphere that *mathematically* solve inversion described by equation 3.8. However, physical reality precludes many solutions, and physical plausibility adds further constraints. The primary uncertainty under the current formulation is that the "true" particle densities are generally unknown for frozen precipitation. The term density is used loosely here, as usual, since we're referring to a spherical approximation to irregular particles, whereby the density acts as a proxy for shape and composition.
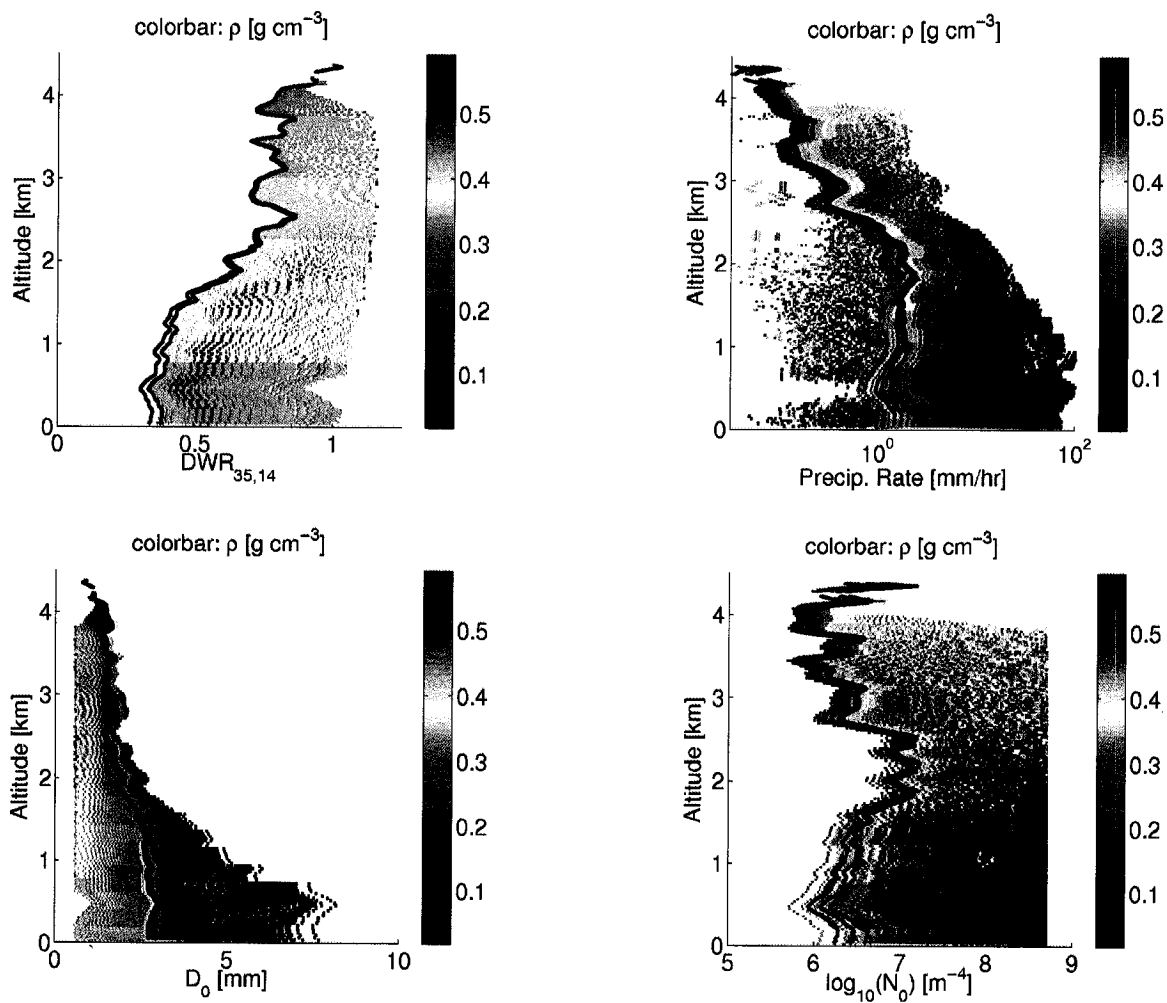
Figure 5.17. 29 January 2003: Scan number 395 single profile range of retrieved properties obtained using the DWR method. Panels show vertical profiles of (a) dual-wavelength ratio, (b) liquid equivalent precipitation rate, (c) mass-weighted median particle diameter: $D_0 = 3.67/\Lambda$, and (d) exponential distribution intercept parameter: $\log_{10}(N_0)$. The black lines represent the 4 optimal retrievals defined by the 4 smallest RMSE values listed in table 5.5.

Simulated passive frequencies were selected to match the MIR "window channel" frequencies at 89, 150, and 220 GHz (see Fig. 2.2). The water vapor channels of $183\pm1,3$, and to a lesser degree 183 ± 7 GHz, were difficult to correctly simulate since they are strongly sensitive to the vertical distribution of water vapor within the 1-D profile. Without adequate radiosonde soundings at the time of the T_B observations, it was difficult to correctly simulate the vertical distribution of water vapor throughout the column. The 340 GHz observations were not selected for a similar reason: continuum absorption and emission by water vapor strongly influenced the simulated T_Bs. Having said that, our primary concern was with the retrieval of snow particle properties, rather than water vapor or cloud liquid water, so the channels most suitable for this task (89, 150, and 220 GHz) were used for the remainder of the research

Following the T_B-constraint technique from section 3.4 and using a simple selection criterion based on the root mean square error (RMSE) between the observed and simulated T_Bs, a significant portion of the candidate profiles were readily removed from the solution set. An example of this is illustrated for a single profile in Fig. 5.17.

Accurate simulation of brightness temperatures requires an additional critical assumption, one that is unimportant to the DWR-retrieval method: passive microwave emission from the ocean surface. The primary factors influencing passive microwave emission from the ocean surface are sea surface temperature (SST) and surface emissivity. Section 2.4.1 described the ocean surface emissivity model used herein.

Surface skin temperature and the near surface wind speed were derived from AMSR-E SST observations (see section 5.3.1, Fig. 5.8). However, the wind speed product was not well defined in regions of strong precipitation, indicated by black areas in Fig. 5.8. In an attempt to determine the optimal wind speed, T_B computations for a range of

wind speeds ranging from 9 to 20 m/s were tested in clear-sky regions. This wind speed range was selected to cover the entire range of AMSR-E/radiosonde derived wind speeds in the region surrounding present case studies. Although not shown here, the optimal wind speed was found to be approximately 17 m s^{-1} , the value used in the following case studies.

Nevertheless, a bias still appeared in the clear sky regions, which could not be fully accounted for by wind variations alone. It is believed that undetected cloud liquid water, water vapor distribution uncertainty, or variations in the ocean surface emissivity were responsible for some of the bias. As a result, the regions which were deemed "clear sky" were removed from the analysis, as these regions contribute no new information to the precipitation particle retrievals.

Brightness Temperature Simulation Results

Table 5.5 on page 189 provides an example of the simulated brightness temperatures dataset for scan number 395 of the 29 January 2003 snowfall case, covering the 20 simulated T_B sets having the smallest root mean square error (RMSE) value compared to the observed MIR values. Only T_Bs at frequencies 89, 150, and 220 were simulated. For this detailed case, approximately 60,000 sets of T_Bs were simulated and compared to the single set of MIR observed T_Bs.

Figure 5.17 illustrates the 4 best-fit T_B-constrained profiles (black curves) overlaid on the much more varied DWR-only retrievals. This is a strong visual indicator of the degree of constraint that comparison with the T_B observations can provide. However, as table 5.5 shows, even variations on the order of 1-2 K in the RMSE can result in a wide variety of retrieved properties. For the lowest three RMSE values, the density

Table 5.5

29 January 2003: MIR observed T_Bs and 20 best-fit simulated T_Bs sets for scan number 395. The T_B RMSE is computed for 89, 150, and 220 GHz. Associated retrieval parameters of cloud distribution(n_β), cloud liquid water path (CLWP), and density parameter (n_ρ) are also given.

n_β	CLWP	n_ρ	RMSE	$T_\mathrm{B}(89)$	$T_\mathrm{B}(150)$	$T_\mathrm{B}(220)$
–	[kg m^{-2}]	–	[K]	[K]	[K]	[K]
MIR	–	–	**0.00**	**194.2**	**194.2**	**200.1**
6	0.050	13	0.90	194.0	196.0	204.7
9	0.050	9	1.45	193.2	197.8	208.2
9	0.025	2	1.52	195.2	198.6	205.8
6	0.025	6	1.65	195.7	198.4	205.4
5	0.300	12	1.69	192.8	196.7	203.5
7	0.025	2	1.71	194.7	198.8	207.7
6	0.150	1	1.74	193.0	197.7	208.8
8	0.025	2	1.84	194.9	199.0	207.7
5	0.025	6	1.86	195.4	198.0	203.9
5	0.150	5	1.94	196.6	197.9	205.0
5	0.050	13	2.18	194.2	195.8	202.5
6	0.025	2	2.19	195.2	196.9	202.7
1	0.000	10	2.25	194.6	198.1	202.8
6	0.100	5	2.27	190.4	194.5	206.0
4	0.025	6	2.34	195.3	197.5	202.6
1	0.005	10	2.47	195.4	198.6	202.9
4	0.005	10	2.49	195.6	200.2	205.2
8	0.025	13	2.52	190.2	194.1	205.4
2	0.005	10	2.54	195.7	199.0	203.2
9	0.025	6	2.64	195.6	200.0	208.4

parameters cover similar particle density ranges. However, within a RMSE of 2.6 K, it is evident that a much larger range of density parameters was covered. These results are not particularly troublesome, although it is evidence that the combined observation sets did not fully constrain the retrieval.

T_B-Constrained Retrieval Results

Logically extending the previous single-profile analysis to all observed scans in the flight segment provided a multiparameter retrieval at each scan position. The goal of this approach was to find the DWR-retrieved physical profiles that produced simulated T_Bs similar to the observed MIR T_Bs. Figure 5.18 shows the simulated T_Bs, indicated by black traces, that minimize the RMSE as compared to the MIR-observed T_Bs, indicated by red traces. Qualitatively speaking, the fit appears to be quite good in most regions. The mean RMSE values were around 2.6 K, with a standard deviation of 2.2 K – nearly 2 K lower than the earlier case having a fixed density parameter, $n_\rho = 10$ (Fig. 5.16). Regions without simulated T_Bs are clear-sky regions.

For each of the 450 scans, the best-fit T_B set had an associated 1-D physical profile which produced those T_Bs. These represented the best-fit "retrieved" profiles. More specifically, the best-fit profiles consisted of: Λ and N_0 values at each vertical level, the linear density parameter n_ρ , the cloud liquid water path, and the cloud liquid water distribution parameter n_β . As seen in table 5.5, a number of different parameter combinations provided RMSE values which fell within one standard deviation from the mean minimum RMSE value (2.6 ± 2.2 K).

Figure 5.19, shows only the singular set of parameters which resulted in the minimum T_B RMSE values shown in Fig. 5.18, considering all possible combinations of
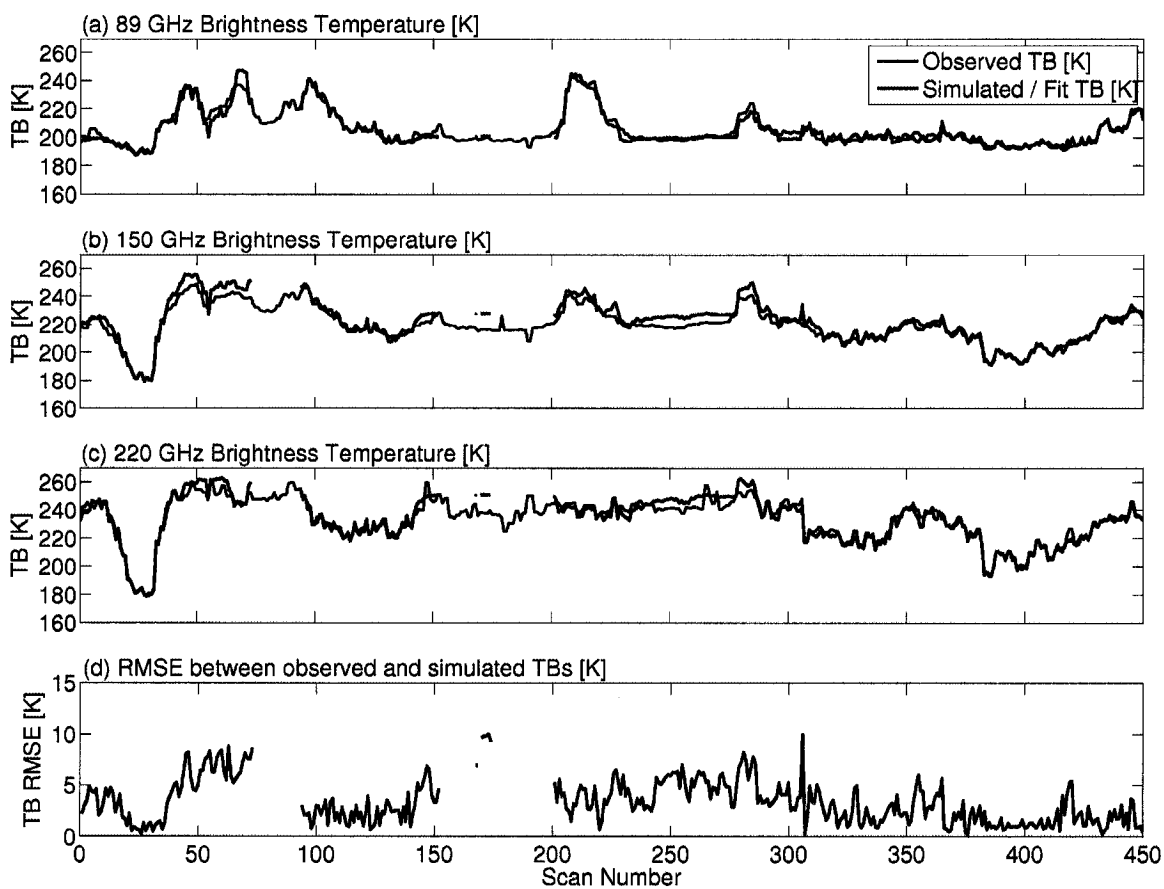
Figure 5.18. 29 January 2003: Red lines represent the observed MIR T_Bs, and black lines are the simulated, best-fit T_Bs. No density constraints are applied. The best fit was obtained by minimizing the T_B RMSE across all three channels. Panels: (a) T_B at 89 GHz, (b) T_B at 150 GHz, (c) T_B at 220 GHz, and (d) RMSE for simulated T_Bs compared to MIR T_Bs.

parameters. It is clear that this method produced wide variations in the particle density and cloud liquid water contents. Part of the reason for this is the sensitivity of the retrieval to relatively small variations in the brightness temperatures.

Figure 5.20 shows the T_B-constrained retrieved mass-weighted median diameter, $D_0 = 3.67/\Lambda$, exponential distribution intercept parameter, $\log_{10}(N_0)$, and derived liquid equivalent precipitation rate [mm h^{-1}]. Casual inspection of the precipitation rate in panel (c) of Fig. 5.20 indicates that the retrieval was not completely physically plausible, despite having the "best-fit" determined by the RMSE values.

At this point there was no additional information to further constrain the retrievals. If one considered the DWR-retrieval only, the solution set for a single profile was quite large, even after the density and cloud distribution parameterizations. The key point is that the T_B-constraint method was not intended, by design, to identify/retrieve a single correct retrieved profile, but rather it was designed to *exclude* candidate profiles inconsistent with the simulations, and radar/radiometer observations. The resulting "reduced" dataset provides a range of probable PSD properties and density parameters.

5.3.4 Parameterization of the T_B-Constrained Profiles

For the present case, there were 450 individual scans, some of which did not record any reflectivity from the aircraft to the surface, presumably indicating a precipitation-free scene. Of those 450 scans, 388 had radar reflectivity profiles that were determined to be originating from precipitating and/or thick clouds. The DWR-retrieval operated on each scan using the 14 different particle density profiles (n_ρ), 10 cloud liquid water distributions (n_β), and 11 values of CLWP, resulting in as many as 1400 retrievals per scan. Many profiles had 896 retrievals per scan, under the assumption that the CLWP
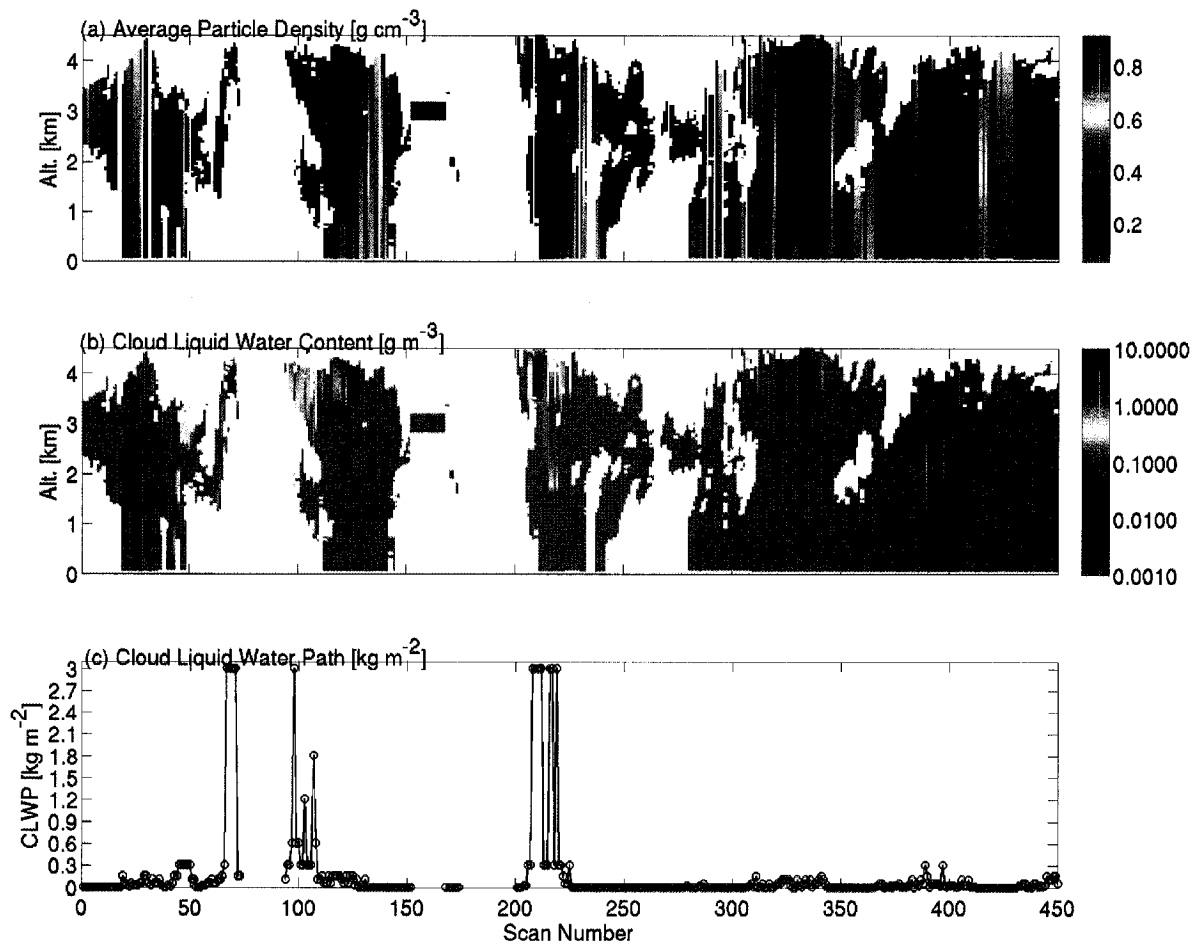
Figure 5.19. 29 January 2003: Parameters resulting in the best-fit T_B values shown in figure 5.18: (a) Particle density, (b) cloud liquid water content, and (c) cloud liquid water path
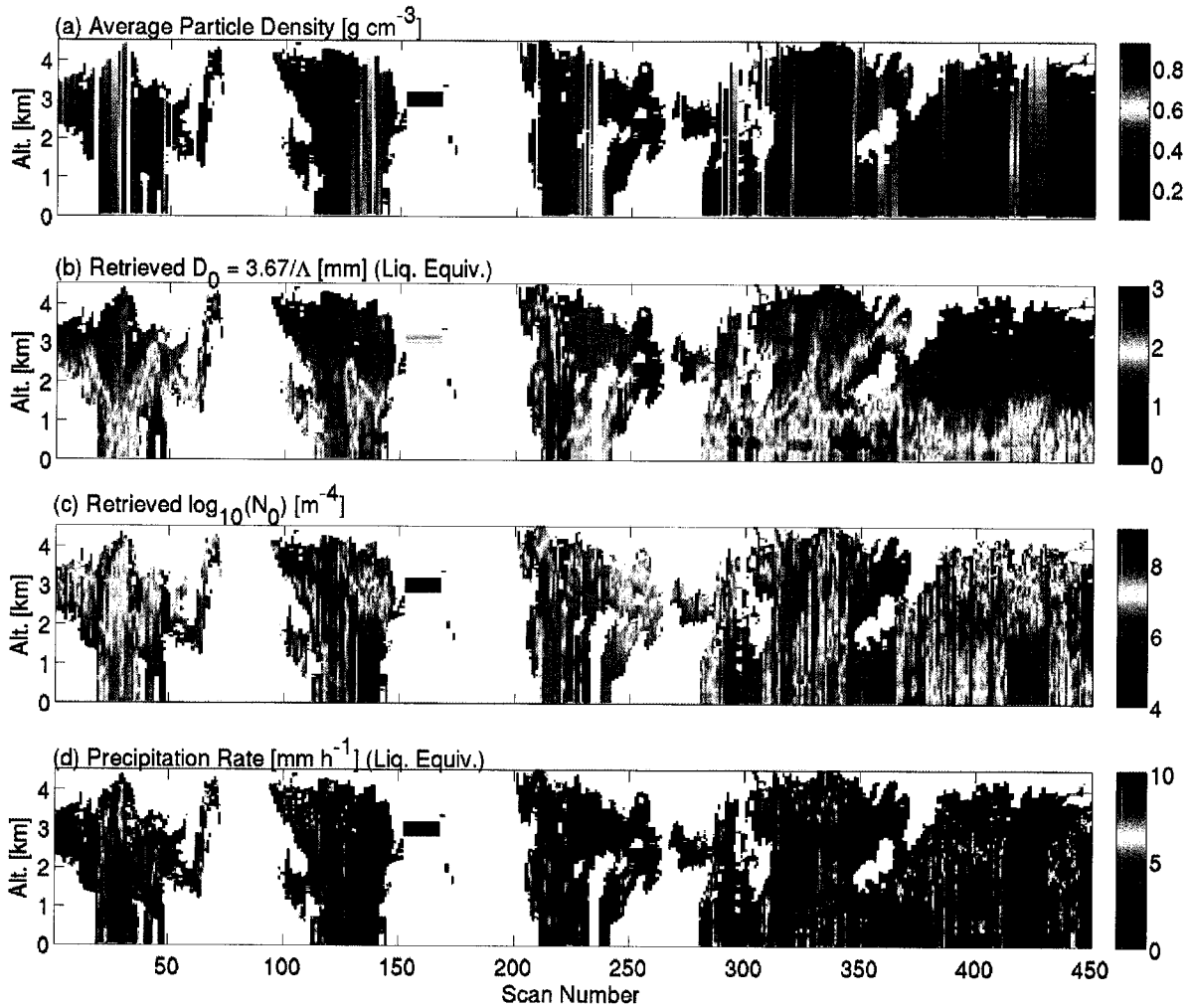
Figure 5.20. 29 January 2003: The profiles resulting in the best fit T_B shown in figure 5.18. The following panels show (a) the particle density [g cm^{-3}]; (b) T_B-constrained retrieved mass-weighted median diameter: $D_0 = 3.67/\Lambda$ [mm]; (c) the T_B-constrained retrieved exponential distribution intercept parameter, $\log_{10}(N_0)$ [m^{-4}], and (d) the derived liquid equivalent precipitation rate [mm h^{-1}].

would not go above 0.3 kg m^{-2} . For the present case study, there were 450,000 total retrieved profiles. It bears repeating that each profile represents a mathematically valid, although not necessarily physically realistic, retrieval using only the DWR-retrieval method.

For each of the 450,000 1-D profiles from the DWR-retrieval, the forward model was run using each profile as the input. The resultant simulated T_Bs were compared to the observed MIR T_Bs, and the RMSE was calculated. At the end of chapter 4, a T_B RMSE constraint was chosen at a 10 K maximum based primarily on the uncertainty analysis. Those profiles resulting in a T_B RMSE value of less than 10 K were, therefore, selected as our T_B-constrained solutions. This constraint reduced the number of profiles from 450,000 to 81,000 profiles. Additionally, the removal of redundant retrievals brought the number down to 63,171 profiles.

For testing purposes, an additional subjective constraint on the T_B RMSE was also imposed, such that the maximum RMSE for a given scan was no larger than 2.5 K plus the minimum RMSE value for the scan. For example, if the minimum RMSE value for a set of candidate profiles was 1.0 K, all profiles yielding RMSE values up to 3.5 K would be considered as solutions. This resulted in a further reduction in the total number of profiles from 63,171 to 17,469 profiles, 4% of the original 450,000 candidate profiles.

Figures 5.18 through 5.20 showed the T_Bs and retrieval parameters for the best RMSE values under this constraint. However, little useful information is obtained from the images. It is more insightful to characterize the ranges of the physical properties consistent with the current retrieval.

Using the retrieval parameters from scan 395, described in table 5.5, the minimum, mean, and maximum values of the retrieved particle size distribution properties, N_0

and Λ, are examined in table 5.6. The key features are that most of the Λ values are reasonably consistent with each other, with a couple of exceptions. The exceptions can be explained by the unusually low particle density parameters chosen due to the T_{B} constraint. The N_0 parameters tend to vary more widely in response to changes in the particle density.

Extending the above analysis to all 450 scans in the 29 January 2003 case, figures 5.21 through 5.24 show the histograms of the various properties of interest in the retrieval. Figures 5.25 through 5.30 show scatterplots of these quantities vs. each other, giving an indication of both range and inter-dependence.

The histogram of retrieved liquid equivalent mass-weighted median diameter $D_0 = 3.67/\Lambda$ is shown in figure 5.21, encompassing retrieved values for the entire 29 January 2003 WBAY03 flight segment, subject to the 2.5 K + min(RMSE) T_{B}-constraint. Most of the values range in the $D_0 = 1$ to 2 mm range, with a mean value of 1.6 mm and standard deviation of 0.6 mm. The shape of the distribution more closely follows a Gamma or Beta distribution, rather than a normal distribution.

Figure 5.22 shows the histogram of retrieved N_0 values ($\log_{10}$ scale). The mean $\log_{10}(N_0)$ value is -1.0 (0.1 cm^{-4}), and the standard deviation of $\log_{10}(N_0)$ is 1.2 (a range of 0.006 to 1.6 cm^{-4}). The shape of the distribution is nearly normal (in $\log_{10}(N_0)$).

From D_0, N_0, and the particle density ρ_{snow}, the histogram liquid equivalent precipitation rate R (for all vertical levels) is shown in figure 5.23. Here the distribution of $\log_{10}(R)$ is nearly normal, with a mean of 0.5 (3.2 mm h^{-1}) and standard deviation of 0.7 (approximately 0.6 mm h^{-1} to 16 mm h^{-1}) – a reasonable range, although it is expected that the actual liquid equivalent precipitation rates are less than 5 mm h^{-1} (based on the Z_{35}-R relationships). A significant second hump is notice-

Table 5.6

Ranges of retrieved parameters for a single-profile T_B-constrained retrieval using scan number 395. The retrieval parameters are listed in table 5.5

RMSE [K]	$\min(\Lambda)$ [cm^{-1}]	$\mathrm{mean}(\Lambda)$ [cm^{-1}]	$\max(\Lambda)$ [cm^{-1}]	$\min(N_0)$ [cm^{-4}]	$\mathrm{mean}(N_0)$ [cm^{-4}]	$\max(N_0)$ [cm^{-4}]
0.90	18.9	33.3	94.2	0.09	1.43	20.43
1.45	18.9	34.1	99.6	0.09	2.45	47.02
1.52	18.5	33.2	98.5	0.03	1.40	37.57
1.65	18.7	32.4	90.2	0.04	0.73	11.25
1.69	21.4	38.1	105.2	1.34	53.80	1195.8
1.71	18.5	33.3	98.5	0.03	1.44	37.57
1.74	19.6	35.7	102.9	0.20	10.72	184.49
1.84	18.5	33.3	98.5	0.03	1.44	37.58
1.86	18.7	32.4	90.2	0.04	0.73	11.25
1.94	19.8	35.3	101.8	0.23	5.73	81.93
2.18	18.9	33.3	94.2	0.08	1.39	20.42
2.19	18.5	33.0	98.5	0.03	1.36	37.57
2.25	18.5	31.8	88.2	0.02	0.45	8.50
2.27	19.4	35.0	101.8	0.25	5.44	81.81
2.34	18.7	32.4	90.2	0.04	0.71	11.25
2.47	18.5	31.8	88.2	0.02	0.45	8.50
2.49	18.5	31.8	88.2	0.02	0.45	8.50
2.52	18.7	33.3	94.2	0.09	1.46	20.43
2.54	18.5	31.8	88.2	0.02	0.45	8.50
2.64	18.7	32.6	90.2	0.04	0.77	11.25
2.75	18.7	33.4	94.2	0.10	1.46	20.42
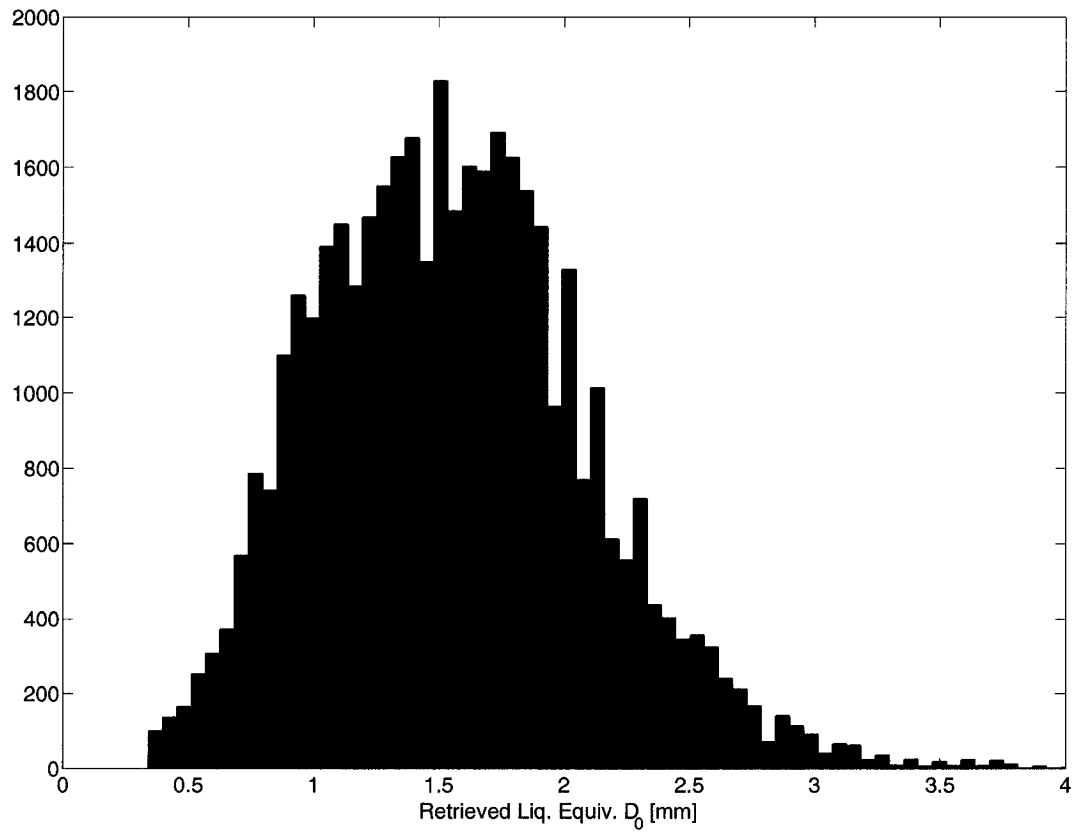
Figure 5.21. 29 January 2003: Histogram of D_0 $[mm]$ for the T_B-constrained case.
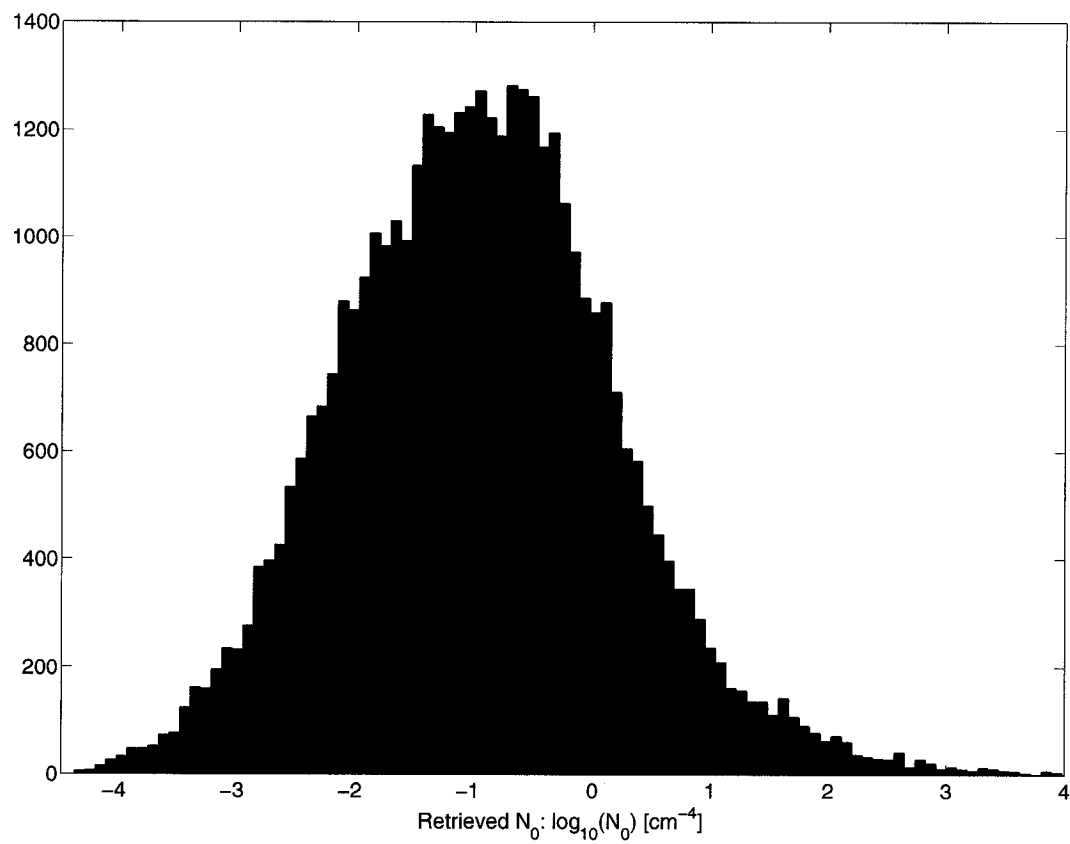
Figure 5.22. 29 January 2003: Histogram of N_0 [cm^{-4}] for the T_B-constrained case.
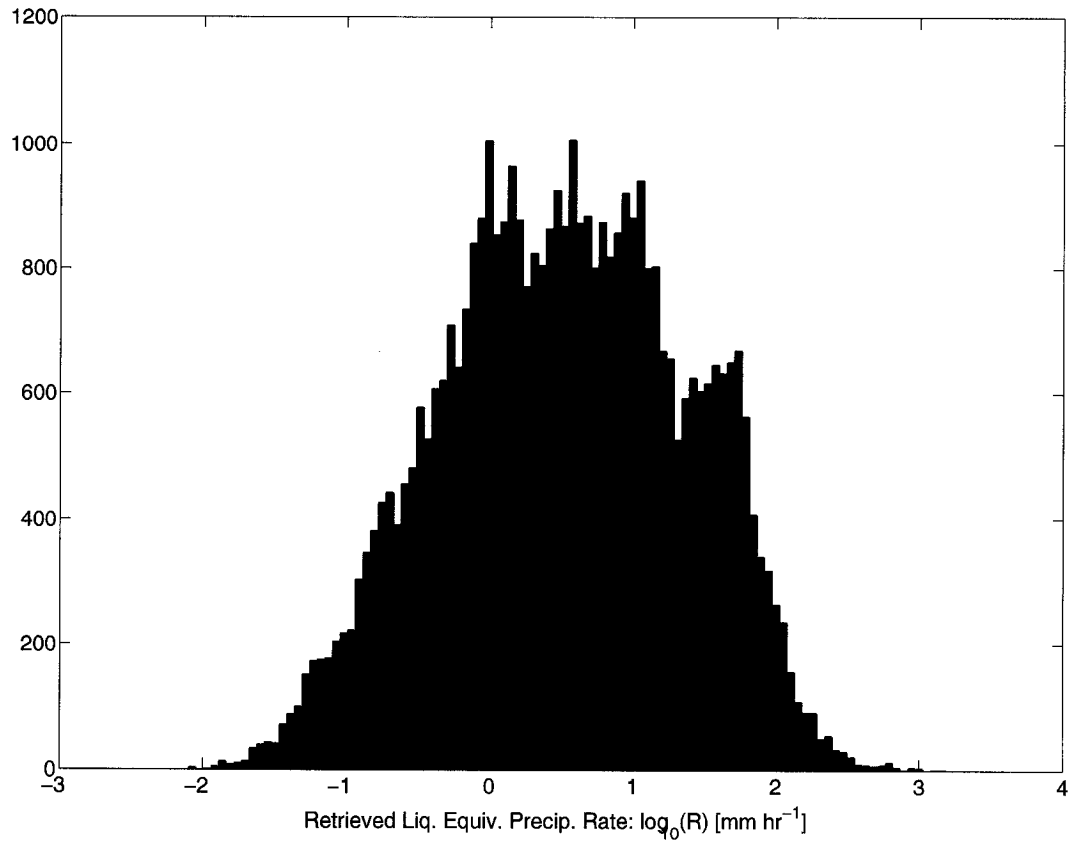
Figure 5.23. 29 January 2003: Histogram of liquid equivalent precipitation rate R [mm h^{-1}] for the T_{B}-constrained case.

able for $R > 10$ mm h^{-1} , indicating that there may be two largely different particle density parameters (i.e., a low density and high density) providing equally acceptable T_B-RMSE values. These higher R values are positively correlated with larger mass per unit volume M.

A relatively unambiguous measure of the overall retrieval is the retrieved distribution of total precipitation mass per unit volume of air (also known as ice/liquid water content), shown in figure 5.24. Like precipitation rate, a nearly bimodal distribution is observed in the retrieved mass, expressed in $\log_{10}(M)$. The second (right-most) hump is strongly associated with high precipitation rates, as is shown in figure 5.27.

The mean value for $\log_{10}(M)$ is approximately -0.7 (0.2 g m^{-3}) with a standard deviation of 0.6725 (0.04 to 1.0 g m^{-3}), which according to McFarquhar and Black (2004) is with the nominal range for stratiform precipitating clouds observed in the tropics. Schols et $al.$ (1999) found that ice water contents (mass of ice per unit volume) were less than 0.2 g m^{-3} for frozen stratiform precipitation (above the melting layer), and less than 3.0 g m^{-3} for a frozen precipitation in an intense squall line in the middle of a North-Atlantic cyclone.

Figures 5.25 shows the retrieved N_0 and liquid equivalent precipitation rate (at all vertical levels) as a function of the particle density ρ_{snow} depicted by the the color bar. Both N_0 and precipitation rate cover a large range of variability. The particle density influence is also evident, but much less clearly defined. The highest precipitation rates appear to be associated with the largest N_0 values, consistent with equation 2.34.

Figure 5.26 indicates a much less cohesive relationship between the precipitation rate and the liquid equivalent diameter, D_0. The density dependence is still evident.
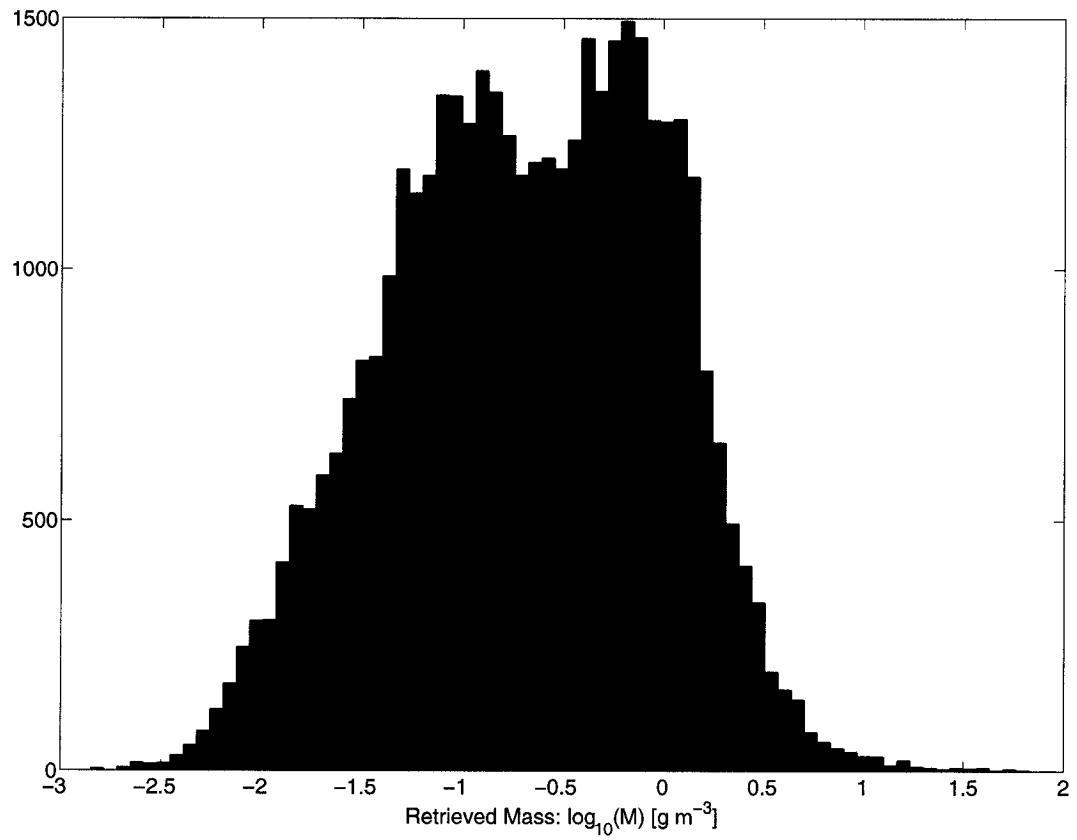
Figure 5.24. 29 January 2003: Histogram of retrieved mass (per unit volume of air) M [g m^{-3}] for the T_B-constrained case.

Figure 5.25. 29 January 2003: Scatterplot of N_0 vs. precipitation rate for the T_B-constrained case. Color variations are represented by the snow particle density, ρ_{snow}.

Figure 5.26. 29 January 2003: Scatterplot of D_0 [mm] vs. precipitation rate for the T_B-constrained case. Color variations are represented by the snow particle density, ρ_{snow}.

In figure 5.27, the retrieved mass per unit volume is plotted vs. retrieved precipitation rate. There is a strong positive correlation between mass and precipitation rate (as noted previously), with the largest mass values being associated with the highest precipitation rates. If one selects a nominal precipitation rate of 1 mm h^{-1}, nearly the entire range of particle densities is covered, while the range of masses per unit volume covers a relatively small range from about 0.02 to 0.2 g m^{-3}, depending on the particle density.

Figure 5.28 shows the relationship between D_0 and N_0. Colors indicate the density variations, and it's clear that there is a dependence in both parameters, slightly stronger in the N_0 parameter. Inspection of the equation for retrieving N_0 (eq. 3.9) shows that there's a primary dependence on the single channel radar reflectivity, which itself is sensitive to changes in particle density.

Figures 5.29 and 5.30 show the relationships between the radar reflectivities (attenuation corrected), and the liquid equivalent precipitation rate. The colors represent N_0. Of note is the strong N_0 dependence in these relationships, with the highest precipitation rates corresponding to highest N_0 and reflectivity values.

Many of the above scatterplots simply show relationships that are already known from the relationships provided by the forward model and retrieval algorithm. However, of interest is not necessarily the relationships, but the *range and distribution* of the T_B-constrained retrieved properties, especially N_0 and D_0. With the above dataset, we now have a reasonable estimate of the expected range of relevant particle size distribution parameters (if one assumes an exponential distribution). If the particle composition/densities were are able to be estimated prior to the retrieval (e.g., using aircraft
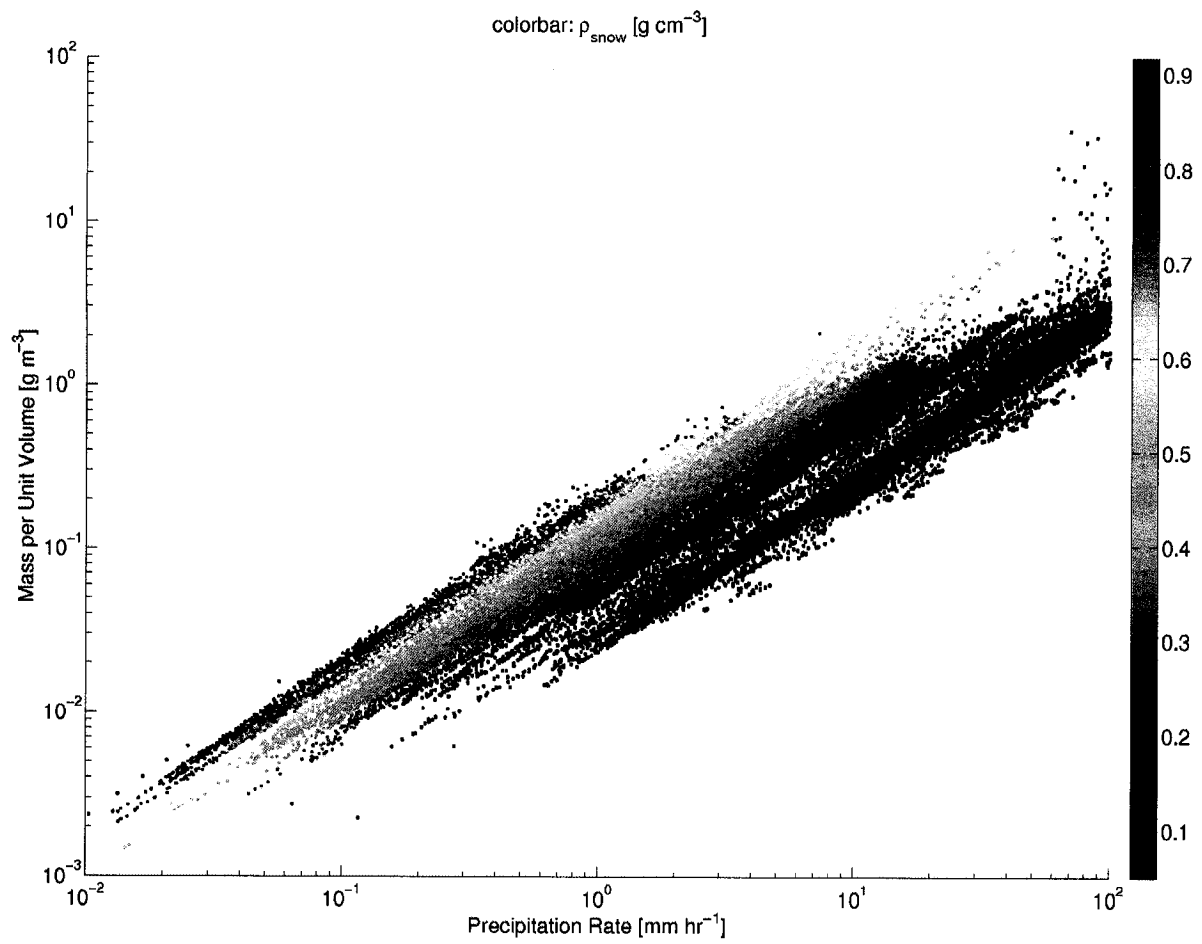
Figure 5.27. 29 January 2003: Scatterplot of liq. equiv. precipitation rate R vs. mass per unit volume, M, for the T_B-constrained case. Color variations are represented by the snow particle density, ρ_{snow}.
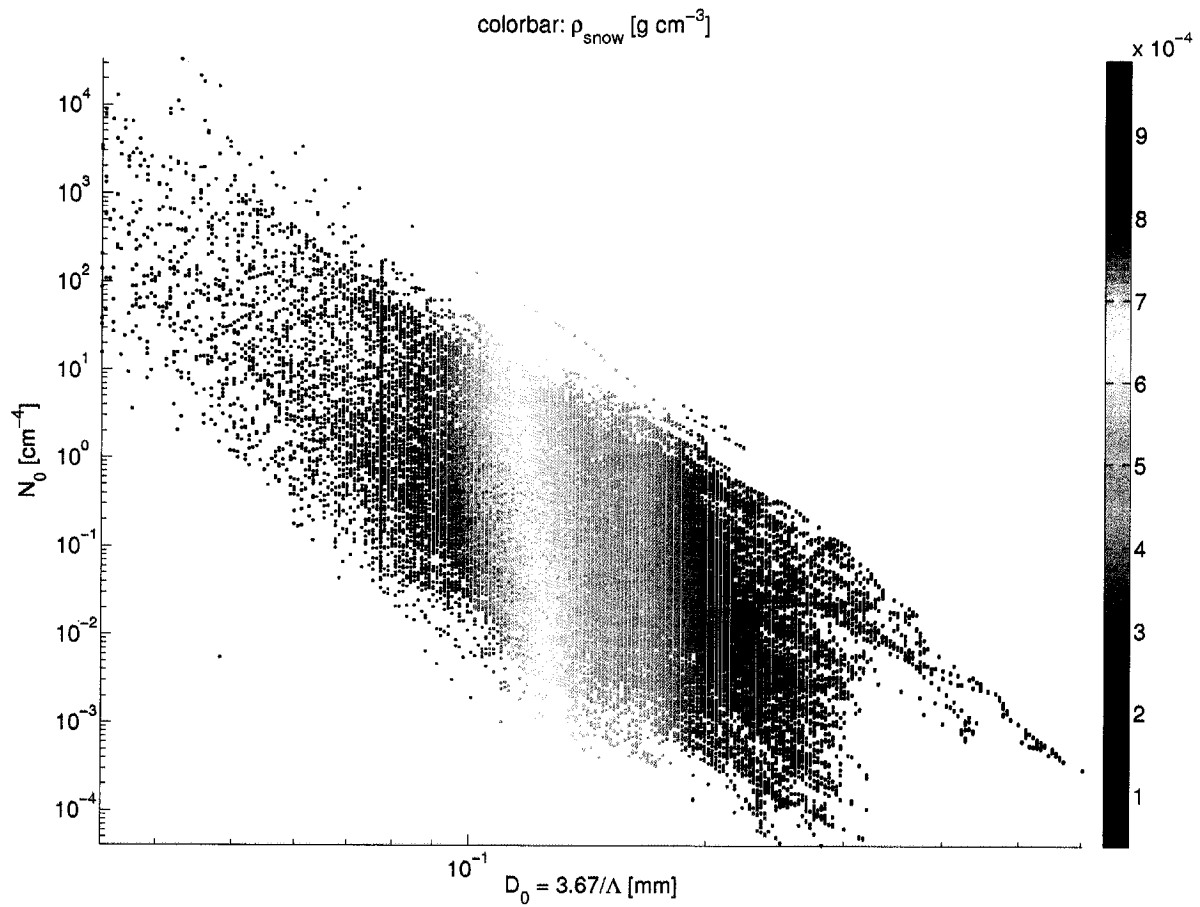
Figure 5.28. 29 January 2003: Scatterplot of N_0 vs. D_0 for the T_B-constrained case. Color variations are represented by the snow particle density, ρ_{snow}.
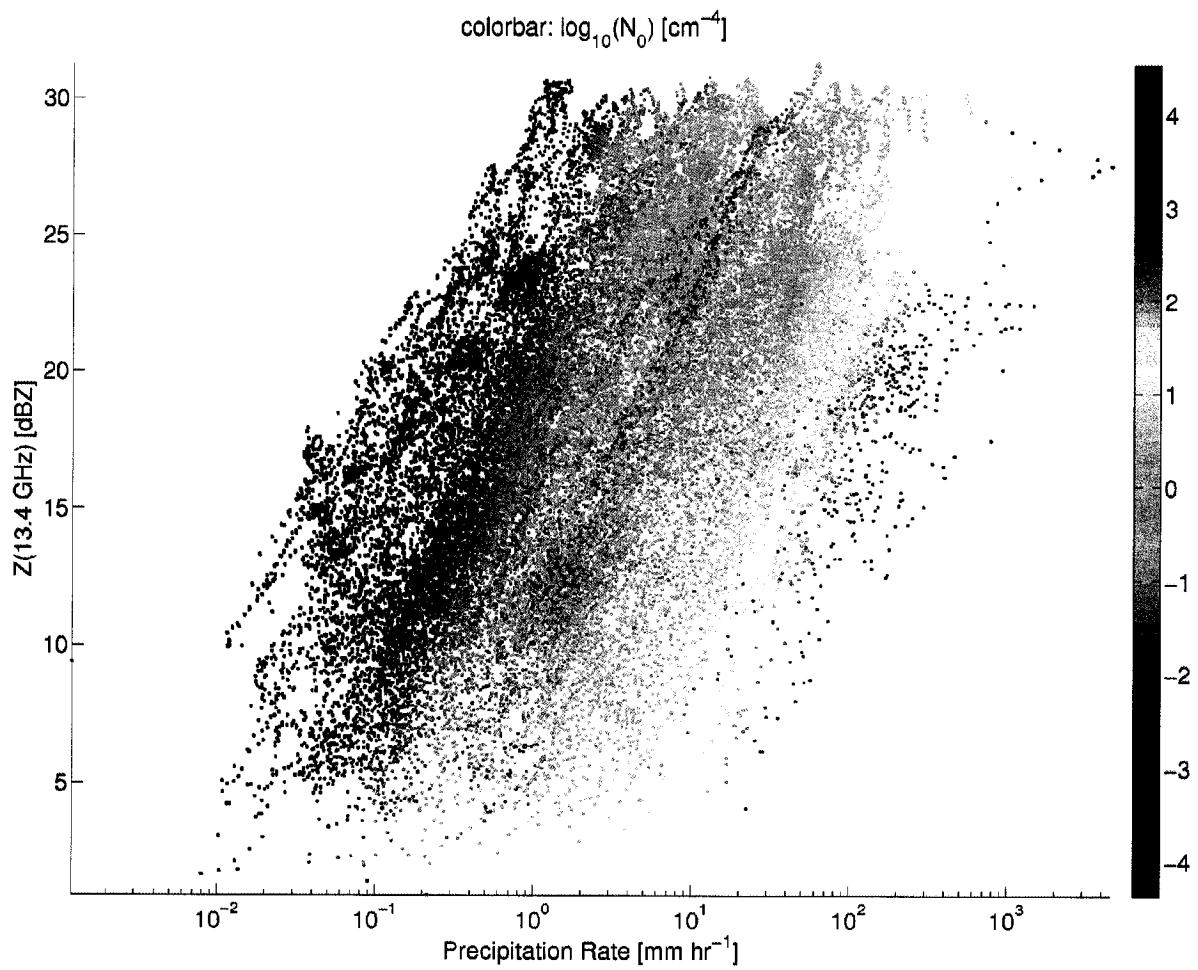
Figure 5.29. 29 January 2003: Scatterplot of Z_{14} vs. precipitation rate for the T_B-constrained case. Color variations are represented by N_0.
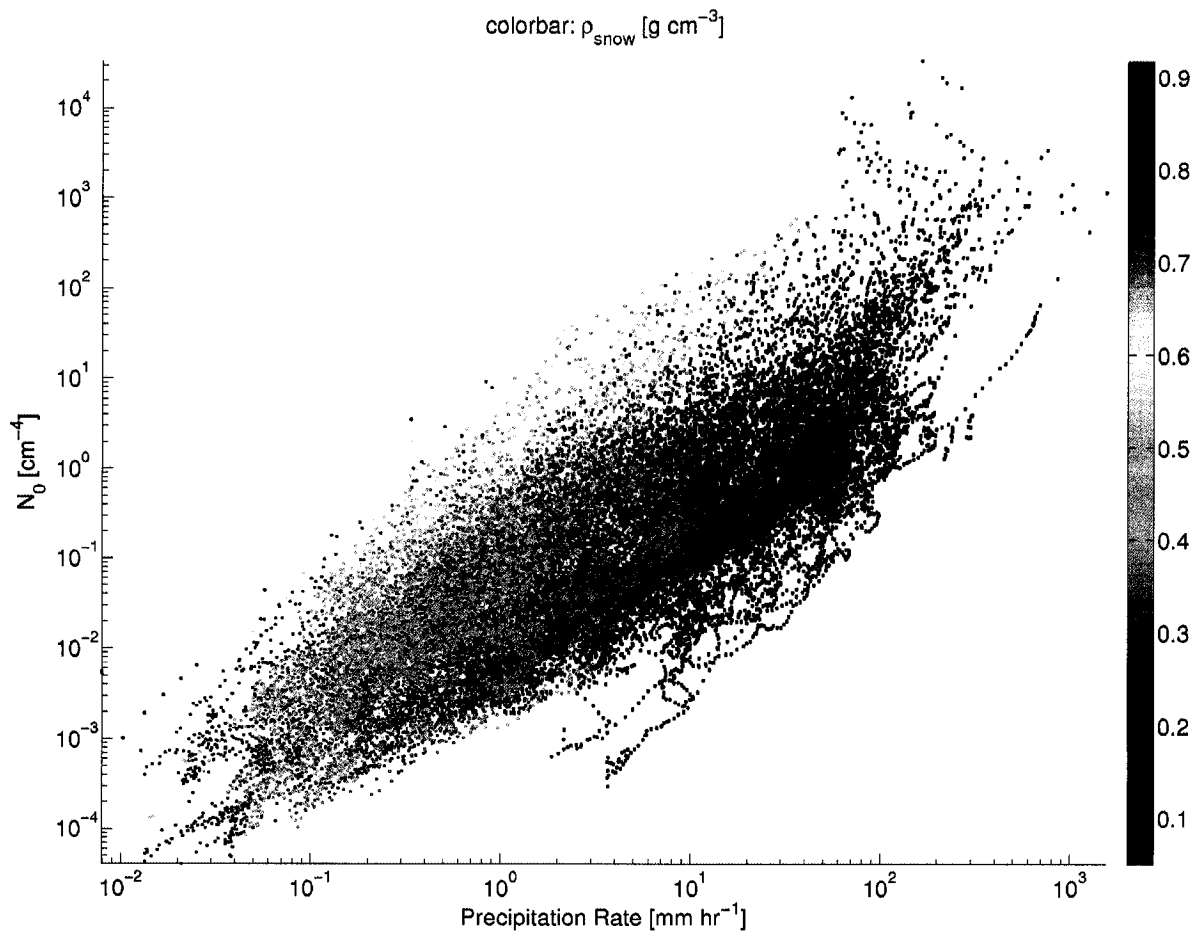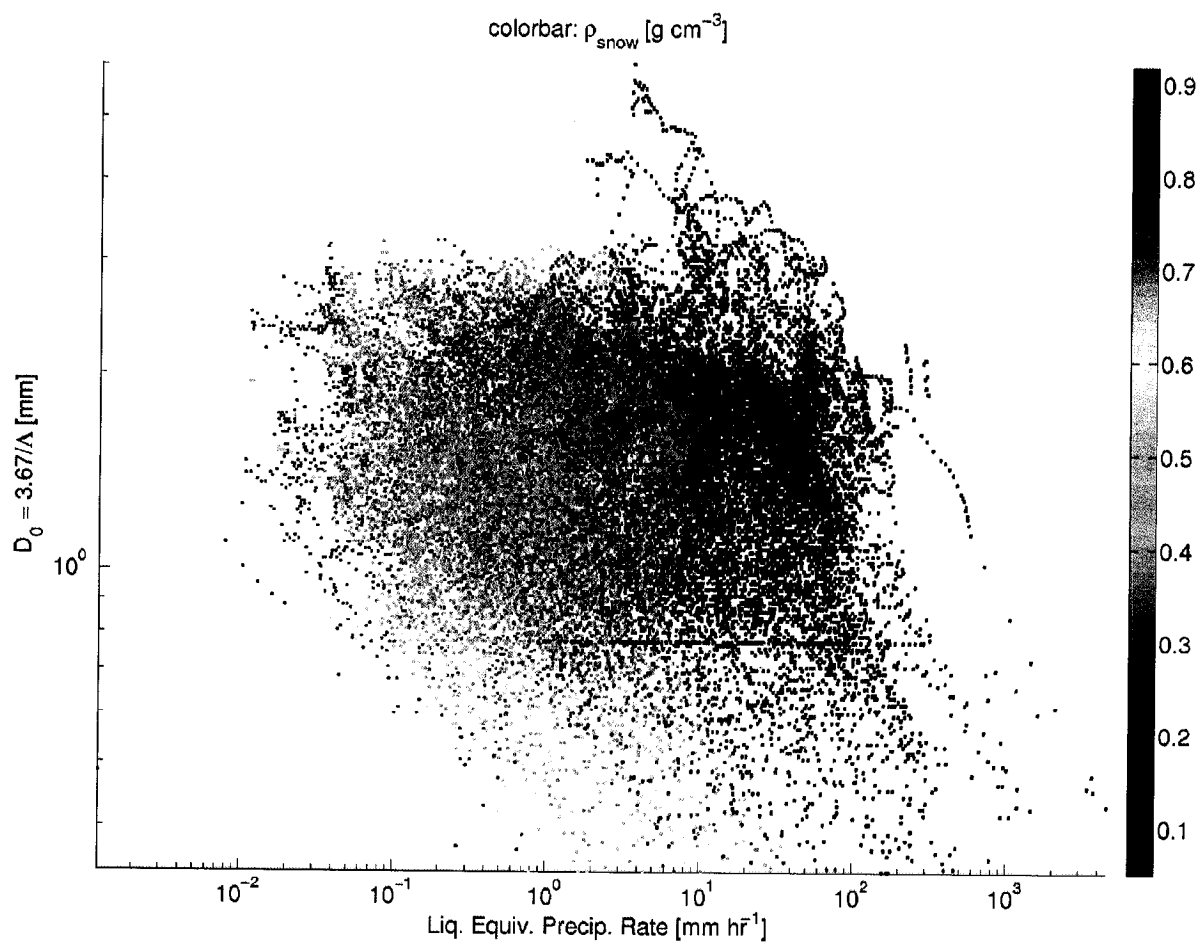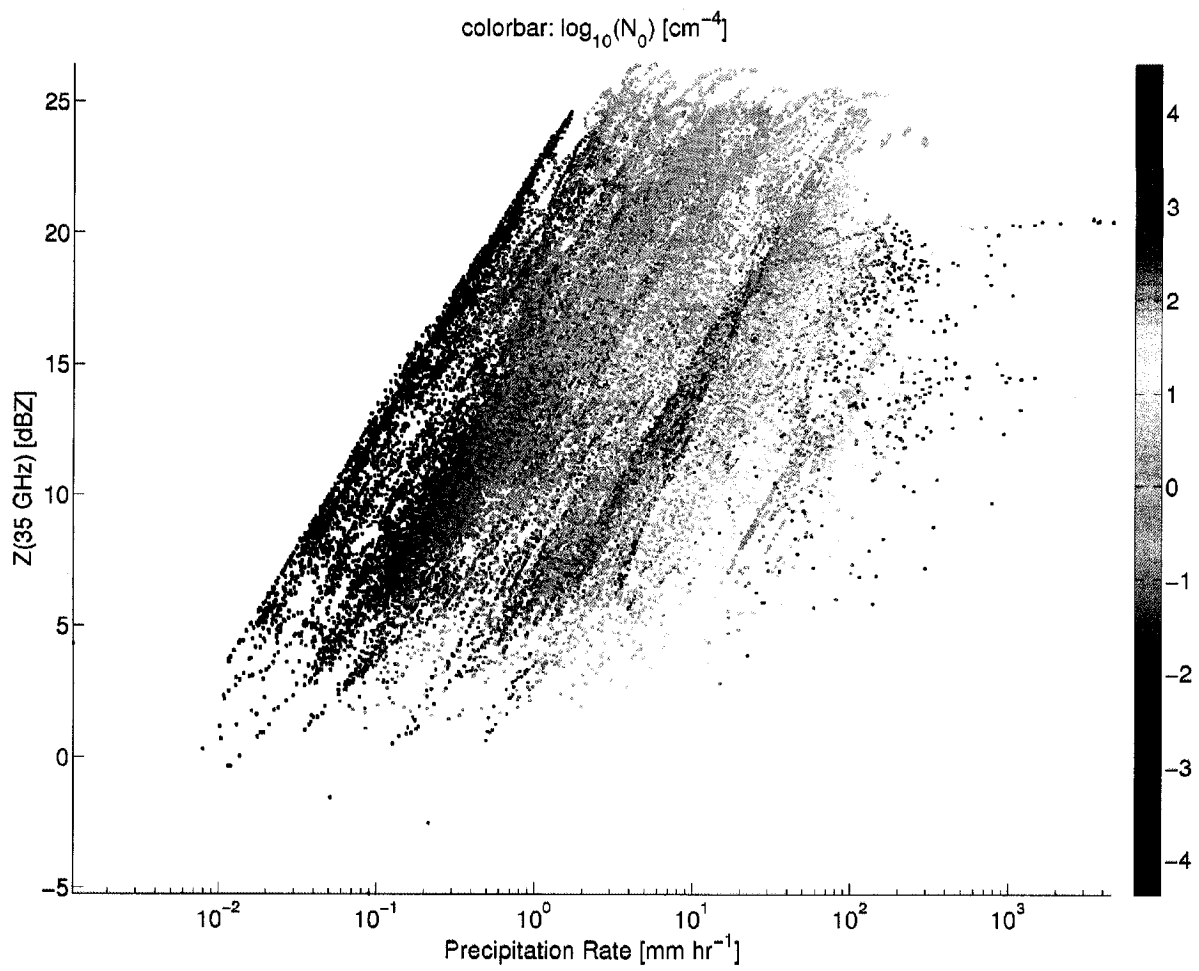
Figure 5.30. 29 January 2003: Scatterplot of Z_{35} vs. precipitation rate for the T_B-constrained case. Color variations are represented by N_0.

or ground based observations), this would provide a much stronger constraint on the retrieval.

5.4 Summary

In this chapter, the 2003 Wakasa Bay field experiment was described, including instrumentation and relevant data collection procedures. The techniques for data rejection and acceptance were also outlined. On 29 January 2003, the P-3 aircraft made observations of several snow events; and data from the APR-2 radar and co-located MIR radiometer was used as a test-case for the present retrieval method.

It was found that selecting a fixed density value for the snow particles of (n_ρ =10 (0.45 to 0.6 g cm^{-3}) resulted in the closest match to published Z_{35}-R relationships from Noh *et al.* (2006). The simulated vs. observed T_Bs for this single density profile case exhibited a mean RMSE on the order of 5 K, with several regions crossing above 10 K RMSE mark. This indicated that either the Z_{35}-R relationship does not strictly apply to the current observations, or that there some sort of bias in the three-way relationship between simulation, radar observation, and radiometer observation.

In order to further constrain the retrieval and better select the appropriate density parameters, the T_B-constraint method was applied to the 450,000 candidate profiles, obtained from the DWR-method, in an attempt to constrain the parameter space and number of retrieved profiles for this case study. It was found that the "best-fit" case provided a wide variety results in retrieved properties, mostly due to the lack of particle density information.

The real utility of the T_B-constraint method lies in not what it provides, but what it leaves out. From the 450,000 candidate profiles, the basic T_B-constraint requirement of a

maximum 10 K RMSE across all scans reduced the number of profiles to approximately 63,000, thereby eliminating a large number of profiles which did not fit into the three-way relationship.

An example case for "subjective" constraints was examined. The results indicate that additional constraints to the T_B RMSE value results in a more compact agreement among the ranges of retrieved parameters N_0 and Λ, although it appears that additional information is required to have a stronger constraint on the retrieval. One such piece of information would be cloud liquid water content and, more preferably, an estimate of the particle density, which would help significantly in nailing down the potential variations in the retrieval.

Using the subjective T_B constraints, the relationships between key variables: size distribution parameters N_0 and D_0, precipitation rate, particle density ρ_{snow}, mass per unit volume M, the radar dual wavelength ratio (DWR), and the radar reflectivities themselves (Z_{14} and Z_{35}) were shown. The distribution of retrieved properties, compared with previously published values indicate that the retrieval is generally providing consistent reasonable ranges of values. The presence of unrealistically high precipitation rates (ι 50 mm h^{-1}) indicates that the combined retrieval does not quite remove all of the physically unrealistic profiles. In order to accomplish a more precise retrieval, additional observational constraints are required.

6 SUMMARY AND CONCLUSION

Accurate local measurement of precipitation is a critical component of understanding the larger-scale water, energy, and climate across the entire globe. The present research has described a method for combining passive microwave (PMW) observations and active radar observations to retrieve snow particle size distribution (PSD) properties, assuming exponentially distributed particle sizes.

Specifically, a dual-wavelength ratio (DWR) retrieval technique, following Meneghini et al. (1997), was developed with the express purpose of retrieving particle exponential size distribution parameters N_0 and Λ (or D_0). The DWR method is strongly sensitive to particle size, independent of number density and physical particle composition/density. We chose to use spheres composed of ice and air to simulate actual ice-phase precipitation particles, primarily so that standard Mie-theory could be used to compute the radiometric properties of the precipitation particles. However, due to the relative insensitivity of the DWR-method to particle "density", is inherently ill-posed unless the physical composition of the ice particles (density for ice spheres) is known prior to the retrieval. To limit the density options, a set of 14 linear density profiles were selected to cover a large range of possible density configurations.

Since explicit particle shape/composition information is not generally available, an additional constraint was imposed on the DWR-retrieval technique. For each of the many DWR-retrieved profiles, the top-of-the atmosphere passive microwave brightness temperatures (T_Bs) were computed using a forward radiative transfer model, which exhibits a stronger sensitivity to particle density than the DWR-technique. The simulated

$T_B$scan then be compared to observed T_Bs, providing a stronger constraint. Presumably this would allow for a more well constrained set of retrieved profiles.

As a first step in testing the retrieval method, a series of contrived cases were created using the forward model. The forward model was used to produce a 1-D profile of ice-phase precipitation, associated radar reflectivities at 13.4 and 35.6 GHz, and top-of-the-atmosphere PMW $T_B$sat 89, 150, and 220 GHz. These simulated quantities were treated as input to the retrieval. Since the retrieval and forward model are based on the same set of physical relationships, it was expected that the retrieval method would perfectly retrieve the PSD parameters (for which the true values are known).

In the most simple contrived cases the retrieval worked flawlessly, however when random noise was added to the density profile, the retrieval was no longer able to accurately retrieve the PSD properties, since it always assumes some sort of linear profile. However, using the T_B-constraint method described in section 3.4, the combined retrieval was generally able to accurately retrieve the PSD properties and provide the correct density parameter. These tests showed that the T_B-constraint approach was critical at culling out those particle density profiles which were not consistent with the radar/radiometer observations and simulated relationships.

The next step was to estimate the primary sources of uncertainty within the retrieval and observational data from the 2003 Wakasa Bay AMSR/AMSR-E ground validation experiment (WBAY03). In WBAY03, a P-3 Orion aircraft carrying a suite of instruments including the Millimeter-wave Imaging Radiometer (MIR) and the Advanced Precipitation Radar 2 (APR-2) made co-located nadir viewing observations of shallow convective snowfall events on 29 January 2003 over the Sea of Japan. These observations were consistent with the present retrieval scheme, so they were selected as

a case study. However, the uncertainties of the observations and the subsequent impact on retrievals was unknown.

To address this, the estimated uncertainty of each of the primary observations (two radar frequencies: 13.4 and 35.6 GHz, and three PMW channels: 89, 150, and 220 GHz was determined. Using sensitivity analyses, the impact of the observation uncertainties on retrieved PSD parameters was estimated. It was found that the uncertainties in the radar observations, on the order of ± 1 dBZ at 13.4 and ± 2 dBZ at 35.6 strongly influenced the retrieval, being a factor of 10 larger than the uncertainties arising from PMW and radiosonde observations.

A simple radar-only retrieval on the WBAY03 29 January 2003 snowfall case (section 5.3) involves simply selecting a fixed density parameter, and performing the DWR-only retrieval. For DWR values less than unity (and greater than about 0.1-0.2), and a fixed particle density, a monotonic relationship exists between the mass-weighted median diameter D_0 and the DWR. By comparison with a published Z_{35}-R relationship (Noh et al., 2006), a linear density profile of (0.1 to 0.4 g cm^{-3}, n_ρ =5) was found to provide a similar fit for many of the 450 observed profiles of radar data. However, subsequent T_B computations showed that the root-mean-square error (RMSE) between observed and simulated T_Bs was rather large, having an average of approximately 5 K for the entire flight segment, with some individual RMSE values higher than 10 K.

Given the large uncertainties in the radar observations, and the propagation of these uncertainties to the simulated PMW T_Bs, additional subjective constraints were deemed necessary for the retrievals performed on the WBAY03 datasets. In order to provide a more constrained retrieval, the RMSE criterion was reduced from 10 K (obtained via sensitivity analysis, chapter 4), to a floating value of 2.5 K plus the minimum RMSE

for all profiles at a given scan. The maximum of 10 K was still held. This provided a 94% reduction in the number of candidate profiles from 450,000 using the DWR-only retrieval, to 17,500 T_B-constrained profiles. These profiles were selected as the "solutions" to the retrieval in that they exhibited consistency with both observation and simulation.

Despite the strong constraints, the quantities still represented a diverse range of retrieved and derived parameters. Figures 5.21 through 5.30 attempted to capture the key features of the retrieved properties for the entire dataset. In spite of a small fraction of physically implausible values, the retrieved dataset was found to be consistent with published ranges of the relevant quantities.

In short, the primary utility of the present combined radar-radiometer algorithm is that it selects sets of "candidate" profiles of PSD properties which have radar and radiometric consistency with observations, and is consistent with the physical relationships employed by the forward model and retrieval algorithm. When the composition of the particle can be known or estimated *a priori*, the retrieval becomes much more well posed.

A primary goal of the present research was to develop and test a retrieval method for instrumentation similar to what is proposed for the upcoming Global Precipitation Measurement Mission (GPM). GPM will contain a dual-wavelength radar (at 14 and 35 GHz), and a co-located passive microwave radiometer. However, GPM differs from the present observations in that the GPM GMI radiometer is conically scanning, offset from nadir at an angle of approximately 52 degrees, rather than viewing at nadir like the MIR does. However, using techniques developed for the Tropical Rainfall Measurement Mission (TRMM) spacecraft, these geometry issues can be addressed. Regardless, the

same physical principles in the retrieval will apply. There will also be a further key advantage to using the GPM PMW T_Bs in that the conically scanning observations, over ocean, have polarization information, which is useful for determining the optical depth of a precipitating cloud.

A APPENDIX

A.1 Dielectric Mixing

In order to satisfy the homogeneity requirement for the dielectric constant of a simulated 2 or 3 component particle, methods for averaging the dielectric properties of these components are required. They are described here and in section 2.8.

A.1.1 Two-Component Dielectric Mixing

The Bruggeman method (Bruggeman, 1935) has the following form

$$f_1 \frac{\epsilon_1 - \epsilon_{\langle 1\,2\rangle}}{\epsilon_1 + 2\epsilon_{\langle 1\,2\rangle}} + (1 - f_1) \frac{\epsilon_2 - \epsilon_{\langle 1\,2\rangle}}{\epsilon_2 + 2\epsilon_{\langle 1\,2\rangle}} = 0, \tag{A.1}$$

where ϵ_1 is the dielectric permittivity of component 1, ϵ_2 is the dielectric permittivity of component 2, $\epsilon_{\langle 1\,2\rangle}$ is the effective dielectric permittivity of the two materials, and f_1 is the volume fraction of material 1.

Algebraic manipulation of (A.1) yields an equation with the form

$$\epsilon_{\langle 1\,2\rangle} = -\frac{1}{2}\beta_0 + \frac{1}{2}\left(\beta_0^2 + 2\epsilon_2\epsilon_1\right)^{\frac{1}{2}}, \tag{A.2}$$

where

$$\beta_0 = \frac{1}{2}\left[(1 - 3(1 - f_1))\epsilon_2 + (1 - 3f_1)\epsilon_1\right]. \tag{A.3}$$

The Maxwell Garnett method (Maxwell Garnett, 1904) for two components is written as

$$\epsilon_{\langle 1\,2\rangle} = \epsilon_2 \left[1 + \frac{3f_1(\epsilon_1 - \epsilon_2)/(\epsilon_1 + 2\epsilon_2)}{1 - f_1(\epsilon_1 - \epsilon_2)/(\epsilon_1 + 2\epsilon_2)}\right]. \tag{A.4}$$

In the complex plane, figure A.1 illustrates the effects of the permutations on the real and imaginary components of the dielectric permittivity for continuously varying fractions of ice and water (e.g., a melting particle) at 10.65 GHz and 89.0 GHz and a temperature of $0°$ C. Each curve represents the application of the three permutations of the two-component averaging methods. Figure A.2 shows the dielectric permittivity's dependence on averaging method for varying fractions of ice and air (e.g., a frozen particle).

A.1.2 Extension to Three Components

Both the Bruggeman and Maxwell Garnett methods may be extended to three components by applying the two-component form once for the first two components and again for the two-component mixture and the third component. A volume fraction is defined for the first two components 1 and 2

$$f_1 = F_1/(F_1 + F_2), \tag{A.5}$$

where f_1 is the volume fraction of component 1. For the two-component form, the denominator is unity. The second volume fraction, for components 1 and 2 mixed with component 3, is given by

$$f_{\langle 1\,2 \rangle} = F_1 + F_2. \tag{A.6}$$

For the MG method, applying the similar technique results in two possible sets of combinations. The first set is the "two-component inclusion" method

$$\epsilon_{\text{av}} = \epsilon_3 \left[1 + \frac{3 f_{\langle 1\,2 \rangle} \left(\epsilon_{\langle 1\,2 \rangle} - \epsilon_3 \right) / \left(\epsilon_{\langle 1\,2 \rangle} + 2\epsilon_3 \right)}{1 - f_{\langle 1\,2 \rangle} \left(\epsilon_{\langle 1\,2 \rangle} - \epsilon_3 \right) / \left(\epsilon_{\langle 1\,2 \rangle} + 2\epsilon_3 \right)} \right]. \tag{A.7}$$
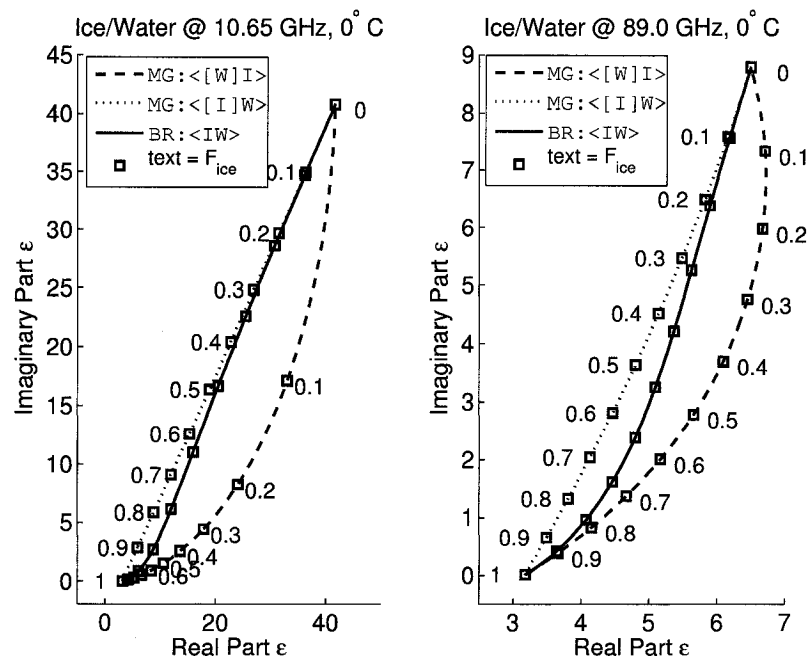
Figure A.1. Real and imaginary components of the dielectric permittivity of a melting particle for varying volume fractions of ice and water at 10.65 GHz and 89.0 GHz at 0° C. Text labels indicate F_{ice}, where $F_{\text{ice}} + F_{\text{liq}} = 1$ at all points.
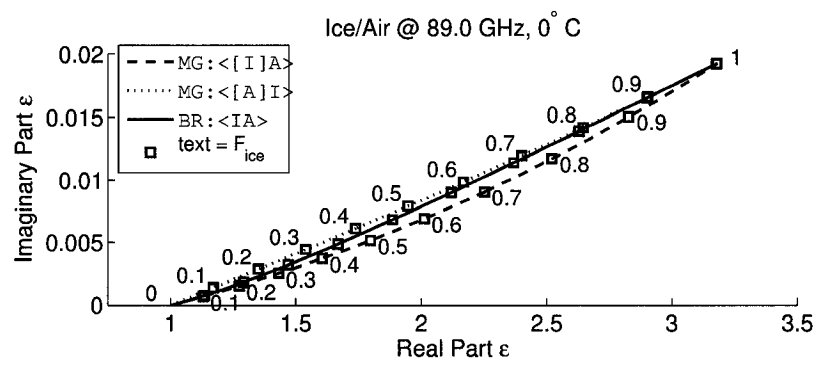
Figure A.2. Real and imaginary components of the dielectric permittivity of a frozen particle for varying volume fractions of ice and air at 10.65 GHz and 89.0 GHz at 0° C. Text labels indicate $F_{\rm ice}$, where $F_{\rm ice} + F_{\rm air} = 1$ at all points.

Alternatively, the intermediate value $\epsilon_{\langle 1\,2\rangle}$ can be used as the outer matrix, with component 3 as the inclusion. The "two-component matrix" method is written

$$\epsilon_{\mathrm{av}} = \epsilon_{\langle 1\,2\rangle}\left[1 + \frac{3\,f_3\left(\epsilon_3 - \epsilon_{\langle 1\,2\rangle}\right)/\left(\epsilon_3 + 2\epsilon_{\langle 1\,2\rangle}\right)}{1 - f_3\left(\epsilon_3 - \epsilon_{\langle 1\,2\rangle}\right)/\left(\epsilon_3 + 2\epsilon_{\langle 1\,2\rangle}\right)}\right] \tag{A.8}$$

The asymmetrical nature of the MG form leads to a different set of dielectric permittivities depending on the ordering of components 1, 2, and 3. In total there are twelve possible permutations for MG three-component mixing: six for the "two-component inclusion" variations, and six for the "two-component matrix" variations. Table A.1 provides a summary of the computationally distinct permutations.

A similar approach for the Bruggeman method results in

$$\epsilon_{\mathrm{av}} = -\frac{1}{2}\beta + \frac{1}{2}\left(\beta^2 + 2\epsilon_3\epsilon_{\langle 1\,2\rangle}\right)^{\frac{1}{2}}, \tag{A.9}$$

where

$$\beta = \frac{1}{2}\left[\left(1 - 3\left(1 - f_{\langle 1\,2\rangle}\right)\right)\epsilon_3 + \left(1 - 3f_{\langle 1\,2\rangle}\right)\epsilon_{\langle 1\,2\rangle}\right].$$

As shown by Meneghini and Liao (2000), the Bruggeman mixing formula for three components has an order dependence, despite the symmetry of the two-component form. Specifically, swapping components 1 and 2 in (A.9) does not affect the result. However, swapping 1 with 3 or 2 with 3 in (A.9) does affect the mixture, resulting in three permutations of the Bruggeman mixing formula in the case of three dielectric material components.

Table A.1

Maxwell Garnett (MG) and Bruggeman (BR) combinations for water (W), ice (I), and air (A) mixtures. Column 1 consists of the two-component mixture as the inclusion in the third component matrix. Column 2 has the single component in a two-component mixture matrix. Angle brackets denote a two-component mixture with square brackets representing the inclusion.

MG		Bruggeman
$\langle[\text{W}]\text{I}\rangle\text{A}$	$\text{W}\langle[\text{I}]\text{A}\rangle$	
$\langle[\text{I}]\text{W}\rangle\text{A}$	$\text{I}\langle[\text{W}]\text{A}\rangle$	$\langle\text{WI}\rangle\text{A}$
$\langle[\text{W}]\text{A}\rangle\text{I}$	$\text{W}\langle[\text{A}]\text{I}\rangle$	
$\langle[\text{A}]\text{W}\rangle\text{I}$	$\text{A}\langle[\text{W}]\text{I}\rangle$	$\langle\text{AW}\rangle\text{I}$
$\langle[\text{I}]\text{A}\rangle\text{W}$	$\text{I}\langle[\text{A}]\text{W}\rangle$	
$\langle[\text{A}]\text{I}\rangle\text{W}$	$\text{A}\langle[\text{I}]\text{W}\rangle$	$\langle\text{IA}\rangle\text{W}$

Symmetric Bruggeman Formula

To address the asymmetry in the successive application method for the Bruggeman formula, we propose a logical extension of (A.1) to include three dielectric components

$$f_1 \left(\frac{\epsilon_1 - \epsilon_{av}}{\epsilon_1 + 2\epsilon_{av}} \right) + f_2 \left(\frac{\epsilon_2 - \epsilon_{av}}{\epsilon_2 + 2\epsilon_{av}} \right) + \tag{A.10}$$

$$(1 - f_1 - f_2) \left(\frac{\epsilon_3 - \epsilon_{av}}{\epsilon_3 + 2\epsilon_{av}} \right) = 0 \tag{A.11}$$

where ϵ_{av} is the effective dielectric permittivity. It is easy to verify that interchanging constituents has no effect on ϵ_{av}. We conjecture that this is the general symmetric form for the three-component Bruggeman formula. This suggests that, by following the same logic, the form can be extended to N dielectric components. However, a solution for ϵ_{av} may not be easy to compute for $N > 4$ constituents.

Seeking to solve (A.10) explicitly for ϵ_{av}, we rewrite it in the form of a cubic equation

$$a_3 \epsilon_{av}^3 + a_2 \epsilon_{av}^2 + a_1 \epsilon_{av} + a_0 = 0, \tag{A.12}$$

where algebraic manipulation of (A.10) yields the polynomial coefficients

$$a_3 = 1 \tag{A.13}$$

$$a_2 = \frac{1}{2} (\epsilon_1 + \epsilon_2 - 2\epsilon_3) + \frac{1}{2} f_1 (-3\epsilon_1 + 3\epsilon_3) + \frac{1}{2} f_2 (-3\epsilon_2 + 3\epsilon_3)$$

$$a_1 = \frac{1}{4} (\epsilon_1 \epsilon_2 - 2\epsilon_1 \epsilon_3 - 2\epsilon_2 \epsilon_3) + \tag{A.14}$$
$$\frac{1}{4} f_1 (-3\epsilon_1 \epsilon_2 + 3\epsilon_2 \epsilon_3) + \frac{1}{4} f_2 (-3\epsilon_1 \epsilon_2 + 3\epsilon_1 \epsilon_3)$$

$$a_0 = -\frac{1}{4} \epsilon_1 \epsilon_2 \epsilon_3. \tag{A.15}$$

If we further define

$$p = \frac{3a_1 - a_2^2}{3}, \tag{A.16}$$

$$q = \frac{9a_1 a_2 - 27a_0 - 2a_2^3}{27};$$ (A.17)

one root of (A.10) can be expressed as

$$\epsilon_{\mathrm{av}} = w - \frac{p}{3w} - \frac{1}{3}a_2,$$ (A.18)

where

$$w = \sqrt[3]{\frac{1}{2}\left(q + \sqrt{q^2 + \frac{4}{27}p^3}\right)}.$$ (A.19)

Of six possible solutions in w (only one shown here), this one was chosen such that the one complex root having both positive real and imaginary components is obtained, consistent with the constituent permittivities. Although the expression is somewhat cumbersome, it has the desirable advantage of being easily programmable. Unfortunately, there does not appear to be a reasonably simple closed-form expression for ϵ_{av} for the general case of N constituents.

A.2 Code

In creating the forward model and retrieval algorithm, over 10,000 lines of customized code were created. Several times that many were borrowed from existing subroutines. The programs and subroutines used in the present research were primarily written in Fortran 90/95. Several Matlab scripts were created to aid in the analysis and processing of the aircraft data and retrieval results. The relevant set of Fortran codes, Matlab scripts, and datafiles are available (subject to copyright) online at:

http://rain.aos.wisc.edu/MWWiki/index.php/JbenJam:Dissertation

A.3 Additional Technical Details

This section contains the miscellaneous technical details that did not comfortably fit into the regular chapters in the dissertation. Nevertheless they provide important information required to reproduce and clearly understand the concepts presented in the main body.

A.3.1 APR-2 Data Format

Each WBAY03 APR-2 data-file is organized on a flight segment-by-segment basis. Tables A.2 and A.3, reproduced from `http://nsidc.org/data/docs/daac/nsidc0195_rainfall_wakasa_apr2.gd.html`, contain the details of the data format for a given flight segment file, where

- `nscan` is the number of scans in a file;

- `nray` is the number of rays, or beams, within a cross-track scan;

- and `nbin` is the number of bins within a ray.

The altitude and look vector are provided in two estimates: `alt_nav` and `look_vector` items are calculated based on the aircraft navigation information, but `alt_radar` and `look_vector_radar` are calculated based on the observed surface return in APR-2 data. The latter pair is reliable only when flying over the ocean, as it provides a more accurate geolocation than the navigation-based pair. The look vector is a 3-element vector of direction of the antenna relative to a global coordinate system where x is along the aircraft ground track and z is vertical.)

Table A.2

APR-2 data format, part 1, aircraft and geolocation information

Name	Format	Size	Notes
fileheader	int32	18	
scantime	int32	nscan × nray	Beginning of scan in seconds since 1 January 1970
scantimus	int32	nscan × nray	Beginning of scan; microseconds past scantime
lat	float	nscan × nray	From P-3 navigation files
lon	float	nscan × nray	From P-3 navigation files
roll	float	nscan × nray	From P-3 navigation files
pitch	float	nscan × nray	From P-3 navigation files
drift	float	nscan × nray	From P-3 navigation files
alt_nav	float	nscan × nray	From P-3 navigation files (meters)
alt_radar	float	nscan × nray	From APR-2 surface echo (meters)
look_vector	double	nscan × nray × 3	From P-3 navigation files
look_vector_radar	double	nscan × nray × 3	From APR-2 surface echo
range0	float	nscan × nray	Distance of the first radar range bin from aircraft
isurf	int32	nscan × nray	Index of radar range bin intersecting surface (starting from 0).
sequence	int32	nscan × nray	Ray number within the file
v_surfdc8	float	nscan × nray	Apparent surface Doppler velocity as estimated from P-3 navigation
v_surf	float	nscan × nray	APR-2 measured surface Doppler velocity
beamnum	float	nscan × nray	Ray number within a scan
surface_index	float	nscan × nray	Preliminary surface classification index

Table A.3

APR-2 data format, part 2, reflectivity data

Name	Format	Size	Notes
zhh14	int16	nscan × nray × nbin	Radar Reflectivity at K_u-band (scaled dBZ, scaling factor is given in file header)
zhh35	int16	nscan × nray × nbin	Radar Reflectivity at K_a-band (scaled dBZ, scaling factor is given in fileheader)
ldr14	int16	nscan × nray × nbin	Linear Depolarization Ratio at K_u-band (scaled dB, scaling factor is given in fileheader)
vel14	int16	nscan × nray × nbin	Doppler Velocity at K_u-band (scaled m s^{-1}, scaling factor is given in fileheader)

The `surface_index` is estimated by analyzing APR-2 surface return. Roughness, angle dependence of the surface normalized radar cross section, apparent surface inclination, and LDR at nadir contribute to the surface return (Tanelli *et al.*, 2006). `surface_index` assumes one of six values listed in table A.4. In the present research, only the observations having a `surface_index` = 1 are used to ensure reasonably level flight over ocean.

A.3.2   MIR Data Format

The MIR data sets are stored in binary files. All values are in four-byte IEEE floating point. Each logical record contains one calibrated MIR scan. Each logical record has a length of 4 bytes-per-word and 579 words of data. For the sake of compactness, only the relevant variables are described here, the remainder of the information is located to appendix A.3 for completeness.

Table A.4

APR-2 surface_index values used as a preliminary classification of surface type.

surface_index	Description
0	Rough land
1	Ocean (level flight)
2	Ocean (roll maneuver)
3	Flat land (level flight)
4	Flat land (rolling maneuver)
5	Antenna not scanning (unknown surface)

Table A.5

MIR data format, part 1, aircraft and geolocation information

Word #	Description	Notes/Units
1	Record Number	
2	Month	Real time clock (RTC)
3	Day	Real time clock (RTC)
4	Hour	IRIG
5	Minute	IRIG
6	Second	IRIG
7	Julian Day	Navigation
8	Hour	Navigation
9	Minute	Navigation
10	Second	Navigation
11	Latitude	Degrees
12	Longitude	Degrees (-West, +East)
13	Air Temperature	°C
14	Altitude	feet
15	Pitch	Degrees (+ for nose down)
16	Roll	Degrees (+ for roll right)
17	Heading	Degrees

Table A.6

MIR data format, part 2, calibration information

Word #	Description
18–26	HouseKeeping Temperatures
27	Hot average temperature for this scan
28	Cold average temperature for this scan
29	Hot temperature, 8-scan moving average
30	Cold temperature, 8-scan moving average
31–39	Hot average counts for this scan
40–48	Cold average counts for this scan
49–57	Hot counts, 8-scan moving average
58–66	Cold counts, 8-scan moving average

Table A.7

MIR Data Format, Part 3, brightness temperature observations.

Word #	Description
67-123	57 brightness temperatures degrees Kelvin at 89 GHz
124-180	57 brightness temperatures degrees Kelvin at 150 GHz
181-237	57 brightness temperatures degrees Kelvin at 183.3 ± 1 GHz
238-294	57 brightness temperatures degrees Kelvin at 183.3 ± 3 GHz
295-351	57 brightness temperatures degrees Kelvin at 183.3 ± 7 GHz
352-408	57 brightness temperatures degrees Kelvin at 220 GHz
409-465	unused
466-522	57 brightness temperatures degrees Kelvin at 340 GHz

LIST OF REFERENCES

Adler, R., G. J. Huffman, A. Chang, R. Ferraro, P. Xie, J. Janowiak, B. Rudolf, U. Schneider, S. Curtis, D. Bolvin, A. Gruber, J. Susskind, and . P. Arkin, 2003: The version-2 Global Precipitation Climatology Project (GPCP) monthly precipitation analysis (1979-present). *J. Hydrometeor.*, **4**(6), 1147–1167.

Adler, R. F., C. Kidd, G. Petty, M. Morrissey, and H. M. Goodman, 2001: Intercomparison of global precipitation products: The Third Precipitation Intercomparison Project (PIP-3). *Bull. Amer. Meteorol. Soc.*, **82**(7), 1377–1396.

Atlas, D., 1990: *Radar in Meteorology: Battan Memorial and 40th Anniversary Radar Meteorology Conference*. American Meteorological Society, Boston, 1st edn.

Barrett, C. K. D., E. C.; Kidd, 10-14 Jul. 1995: The first WetNet Precipitation Intercomparison Project (PIP-1): reflections on the results. *Geoscience and Remote Sensing Symposium, 1995. IGARSS '95. 'Quantitative Remote Sensing for Science and Applications', International*, **1**, 649–651 vol.1.

Battaglia, A., C. Kummerow, D.-B. Shin, and C. Williams, 2003: Constraining microwave brightness temperatures by radar brightband observations. *J. Atmos. Ocean. Tech.*, **20**(6), 856–871.

Bauer, P., 2001: Over-ocean rainfall retrieval from multisensor data of the Tropical Rainfall Measuring Mission. Part I: Design and evaluation of inversion databases. *J. Atmos. Ocean. Technol.*, **18**(8), 1315–1330.

Bauer, P., A. Khain, A. Pokrovsky, R. Meneghini, C. Kummerow, F. Marzano, and J. P. V. Poiares Baptista, 2000: Combined cloud–microwave radiative transfer modeling of stratiform rainfall. *J. Atmos. Sci.*, **57**, 1082–1104.

Beard, K. V. and C. Chuang, 1987: A new model for the equilibrium shape of raindrops. *J. Atmos. Sci.*, **44**(11), 1509–1524.

Bennartz, R. and G. W. Petty, 2001: The sensitivity of microwave remote sensing observations of precipitation to ice particle size distributions. *J. Appl. Meteor.*, **40**(3), 345–364.

Bohren, C. F. and D. R. Huffman, 1983: *Absorption and Scattering of Light by Small Particles*. Wiley-Interscience.

Bosilovich, M. G., S. D. Schubert, and G. K. Walker, 2005: Global changes of the water cycle intensity. *J. Climate*, **18**(10), 1591–1608.

Bruggeman, D. A. G., 1935: Berechnung verschiedener physikalischer Konstanten von heterogenen Substanzen. I. Dielektrizitatskonstanten und Leitfahigkeiten der Mischkorper aus isotropen Substanzen. *Ann. Phys.*, **24**, 636–679.

Chahine, M. T., 1992: The hydrological cycle and its influence on climate. *Nature*, **359**, 373–380.

Czekala, H. and C. Simmer, 2002: On precipitation induced polarization of microwave radiation measured from space. *Meteorologische Zeitschrift*, **11**(1), 49–60.

Ebert, E. E., M. J. Manton, P. A. Arkin, R. J. Allam, C. E. Holpin, and A. Gruber, 1996: Results from the GPCP Algorithm Intercomparison Programme. *Bull. Amer. Met. Soc.*, **77**, 2875–2887.

English, S. J. and T. J. Hewison, 1998: A fast generic millimetre-wave emissivity model. *Proceedings of SPIE*, **3503**, 22–30.

Evans, K. F. and G. L. Stephens, 1995a: Microwave radiative transfer through clouds composed of realistically shaped ice crystals. Part I: Single scattering properties. *J. Atmos. Sci.*, **52**, 2041–2057.

Evans, K. F. and G. L. Stephens, 1995b: Microwave radiative transfer through clouds composed of realistically shaped ice crystals. Part II: Remote sensing of ice clouds. *J. Atmos. Sci.*, **52**, 2058–2072.

Fabry, F. and W. Szyrmer, 1999: Modeling of the melting layer. Part II: Electromagnetics. *J. Atmos. Sci.*, **56**(20), 3593–3600.

Ferraro, R. R., F. Z. Weng, N. C. Grody, and A. Basist, 1996: An eight-year (1987-1994) time series of rainfall, clouds, water vapor, snow cover, and sea ice derived from SSM/I measurements. *Bull. Amer. Meteorol. Soc.*, **77**(5), 891–905.

Fetzer, E. J., L. M. McMillin, D. Tobin, H. H. Aumann, M. R. Gunson, W. W. McMillan, D. E. Hagan, M. D. Hofstadter, J. Yoe, D. N. Whiteman, J. E. Barnes, R. Bennartz, H. Vmel, V. Walden, M. Newchurch, P. J. Minnett, R. Atlas, F. Schmidlin, E. T. Olsen, M. D. Goldberg, S. Zhou, H. Ding, W. L. Smith, and H. Revercomb, 2003: Airs/amsu/hsb validation. *IEEE Trans. Geosci. Remote Sens.*, **41**(2), 418–431.

Gloersen, P. and F. T. Barath, 1977: A Scanning Multichannel Microwave Radiometer for Nimbus-G and SeaSat-A. *IEEE J. Ocean. Eng.*, **2**(2), 172–178.

Guillou, C., W. Ellison, L. Eymard, K. Lamkaouchi, C. Prigent, G. Delbos, G. Balana, and S. A. Boukabara, 1998: Impact of new permittivity measurements on sea surface emissivity modeling in microwaves. *Radio Sci.*, **33**(3), 649–668.

Hadamard, J., 1902: Sur les problemes aux derivees partielles et leur signification physique. Tech. Rep. 13, Princeton U. Bull.

Haddad, Z. S., E. A. Smith, C. D. Kummerow, T. Iguchi, M. R. Farrar, S. L. Durden, M. Alves, and W. S. Olson, 1997: The TRMM 'day-1' radar/radiometer combined rain-profiling algorithm. *J. Meteor. Soc. Japan*, **75**(4), 799–809.

Hansson, L. and H. Henttonen, 1985: Gradients in density variation of small rodents: the importance of latitude and snow cover. *Oecologia*, **67**, 394–402.

Hewison, T. J. and S. J. English, Jul 1999: Airborne retrievals of snow and ice surface emissivity at millimeter wavelengths. *IEEE Trans. Geosci. Rem. Sens.*, **37**(4), 1871–1879.

Heymsfield, G. M., S. W. Bidwell, I. J. Caylor, S. Ameen, S. Nicholson, W. Boncyk, L. Miller, D. Vandemark, P. E. Racette, and L. R. Dod, 1996: The edop radar system on the high-altitude nasa er-2 aircraft. *J. Atmos. Ocean Technol.*, **13**, 795–809.

Heymsfield, G. M., J. B. Halverson, and I. J. Caylor, 1999: A wintertime gulf coast squall line observed by edop airborne doppler radar. *Mon. Wea. Rev.*, **127**, 2928–2950.

Hollinger, J. P., 1971: Passive microwave measurements of sea surface roughness. *IEEE Trans. Geosci. Elect.*, **9**(3), 165–169.

Hollinger, J. P., 1989: DMSP Special Sensor Microwave/Imager calibration/validation, final report Vol. I. Tech. rep., Naval Research Laboratory, Washington, D.C.

Houze, R. A., 1989: Observed structure of mesoscale convective systems and implications for large-scale heating. *Quart. J.Roy. Meteor. Soc.*, **115**, 425–461.

Houze, R. A., 1997: Stratiform precipitation in regions of convection: A meteorological paradox? *Bull. Amer. Meteorol. Soc.*, **78**, 2179–2196.

Houze, R. A., P. V. Hobbs, P. H. Herzegh, and D. B. Parsons, 1979: Size distributions of precipitation particles in frontal clouds. *J. Atmos. Sci.*, **36**, 156–162.

Houze, R. A., Jr, 1993: *Cloud Dynamics*. Academic Press.

Huang, R. X., 1993: Real freshwater flux as a natural boundary condition for the salinity balance and thermohaline circulation forced by evaporation and precipitation. *J. Phys. Oceanogr.*, **23**, 2428–2446.

Huffman, G. J., R. F. Adler, P. Arkin, A. T. Chang, R. Ferraro, A. Gruber, J. Janowiak, A. McNab, B. Rudolph, and U. Schneider, 1997: The global precipitation climatology project (gpcp) combined precipitation dataset. *Bull. Amer. Meteor. Soc.*, **78**, 5–20.

Hulme, M., 1991: An intercomparison of model and observed global precipitation climatologies. *Geophys. Res. Lett.*, **18**, 1715–1718.

Im, E., 2003: Apr-2 dual-frequency airborne radar observations, Wakasa Bay. National Snow and Ice Data Center, Digital Media.

Im, E., S. L. Durden, Z. S. Haddad, G. Sadowy, A. Berkun, J. Huang, M. Lou, B. C. Lopez, Y. Rahmat-Samii, and S. Rengarajan, 2000: Second-generation spaceborne precipitation radar. In *Geoscience and Remote Sensing Symposium, 2000. Proceedings.* (I. . International, ed.), IGARSS 2000, pp. 1361–1363. IEEE 2000 International, IEEE, Honolulu, HI, USA.

Janssen, M. A., 1993: *An Introduction to the Passive Microwave Remote Sensing of Atmospheres*. Wiley-Interscience, New York.

Kidd, C., 1998: On rainfall retrieval using polarization-corrected temperatures. *Int. J. Remote Sens.*, **19**(5), 981–996.

Kim, M.-J., 2004: *A physical model to estimate snowfall over land using microwave measurements*. Ph.D. thesis, University of Washington, Seattle, Washington.

Kim, M.-J., 2006: Single scattering parameters of randomly oriented snow particles at microwave frequencies. *J. Geophys. Res.*, **111**(D14201), 8.

Klein, L. A. and C. T. Swift, 1977: An improved model for the dielectric constant of sea water at microwave frequencies. *IEEE Trans. Ant. Prop.*, **AP-25**(1), 104–111.

Kummerow, C. and L. Giglio, 1994: A passive microwave technique for estimating rainfall and vertical structure information from space. Part II: Applications to SSM/I data. *J. Appl. Meteorol.*, **3**(1), 19–34.

Kummerow, C., Y. Hong, W. S. Olson, S. Yang, R. F. Adler, J. McCollum, R. Ferraro, G. W. Petty, D. B. Shin, and W. T. T., 2001: The evolution of the Goddard profiling algorithm (GPROF) for rainfall estimation from passive microwave sensors. *J. Appl. Meteorol.*, **40**(11), 1801–1820.

Kummerow, C. D., 1998: Beamfilling errors in passive microwave rainfall retrievals. *J. Appl. Meteorol.*, **37**(4), 356–370.

Kummerow, C. D. and P. Poyner, 2004: The effects of rainfall inhomogeneity on climate variability of rainfall estimated from passive microwave sensors. *J. Atmos. Ocean. Tech.*, **21**(4), 624–638.

Kuo, K.-S., E. A. Smith, Z. Haddad, E. Im, T. Iguchi, and A. Mugnai, 2004: Mathematical-physical framework for retrieval of rain dsd properties from dual-frequency ku-ka-band satellite radar. *J. Atmos. Sci.*, **61**(19), 2349–2369.

Lakhtakia, A., 1998: Incremental Maxwell Garnett formalism for homogenizing particulate composite mediums. *Micro. Opt. Tech. Let.*, **17**, 276–279.

Lakhtakia, A. and B. Shanker, 1993: Beltrami fields within continuous source regions, volume integral equations, scattering algorithms, and the extended Maxwell-Garnett model. *Int. J. Appl. Electromag. in Mater.*, **4**, 65–82.

Liao, L. and R. Meneghini, 2005a: On modeling air/spaceborne radar returns in the melting layer. *IEEE Trans. Geosci. Remote*, **43**(12), 2799–2809.

Liao, L. and R. Meneghini, 2005b: A study of air/space-borne dual-wavelength radar for estimation of rain profiles. *Adv. Atmos. Sci.*, **22**(6), 841–851.

Liebe, H. J., G. A. Hufford, and T. Manabe, 1991: A model for the complex permittivity of water at frequencies below 1 THz. *Int. J. Infrared and Millimeter Waves*, **12**, 659–675.

Liou, K. N., 2002: *An Introduction to Atmospheric Radiation*. International Geophysical Series, Volume 84. Academic Press, 2nd edn.

Lipton, A. E., M. K. Griffin, and A. G. Ling, 1999: Microwave transfer model differences in remote sensing of cloud liquid water at low temperatures. *IEEE Trans. Geosci. Remote Sens.*, **37**(1), 620–623.

Liu, G., 2004: Approximation of single scattering properties of ice and snow particles for high microwave frequencies. *J. Atmos. Sci.*, **61**, 2441–2456.

Liu, G. and J. A. Curry, 1992: Retrieval of precipitation from satellite microwave measurement using both emission and scattering. *J. Geophys. Res.*, **97**(9), 9959–9974.

Lobl, E. S., K. Aonashi, B. Griffith, C. Kummerow, G. Liu, M. Murakami, and T. T. Wilheit, 2007: Wakasa Bay: An AMSR precipitation validation campaign. *Bul. Amer. Meteor. Soc.*, **88**, 551–558.

Mackay, T. G., 2005: Linear and nonlinear homogenized metamaterials. *Electromagnetics*, **25**, 461–481.

Marshall, J. S. and W. H. Palmer, 1948: The distribution of raindrops with size. *J. Meteorol.*, **5**, 165–166.

Masunaga, H., T. Iguchi, R. Oki, and M. Kachi, 2002: Comparison of rainfall products derived from TRMM microwave imager and precipitation radar. *J. Appl. Meteor.*, **41**, 849–862.

Matrosov, S. Y., 1998: A dual-wavelength radar method to measure snowfall rate. *J. Appl. Meteor.*, **37**(11), 1510–1521.

Matrosov, S. Y., A. J. Heymsfield, and Z. Wang, 2005: Dual-frequency radar ratio of nonspherical atmospheric hydrometeors. *Geophys. Res. Let.*, **32**, 1–4.

Matzler, C., 2006: *Microwave dielectric properties of ice*, chap. 5. 52. IET Electromagnetic Waves Series, London, UK.

Maxwell Garnett, J. C., 1904: Colours in metal glasses and in metallic films. *Philos. Trans. R. Soc.*, **203**, 385–420.

McFarquhar, G. M. and R. A. Black, 2004: Observations of particle size and phase in tropical cyclones: Implications for mesoscale modeling of microphysical processes. *J. Atmos. Sci.*, **61**(4), 422–439.

Meissner, T. and F. J. Wentz, 2004: The complex dielectric constant of pure and sea water from microwave satellite observations. *IEEE T. Geosci. Remote*, **42**(9), 1836–1849.

Meneghini, R., H. Kumagai, J. Wang, T. Iguchi, and T. Kozu, 1997: Microphysical retrievals over stratiform rain using measurements from an airborne dual-wavelength radar-radiometer. *IEEE T. Geosci. Remote*, **35**(3), 487 – 506.

Meneghini, R. and L. Liao, 2000: Effective dielectric constants of mixed-phase hydrometeors. *J. Atmos. Ocean. Technol.*, **17**, 628–639.

Michel, B., A. Lakhtakia, W. S. Weiglhofer, and T. G. Mackay, 2001: Incremental and differential Maxwell Garnett formalisms for bianisotropic composites. *Compos. Sci. Tech.*, **61**, 13–18.

Mie, G., 1908: Beiträge zur Optik trüber Medien, speziell kolloidaler Metallösungen. *Ann. Phys.*, **26**, 597–614.

Mitchell, D. L., 1991: Evolution of snow-size spectra in cyclonic storms. Part II: Deviations from the exponential form. *J. Atmos. Sci.*, **48**, 1885–1899.

Mitra, S., O. Vohl, M. Ahr, and H. Pruppacher, 1990: A wind tunnel and theoretical study of the melting behavior of atmospheric ice particles. IV: Experiment and theory for snow flakes. *J. Atmos. Sci.*, **47**(5), 584 – 591.

Monahan, E. C. and D. K. Woolf, 1989: A comprehensive model relating the marine aerosol population of the atmospheric boundary layer to the bubble population of the oceanic mixed layer. In *AIP Conference Proceedings 197, Drops and Bubbles* (T. Wang, ed.), vol. 197 of *Third International Colloquium*, pp. 451–457. American Institute of Physics.

Negri, A. J., E. J. Nelkin, R. F. Adler, G. J. Huffman, and C. D. Kummerow, 1995: Evaluation of passive microwave precipitation algorithms in wintertime midlatitude situations. *J. Atmos. Ocean. Tech.*, **12**(1), 20–32.

Noh, Y.-J., G. Liu, E.-K. Seo, and J. R. Wang, 2006: Development of a snowfall retrieval algorithm at high microwave frequencies. *J. Geophys. Res.*, **111**(D22216), 1–16.

Olson, W., C. Kummerow, G. Heymsfield, and L. Giglio, 1996: A method for combined passive–active microwave retrievals of cloud and precipitation profiles. *J. Appl. Meteor.*, **35**, 1763–1789.

Olson, W. S., P. Bauer, C. D. Kummerow, Y. Hong, and T. Wei-Kuo, 2001a: A melting-layer for passive/active microwave remote sensing applications. Part II: Simulation of TRMM observations. *J. Appl. Meteorol.*, **40**(7), 1164–1172.

Olson, W. S., P. Bauer, N. F. Viltard, D. E. Johnson, T. Wei-Kuo, R. Meneghini, and L. Liao, 2001b: A melting-layer for passive/active microwave remote sensing applications. Part I: Model formulation and comparison with observations. *J. Appl. Meteorol.*, **40**(7), 1145–1163.

Oraltay, R. G. and J. Hallett, 2005: The melting layer: A laboratory investigation of ice particle melt and evaporation near 0c. *J. Appl. Meteor.*, **44**(2), 206–220.

Petrenko, B. Z., 2001: Retrieval of parameters of a horizontal hydrometeor distribution within the field of view of a satellite microwave radiometer. *IEEE T. Geosci. Remote*, **39**(9), 1871–1878.

Petty, G. W., 1994a: Physical retrievals of over-ocean rain rate from multichannel microwave imagery. Part I: Theoretical characteristics of normalized polarization and scattering indices. *Meteorol. Atmos. Phys.*, **54**(1-4), 79–99.

Petty, G. W., 1994b: Physical retrievals of over-ocean rain rate from multichannel microwave imagery. Part II: Algorithm implementation. *Meteorol. Atmos. Phys.*, **54**(1-4), 101–121.

Petty, G. W., 2001a: Physical and microwave radiative properties of precipitating clouds. Part I: Principal component analysis of observed multichannel microwave radiances in tropical stratiform rainfall. *J. Appl. Meteorol.*, **40**(12), 2105–2114.

Petty, G. W., 2001b: Physical and microwave radiative properties of precipitating clouds. Part II: A parametric 1D rain-cloud model for use in microwave radiative transfer simulations. *J. Appl. Meteorol.*, **40**(12), 2115–2129.

Petty, G. W., 2004: *A First Course in Atmospheric Radiation*. Sundog Publishing.

Pitman, A. J., A. Henderson-Sellers, and Z.-L. Yang, 1990: Sensitivity of regional climates to localized precipitation in global models. *Nature*, **346**, 734–737.

Prabhakara, C., G. Dalu, G. L. Liberti, J. J. Nucciarone, and R. Suhasini, 1992: Rainfall estimation over oceans from SMMR and SSM/I microwave data. *J. Appl. Meteorol.*, **31**(6), 532–552.

Prigent, C., J. R. Pardo, M. I. Mishchenko, and W. B. Rossow, 2001: Microwave polarized signatures generated within cloud systems: Special Sensor Microwave Imager (SSM/I) observations interpreted with radiative transfer simulations. *J. Geophys. Res.-Atmos.*, **106**(D22), 28243–29258.

Pruppacher, H. R. and J. D. Klett, 1997: *Microphysics of Clouds and Precipitation (2nd Ed.)*. Kluwer Academic Publishers.

Racette, P., R. F. Adler, A. J. Gasiewski, D. M. Jackson, J. R. Wang, and D. S. Zacharias, 2006: An airborne millimeter-wave imaging radiometer for cloud, precipitation, and atmospheric water vapor studies. *J. Atmos. Ocean. Tech.*, **13**(3), 610–619.

Ray, P. S., 1972: Broadband complex refractive indices of ice and water. *Appl. Optics*, **11**, 1836–1843.

Roberti, L. and C. D. Kummerow, 1999: Monte carlo calculations of polarized microwave radiation emerging from cloud structures. *J. Geophys. Res.*, **104**(D2), 2093–2104.

Rogers, R. R. and M. K. Yau, 1989: *A Short Course in Cloud Physics*. Pergamom Press, New York, 3rd edn.

Rose, C. R. and V. Chandrasekar, 2004: Space borne GPM dual-frequency radar simulation from high resolution ground radar observations. In *Geoscience and Remote Sensing Symposium, 2004. Proceedings.* (I. International, ed.), vol. 2 of *IGARSS 2004*, pp. 929–932. IEEE International, IEEE.

Rosenkranz, P. W., 1998: Water vapor microwave continuum absorption: A comparison of measurements and models. *Radio Sci.*, **33**, 919–928.

Rutledge, S. A. and P. V. Hobbs, 1984: The mesoscale and microscale structure and organization of clouds and precipitation in midlatitude cyclones. xii: A diagnostic modeling study of precipitation development in narrow cold-frontal rainbands. *J. Atmos. Sci.*, **41**, 2949–2972.

Sadowy, G. A., A. C. Berkun, W. Chun, E. Im, and S. L. Durden, 2003: Development of an advanced airborne precipitation radar. *Microwave J.*, **46**(1), 86–88.

Sassen, K., J. R. Campbell, J. Zhu, P. Kollias, M. D. Shupe, and C. Williams, 2005: Lidar and triple-wavelength doppler radar measurements of the melting layer: A revised model for dark- and brightband phenomena. *J. Appl. Meteor.*, **44**, 301–312.

Schols, J. L., J. A. Weinman, G. D. Alexander, R. E. Stewart, L. J. Angus, and A. C. L. Lee, 1999: Microwave properties of frozen precipitation around a North Atlantic cyclone. *J. Appl. Meteorol.*, **38**, 29–43.

Sekhon, R. S. and R. C. Srivastava, 1970: Snow size spectra and radar reflectivity. *J. Atmos. Sci*, **27**, 299–307.

Simpson, J., C. Kummerow, W. K. Tao, and R. F. Adler, 1996: On the Tropical Rainfall Measuring Mission (TRMM). *Meteorol. Atmos. Phys.*, **60**, 19–36.

Singh, P. and V. P. Singh, 2001: *Snow and Glacier Hydrology*, vol. 37. Kluwer Academic Publishers, Boston.

Skofronick-Jackson, G., 2003: Combined radiometer–radar microphysical profile estimations with emphasis on high–frequency brightness temperature observations. *J. Appl. Meteor.*, **42**, 476–487.

Skofronick-Jackson, G. J., J. R. Wang, G. M. Heymsfield, R. Hood, W. Manning, R. Meneghini, and J. A. Weinman, 2003: Radiometer-radar microphysical profile estimations with emphasis on high-frequency brightness temperature observations. *J. Appl. Meteor.*, **42**(4), 476–487.

Skofronick-Jackson, G. M., M.-J. Kim, J. A. Weinman, and C. D. E., 2004: A physical model to determine snowfall over land by microwave radiometry. *IEEE T. Geosci. Remote*, **42**(5), 1047–1058.

Skolnik, M. I., 1990: *Radar Handbook*. McGraw-Hill Book Co., New York, NY.

Smith, E. A., 2007: *Measuring Precipitation from Space: EURAINSAT and the Future*, vol. 28 of *Advances in Global Change Research*, chap. International Global Precipitation Measurement (GPM) Program and Mission: An overview. Springer, 1st edn.

Smith, E. A., J. E. Lamm, R. Adler, J. Alishouse, K. Aonashi, E. Barrett, P. Bauer, W. Berg, A. Chang, R. Ferraro, J. Ferriday, S. Goodman, N. Grody, C. Kidd, D. Kniveton, C. Kummerow, G. Liu, F. Marzano, A. Mugnai, W. Olson, G. Petty, A. Shibata, R. Spencer, F. Wentz, T. Wilheit, and E. Zipser, 1997: Results of WetNet PIP-2 project. *J. Atmos. Sci.*, **55**(9), 1483–1536.

Smith, P. L., 1984: Equivalent radar reflectivity factors for snow and ice particles. *J. Appl. Meteor.*, **23**, 1258–1260.

Spencer, R., B. Hinton, and W. Olson, 1983: Nimbus-7 37 GHz radiances correlated with radar rain rates over the Gulf of Mexico. *J. Clim. Appl. Meteorol.*, **22**, 2095–2099.

Spencer, R. W., 1986: Satellite passive 37-GHz scattering-based method for measuring oceanic rain rates. *J. Clim. Appl. Meteorol.*, **25**(6), 754–766.

Spencer, R. W., H. M. Goodman, and R. E. Hood, 1989: Precipitation retrieval over land and ocean with the SSM/I: identification and characteristics of the scattering signal. *J. Atmos. Ocean. Technol.*, **6**(2), 254–273.

Stocker, T. F., G. K. C. Clarke, H. Le Treut, R. S. Lindzen, V. P. Meleshko, R. K. Mugara, T. N. Palmer, R. T. Pierrehumbert, P. J. Sellers, K. E. Trenberth, and J. Willebrand, 2001: Physical climate processes and feedbacks. In *Contribution of Working Group I to the Third Assessment Report of the Intergovernmental Panel on Climate Change (IPCC)* (J. T. Houghton, Y. Ding, D. J. Griggs, M. Noguer, P. J. van der Linden, and D. Xiaosu, eds.), Climate Change 2001, Third Assessment Report, chap. Physical Climate Processes and Feedbacks. Cambridge University Press.

Stogryn, A. P., H. T. Bull, K. Rubayi, and S. Iravanchy, 1995: The microwave permittivity of sea and fresh water. *GenCorp Aerojet Report*.

Szyrmer, W. and I. Zawadzki, 1999: Modeling of the melting layer. Part I: Dynamics and microphysics. *J. Atmos. Sci.*, **56**(20), 3573–3592.

Tanelli, S., S. L. Durden, and E. Im, 2006: Simultaneous measurements of ku- and ka-band sea surface cross sections by an airborne radar. *IEEE Geosci. Remote. Sens. Let.*, **3**(3), 359–363.

Tanelli, S., E. Im, S. L. Durden, and J. P. Meagher, 2004: Rainfall and snowfall observations by the airborne dual-frequency precipitation radar during the Wakasa Bay experiment. vol. 5 of *Geoscience and Remote Sensing Symposium. IGARSS '04*. IEEE International.

Tao, W. K., S. Lang, W. S. Olson, R. Meneghini, S. Yang, J. Simpson, C. Kummerow, E. Smith, and J. Halverson, 2001: Retrieved vertical profiles of latent heat release using TRMM rainfall products for February 1998. *J. Appl. Meteor.*, **40**, 957–982.

Taylor, J., 1997: *An Introduction to Error Analysis*. University Science Books, Sausalito, California.

Testud, J., S. Oury, R. A. Black, P. Amayenc, and X. Dou, 2001: The concept of "normalized" distribution to describe raindrop spectra. A tool for cloud physics and cloud remote sensing. *J. Appl. Meteorol.*, **40**(6), 1118–1140.

Thériault, J. M., R. E. Stewart, J. A. Milbrandt, and M. K. Yau, 2006: On the simulation of winter precipitation types. *J. Geophys. Res.*, **111**(D18202).

Tikhonov, A. and V. Arsenin, 1977: *Solution of Ill-Posed Problems*. Wiley, New York.

Tran, N., D. Vandemark, C. S. Ruf, and B. Chapron, 2002: The dependence of nadir ocean surface emissivity on wind vector as measured with microwave radiometer. *IEEE T. Geosci. Remote*, **40**(2), 515–523.

Trenberth, K. E., 1998: Atmospheric moisture residence times and cycling: Implications for rainfall rates and climate change. *Climatic Change*, **39**, 667–694.

Ulbrich, C. W., 1983: Natural variations in the analytical form of the raindrop size distribution. *J. Clim. Appl. Meteorol.*, **22**, 1764–1775.

Vivekanandan, J., L. Li, L. Tsang, and C. Chan, 1997: Microwave radiometric technique to retrieve vapor, liquid and ice: Part II – Joint studies of radiometer and radar in winter clouds. *IEEE T. Geosci. Remote*, **35**, 237–247.

Wang, J., 2003: Millimeter-wave imaging radiometer (MIR) brightness temperatures, Wakasa Bay, Japan. National Snow and Ice Data Center, Digital Media.

Warren, S. G., 1984: Optical constants of ice from the ultraviolet to the microwave. *Appl. Optics*, **23**, 1206–1225.

Weinman, J. A. and P. J. Guetter, 1977: Determination of rainfall distributions from microwave radiation measured by the Nimbus 6 ESMR. *J. Clim. Appl. Meteorol.*, **16**, 437–442.

Wentz, F. J., 1999: Algorithm Theoretical Basis Document (ATBD) Version 2: AMSR ocean algorithm. Tech. rep., Remote Sensing Systems, Inc., 1101 College Ave., Suite 220, Santa Rosa, CA 95404.

Wentz, F. J., 2000: Algorithm Theoretical Basis Document (ATBD): AMSR ocean algorithm. Tech. rep., Remote Sensing Systems, Inc., 1101 College Ave., Suite 220, Santa Rosa, CA 95404.

Wentz, F. J. and R. W. Spencer, 1998: SSM/I rain retrievals within a unified all-weather ocean algorithm. *J. Atmos. Sci.*, **55**(9), 1613–1627.

Wilheit, T., 1972: *The Electrically Scanning Microwave Radiometer (ESMR) Experiment. Nimbus-5 User's Guide*. NASA/Goddard Space Flight Center.

Wilheit, T. T., 1979: A model for the microwave emissivity of the ocean's surface as a function of wind speed. *IEEE Trans. Geosci. Elec.*, **17**, 244–249.

Wilheit, T. T., 1986: Some comments on passive microwave measurement of rain. *Bull. Amer. Meteorol. Sci.*, **67**, 1226–1232.

Wilheit, T. T., A. T. C. Chang, and L. S. Chiu, 1991: Retrieval of monthly rainfall indices from microwave radiometric measurements using probability distribution functions. *J. Atmos. Ocean. Technol.*, **8**(1), 118–136.

Wilheit, T. T., A. T. C. Chang, M. S. V. Rao, E. B. Rodgers, and J. S. Theon, 1977: A satellite technique for quantitatively mapping rainfall rates over the oceans. *J. Appl. Meteor.*, **16**, 551–560.

Wilheit, T. T., C. Kummerow, R. Ferraro, R. Austin, R. Bennartz, and T. Bell, 2002: AMSR rainfall validation implementation strategy. Tech. rep., `http://rain.atmos.colostate.edu/Wakasa/V-Implement_plan.pdf`.

Woodruff, S. D., H. F. Diaz, J. D. Elms, and S. J. Worley, 1998: COADS release 2 data and metadata enhancements for improvements of marine surface flux fields. *Phys. Chem. Earth*, **23**(5), 517–526.

Zawadzki, I., W. Szyrmer, C. Bell, and F. Fabry, 2005: Modeling of the melting layer. Part III: The density effect. *J. Atmos. Sci.*, **62**(10), 3705–3723.